Development of Novel Macromolecular Organic Semiconductors for their Applications in Organic Electronics

by

Mélanie Cyr

Thesis submitted to the University of Ottawa in partial fulfillment of the requirements for the Doctorate in Philosophy degree in Chemistry

Department of Chemistry and Biomolecular Sciences
Faculty of Science
University of Ottawa

Candidate	**Supervisors**
Mélanie Cyr	Dr. Jaclyn L. Brusso
	Dr. Benoît H. Lessard

Abstract

Organic semiconducting (OSC) materials are now more than ever being exploited in modern technology for the development of next-generation organic electronic devices. These types of materials hold many advantages over their inorganic counterparts such as their mechanical flexibility, solution processibility, lighter density and strong light-matter interactions, to name a few. Nevertheless, their most attractive feature remains their ease of functionalization to adjust and optimize their optical and electronic properties. The slightest change in molecular structure can have a significant impact on the materials' ability to interact with analytes, absorb light and transport charges. This has led OSCs to be exploited in a wide array of fields including optoelectronics, sensors and actuators, energy storage, printed electronics, biomedical applications and more. This thesis looks to developing new donor-acceptor (D-A) small molecules and porphyrinoid macrocycles and evaluate their potential as *n*-type and *p*-type OSCs in organic thin-film transistors (OTFTs) as well as their potential in chemical sensing. I synthesized and characterized each novel material at the molecular level and in the solid state when processed into thin-films. The chemical derivatizations allowed to adjust the frontier molecular orbitals (FMOs) and molecular bandgap adopted by each material. I also studied their semiconducting potential in different OTFT device architectures as well as explored different device fabrication conditions to optimize their semiconducting abilities. In the latter work of this thesis, I also explored electropolymerization of silicon phthalocyanine materials to create sensing films onto quartz microbalance (QMB) sensors for mass-based detection and interdigitated electrode (IDE) sensors for electronic-based detection of various gases and volatile organic compounds (VOCs). Overall, this thesis demonstrates the design and functionalization of OSC materials and portrays the importance of structure-property relationships adopted by these materials as they are processed into thin-films for specific organic electronic applications.

Résumé

Les matériaux semi-conducteurs organiques (OSC) sont aujourd'hui plus que jamais exploités dans les technologies modernes pour le développement de dispositifs électroniques organiques de nouvelle génération. Ces types de matériaux présentent de nombreux avantages par rapport à leurs homologues inorganiques, tels que leur flexibilité mécanique, leur aptitude à être mis en solution, leur densité plus faible et leurs fortes interactions lumière-matière, pour n'en citer que quelques-uns. Néanmoins, leur caractéristique la plus attrayante reste leur facilité de fonctionnalisation pour ajuster et optimiser leurs propriétés optiques et électroniques. Le moindre changement dans la structure moléculaire peut avoir un impact significatif sur la capacité des matériaux à interagir avec les analytes, à absorber la lumière et à transporter des charges. Cela a conduit à l'exploitation des OSC dans de nombreux domaines, notamment l'optoélectronique, les capteurs et actionneurs, le stockage d'énergie, les électroniques imprimés, les applications biomédicales, etc. Cette thèse vise à développer de nouveaux composés ayant des fragments alternés donneur-accepteur (D-A) et des matériaux porphyrinoïdes, ainsi qu'à évaluer leur potentiel en tant qu'OSC de type *n* et de type *p* dans les transistors à couche mince organique (OTFT). J'ai synthétisé et caractérisé chaque nouveau matériel au niveau moléculaire et à l'état solide lorsqu'ils ont été transformé sous forme de couches minces. Les dérivations chimiques ont permis d'ajuster les orbitales moléculaires frontalières (OMF) et les bandes interdites moléculaires adoptées par chaque matériel. J'ai également étudié leur potentiel semi-conducteur dans différentes architectures de dispositifs OTFT et exploré différentes conditions de fabrication de dispositifs afin d'optimiser leurs capacités semi-conductrices. Dans la dernière partie de cette thèse, j'ai également exploré l'électropolymérisation de matériaux à base de phtalocyanine de silicium afin de créer des films de détection sur des capteurs à microbalance à quartz (QMB) pour la détection basée sur la masse et des capteurs à électrodes interdigitées (IDE) pour la détection électronique de divers gaz et composés organiques volatils (COV). Dans l'ensemble, cette thèse présente la conception et la fonctionnalisation des matériaux OSC et souligne l'importance des relations structure-propriété adoptées par ces matériaux lorsqu'ils sont transformés en films à couche minces pour des applications électroniques organiques.

Acknowledgments

As the final chapter of my graduate career finally comes to an end I cannot help but feel immense gratitude towards everyone that has been there along my journey. First off, I would like to thank my co-supervisors, Dr. Jaclyn Brusso and Dr. Benoît Lessard. You both took a chance on a very ambitious undergrad that knew very little about organic semiconductors and organic electronics and provided amazing environments where I was able to learn, grow and find a true passion in this field. For that, I am very grateful. Jaclyn, you have been such an amazing mentor to me these past 6 years. The trust you held in me over the course of my PhD has helped me gain independence and surety in my work and it also gave me confidence to keep aiming high in my career goals. I truly cherish our relationship and I honestly could not imagine having a better supervisor to have gone through this experience with. Benoît, I am so thankful to have been co-supervised by you. You made me realize that it's ok to bet on yourself and that if you don't take the risk you might just miss out on some truly great opportunities! You have been a wonderful supervisor and I feel incredibly fortunate to call myself an "honorary engineer".

I would like to thank my collaborators – Dr. Roberto Paolesse, Dr. Gabriele Magna, Dr. Francesco Pizzoli and Dr. Lorena Di Zazzo – you have not only given me amazing insight in the world of gas sensing, but you have also provided me with a wonderful Roman experience, grazie mille! I would also like to thank my doctoral committee members, Dr. Tito Scaiano, Dr. Eva Hemmer, Dr. Anatoli Ianoul and Dr. Gemma De La Torre, for reviewing my thesis and serving on my oral defense. I truly appreciate all your comments and valuable feedback on my work.

To all of my fellow Brusso and LRG lab members, thank you for being such an amazing bunch and I thoroughly enjoyed collaborating with you, and I'm sorry I did not discover the secret for F_{26}-SiPc mass production – godspeed to the chemist that will be taking over synthesizing it for the LRG army. A special shoutout to Dr. Joseph Manion, thank you to listening to my many lab crash outs, hot girls do be spiraling sometimes, but I'm happy to have had you as a lab manager and friend to come to when things got too heavy.

To my STEMM girl gang, you have no idea how finding a deep friendship with each and every one of you has had such an impact on my life. To my chem eng girlies – Kaitlyn, Halynne, Rose and May – you are the kindest and most amazing group of baddies I know. You have also taught me that literally anything is possible if you have the right amount of coffee and delusion. To my chem girlies – Meredith, Mel, Leah and Eda – my soul friends. You guys entered my life and left such a huge positive impact and I truly am so grateful for your friendship <3 you guys have been a major support system for me both in and out of the lab and I love you all so much.

À ma famille, merci beaucoup pour votre support continuel pendant tous ces années. À mes parents, Nathalie et Jimmy, vous m'aviez toujours encouragé dans tous les projets que j'ai entamé depuis mon enfance et ce dernier en n'ai aucune exception. Je vous aime énormément. Maman, je ne peux pas mettre en mots comment ton support et ton amour pendant ces dernières années me rend reconnaissante. Tu es ma plus grande cheerleader je t'adore plus que tout! À Chantale, ma 2^{e} maman, merci pour être là pour moi, je t'aime xoxo.

To my amazing friends – Emelie, Catherine, Ashley, Hanna and Nick – you guys bring so much joy in my life and you have all played an important role in keeping me sane when the going got tough. To my fur babies, Lewis, Clark and Nala, you are the best emotional support animals and the best thesis-writing company I could've asked for. And last but not least, to my Brandon, thank you simply for being you. I know I may not tell you enough, but please know that your unwavering love and support has not gone unnoticed for a single moment. I love you so much and I am so deeply fortunately to have had such a kind, loving and amazing partner cheering me on this entire time.

“What? Like it’s hard?”

– Elle Woods

(It actually really was.)

– Me

Peer-Reviewed Journal Article Contributions

Publications as Lead Author

1. **Cyr, M.**; King, B.; Lessard, B. H.*; Brusso, J. L.* Exploring ellagic acid as a building block in the design of organic semiconductors. *Dyes and Pigments*, **2022**, 199, 109998.

2. **Cyr, M.**; Brixi, S.; Ganguly, A.; Lessard, B. H.*; Brusso, J. L.* Synthesis of thieno[3,4-c] pyrrole-4,6-dione-based small molecules for application in organic thin-film transistors. *Dyes and Pigments,* **2023**, 210, 110964.

3. **Cyr, M.**; Lamontagne, H.; Lessard, B. H.*; Brusso, J. L.* Oxy Phosphorus Triazatetrabenzocorrole as a p-Type Organic Semiconductor in Organic Thin Film Transistors. *ACS Applied Electronic Materials*, **2024**, 6, 6275-6283.

4. **Cyr, M.**; Magna, G.; Pizzoli, F.; Mita, A.; Di Zazzo, L.; Paolesse, R.*; Lessard, B. H.*; Brusso, J. L.* Synthesis and Axial Electropolymerization of Novel Amino-Derived Silicon Phthalocyanine-Based Organic Semiconductors. *Journal of Materials Science*, **2026**, 61, 7621-7632.

5. **Cyr, M.**; Magna, G.; Pizzoli, F.; Di Natale, C.; Brusso, J. L.*; Lessard, B. H.*; Paolesse, R.* Electropolymerization of Phthalocyanine and Corrole Materials for Mass-Based Chemical Sensing and e-Nose Applications. *ACS Sensors*, **2026**, 11, 1625-1633.

Publications as Co-Author

6. Lamontagne, H. R.; **Cyr, M.**; Vebber, M. C.; Swaraj, S.; Harris, C. S.; Brusso, J. L.; Shuhendler, A. J.; Lessard, B. H.* $(F_5PhO)_2$-F_{16}-SiPc as an Air-Stable, High-Performance n-Type Semiconductor with Poor Cannabinoid Sensing Capabilities. *RCS Applied Interfaces*, **2024**, 1, 1222-1232.

7. Cruz, M. V.‡; **Cyr, M.**‡; Boughanmi, H.; Calvo J. G.; Brusso, J. L.; Torres, T.; Lessard, B. H.* Coordination of Ruthenium Phthalocyanine with Poly(4-vinylpyridine). *Polymer Chemistry*, **2024**, 15, 3475-3479.

8. Ourabi, M.; Vebber, M. C.; **Cyr, M.**; Weintrager, F. S-D.; Ledos, N.; Lamontagne, H. R.; Nyayachavadi, A.; Brusso, J. L.; Lessard, B. H.* Silicon Phthalocyanine-based N-Type Organic Mixed Ionic-Electronic Conductor in Organic Electrochemical Transistors. *Journal of Materials Chemistry C*, **2025**, 13, 18167-18175.

9. Tilahun, T.; **Cyr, M.**; Ourabi, M.; Lessard, B. H.; Brusso, J. L.* Development of novel symmetrical and asymmetrical alkyne-functionalized silicon phthalocyanines, a potential functionality control for organic semiconductors. *Journal of Porphyrins and Phthalocyanines*, **2026**, 30, 125-136.

Table of Contents

List of Figures

List of Tables

List of Key Abbreviations

AFM	Atomic Force Microscopy
BGBC	Bottom-Gate Bottom-Contact
BGTC	Bottom-Gate Top-Contact
CA	Chronoamperometry
CuCorr	Copper Corrole
CV	Cyclic Voltammetry
D-A	Donor-Acceptor
DBU	1,8-diazabicyclo[5.4.0]undec-7-ene
DSC	Differential Scanning Calorimetry
EI	Electron Impact
ESI	Electrospray Ionisation
e-Nose	Electronic Nose
FMO	Frontier Molecular Orbital
FT-IR	Fourier Transform Infrared
GC-MS	Gas Chromatography-Mass Spectrometry
HPLC	High-Performance Liquid Chromatography
HOMO	Highest Occupied Molecular Orbital
HRMS	High-Resolution Mass Spectrometry
ICT	Intramolecular Charge Transfer
IDE	Interdigitated Electrode
ITO	Indium Tin Oxide
LOD	Limit of Detection
LSER	Linear Solvation-Energy Relationship
LUMO	Lowest Unoccupied Molecular Orbital
MALDI	Matrix-Assisted Laser Desorption/Ionization
MOSFET	Metal-Oxide Semiconductor Field-Effect Transistor
MPc	Metal Phthalocyanine
MPor	Metal Porphyrinoid
NMR	Nuclear Magnetic Resonance
ODTS	*n*-octadecyltrichlorosilane
OFET	Organic Field Effect Transistor

OLED	Organic Light Emitting Diode
OPV	Organic Photovoltaic
OSC	Organic Semiconductor
OTS	*n*-octyltrichlorosilane
PAH	Polyaromatic Hydrocarbons
Pc	Phthalocyanine
PC	Principal Component
PCA	Principal Component Analysis
PFTS	3,3,3-trifluoropropyl trichlorosilane
PL	Photoluminescence
PO-Tbc	Phosphorus^{V} oxide triazatetrabenzocorrole
PTFE	Polytetrafluoroethylene
PTS	Phenyltrichlorosilane
PVD	Physical Vapour Deposition
p-6P	*para*-sexiphenylene
QMB	Quartz Microbalance
SAM	Self-Assembled Monolayer
SCE	Saturated Calomel Electrode
SEM	Scanning Electron Microscopy
SiPc	Silicon Phthalocyanine
TBAP	Tetrabutyl Ammonium Perchlorate
TD-DFT	Time-Dependent Density-Functional Theory
TEA	Triethylamine
TGA	Thermogravimetric Analysis
TMA	Trimethylamine
TOF	Time-of-Flight
TPD	Thieno[3,4-c] pyrrole-4,6-dione
UV-Vis-NIR	Ultraviolet–Visible–Near Infrared
VOC	Volatile Organic Compound
WF	Work Function
XRD	X-ray Diffraction

List of Key Variables

C_i	Capacitance Density
E	Energy
E_g^{opt}	Optical Bandgap Energy
$E^{0/-1}$	Radical Anion Energy
$E^{0/+1}$	Radical Cation Energy
E_{HOMO}^{th}	Theoretical HOMO Energy
E_{LUMO}^{th}	Theoretical LUMO Energy
E_g^{th}	Theoretical bandgap Energy
e^-	Electron
g_m	Transconductance
h^+	Hole
$I_{on/off}$	on/off Current Ratio
I_{SD}	Source-Drain Current
L	Channel Length
$\mathrm{Log}L^{16}$	Solubility Term
N	Defect Density
R	Polarizability
R_C	Contact Resistance
S	Sensitivity
t	Time
T	Temperature
$\mathrm{T_d}$	Decomposition Temperature
V_{GS}	Gate-Source Voltage
V_{SD}	Source-Drain Voltage
V_T	Threshold Voltage
W	Channel Width
α^H	Hydrogen Bond Acidity
β^H	Hydrogen Bond Basicity
f	Oscillator Strength
δ	Chemical Shift
λ	Wavelength
μ	Field-Effect Mobility
μ_e	Electron Mobility
μ_h	Hole Mobility
θ_w	Water Contact Angle
π	Dipolarity

List of Key Units

A	Ampere
Å	Angstrom
a.u.	Arbitrary Unit
cm^{-1}	Reciprocal Centimeter
eV	Electron Volt
h	Hour
M	Molar
MHz	Megahertz
mL	Millilitre
mmol	Millimole
nm	Nanometer
ppm	Parts Per Million
s	Second
V	Volt
W	Watt
°C	Degree Celsius
µm	Micrometer

Summary of Chemical Structures

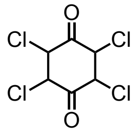

1-1

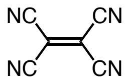

1-2

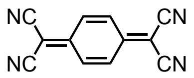

1-3

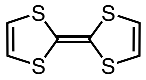

1-4

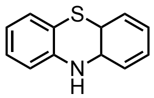

1-5

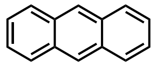

1-6

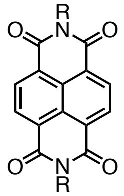

1-7
2-8

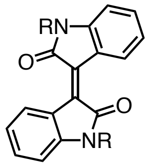

1-8
2-7

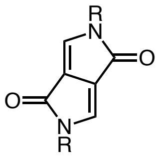

1-9

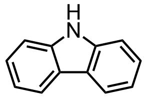

1-10

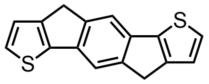

1-11

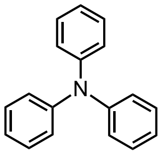

1-12

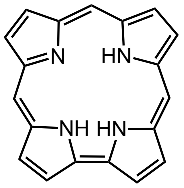

1-13

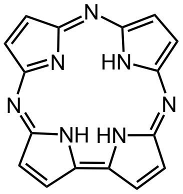

1-14

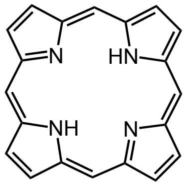

1-15

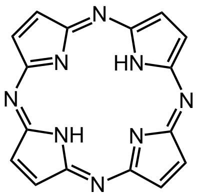

1-16

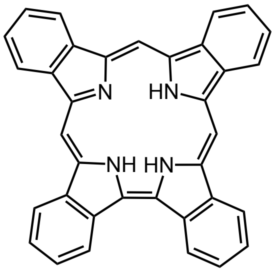

1-17

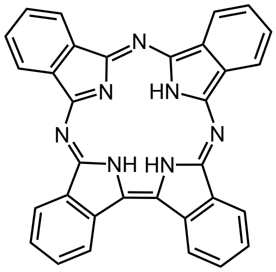

1-18

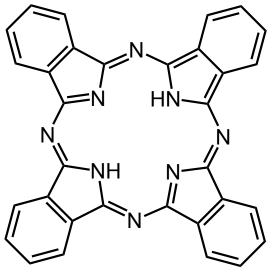

1-19
3-1

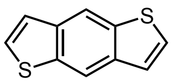

2-1

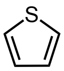

2-2

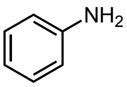

2-3

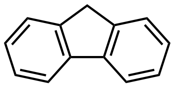

2-4

2-5

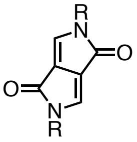

2-6

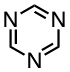

2-9

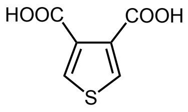

2-10

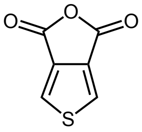

2-11

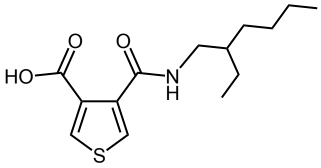

2-12

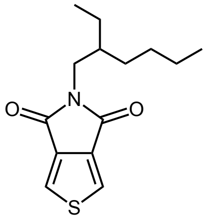

2-13

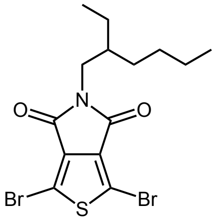

2-14

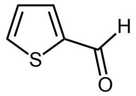

2-15

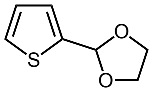

2-16

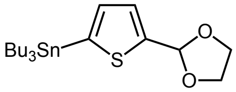

2-17

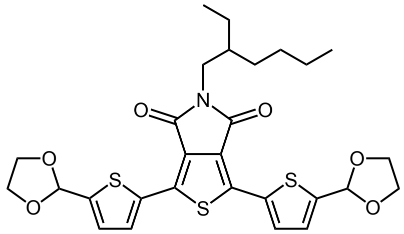

2-18

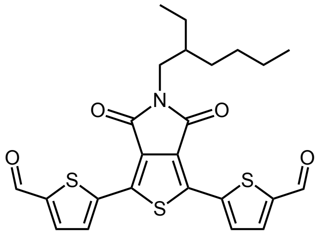

2-19

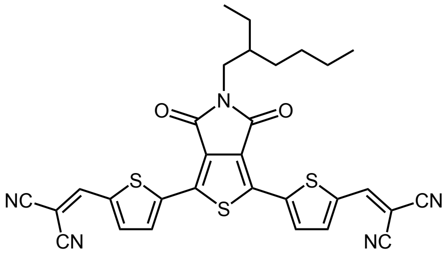

2-20

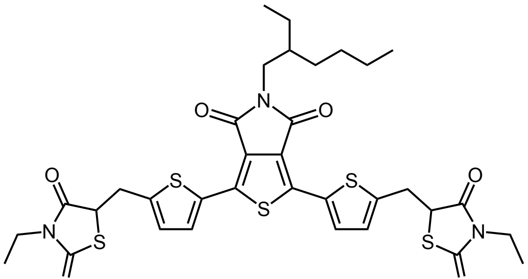

2-21

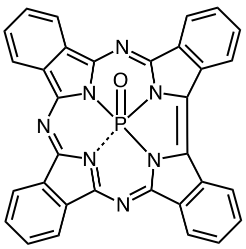

3-2

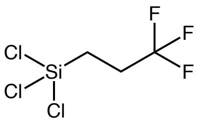

3-3

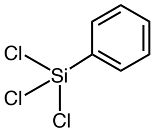

3-6

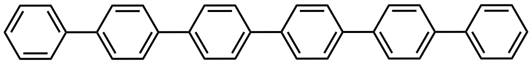

3-4

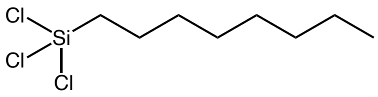

3-5

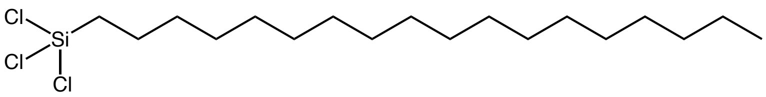

3-7

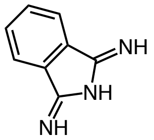

4-1

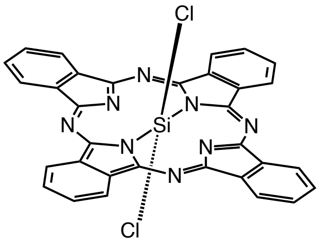

4-2

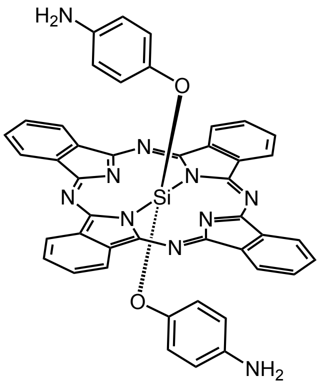

4-3

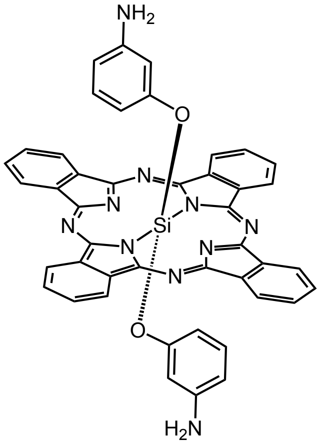

4-4

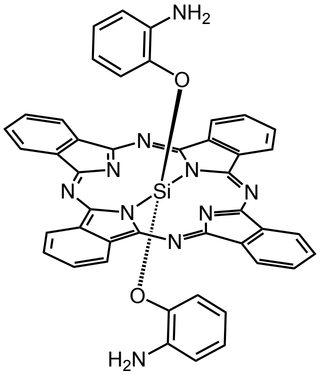

4-5

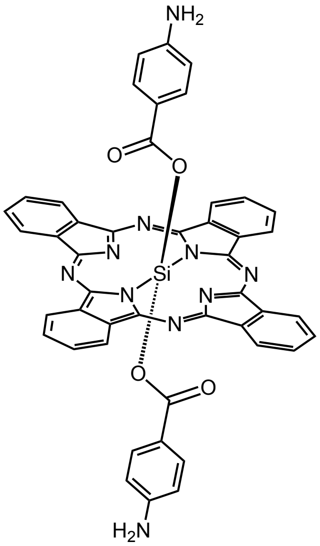

4-6

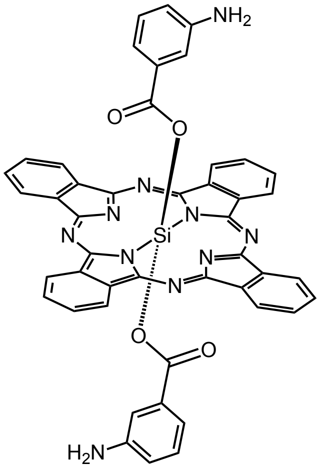

4-7

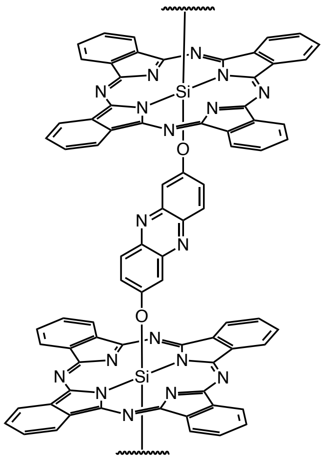

5-1
6-1

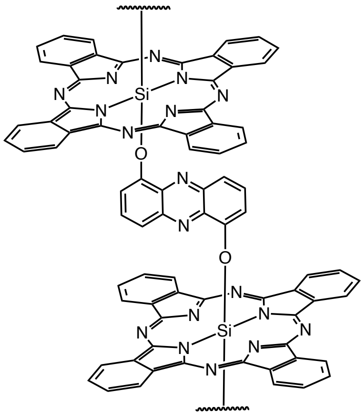

5-2
6-2

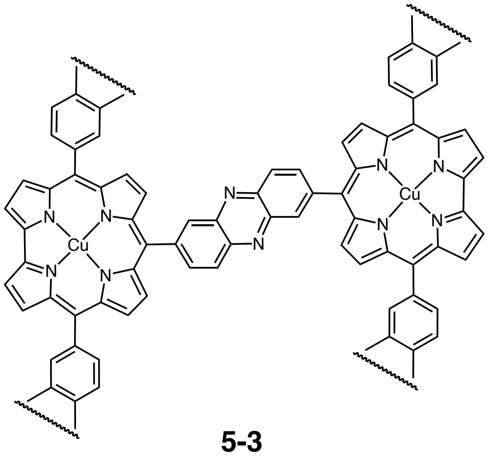

5-3

Chapter 1. Introduction

This chapter will provide an overview on organic semiconducting materials and their key components as well as a summary of various organic electronic devices, and how they are built and function alongside the key parameters used to evaluate their performance.

1.1 Organic Semiconductors

Organic semiconducting (OSC) materials have made tremendous progress since their first appearance in the mid 20th century (**Figure 1.1**). The first organic semiconducting material made its debut in 1948 when the photoconductivity of anthracene was discovered by A. V. Volkov and coworkers[1] thus leading to exploration of polyaromatic hydrocarbons (PAHs) for their semiconducting abilities in the 1950s.[2] Transitioning into the 1960s, the development of organic semiconductors took a turn towards the design of donor-acceptor complexes where tetrathiafulvalene–tetracyanoquinodimethane (TTF-TCNQ) became the first intentionally designed organic material exhibiting metallic behaviour in 1973.[3] These findings help modulate the partial electron transfer from donor to acceptor in a more “band-like” manner compared to “charge hopping” seen in earlier materials. In 1977 the field of organic semiconductors experienced groundbreaking advancements through the achievement of metal-like conductivity using doped polyacetylene.[4] This discovery was made by Shirakawa, MacDiarmid and Heeger and later won the 2000 Nobel prize in Chemistry.[5] Their discovery ultimately laid the foundation for the development of organic semiconducting polymers and the establishment of organic electronics such as organic light emitting diodes (OLEDs), organic photovoltaics (OPVs), organic field effect transistors (OFETs) and more.[6–8]

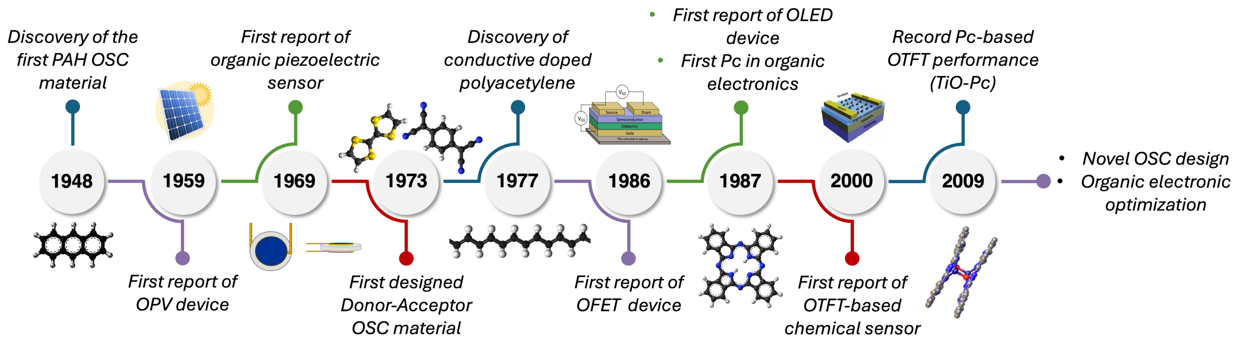

Figure 1.1 *Timeline depicting key discoveries having a large impact in the fields of organic semiconductors and organic electronics ultimately leading to today’s progress in these domains.*

More specifically, semiconducting materials consist of a class of solids that hold electrical properties that sit intermediately between conductive materials, like metals, and insulating materials, like glass or rubber.[9] For organic semiconductors, the semiconducting behaviour stems from the conjugated π-system embedded in the molecule. The π-system is composed of alternating single and double bonds, leading to delocalization of the π-electrons over the molecule, which can be exploited for the transport of either positive (*p*-type) or negative (*n*-type) charges along the conjugated backbone.[10] From a molecular orbital standpoint, the conjugated system forms a linear combination of atomic *p*-orbitals from which delocalization creates a series of bonding (π) and antibonding (π^*) molecular orbitals.[11,12] The bonding orbitals are present at a lower energy and possess the ground state π-electrons, whereas the antibonding orbitals will sit at a higher energy and are generally empty. As the π-system grows, more bonding and antibonding orbitals are added, rendering the energetic difference between each orbital smaller (as seen in **Figure 1.2**).[9] When transitioning from the molecular state to a bulk solid state, the energetic spacing between the orbitals gets infinitely small, where one can consider fusion of the bonding and antibonding orbitals ultimately leading to what is commonly known as the valence and conduction bands, respectively.[13]

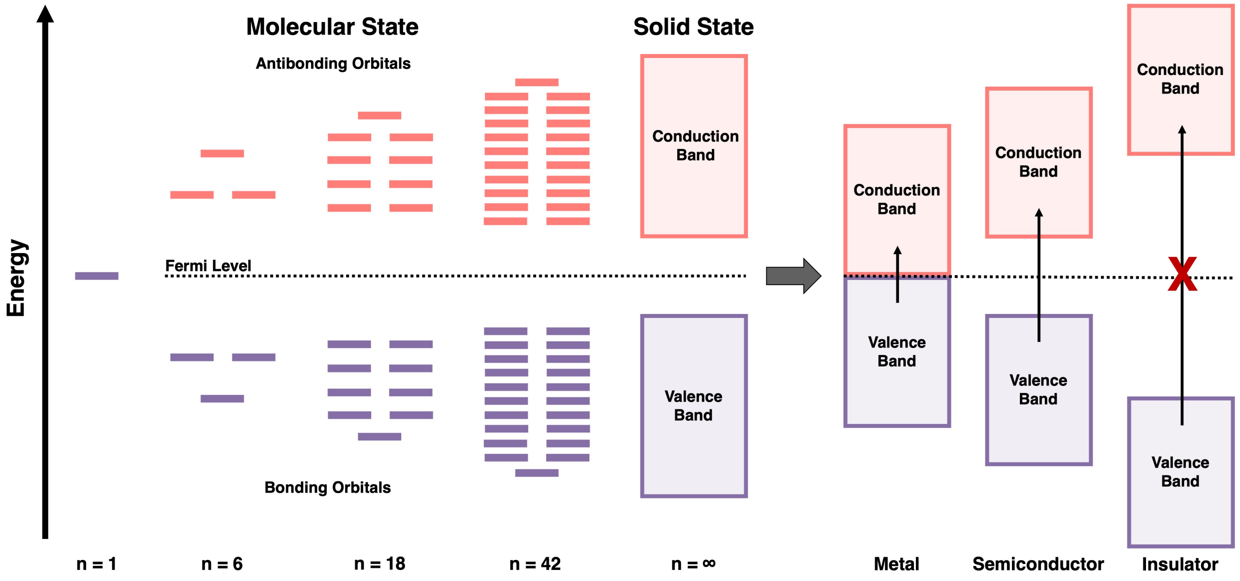

Figure 1.2 *Energy level diagram distinguishing the MOs of a growing π-system leading towards the transition into solid state and how these MOs result in energetic bands as well as how these energetic bands vary in terms of different types of materials.(Figure adapted from [15])*

The inner boundaries of these bands are analogous to the Highest Occupied Molecular Orbital (HOMO) and Lowest Unoccupied Molecular Orbital (LUMO) represented in the molecular state. The bandgap present between the inner boundaries of the valence and conduction bands is distinguished by the Fermi Level which is representative of the energy at which the probability of finding an electron is at 50%.[14] Furthermore, due to the bandgap being neither too small nor too large, electrons in an OSC can be excited into the conduction band through manageable inputs of energy such as heat, light or electric fields.

Although their conductivity is lower than what is typically observed in other conductive materials (i.e. metals), the attractive features held by semiconductors, like their ability to be turned "on" and "off", uniquely sets them apart to be exploited in distinct applications.[16] The ability to apply structural modifications through established synthetic pathways enables finetuning of optoelectronic properties *via* direct molecular design.[17–19] Over the many decades of OSC material development, there have been many different classes of conjugated materials that have been explored for their semiconducting abilities.[19–21] This now leads OSCs into the 21st century with the evolution of new classes of materials within the families of donor-acceptor small molecules, porphyrinoids and organic polymers, opening pathways to flexible and low-cost electronics.[20,21]

1.1.1 Donor-Acceptor Semiconducting Small Molecules

Donor-Acceptor (D-A) small molecules stand at the forefront of OSC material development in the advancement of optoelectronic technologies. These materials are designed by covalently linking electron-rich (donor) and electron-deficient (acceptor) units within a π-conjugated system.[22,23] Furthermore, changing the molecular design of these materials through the inclusion of various donor and acceptor moieties enables precise control over the frontier molecular orbital (FMO) energies,[24] leading to the modulation of their absorption profile and redox characteristics.[25,26] Generally, donor moieties are engineered to have an increased (higher energy) HOMO level and acceptor moieties have a lowered (lower energy) LUMO level. This strategic energy-level alignment is crucial for efficient charge transfer.[24] Additionally, having varying electron densities throughout the molecular framework will in turn produce a "push-pull" effect caused by the different D-A linkers, ultimately enhancing the intramolecular charge transfer (ICT) interactions.[27] This effect not only plays a crucial role in the potential narrowing of the solid-state bandgap (i.e. red-shifted optical absorption properties), but also facilitates efficient exciton dissociation, a key criterion in operating high-performance organic electronics.[28] Exciton dissociation refers to the process of excited charge separation. More specifically, when a photon is absorbed by a semiconducting material, an electron is promoted from its ground state (valence band) to its excited state (conduction band), generating an electron-hole pair which are bound together by Coulomb forces. In order to have charge transport occur, there needs to be sufficient energy to allow for the electron-hole pair to separate and move independently.[29]

Over the course of almost a century, the design and development of different donor and acceptor moieties commonly used in D-A materials has evolved tremendously. During the dawn of organic semiconductors, the linkers used for D-A materials adopted much simpler and smaller frameworks (as seen in **Figure 1.3**).[30] For donors in particular, aromatic amines (e.g. aniline), polycyclic hydrocarbons (PAHs) and phenothiazine derivatives were commonly employed.[31–33] As for acceptors, electron poor aromatics served as the foundation for the first charge-transfer complexes. This included quinone derivatives, halogenated and nitro-substituted aromatics and tetracyanoethylene (TCNE).[34] However, it was not until the mid 1970s, when tetrathiafulvalene–tetracyanoquinodimethane (TTF-TCNQ) was designed, that the field of D-A materials began advancing. TTF-TCNQ was the first material that provided measurable electronic conductivity through the formation of a crystalline salt.[3,35] This breakthrough not only highlighted the importance of π-conjugation and charge delocalization, but it also emphasized the significance of lattice stacking to obtaining highly conductive properties.[36] Now moving towards modern advancements, D-A materials are synthesized to include both the donor and acceptor within a single π-conjugated backbone to induce intramolecular charge transfer (ICT).[37] Acceptor moieties have also evolved towards larger fused-ring frameworks such as diketopyrrolepyrrole (DPP),[38] naphthalene diimide (NDI),[39] isoindigo (IID),[40] and benzothiadiazole (BT),[41] to name a few. These acceptors all possess planar electron deficient cores with tunable functionalities at the amine positions, allowing for further modulation of the moiety to tailor the energetic bandgap of the materials. On the other hand, commonly used donors have also evolved into larger planar fused frameworks like carbazole,[42] benzodithiophene (BDT)[43] and indacenodithiophene (IDT)[44] which allow for a strong push-pull effect. Thus, modern D–A semiconductors directly evolved from principles uncovered in early charge-transport complexes such as orbital complementarity, charge-transfer energetics and structure-dependent electronic coupling.

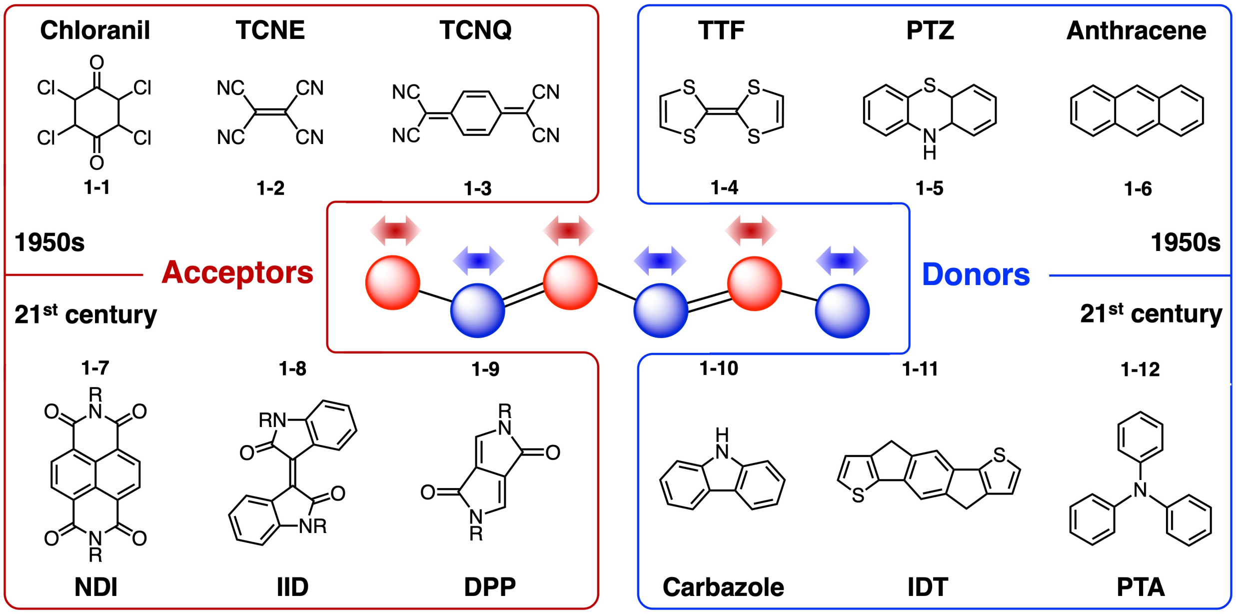

Figure 1.3 *Ball and stick representation of a conjugated donor (blue) acceptor (red) molecule with arrows demonstrating the intramolecular push-pull effect caused by the varying electron density from the D-A linkers. List of common donor (blue, right) and acceptor (red, left) moieties used in the mid 1900s (top) and in the 21st century (bottom).*

1.1.2 Porphyrinoid-Based Semiconductors

One of the largest and most structurally diverse families of π-conjugated macrocyclic materials are the porphyrinoids. The term porphyrinoid is used relatively broadly as it encompasses a wide variety of molecular subclasses that can vary in ring sizes, number of π-electrons, heteroatom positioning and oxidation states. However, what unifies them as a collective family is that they all represent a cyclic array of pyrrolic-like units linked through methine or aza-groups to form a delocalized aromatic framework.[45] Commonly known porphyrinoid materials include porphyrins, corroles, porphyrazines and phthalocyanines (**Figure 1.4**).

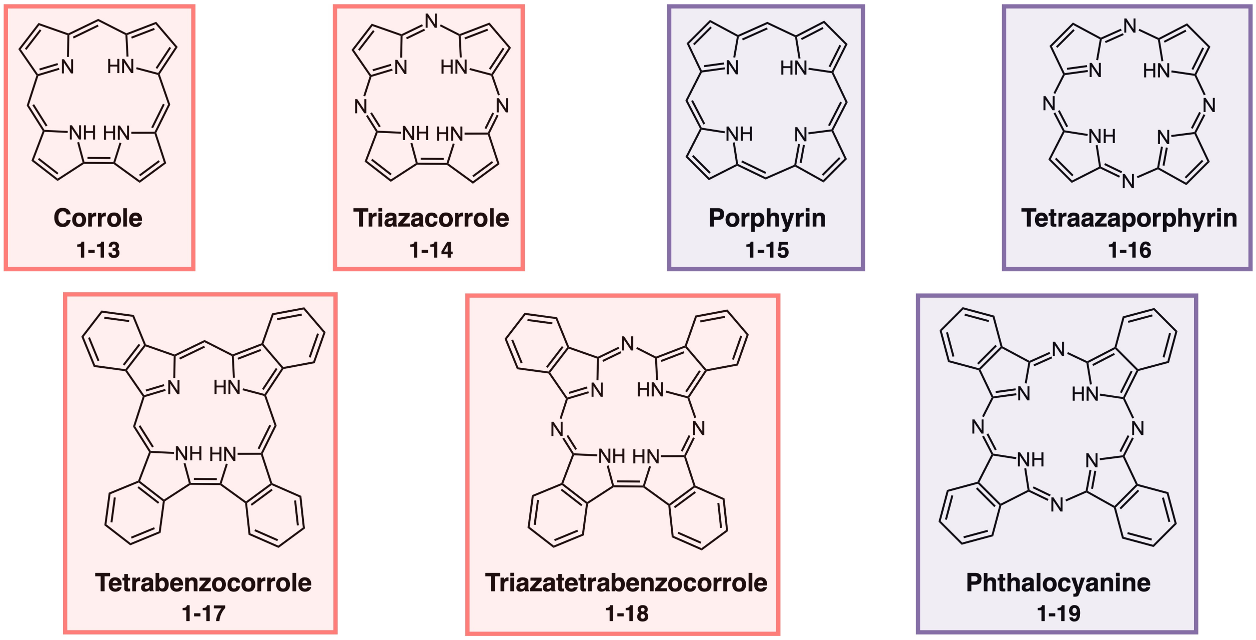

Figure 1.4 *Subclasses of corroles (pink) and porphyrins (purple) encompassed by the porphyrinoid family.*

Despite their discovery as prominent organic semiconducting materials in mid-late 1900s, porphyrinoid materials remain one of the most sought out and studied families of OSCs as they offer a combination of molecular and electronic tunability through modulation *via* metal coordination, peripheral substituents, ring fusion, or controlled distortion of the π-system.[45] These key modulations allow porphyrinoids to stand out from other OSC materials as they allow researchers to tailor a wide variety of their chemical properties such as their absorption onsets,[46] redox potentials[47] and solid-state organization[48,49] with a degree of precision that is difficult to attain in other OSC families, all while maintaining a high degree of chemical and thermal stability. This has led porphyrinoid materials to be employed in many different organic electronic applications, including photodetectors,[50–52] OFETs,[53–55] OPVs,[56,57] OLEDs[58,59] and chemical sensors.[60–62] Furthermore, given their prominent planarity, porphyrinoids also tend to exhibit supramolecular behaviour in their solid-state due to their strong intermolecular π–π interactions that enables them to adopt a highly ordered packing arrangement.[63] From an organic electronics perspective, the adopted packing arrangement becomes highly important as it can dictate the charge carrier mobility, exciton diffusion and optical properties of these materials, intertwining molecular structure and solid-state morphology in device optimization.[49,64–66]

In terms of chemical structure, the porphyrinoid family can be divided up into two main subclasses, corroles and porphyrins. Both corroles and porphyrins possess a four-unit pyrrole macrocycle, however they distinguish themselves by the number of methine spacings present between each pyrrole. Whereas porphyrins contain a methine bridge between each pyrrole unit, corroles only have three methine bridges in total, leading two pyrrole units to be directly bonded together. This in turn alters the ring size and the number of π-electrons present (18 π-electrons for porphyrins vs. 17 π-electrons for corroles). Additionally, both corroles and porphyrins can be further chemically altered by either adding benzyl groups on the outer edges of the pyrrole units or by swapping the methine bridging linkers for imines. Another key feature in the structural diversity of porphyrinoids is the possibility to incorporate a metal at the centre of the macrocycle. This distinct functionality plays a crucial role for the porphyrinoid to adopt distinctive electronic,[67,68] magnetic[69–71] and optical characteristics[72,73] that can be capitalized for precise applications.

Among this expansive family, phthalocyanines (Pcs) hold a particularly prominent position. Pcs consist of the largest macrocycle subclass among all porphyrinoids, holding four benzyl groups off all four pyrrolic edges and four bridging imines between each unit. In particular, Pcs stand out due to their Q-band property, a broad and intense absorption that extends into the visible and near-infrared regions (500-700 nm).[74] Initially discovered for their intense pigmentation as a commercial dye in early 1900s,[75,76] researchers soon discovered that Pcs have far more to offer with impressive thermal, photochemical and oxidative stability leading them to be exploited as efficient organic semiconducting materials.[74] Pcs are particularly attractive functional materials because they can be synthesized in only a few, high-yielding steps from inexpensive and readily available precursors. This synthetic simplicity stands in contrast to many donor–acceptor (D–A) organic materials, which often require lengthy, multi-step routes involving costly intermediates and extensive purification, significantly increasing overall expense and limiting scalability. As a result, there is growing interest in developing alternative synthetic strategies that prioritize efficiency, robustness and large-scale viability. Importantly, phthalocyanines already demonstrate this scalability in everyday life: they are produced on multi-ton scales for commercial applications such as pigments (e.g. Phthalo Green and Phthalo Blue), highlighting both their synthetic maturity and their compatibility with industrial manufacturing. Form a structural standpoint, Pcs are extremely versatile as they house multiple areas that can be targeted to help tune the material's bulk or optoelectrical properties, namely at the bay and peripheral positions. However, the most attractive feature for Pc modulation is the ability to incorporate a metal or metalloid at the centre of the macrocycle. Over the years, over 70 different elements have been incorporated, ranging from Groups 1 to 15.[77,78] These metals play a crucial role in the diversification of the optical, electrical and magnetic features held by MPcs.

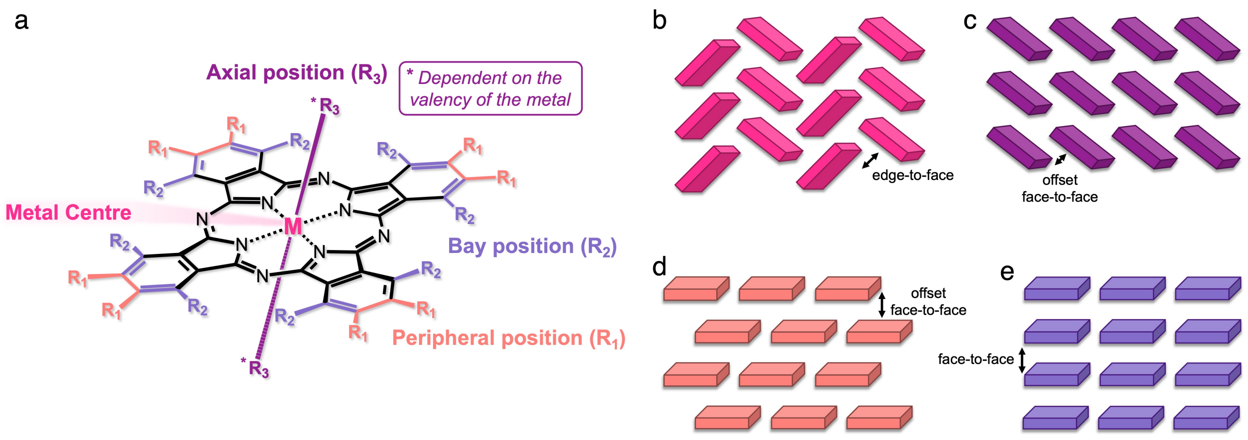

Figure 1.5 *(a) General metal phthalocyanines structure alongside the three key areas that can undergo functionalization, namely the bay, peripheral and axial positions. Packing motifs that can be adopted by MPcs: (b) herringbone, (c) slipped stack, (d) brickwork and (e) cofacial.*

Depending on the target metal, different valencies will be acquired, which can also lead the MPc to possessing axial components in and out of plane of the macrocycle.[48,68,79,80] Geometrically, like all other porphyrinoids, Pcs are comprised of a planar macrocyclic framework; however, certain MPcs will hold an umbrella shape depending on the size of the metal that is coordinated at centre.[81,82] This in turn can influence the crystal packing and solid-state morphology of the material.[83–85] Additionally, the presence or absence of axial components will also have a large impact on the solid-state packing structure of MPcs as these can also change the material from a 2-D to 3-D conformation. One of the attractive qualities of MPcs is that they are known to often adopt unique polymorphs when implemented into thin-films (as highlighted in **Figure 1.5b-e**).[86–88] This is largely due to the intricate π–π stacking and intermolecular Van Der Waals forces present between molecules. Having Pcs adopt an ordered polymorph, a strong overlap of the electron density clouds can ultimately lead to more efficient intermolecular charge transport. As a result, this has led MPcs to serve as remarkable organic semiconductors and still to this day MPcs serve as benchmark materials in applications such as organic thin-film transistors, organic photovoltaics, photodiodes, and more.

1.1.3 Semiconducting Polymers

Complementary to their small molecular counterparts, semiconducting polymers are another major category of OSC materials. Designed to include a continuous π-conjugated backbone, polymeric OSCs offer a number of advantages and trade-offs that sets them apart from small molecule OSCs. Whereas small molecule frameworks highly rely on crystallinity and ordered packing arrangements to convey good intermolecular charge transport, the inherently larger π-system present in OSC polymers lessens the need to obtain highly ordered packing as these materials tend to possess more efficient intramolecular charge transport.[89] Similar to small molecules, polymeric OSCs can also undergo a variety of structural modifications to help finetune their optoelectronic properties, namely through monomeric molecular design, side-chain engineering and copolymerization processes.

Since the report of the first doped polyacetylene in the 1970s,[4] polymeric OSCs have also undergone a massive evolution to arrive at the current leading polymers used today. The early leading OSC polymers consisted of polyacetylene,[4] polyaniline[90] and polypyrrole[91] frameworks. Although these served as a good foundation in the field, issues were raised in terms of their durability and longevity as these materials lacked stability and were also difficult to process which led to non-uniform thin-films and ultimately limited their potential for organic electronic applications. A few decades later, the design of poly(*para*-phenylenevinylene) (PPV)[92] and poly(3-hexylthiophene) (P3HT)[93] sought to address these concerns with higher overall stability and better solution processability. This led PPV to be incorporated in the first ever reported OLED device[94] and P3HT became a benchmark OSC polymer used for OTFTs and OPVs due to its improved solubility, thin-film quality and semicrystalline ordering.[95,96] Moving into recent decades, OSC polymers are now being designed with the concept of D-A copolymerization to hold the same push-pull effect that was initially installed in small molecule OSCs.[37] This served as a big step forward in material development as it allowed for OSC polymers to maintain their good solution processing qualities while implementing finite bandgap tuning and enhancing their absorption profiles. Currently used D-A polymers in the field include common DPP, NDI and IID-based polymers that are copolymerized with either thiophene, BDT or IDT donors. Given the range of available donor and acceptor moieties, D-A polymers remain prevalent in the design of new materials used in applications such as flexible displays, wearable sensors, and next-generation bioelectronics.[97–99] Overall, OSC polymers offer several relative advantages over small-molecule OSCs, including compatibility with multiple processing techniques such as solution casting, printing, coating and roll-to-roll fabrication, as well as improved tolerance to defects and, in many cases, better control over batch-to-batch variation once synthesis and formulation are optimized. Their mechanical flexibility and ease of chemical tunability further enable property control across large areas and diverse device architectures. However, from an industrial perspective, these advantages have not yet translated into widespread commercial adoption. Despite extensive academic research, there are relatively few realized applications of conjugated polymers, especially when compared with small-molecule OSCs, which are already employed in a broader range of established and emerging technologies.

1.1.4 Thin-Film Processing of OSCs

Although the molecular design of novel OSC materials is crucial for achieving semiconductors with favorable redox behavior, broad absorption profiles, and energy levels compatible with the work functions of target electrodes, these properties are strongly influenced at the operational level once the materials are processed into solid-state thin-films. The performance of organic electronic devices, including OTFTs, OPVs, OLEDs and organic sensors is critically dependent on the structure and morphology of OSC thin-films. For this reason, the deposition method used to create OSC thin-films will have a large impact on the resulting structure-property relationships of these materials. There are two main techniques that are used in thin-film processing of OSCs, which are vacuum-based thermal deposition and solution processing. Among these two categories are physical vapour deposition (PVD), a vacuum-induced sublimation of the OSC material directly onto a substrate,[100] and spin coating, a rapid solution spreading of the OSC material by centrifugal force (**Figure 1.6**).[101] While both techniques are broadly used in small-scale laboratory research and large-scale industrial applications, they vary significantly in their processing mechanisms, material demands and the thin-film qualities they produce.

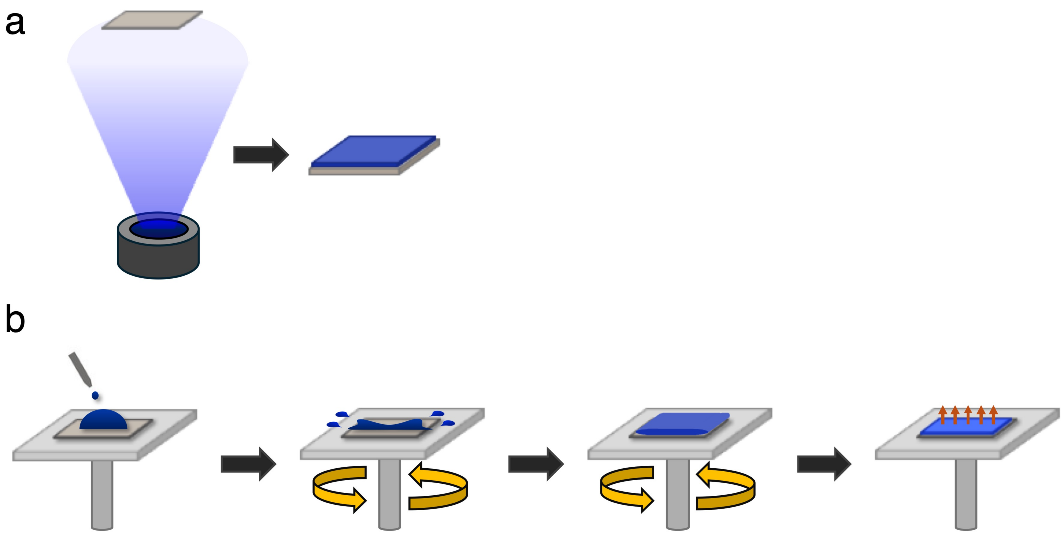

Figure 1.6 *Diagram of two OSC deposition methods used in thin-film processing. (a) Physical vapour deposition (PVD). (b) Spin coating.*

More precisely, PVD is a high-vacuum deposition technique where the OSC material is sublimed and subsequently condensed onto a cooled substrate surface.[102] In order for a material to undergo this type of processing it needs to adhere to several requirements to ensure the sublimation occurs smoothly. Such requirements include high thermal and chemical stability, low-volatility, weak intermolecular interactions, clean phase transition (i.e. no melting or decomposition), low impurity content and structural integrity upon re-condensation. Despite its higher cost in energy, this method holds multiple advantages, namely it will generally produce higher purity thin-films without exposing underlying layers to solvents while also affording high precision in thickness control. With the option of controlling the deposition rate and the substrate temperature independently, PVD can also play an active role in optimizing the molecular orientation of the OSC directly during the deposition process. In the context of small molecule OSCs (e.g. MPcs) this can dictate whether the molecules adopt a more edge-on (i.e. where the molecular plane sits perpendicularly with respect to the substrate surface) or more face-on (i.e. where the molecular plane sits parallel with respect to the substrate surface) configuration.[103] From a semiconducting perspective, this can influence the charge transport properties of the material.[104] These qualities of PVD make it a suitable deposition technique to prepare uniform thin-films with minimal defects used for high-performance OLED manufacturing and small molecule OFETs and OPVs.

Alternatively, spin coating is a solution-based deposition technique where the OSC material is dissolved in solution and dispensed directly onto a substrate that is rapidly spinning, leading the centrifugal force to spread the solution to form a thin-film upon solvent evaporation.[105] This process can be done dynamically (i.e. where the solution is dispensed while the substrate is already in motion) or statically (i.e. where the solution is dispensed on an immobile substrate and subsequently spun afterwards).[12] Although spin coating does not hold the same amount of precision when it comes to thin-film formation, its attractiveness stems from its simplicity, low operational costs, and simpler compositional control (e.g. incorporation of blends, additives or dopants). Additionally, spin coating (alongside other solution processing methods) accommodate a wider range of OSC materials that are otherwise not capable of being sublimed including semiconducting polymers, carbon nanotubes and soluble small molecule OSCs. Unlike PVD where molecular ordering is governed by substrate temperature and deposition rate, spin coating molecular ordering can be modulated by solvent choice and drying kinetics, parameters which are dependent on viscosity, solvent evaporation rate and solute aggregation behaviour.[106,107] For that reason, spin-coated films will often exhibit greater variability in their resulting morphology and may require post-processing treatments such as thermal annealing to achieve the desired molecular ordering.[108–110]

1.2 Organic Thin-Film Transistors

Organic thin-film transistors (OTFTs) (**Figure 1.7a**) are a class of organic electronic devices that make use of organic semiconducting materials as their primary active layer. OTFTs consist of a multi-layer solid-state stack comprised of four key components: a gate electrode, an insulating dielectric layer, an active semiconducting layer and source-drain electrodes. These layers are arranged together on top of a solid or flexible substrate in one of four ways (**Figure 1.7b-e**) where the general guideline is that the gate should always be in direct contact with the dielectric material and the source-drain electrodes should always be in direct contact with the semiconducting material.[111] Unlike traditional silicon-based inorganic transistors, using OSCs in their fabrication process allows OTFTs to bend, stretch and conform to unconventional surfaces. This ultimately opens their applicability in avenues that simply could not be obtained by inorganic electronics such as flexible displays, wearable sensors and electronic skins.[112–114]

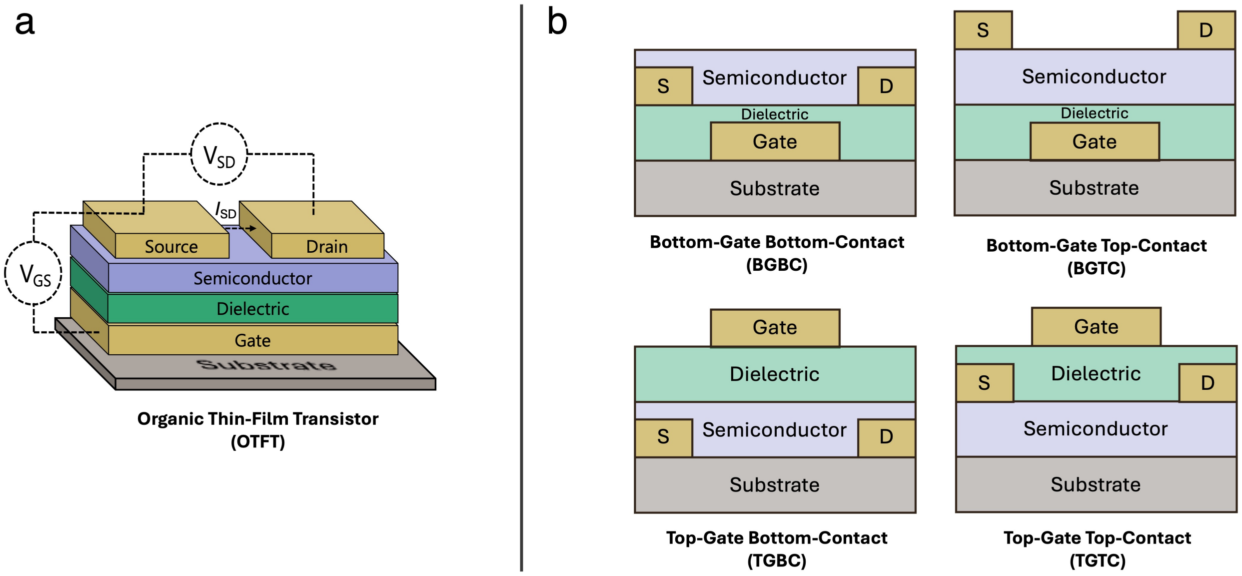

Figure 1.7 *(a) Organic thin-film transistor (OTFT) architecture with the applied voltages (V_{GS} and V_{SD}) and measured current (I_{SD}) during normal operation. (b) Different device configurations that can be adopted by OTFTs such as bottom-gate bottom-contact (top left), bottom-gate top-contact (top right), top-gate bottom-contact (bottom left) and top-gate top-contact (bottom right).*

1.2.1 OTFT Operation

In the simplest definition, OTFTs serve as "on" / "off" switches and operate in a similar fashion to conventional field-effect transistors (**Figure 1.8**). OTFTs rely on the application of external voltage biases between the gate-source (V_{GS}) and source-drain (V_{SD}) to produce an output current response (I_{SD}). In its "off" state, either no voltage bias is applied or the bias is too low to induce charge transport through the OSC, which means no output current is produced. When the OTFT is in the process of turning "on", the applied V_{GS} will generate an electric field that will promote dipoles throughout the dielectric layer. These dipoles will in turn promote opposing charges at the semiconductor-thin-film interface. These resulting charges will accumulate until current can flow freely from the source electrode, through the semiconducting layer and out of the drain, ultimately closing the electric circuit.[115] OTFTs can operate under two conditions: *p*-type or *n*-type. In *p*-type OTFTs, the applied gate voltage will be negative leading to holes (h^+) being transported through the semiconductive material, while the inverse occurs in *n*-type devices where a positive gate voltage is applied and electrons (e^-) are transported through the material.

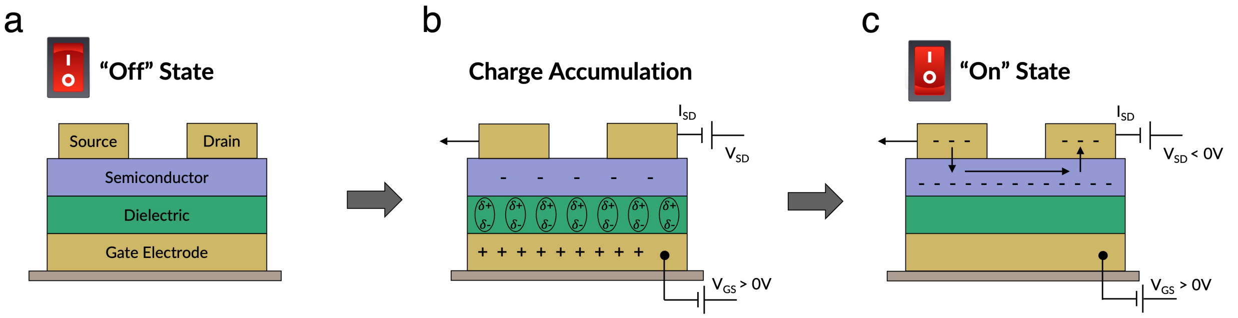

Figure 1.8 *Sequential process during n-type OTFT operation going from an "off" to "on" state. (a) OTFT in an "off" state with no applied* V_{GS} *or* V_{SD} *and no mobile charges within the semiconducting material. (b) Voltage bias applied at the gate-source (*V_{GS}*) and source-drain (*V_{SD}*) electrodes, creating dipoles in the dielectric layer which promotes charges at the surface of the semiconducting material. (c) When enough charges have been accumulated at the semiconductor surface, charges can now travel from the source, through the semiconductor and out of the drain, closing the circuit and current can be measured (*I_{SD}*), indicating that your OTFT is now "on".*

1.2.2 OTFT Characterization

When evaluating OTFT performance, two characteristic curves are evaluated and described as the "output" curve and the "transfer" curve (**Figure 1.9**). The output curve is a function of the I_{SD} with respect to V_{SD} and is measured sequentially at different gate voltages. The output curve can be divided into two regimes, the linear and the saturation regime. In the linear regime, the V_{SD} remains below the threshold voltage (V_T), i.e. $|V_{SD}| < |V_{GS} – V_T|$, and charges cannot move smoothly through the channel between the source and drain. In this regime I_{SD} increases proportionally to V_{SD}, giving the device a resistor-like behavior. As V_{SD} comes to exceed $|V_{GS} – V_T|$, the device enters the saturation regime where I_{SD} now becomes independent of V_{SD}. This regime is denoted by a plateau of the I_{SD}, however, it is common in OTFTs that the plateau is not perfectly flat due to material imperfections, but the key idea is that the current becomes mostly controlled by the gate, not the drain. On the other hand, the transfer curve is collected where the V_{SD} is maintained steady and the I_{SD} is plotted with respect to V_{GS}. Typically, transfer curves are collected in the saturation regime as this allows to show how the gate controls the formation of the conductive channel in the OSC material. The transfer curve is collected in a forward and reverse sweep, showing the exact moment where your device is in turning on and off.

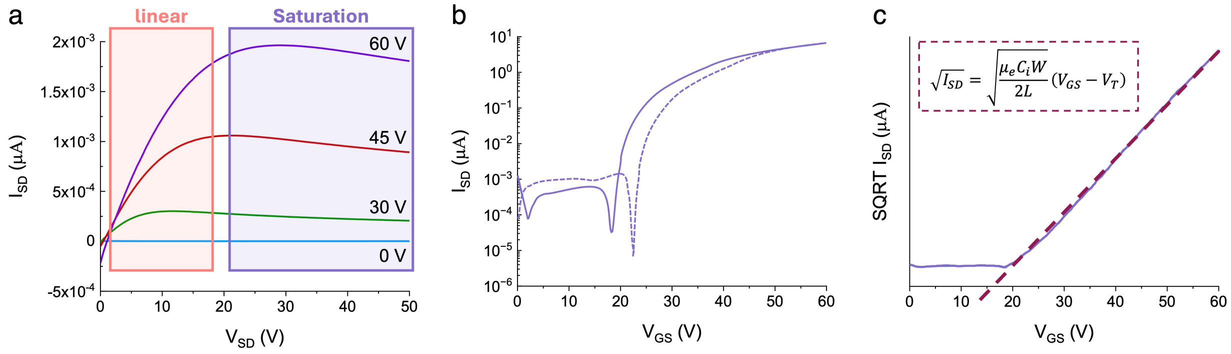

Figure 1.9 *(a) Characteristic output curve at stepwise gate voltages of 0, 30, 45 and 60 V. (b) Characteristic transfer curve of the forward (solid line) and reverse (dotted line) sweeps of the* V_{GS}. *(c) Modified forward sweep transfer curve depicting the square root of* I_{SD} *with respect to* V_{GS} *alongside the tangent used to calculate* μ *and* V_T. *All curves are taken from a n-type OTFT device. (Figure adapted from* [116]*)*

There are typically three key parameters used to evaluate the performance of an OTFT device. These parameters are the field-effect mobility (μ), threshold voltage (V_T) and on/off current ratio ($I_{on/off}$). μ describes how effectively charges (electrons or holes) can move inside the semiconducting channel. Another parameter that can be studied in OTFTs is transconductance (g_m), which reflects how strongly a device current responds to gate voltage, but it depends on geometry, capacitance as well as the OSC material itself. Mobility, in contrast, is an intrinsic material property that describes how easily carriers move in an electric field. By normalizing transconductance to device dimensions and gate capacitance, mobility effectively “standardizes” performance, enabling fair comparison of carrier transport across different materials and device structures. A smoother and cleaner OSC surface allows charges to move more freely, resulting in higher mobility. Alternatively, if the OSC surface is rough or contains impurities or traps, charges are scattered and travel more slowly through the channel, lowering the mobility. V_T represents the minimum gate voltage needed for the device to turn on. Once the gate voltage passes this threshold, charges are now flowing through the semiconducting channel and the device starts conducting. $I_{on/off}$ indicates the current gap between the device's "on" and "off" states. A high on/off ratio means the transistor passes a large amount of current when it turns "on" which translates to the device serving as a good, clean switch. As such, a high performing OTFT device should strive for high μ and $I_{on/off}$ values alongside a low V_T. Whereas $I_{on/off}$ can be extracted directly from the transfer curve, both μ and V_T can be derived from the metal-oxide semiconductor field-effect transistor (MOSFET) model.[111,117] Despite being intended for inorganic semiconducting materials, the MOSFET model is still commonly used to evaluate OTFTs. Since μ can be calculated either in the linear or saturation regimes, two equations can be used to obtain these parameters:

$$I_{SD,lin.} = \frac{\mu C_i W}{L}\left[(V_{GS} - V_T)V_{SD} - \frac{V_{SD}^2}{2}\right] \qquad \textbf{[1.1]}$$

$$I_{SD,sat.} = \frac{\mu C_i W}{2L}(V_{GS} - V_T)^2 \qquad \textbf{[1.2]}$$

Where L is the channel length, W is channel width and C_i is the capacitance of the dielectric material. Given that **Equation 1.2** can assume a linear dependence, the equation can be fitted to a modified transfer curve that plots the square root of I_{SD} against V_{GS}. The resulting slope can be used to calculate μ while the x-intercept can be used to determine V_T.

1.2.3 OTFT Performance Impact Factors

While all of the aforementioned parameters are indicative of whether the semiconducting material is efficient in OTFTs, it is important to also take into consideration external factors that may also have an effect on the device performance such as the OTFT configuration, OSC channel length, selection of the electrode and dielectric materials and surface hydrophobicity. The difference between a "top-contact" and "bottom-contact" configuration will impact the direction in which the charges are injected into the semiconducting layer.[118] A "bottom-contact" OTFT will have the OSC thin-film pool overtop and onto the sides of the source and drain electrodes, which can produce gaps between the electrode and semiconductor, leading to contact resistance (R_C). Conversely, a "top-contact" configuration will allow the electrodes to be deposited in a flush manner directly overtop the semiconducting layer, lowering the risk of gaps appearing between the materials. It is also important to select an electrode material that has a work function (WF) compatible with either the HOMO (*p*-type) or LUMO (*n*-type) levels of the OSC to ensure proper charge injection.[119] The selected channel length between the source and drain electrode can also have an effect on the device performance. Whereas a shorter channel length can allow for a faster switching, which may become a relevant factor depending on the application the OTFT is intended for, it also increases the risk of current leakage and can also lower the $I_{on/off}$. A longer channel length can help improve control over the I_{SD} and reduce leakage, and as a result it will slow down the switching speed of the device. Lastly, since the OSC and dielectric are directly in contact with one another, it is important to ensure that the surface energy of the dielectric is also compatible with the semiconducting material. If the surface energy is not compatible with the active layer, this can lead to issues in how the OSC will adhere to the surface as well as the molecular packing it will adopt. To address this issue, a dielectric surface treatment can be employed to modulate the surface energy, thereby playing a critical role in OSC thin-film formation. Many techniques can be used to modify the dielectric surface, such as plasma cleaning, chemical coating or applying self-assembled monolayers (SAMs).[120,121] All of these techniques can change the surface energy and roughness of the dielectric, which can ultimately encourage more uniform nucleation and crystal growth of the OSC material thereby improving charge transport. In contrast, untreated or poorly treated surfaces can lead to disorganized films, small grains and traps, which reduce device performance.[122–124] In summary, OTFT device performance goes beyond simply designing and utilizing a high performing OSC material, but also relies heavily on how it is processed as well as how other OTFT layers interact with the OSC thin-film.

1.3 Organic Sensors

Another class of devices that can effectively leverage the unique characteristics of organic semiconductors is that of chemical sensors. Chemical sensors have become crucial in modern technology with their ability to detect, identify and quantify various chemical species. The technical definition of chemical sensors refers to a device that can convert chemical information, such as analyte concentration or chemical composition, into an analytically interpreted signal. In a laboratory setting, chemical sensing can be done using complex instrumentation like gas chromatography-mass spectrometry (GC/MS), mass spectrometry (MS), atomic absorption spectroscopy (AAS) and X-ray fluorescence (XRF), to name a few. However, from a commercial standpoint, these instruments are very costly, require highly trained operators and are not suitable for field applications and continuous monitoring. For this reason, in the past decades there has been significant interest in developing small and simplistic devices that can satisfy the analytical requirements provided by the aforementioned instruments in a rapid and efficient manner. With continuous development of new sensing materials, chemical sensors are now being used in a multitude of different fields such as environment monitoring, medical diagnostics, food quality control and industrial safety control.

Modern chemical sensors are typically made up of two key components: the receptor, also known as the sensing material, and the transducer. The main function of the sensing material is to interact with the target analyte in a way that will cause a change in one of its chemical/electrical properties, whereas the purpose of the transducer is to transform that change in property into a measurable signal. The transducer signal can be electrical (which would involve a change in current, resistance or potential), optical (causing change in absorbance or fluorescence) or mechanical (where changes in mass will cause a frequency shift).[61] Given the diverse nature of sensing materials developed over the years and the different properties they contain, there are many different types of chemical sensors that are commonly used such as electrochemical sensors, thermoconductive sensors and spectroscopic sensors.

There are multiple aspects to consider when evaluating the performance of a chemical sensor. They should provide high accuracy and precision by delivering readings that are in close proximity to the true value and consistently repeatable. The devices must also maintain high sensitivity and high resolution, meaning they are able to detect small changes in the measured quantity. The sensors must also operate effectively within an appropriate measurement range and respond quickly enough for the intended application. Additionally, other qualities like good selectivity, linear response and low signal to noise ratio also help produce clear and reliable data.

1.3.1 Quartz Microbalances

One of the earliest reported chemical sensors is the quartz microbalance (QMB). QMBs consist of piezoelectric mass-based operated sensors. They are built using a piezoelectric quartz crystal sandwiched between metallic pads to serve as electrodes (**Figure 1.10a**).[125] The quartz crystal is cut in a precise AT-direction so that when an external electric field is applied it will oscillate to a frequency typically within the megahertz range. QMBs are among the most sensitive mass-measurement devices ever developed, rendering their mass detection range down to the nanogram and even picogram scale. The concept of QMBs made its first appearance in 1959 when G. Sauerbrey reported the resonance frequency of an AT-cut quartz crystal and how it decreased linearly with respect to the mass deposited on its surface.[126]

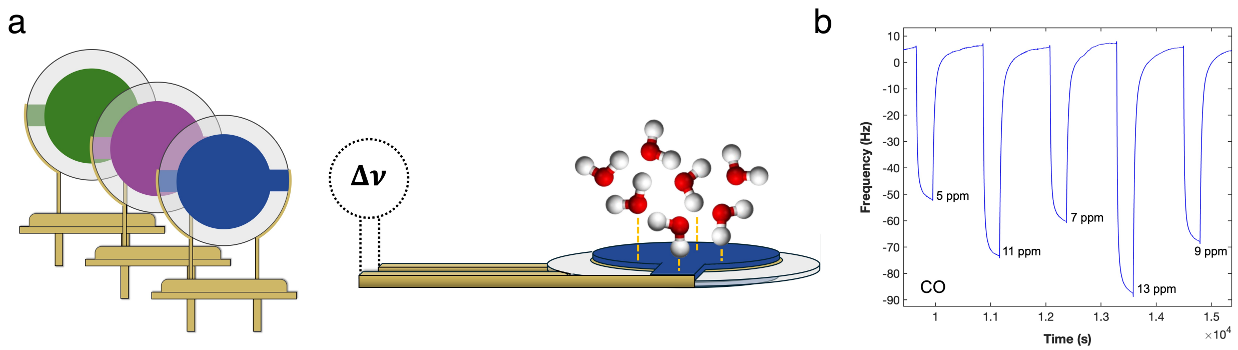

Figure 1.10 *(a) Schematic of three organic quartz microbalance (QMB) sensors containing different sensing materials coated onto the surface (left) and a visual representation of a target analyte interacting with a QMB sensor (right). (b) Frequency variation as a function of time of a polymeric SiPc QMB sensor exposed to* CO_2 *for 5 min-long periods separated by 15 min-long recovery periods in nitrogen.*

In the decades that followed, QMBs quickly became an indispensable piece of instrumentation in the field of surface science. In the 1970-80s, QMBs were being used in laboratories for real-time monitoring of monolayer adsorption, thin-film growth and vapour deposition processes.[127] By the early 2000s, QMBs were evolving into well-defined platforms for biochemical and environmental sensing. Advances in surface functionalization of the quartz crystal and nanostructured coatings enabled QMBs to progress from simple mass-sensing to selective detection of biomolecules, pollutants and gases. This rendered QMBs suitable for point-of-care diagnostics and lab-on-a-chip systems.[128,129]

Fast-forward to recent years, QMB sensors now sit at the intersection of materials science, microfabrication processes, electronic devices and advanced data processing. Developments such as polymer-coated crystals allow for enhanced chemical selectivity sensing, hybrid QMB-optical platforms and the evolution of compact low-power devices used in applications like biotechnology, energy storage, catalysis and environmental monitoring. Their evolution reflects a broader scientific shift toward precision, real-time, nanoscale measurement. As the demand for non-invasive and versatile surface-analysis tools continues to grow, QMB technology is set for further innovation to continue expanding its influence on nanoscale surface sciences.

1.3.2 Interdigitated Electrodes

Another widely popular type of sensors used in modern chemical, biological and physical sensing is the interdigitated electrode (IDE) sensor. Harvesting its sensing abilities from the change in conductive properties of its sensing material, IDEs rely on a change in resistance of the circuit to produce an analyte detection signal. IDEs are designed by having a series of metallic microelectrodes that comb through each other in an interlock geometry without touching one another onto a substrate surface (**Figure 1.11a**).[130] Once the sensing material is deposited overtop the electrodes, this will close the circuit and a resistance output can then be measured.

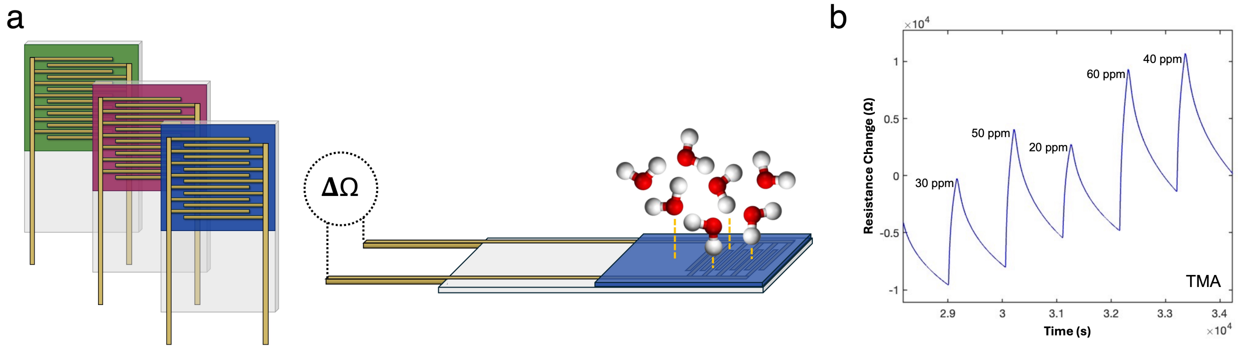

Figure 1.11 *(a) Schematic of three interdigitated electrode (IDE) sensors containing different sensing materials coated onto the surface (left) and a visual representation of a target analyte interacting with an IDE sensor (right). (b) Resistance variation as a function of time of a polymeric SiPc IDE sensor exposed to TMA for 5 min-long periods separated by 30 min-long recovery periods in nitrogen.*

Although initially used for electrochemical purposes in the 1990s, it was not until the early 2000s that IDEs started to shift towards biological and chemical sensing applications. The high surface-volume ratio provided by the interlocked electrodes made IDEs well suited to detect small sample volumes of various ions, gases and organic compounds. Soon after, researchers started to functionalize IDE surfaces with different polymers, enzymes and nanoparticles to introduce analyte selectivity.

The 2010s era held major advances in IDE sensor technology, which was heavily driven by the integration of nanomaterials that significantly improve the device performance.[131–133] Materials such as graphene, carbon nanotubes and metal oxide nanostructures held larger surface areas which in turn accelerated electron transfer, thus enabling lower detection limits for target analytes. At the same time, progress in soft lithography, nanoimprint lithography and the development of flexible substrates allowed IDEs to be manufactured on plastics, textiles and even paper. These innovations broadened the scope of applications ultimately giving rise to wearable sensors, disposable diagnostic tools and hybrid electrochemical-electronic biosensors.

Today, IDE sensors continue to advance, propelled by developments in materials engineering, microfabrication techniques, data analytics, and integrated device design. Modern IDEs can be produced on flexible or stretchable substrates using methods such as screen printing and inkjet printing, making them well suited for wearable technologies. Some newer systems incorporate machine learning to interpret impedance spectra or multimodal sensor outputs, while others combine electrochemical and optical elements to enhance detection specificity. Cutting-edge designs include nanoscale IDEs capable of probing single cells or even individual molecules along with sustainable variants constructed from biodegradable or self-healing materials.[134] Furthermore, wireless and battery-free models, which are powered by near field communication (NFC) or energy-harvesting mechanisms, are further extending IDE applications to continuous and remote monitoring.[135,136]

1.3.3 Electronic Noses

Although many different types of sensing materials have been developed over the years to target different analytes, it is still a common occurrence for sensing materials to be responsive to two or more analytes. To remedy this lack of selectivity, multiple sensors harboring different sensing materials can be used together in parallel to isolate the detection of different analytes. This concept is called an electronic nose (e-nose) and is inspired by the human olfactory system.[137] The e-nose is designed to analyze complex mixtures of volatile compounds rather than a single target analyte. An e-nose consists of an array of partially selective sensors that possess different sensitivities towards their response to multiple chemical species. The combined responses provided by the sensor array form a unique pattern also known as a “smell fingerprint”, which can then be used to decode the mixture. Complex statistical and machine learning algorithms are used in order to isolate each chemical species from the mixture. Such algorithms include principal component analysis (PCA), artificial neural networks (ANNs) and support vector machines (SVMs).[138–140] This approach allows e-noses to classify and identify complex odors and have been used in food safety detection, air quality monitoring, medical diagnostics as well as identifying explosives or hazardous chemicals. Unlike conventional chemical sensors, e-noses do not rely on specificity but instead leverage multidimensional data analysis to differentiate complex chemical profiles.

One of the most common algorithms used to evaluate an e-nose is the Principle Component Analysis (PCA).[139] PCA is a statistical technique used to interpret complex datasets by transforming the original variables into a new set of uncorrelated variables called principal components (PCs). These components are constructed to capture the maximum variance in the data while reducing redundancy, thus simplifying the overall analysis. PCA typically relies on singular value decomposition (SVD) or an equivalent eigenvalue-based approach to identify patterns and relationships among variables. The process begins by centering the data, which is achieved by subtracting the mean from each variable, so that the dataset is aligned around the origin. This step ensures that PCA focuses on variation rather than absolute values. Next, a covariance matrix is computed to quantify how variables relate to one another, indicating the strength and direction of their relationships. From this matrix, eigenvectors and eigenvalues are derived. The eigenvector corresponding to the largest eigenvalue defines the first principal component (PC1), which represents the direction of greatest variance in the data. Each subsequent principal component is orthogonal (perpendicular) to the previous ones and captures the next highest amount of remaining variance. For example, the second principal component (PC2) identifies the direction of maximum variance not explained by PC1. Once the principal components are determined, the data can be projected onto this new coordinate system. This transformation reveals underlying structure in the dataset, often making patterns such as clustering more apparent. Points that cluster together in this new space are more closely related, while those that are farther apart, or oriented in different directions, are less correlated.

1.4 Scope of Thesis

The goal of this thesis focuses on the design, synthesis and characterization of novel donor-acceptor and porphyrinoid organic semiconducting materials to explore their potential as active materials in organic thin-film transistor and chemical sensing applications. To achieve this goal, the newly synthesized materials were not only characterized from a molecular standpoint, but optimizing conditions were also explored during the device fabrication process to establish a well-rounded understanding of the structure-property relationship of these materials and how to best implement them in organic electronic devices for optimal performance.

In **Chapter 2**, I explored the design of novel D-A small molecule OSCs as *n*-type active materials in OTFTs. The motivation behind this work stemmed from creating a novel alternating donor-acceptor framework centered around thieno[3,4-c] pyrrole-4,6-dione (TPD), a modern acceptor moiety that has been exploited in D-A materials for OPV devices but had few reports in OTFTs. This study included the synthesis of two novel A^2-D- A^1-D- A^2 materials where TPD served as the core acceptor (A^1) to which thiophene donors (D) were covalently bonded to either side and secondary terminal acceptor moieties (A^2), either dicyanovinyl or rhodanine units, were attached at the periphery of the molecule. These materials were also designed to be solution processed through functionalization with a branched alkyl chain. During the OTFT fabrication process, the effects of using two different chlorinated solvents during the spin coating process as well as altering the post-deposition annealing conditions were evaluated. The resulting devices were tested under vacuum using a manual probe station and X-ray diffraction (XRD) was performed on the thin-films to get a better understanding of the performance changes observed from the different conditions that were applied during the device fabrication process.

Chapter 3 focuses on exploiting a phosphorus-functionalized porphyrinoid material for its *p*-type semiconducting properties in OTFTs. The interest behind this work was centered around exploring a group-15 element to occupy the center of a Pc framework. Group-15 porphyrinoid materials have been reported to have an impact in the stabilization of the resulting LUMO level, thus decreasing the molecular bandgap to facilitate charge excitation. To successfully insert phosphorus at the centre of the Pc core, metal-free Pc is reacted with PBr_3, which results in a phosphorus oxide triazatetrabenzocorrole (PO-Tbc) product due to the loss of a bridging imine atom during phosphorus insertion. Given the insolubility of PO-Tbc, this material was incorporated into OTFT devices through physical vapour deposition. For this work I also curated a dielectric surface treatment analysis where I looked at a range of different silanes, as well as *para*-sexiphenylene, that possessed varying water contact angles to modulate the hydrophobicity of the dielectric surface for the potential optimization of the thin-film morphology of PO-Tbc during deposition. The resulting devices were tested both under vacuum (BGBC devices) using a manual probe station and under nitrogen atmospheric conditions (BCTC devices) using an automated tester. The BCTC devices were also analyzed through XRD and Raman mapping to evaluate the crystallinity and relative orientation of the molecules with respect to the substrate surface and how these related to the optimized device performances.

Chapters 4-6 are a continuation of one major project I completed during my time at the University of Ottawa and at the University of Rome Tor Vergata in collaboration with Prof. Roberto Paolesse and his research group. **Chapter 4** explores the synthesis and axial electropolymerization of amino-derived silicon phthalocyanine materials. The inspiration behind this stemmed from exploiting electroactive amino groups to catalyze a polymerization process of phthalocyanine materials. Due to the low solubility generally held by planar MPc materials, a series of silicon phthalocyanine (SiPc) possessing aminoaryl functionalities in-and-out of plane of the macrocycle were designed. This feature not only helped impart solubility in the materials, but it also serves as a gateway for axial electropolymerization by exploiting the amino groups without compromising the structural integrity of the Pc core. Five axially-derived amino SiPc monomers were synthesized and assessed for potential electropolymerization through cyclic voltammetry using either glassy carbon or ITO coated glass as the working electrode. Optical studies, including UV-Vis-NIR spectroscopy and spectroelectrochemistry, were executed to confirm successful electropolymerization on the ITO conductive surface.

Chapter 5 explores the applicability of the polymers synthesized in **Chapter 4**, where the *para*- and *ortho*-bis(aminophenoxy)SiPc materials are electropolymerized directly onto piezoelectric quartz microbalances (QMBs) to explore their potential for mass-based chemical sensing. During this work, both the *para*- and *ortho*-derived amino SiPcs were electropolymerized using cyclic voltammetry (CV) and chronoamperometry (CA). In addition, a peripherally-derived amino copper corrole (CuCorr) was also electropolymerized to compare the sensing behaviour where analyte interaction is centred around the porphyrinoid macrocycle (*poly-SiPcs*) versus centred around a central metal ion (*poly-CuCorr*). I exposed all QMB sensors to a series of different gases and volatile organic compounds (VOCs) to investigate their potential sensitivity and selectivity. Lastly, a Principal Component Analysis was performed on the sensing results to investigate their potential to be used in tandem as an electronic nose (e-nose). This study demonstrated that although individually each sensor was not selective to any particular analyte, when used collectively as an e-nose, the differences in materials and polymerization techniques causes enough orthogonality in their sensing behaviour to successfully distinguish different classes of analytes.

Chapter 6 explores the same electropolymerized *para*- and *ortho*-bis(aminophenoxy)SiPc materials, but now implemented into interdigitated electrode (IDE) sensors. In the previous chapter, these two materials were incorporated into chemical sensors for mass-based detection. However, given the strong conductive properties associated with Pcs, I was also interested in studying their sensing behaviour when they are incorporated in chemiresistor devices. This work explores the incorporation of both *para*- and *ortho*-amino-SiPc polymers electropolymerized through cyclic voltammetry (CV) and chronoamperometry (CA) as sensing materials in IDE chemiresistors. Although this project is currently ongoing, this chapter discusses the initial sensing results obtained when the IDEs were exposed to CO, NO and TMA gases, as well as varying relative humidity levels.

Chapter 7 highlights the key findings and overall conclusions that have come out of each preceding chapter and how these findings can be used in future work to help evolve organic semiconductor design and thin-film processing for organic electronic applications. I also discuss future directions I think would be worthwhile exploring in the development of next-generation semiconducting materials.

References

(1) Volkov, A. V.; Lubimov, A. A. *Doklady Akademii Nauk. SSSR* **1948**, *60*, 833.

(2) Tannenwald, L. M. *J. Appl. Phys.* **1955**, *26* (5), 551.

(3) Ferraris, John.; Cowan, D. O.; Walatka, V.; Perlstein, J. H. *J. Am. Chem. Soc.* **1973**, *95* (3), 948.

(4) Chiang, C. K.; Fincher, C. R.; Park, Y. W.; Heeger, A. J.; Shirakawa, H.; Louis, E. J.; Gau, S. C.; MacDiarmid, A. G. *Phys. Rev. Lett.* **1977**, *39* (17), 1098.

(5) Heeger, A. J. *Rev. Mod. Phys.* **2001**, *73* (3), 681.

(6) Fusella, M. A.; Lin, Y. L.; Rand, B. P. In *Handbook of Organic Materials for Electronic and Photonic Devices*; Elsevier, **2019**; pp 665–693.

(7) Hong, G.; Gan, X.; Leonhardt, C.; Zhang, Z.; Seibert, J.; Busch, J. M.; Bräse, S. *Adv. Mater.* **2021**, *33* (9), 2005630.

(8) Yan, Y.; Zhao, Y.; Liu, Y. *J. Polym. Sci.* **2022**, *60* (3), 311.

(9) Lin, H.; Bai, F. *Organic Optoelectronics*, ed. W. Hu.; Wiley-VCH Verlag GmbH, **2013**.

(10) Bässler, H. *Phys. Status Solidi (b)* **1993**, *175* (1), 15.

(11) Lin, H.; Bai, F. *Organic Optoelectronics*, ed. W. Hu.; Wiley-VCH Verlag GmbH, **2013**.

(12) Myers, J. D.; Xue, J. *Polym. Rev.* **2012**, *52* (1), 1.

(13) Coropceanu, V.; Cornil, J.; Da Silva Filho, D. A.; Olivier, Y.; Silbey, R.; Brédas, J.-L. *Chem. Rev.* **2007**, *107* (4), 926.

(14) Köhler, A.; Bässler, H. *Electronic Processes in Organic Semiconductors: An Introduction*, 1st ed.; Wiley, **2015**.

(15) Magnan, F. *Doctoral Thesis*, University of Ottawa: Ottawa, **2017**.

(16) Gao, X.; Zhao, Z. *Sci. China Chem.* **2015**, *58* (6), 947.

(17) Ogbaje, M.; Bhat, V.; Risko, C. *Annu. Rev. Mater. Res.* **2025**, *55* (1), 285.

(18) Li, X.; Guo, J.; Yang, L.; Chao, M.; Zheng, L.; Ma, Z.; Hu, Y.; Zhao, Y.; Chen, H.; Liu, Y. *Front. Chem.* **2019**, *7*, 362.

(19) Dong, J.; Yan, C.; Chen, Y.; Zhou, W.; Peng, Y.; Zhang, Y.; Wang, L.-N.; Huang, Z.-H. *J. Mater. Sci. Tech.* **2022**, *113*, 175.

(20) Azeem, U.; Khera, R. A.; Naveed, A.; Imran, M.; Assiri, M. A.; Khalid, M.; Iqbal, J. *ACS Omega* **2021**, *6* (43), 28923.

(21) Caballero, R.; De La Cruz, P.; Sharma, G. D.; Langa, F. *Coord. Chem. Rev.* **2026**, *548*, 217199.

(22) Casey, A.; Dimitrov, S. D.; Shakya-Tuladhar, P.; Fei, Z.; Nguyen, M.; Han, Y.; Anthopoulos, T. D.; Durrant, J. R.; Heeney, M. *Chem. Mater.* **2016**, *28* (14), 5110.

(23) Zhang, J.; Xu, W.; Sheng, P.; Zhao, G.; Zhu, D. *Acc. Chem. Res.* **2017**, *50* (7), 1654.

(24) Zhang, Z.; Wang, J. *J. Mater. Chem.* **2012**, *22* (10), 4178.

(25) Cappello, D.; Buguis, F. L.; Gilroy, J. B. *ACS Omega* **2022**, *7* (36), 32727.

(26) Hou, J.; Tan, Z.; Yan, Y.; He, Y.; Yang, C.; Li, Y. *J. Am. Chem. Soc.* **2006**, *128* (14), 4911.

(27) Bureš, F. *RSC Adv.* **2014**, *4* (102), 58826.

(28) Ostroverkhova, O. *Chem. Rev.* **2016**, *116* (22), 13279.

(29) Bardeen, C. J. *Annu. Rev. Phys. Chem.* **2014**, *65* (1), 127.

(30) Mulliken, R. S. *J. Phys. Chem.* **1952**, *56* (7), 801.

(31) Simov, D. .

(32) Mulliken, R. S. *J. Am. Chem. Soc.* **1952**, *74* (3), 811.

(33) Mulliken, R. S. *J. Am. Chem. Soc.* **1950**, *72* (1), 600.

(34) Stewart, F. E.; Eisner, M.; Carper, W. R. *J. Chem. Phys.* **1966**, *44* (8), 2866.

(35) Jérome, D.; Mazaud, A.; Ribault, M.; Bechgaard, K. *J. Phys. Lett.* **1980**, *41* (4), 95.

(36) Fratini, S.; Nikolka, M.; Salleo, A.; Schweicher, G.; Sirringhaus, H. *Nat. Mater.* **2020**, *19* (5), 491.

(37) Biswas, P.; Kong, L.; Tian, Z. *Nanoscale* **2025**, *17* (41), 23896.

(38) Li, Y.; Sonar, P.; Murphy, L.; Hong, W. *Energy Environ. Sci.* **2013**, *6* (6), 1684.

(39) Al Kobaisi, M.; Bhosale, S. V.; Latham, K.; Raynor, A. M.; Bhosale, S. V. *Chem. Rev.* **2016**, *116* (19), 11685.

(40) Randell, N. M.; Kelly, T. L. *Chem. Rec.* **2019**, *19* (6), 973.

(41) Yuan, J.; Zhang, Y.; Zhou, L.; Zhang, C.; Lau, T.; Zhang, G.; Lu, X.; Yip, H.; So, S. K.; Beaupré, S.; Mainville, M.; Johnson, P. A.; Leclerc, M.; Chen, H.; Peng, H.; Li, Y.; Zou, Y. *Adv. Mater.* **2019**, *31* (17), 1807577.

(42) Ledwon, P. *Org. Electron.* **2019**, *75*, 105422.

(43) Wei, M.; Perepichka, D. F. *J. Mater. Chem. A* **2025**, *13* (18), 12785.

(44) Siddiqui, A.; Suman; Singh, S. P. *Mater. Chem. Front.* **2021**, *5* (21), 7724.

(45) *Applications of Porphyrinoids as Functional Materials*; Lang, H., Rueffer, T., Eds.; RCS, **2021**.

(46) Aravindu, K.; Kim, H.-J.; Taniguchi, M.; Dilbeck, P. L.; Diers, J. R.; Bocian, D. F.; Holten, D.; Lindsey, J. S. *Photochem. Photobio. Sci.* **2013**, *12* (12), 2089.

(47) Kadish, K. M.; Caemelbecke, E. V. In *Encyclopedia of Electrochemistry*; Eds.; Wiley, **2002**.

(48) King, B.; Melville, O. A.; Rice, N. A.; Kashani, S.; Tonnelé, C.; Raboui, H.; Swaraj, S.; Grant, T. M.; McAfee, T.; Bender, T. P.; Ade, H.; Castet, F.; Muccioli, L.; Lessard, B. H. *ACS Appl. Electron. Mater.* **2021**, *3* (1), 325.

(49) Cranston, R. R.; Vebber, M. C.; Berbigier, J. F.; Rice, N. A.; Tonnelé, C.; Comeau, Z. J.; Boileau, N. T.; Brusso, J. L.; Shuhendler, A. J.; Castet, F.; Muccioli, L.; Kelly, T. L.; Lessard, B. H. *ACS Appl. Mater. Interfaces* **2021**, *13* (1), 1008.

(50) Gielen, S.; Gómez, V. C.; Brebels, S.; Quill, T. J.; Vanderspikken, J.; Lutsen, L.; De La Cruz, P.; Vandewal, K.; Langa, F.; Maes, W. *J. Mater. Chem. C* **2022**, *10* (30), 10853.

(51) Choi, M.-S.; Lee, S.; Kim, H. J.; Kim, J.-J. *Org. Electron.* **2018**, *61*, 164.

(52) Huang, F.; Liao, G.; Peng, Y.; Liu, G. *ACS Appl. Mater. Interfaces* **2023**, *15* (35), 41634.

(53) Yutronkie, N. J.; King, B.; Melville, O. A.; Lessard, B. H.; Brusso, J. L. *J. Mater. Chem. C* **2021**, *9* (31), 10119.

(54) Cyr, M.; Lamontagne, H. R.; Lessard, B. H.; Brusso, J. L. *ACS Appl. Electron. Mater.* **2024**, acsaelm.4c01129.

(55) Melville, O. A.; Grant, T. M.; Lessard, B. H. *J. Mater. Chem. C* **2018**, *6* (20), 5482.

(56) Vebber, M. C.; Grant, T. M.; Brusso, J. L.; Lessard, B. H. *Langmuir* **2020**, *36* (10), 2612.

(57) Kesters, J.; Verstappen, P.; Kelchtermans, M.; Lutsen, L.; Vanderzande, D.; Maes, W. *Adv. Energy Mater.* **2015**, *5* (13), 1500218.

(58) Ibrahim-Ouali, M.; Dumur, F. *Molecules* **2019**, *24* (7), 1412.

(59) Tejerina, L.; Rapidis, A. G.; Rickhaus, M.; Murto, P.; Genene, Z.; Wang, E.; Minotto, A.; Anderson, H. L.; Cacialli, F. *J. Mater. Chem. C* **2022**, *10* (15), 5929.

(60) Comeau, Z. J.; Rice, N. A.; Harris, C. S.; Shuhendler, A. J.; Lessard, B. H. *Adv. Funct. Mater.* **2022**, *32* (7), 2107138.

(61) Paolesse, R.; Nardis, S.; Monti, D.; Stefanelli, M.; Di Natale, C. *Chem. Rev.* **2017**, *117* (4), 2517.

(62) Di Zazzo, L.; Ganesh Moorthy, S.; Meunier-Prest, R.; Lesniewska, E.; Di Natale, C.; Paolesse, R.; Bouvet, M. *Sensors* **2023**, *23* (15), 6773.

(63) Drain, C. M.; Varotto, A.; Radivojevic, I. *Chem. Rev.* **2009**, *109* (5), 1630.

(64) Ledos, N.; Lamontagne, H. R.; Manion, J.; Castet, F.; Lessard, B. H.; Brusso, J. L. *Adv. Funct. Mater.* **2025**, e14609.

(65) King, B.; Radford, C. L.; Vebber, M. C.; Ronnasi, B.; Lessard, B. H. *ACS Appl. Mater. Interfaces* **2023**, acsami.2c22789.

(66) Hietschold, M. In *Applications of Porphyrinoids as Functional Materials*; Lang, H., Rueffer, T., Eds.; *RCS*, **2021**; pp 91–120.

(67) Melville, O. A.; Lessard, B. H.; Bender, T. P. *ACS Appl. Mater. Interfaces* **2015**, *7* (24), 13105.

(68) Grant, T. M.; Rice, N. A.; Muccioli, L.; Castet, F.; Lessard, B. H. *ACS Appl. Electron. Mater.* **2019**, *1* (4), 494.

(69) Ghosh, A. *Chem. Rev.* **2017**, *117* (4), 3798.

(70) Oliveira, T. A.; Silva, P. V.; De Vasconcelos, F. M.; Meunier, V.; Girão, E. C. *Phys. Chem. Chem. Phys.* **2024**, *26* (42), 26943.

(71) Imran, M.; Ramzan, M.; Qureshi, A. K.; Khan, M. A.; Tariq, M. *Biosensors* **2018**, *8* (4), 95.

(72) Schmidt, A. M.; Calvete, M. J. F. *Molecules* **2021**, *26* (9), 2823.

(73) Arkan, F.; Izadyar, M. *Materials Chemistry and Physics* **2017**, *196*, 142.

(74) Leznoff, C. C.; Lever, A. B. P. *Phthalocyanines: Properties and Applications*; Wiley, **1997**; Vol. 4.

(75) Booth, G. *Chimia* **1965**, *19* (5), 201.

(76) *Advances in Glass Research*; Ikhmayies, S. J., Ed.; Advances in Material Research and Technology; Springer International Publishing: Cham, **2023**.

(77) Thomas, A. L. *Phthalocyanine Research and Applications*, 1st ed.; CRC Press, **1990**.

(78) McKeown, N. B. *Phthalocyanine Materials Synthesis, Structure and Function*; Cambridge University Press, **1998**.

(79) Martins, T. J.; Negri, L. B.; Pernomian, L.; Faial, K. D. C. F.; Xue, C.; Akhimie, R. N.; Hamblin, M. R.; Turro, C.; Da Silva, R. S. *Front. Mol. Biosci.* **2021**, *7*, 595830.

(80) Lamontagne, H. R.; Cranston, R. R.; Comeau, Z. J.; Harris, C. S.; Shuhendler, A. J.; Lessard, B. H. *Adv. Sci.* **2024**, 2305515.

(81) Claessens, C. G.; González-Rodríguez, D.; Rodríguez-Morgade, M. S.; Medina, A.; Torres, T. *Chem. Rev.* **2014**, *114* (4), 2192.

(82) Pode, R. *Adv. Mater. Lett.* **2012**, *2* (1), 3.

(83) Pan, F.; Tian, H.; Qian, X.; Huang, L.; Geng, Y.; Yan, D. *Org. Electron.* **2011**, *12* (8), 1358.

(84) Ji, Z.; Liu, M.; Shang, L.; Hu, W.; Liu, G.; Liu, X.; Wang, H. *J. Mater. Chem.* **2009**, *19* (31), 5507.

(85) Lamontagne, H. R.; Comeau, Z. J.; Cranston, R. R.; Boileau, N. T.; Harris, C. S.; Shuhendler, A. J.; Lessard, B. H. *Sens. Diagn.* **2022**, *1* (6), 1165.

(86) Gonzalez Arellano, D. L.; Burnett, E. K.; Demirci Uzun, S.; Zakashansky, J. A.; Champagne, V. K.; George, M.; Mannsfeld, S. C. B.; Briseno, A. L. *J. Am. Chem. Soc.* **2018**, *140* (26), 8185.

(87) Hoshino, A.; Takenaka, Y.; Miyaji, H. *Acta Crystal. B Struct. Sci.* **2003**, *59* (3), 393.

(88) Xu, J.; Liu, X.; Hou, W.; Guo, H.; Yu, L.; Zhang, H. *Bull. Mater. Sci.* **2018**, *41* (4), 111.

(89) Liu, Y.; Gao, S.; Zhang, X.; Xin, J. H.; Zhang, C. *J. Mater. Chem. C* **2023**, *11* (1), 12.

(90) Józefowicz, M. E.; Epstein, A. J.; Tang, X. *Synth. Met.* **1992**, *46* (3), 337.

(91) Diaz, A. F.; Kanazawa, K. K.; Gardini, G. P. *J. Chem. Soc., Chem. Commun.* **1979**, No. 14, 635.

(92) Gruber, J.; Chia Li, R. W.; Hümmelgen, I. A. In *Handbook of Advanced Electronic and Photonic Materials and Devices*; Elsevier, **2001**; pp 163–184.

(93) McCullough, R. D.; Lowe, R. D.; Jayaraman, M.; Anderson, D. L. *J. Org. Chem.* **1993**, *58* (4), 904.

(94) Burroughes, J. H.; Bradley, D. D. C.; Brown, A. R.; Marks, R. N.; Mackay, K.; Friend, R. H.; Burns, P. L.; Holmes, A. B. *Nature* **1990**, *347* (6293), 539.

(95) Li, G.; Shrotriya, V.; Huang, J.; Yao, Y.; Moriarty, T.; Emery, K.; Yang, Y. *Nat. Mater.* **2005**, *4* (11), 864.

(96) Qiu, L.; Wang, X.; Lee, W. H.; Lim, J. A.; Kim, J. S.; Kwak, D.; Cho, K. *Chem. Mater.* **2009**, *21* (19), 4380.

(97) Beaujuge, P. M.; Ellinger, S.; Reynolds, J. R. *Nat. Mater.* **2008**, *7* (10), 795.

(98) Jia, H.; Huang, Z.; Li, P.; Zhang, S.; Wang, Y.; Wang, J.-Y.; Gu, X.; Lei, T. *J. Mater. Chem. C* **2021**, *9* (14), 4927.

(99) Ding, B.; Jo, I.-Y.; Yu, H.; Kim, J. H.; Marsh, A. V.; Gutiérrez-Fernández, E.; Ramos, N.; Rapley, C. L.; Rimmele, M.; He, Q.; Martín, J.; Gasparini, N.; Nelson, J.; Yoon, M.-H.; Heeney, M. *Chem. Mater.* **2023**.

(100) Baptista, A.; Silva, F.; Porteiro, J.; Míguez, J.; Pinto, G. *Coatings* **2018**, *8* (11), 402.

(101) Diao, Y.; Shaw, L.; Bao, Z.; Mannsfeld, S. C. B. *Energy Environ. Sci.* **2014**, *7* (7), 2145.

(102) Reichelt, K.; Jiang, X. *Thin Solid Films* **1990**, *191* (1), 91.

(103) Khatun, N.; Nkele, A. C.; Bagchi, K. *Phys. Chem. Chem. Phys.* **2025**, *27* (13), 6408.

(104) Ewenike, R. B.; King, B.; Battaglia, A. M.; Quezada Borja, J. D.; Lin, Z. S.; Manion, J. G.; Brusso, J. L.; Kelly, T. L.; Seferos, D. S.; Lessard, B. H. *ACS Appl. Electron. Mater.* **2023**.

(105) Sirringhaus, H. *Adv. Mater.* **2005**, *17* (20), 2411.

(106) Na, J. Y.; Kang, B.; Sin, D. H.; Cho, K.; Park, Y. D. *Sci. Rep.* **2015**, *5* (1), 13288.

(107) Mokarian-Tabari, P.; Geoghegan, M.; Howse, J. R.; Heriot, S. Y.; Thompson, R. L.; Jones, R. A. L. *Eur. Phys. J. E* **2010**, *33* (4), 283.

(108) Cyr, M.; Brixi, S.; Ganguly, A.; Lessard, B. H.; Brusso, J. L. *Dyes Pigm.* **2023**, *210*, 110964.

(109) Aloui, W.; Adhikari, T.; Nunzi, J.-M.; Bouazizi, A.; Khirouni, K. *Mater. Sci. Semicon. Process.* **2015**, *39*, 575.

(110) Hakeem, S.; Ali, S.; Liaqat, M. A.; Jamshed, A.; Basit, M.; Masood, M. T.; Javed, S. In *CEMP 2023*; MDPI, **2024**; p 28.

(111) Klauk, H. *Chem. Soc. Rev.* **2010**, *39* (7), 2643.

(112) Minamiki, T.; Minami, T.; Chen, Y.-P.; Mano, T.; Takeda, Y.; Fukuda, K.; Tokito, S. *Commun. Mater.* **2021**, *2* (1), 8.

(113) Schwartz, G.; Tee, B. C.-K.; Mei, J.; Appleton, A. L.; Kim, D. H.; Wang, H.; Bao, Z. *Nat. Commun.* **2013**, *4* (1), 1859.

(114) Jacob, S.; Abdinia, S.; Benwadih, M.; Bablet, J.; Chartier, I.; Gwoziecki, R.; Cantatore, E.; Van Roermund, A. H. M.; Maddiona, L.; Tramontana, F.; Maiellaro, G.; Mariucci, L.; Rapisarda, M.; Palmisano, G.; Coppard, R. *Solid-State Electron.* **2013**, *84*, 167.

(115) Zaumseil, J.; Sirringhaus, H. *Chem. Rev.* **2007**, *107* (4), 1296.

(116) Cranston, R. *Doctoral Thesis*, University of Ottawa: Ottawa, **2024**.

(117) Kim, C.-H.; Bonnassieux, Y.; Horowitz, G. *IEEE Trans. Electron. Dev.* **2014**, *61* (2), 278.

(118) Kwon, J.-H.; Kim, M.-H.; Bae, J.-H. *J. Mater. Chem. C* **2024**, *12* (1), 29.

(119) Greiner, M. T.; Lu, Z.-H. *NPG Asia Mater.* **2013**, *5* (7), e55.

(120) Casalini, S.; Bortolotti, C. A.; Leonardi, F.; Biscarini, F. *Chem. Soc. Rev.* **2017**, *46* (1), 40.

(121) Liu, D.; Miao, Q. *Mater. Chem. Front.* **2018**, *2* (1), 11.

(122) Padma, N.; Sawant, S. N.; Sudarsan, V.; Sen, S.; Gupta, S. K. *Phys. Status Solidi (a)* **2013**, *210* (10), 2111.

(123) Bolognesi, A.; Berliocchi, M.; Manenti, M.; DiCarlo, A.; Lugli, P.; Lmimouni, K.; Dufour, C. *IEEE Trans. Electron. Dev.* **2004**, *51* (12), 1997.

(124) Park, J. H.; Lee, Y. T.; Lee, H. S.; Lee, J. Y.; Lee, K.; Lee, G. B.; Han, J.; Kim, T. W.; Im, S. *ACS Appl. Mater. Interfaces* **2013**, *5* (5), 1625.

(125) Vellekoop, M. J. *Sens. Actuators A: Phys.* **1997**, *63* (1), 79.

(126) Sauerbrey, G. *Zeitschrift fiir Physik* **1959**, 55, 206-222.

(127) Lu, C.-S.; Lewis, O. *J. Appl. Phys.* **1972**, *43* (11), 4385.

(128) Prakrankamanant, P. *J. Med. Assoc. Thai* **2014**, 97.

(129) Hampitak, P.; Jowitt, T. A.; Melendrez, D.; Fresquet, M.; Hamilton, P.; Iliut, M.; Nie, K.; Spencer, B.; Lennon, R.; Vijayaraghavan, A. *ACS Sens.* **2020**, *5* (11), 3520.

(130) Afsarimanesh, N.; Nag, A.; Alahi, Md. E. E.; Han, T.; Mukhopadhyay, S. C. *Sens. Actuators A: Phys.* **2020**, *305*, 111923.

(131) Sugime, H.; Ushiyama, T.; Nishimura, K.; Ohno, Y.; Noda, S. *Analyst* **2018**, *143* (15), 3635.

(132) Choi, H.-J.; Choi, S.-J.; Choo, S.; Kim, I.-D.; Lee, H. *Sci. Rep.* **2016**, *6* (1), 18731.

(133) Chandran Mukkattu Kuniyil, A.; Zavašnik, J.; Cvejić, Ž.; Sarang, S.; Simić, M.; Srdić, V. V.; Stojanović, G. M. *Sensors* **2020**, *20* (21), 6323.

(134) Hart, C.; Kundu, A.; Kumar, K.; Varma, S. J.; Thomas, J.; Rajaraman, S. *Biosensors* **2018**, *8* (4), 88.

(135) Escobedo, P.; Erenas, M. M.; López-Ruiz, N.; Carvajal, M. A.; Gonzalez-Chocano, S.; De Orbe-Payá, I.; Capitán-Valley, L. F.; Palma, A. J.; Martínez-Olmos, A. *Anal. Chem.* **2017**, *89* (3), 1697.

(136) Naik, A.; Lee, H. S.; Herrington, J.; Barandun, G.; Flock, G.; Güder, F.; Gonzalez-Macia, L. *ACS Sens.* **2024**, *9* (12), 6789.

(137) Gardner, J. W.; Bartlett, P. N. *Sens. Actuators B: Chemical* **1994**, *18* (1–3), 210.

(138) Haykin, S. *Neural Networks: A Comprehensive Foundation*, 2nd ed.; Prentice Hall PTR: USA, **1998**.

(139) Jolliffe, I. *Principle Component Analysis.* Wiley Stats Ref: **2014**.

(140) Cristianini, N.; Shawe-Taylor, J. *An Introduction to Support Vector Machines and Other Kernel-based Learning Methods*; Cambridge University Press: Cambridge, **2000**.

Chapter 2. Development of Thieno[3,4-c] Pyrrole-4,6-Dione-Based Donor-Acceptor Materials for OTFTs

This chapter is adapted from: ***Cyr, M.****, Brixi, S., Ganguly, A., Lessard, B. H., Brusso, J. L. Synthesis of thieno[3,4-c] pyrrole-4,6-dione-based small molecules for application in organic thin-film transistors. Dyes Pigm.* ***2023****, 210, 110964.*

Context

During the first stage of my graduate studies, I focused on designing and synthesizing small molecules incorporating various ring-fused heterocycles as potential organic semiconductors. This project was built upon preliminary concepts that were previously introduced in our research group overlooking benzodifurandione-based organic semiconductors. I expanded the scope of this work to explore a broader range of alternating donor–acceptor small molecules for application in organic thin-film transistors (OTFTs). The work particularly emphasized the thieno[3,4-c] pyrrole-4,6-dione (TPD) building block. This building block was selected as it had been previously reported to show promising semiconducting properties when implemented in organic photovoltaics (OPVs) but had not been explored thoroughly for its promising potential in field effect transistors. The work presented herein overlooks the synthetic development and initial optoelectronic characterization of the novel alternating donor-acceptor small molecules containing a A^2-D-A^1-D-A^2 framework. The resulting materials were implemented in bottom-gate bottom-contact OTFTs and tested as *n*-type organic semiconductors. Since this was a first occurrence for these materials in OTFTs, device optimization was done by looking at different solvents for the spin coating process, as well as different post-deposition annealing temperatures prior to collecting the performance data.

Contribution

This work was completed through contributions of all authors. I synthesized, purified, and characterized the novel materials, performed the computational calculations, fabricated and tested the devices and wrote the manuscript. S.B. trained and assisted me in the device fabrication process and helped interpret the performance data. A.G. assisted in designing the materials. B.H.L. and J.L.B. provided supervision for the project. All authors assisted with editing the manuscript.

Abstract

The synthesis of two alternating donor-acceptor (D-A) small molecules centered around thieno[3,4-c] pyrrole-4,6-dione (TPD) as the main acceptor building block is reported herein. The novel materials are synthesized using a Stille coupling to attach two thiophene donors on either side of the TPD core, followed by an aldol condensation under mild conditions for the addition of terminal secondary acceptor building blocks, representing a sought out A^2-D-A^1-D-A^2 structure. The two newly synthesized materials are to be used as organic semiconductors in organic thin-film transistor (OTFT) devices. Comparative optical, computational, and electrochemical studies were conducted on these new materials to investigate their ability to act as potential *n*-type organic semiconductors. The materials were incorporated into bottom-gate bottom-contact (BGBC) OTFT devices, where subsequent thin-film optimization studies were done to probe the effects that solvent and post-deposition annealing conditions had on the resulting device performance. The results concluded the rhodanine-derived D-A material having the highest performance, with an electron field-effect mobility of 0.011 $cm^2\ V^{-1}\ s^{-1}$ and a threshold voltage of 20.1 V under vacuum, when spin coated in solution with chloroform and annealed at 200 °C after deposition.

2.1 Introduction

Organic thin-film transistors (OTFTs) continue to be a rapidly growing area of research as they are applied in a variety of everyday applications ranging from flexible displays[1], smart packaging[2], E-labels[3], biosensors[4], and more. Their organic nature also provides numerous advantages over traditional inorganic field effect transistors such as cost-efficient processing methods, inherent flexibility, and structural diversity, to name few.[5,6] When fabricating OTFTs, small molecule semiconductors are often chosen to be used as the active layer as they hold many benefits over conjugated polymers like their ease of purification, high mobility averages, as well as their capability to adopt well-defined thin-film morphologies.[7,8]

In the past decades, small molecules comprised of alternating donor (D) and acceptor (A) building blocks, such as A-D-A or D-A-D materials, have shown great promise in organic electronic applications.[9,10] The push-pull effect attained in these carefully designed materials allows for better control over the net dipole moment, which can ultimately lead to a smaller molecular bandgap, thus facilitating charge injection within these types of materials.[11] Over the years, numerous combinations of donors and acceptors have been investigated, where several commonly used building blocks are illustrated in **Figure 2.1**. In both cases, large, fused aromatics are seen in the moiety design as this allows for efficient charge transport throughout the material. Where thiophene-derived aryls are often seen in donor moieties,[12] acceptor building blocks are often comprised of nitrogen- and ketone-derived heteroaryls due to the high electronegative nature of these groups.[13,14] Thieno[3,4-c]pyrrole-4,6-dione (TPD), though less commonly employed, has recently been recognized as a promising acceptor unit in D-A small molecules and polymers in both organic photovoltaic (OPV)[15,16] and OTFT[17] applications. The rigidity of the molecular framework paired with its strong electron withdrawing components makes TPD an ideal candidate, alongside a convenient alkyl region located on the pyrrole group enabling facile functionalization of the building block to finetune its bulk properties.[18,19]

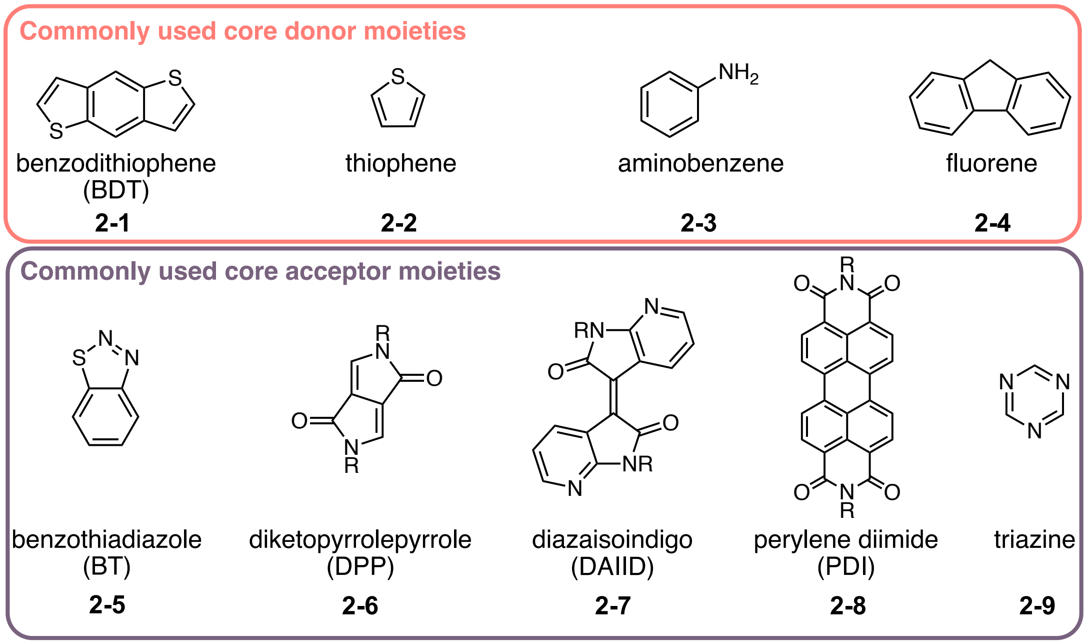

Figure 2.1 *Commonly used donor and acceptor moieties in the design of alternating D-A organic semiconductors.*

TPD can be readily prepared in high yields from commercially available materials and its C_{2v} symmetry enables direct pairing with thienyl substituents to complete the sought-after D-A-D conformation. To pursue this further, additional electron deficient functional groups acting as terminal secondary acceptors were added to the initial D-A-D structure, thus expanding it to a larger A^2-D-A^1-D-A^2 architecture.[20–22] Coupling of a secondary acceptor will further alter the frontier molecular orbital energies of the overall molecule, as the lowest unoccupied molecular orbital (LUMO) is largely governed by electron deficiency, thus rendering A^2-D-A^1-D-A^2 materials suitable for *n*-type electron transfer in OTFTs. From popular terminal acceptor units, dicyanovinyl and rhodanine derivatives are among the more frequently used in the design of D-A molecules due to their strong electron withdrawing effects.[23–25] Overall, the design of a D-A material bearing two varying acceptor units sandwiched between donors will ultimately create a larger conjugated network, thus increasing its potential for enhanced charge transfer due to intramolecular π-π stacking commonly attained by planar molecules in the solid state.[26]

We report in this work the synthesis of extended A^2-D-A^1-D-A^2 frameworks centered around TPD as the acceptor core and expanded with thienyl donor linkers. *N*-ethylrhodanine and dicyanovinyl units were chosen as the secondary terminal acceptors to complete the A^2-D-A^1-D-A^2 framework. The materials were characterized for their electrochemical and optical properties and compared to their simulated computational values. Both materials were integrated in bottom-gate bottom-contact (BGBC) OTFT devices and tested as *n*-type organic semiconductors. A maximum electron mobility of 0.011 $cm^2\ V^{-1}\ s^{-1}$ was attained by the rhodanine-derived material through optimization of spin coating and post-deposition annealing conditions.

2.2 Results and Discussion

2.2.1 Synthesis of A-D Materials

Preparation of the desired A^2-D-A^1-D-A^2 framework involves a multi-step synthetic process, outlined in **Figure 2.2**. The central acceptor moiety, 5-(2-ethylhexyl)thieno[3,4-c]pyrrole-4,6-dione (TPD; **2-13**), was prepared following methods previous reported by *Najari et. al.*[27] involving a condensation reaction achieved *via* reflux with thiophene-3,4-dicarboxilic acid and acetic anhydride. Following the generation of the succinic anhydride intermediate (**2-11**), a primary amine was added to promote a nucleophilic acyl substitution, affording the *N*-alkyl succinic acid monoamide (**2-12**). To increase the overall solubility, a branched 2-ethylhexylamine was used as the nucleophile for the substitution reaction. Once the nucleophilic substitution was complete, the *N*-alkyl succinic acid monoamide was subsequently refluxed with thionyl chloride thus leading to a second condensation, affording **2-13** as a white solid in excellent yield (94%). Note that this building block serves as the core acceptor (A^1) in the D-A molecular design. To facilitate addition of the thienyl donor substituents (D) on either side of the TPD core, subsequent bromination of **2-13** with *N*-bromosuccinimide (NBS) was executed, leading to the dibrominated TPD core (**2-14**) as a white solid in 54% yield.

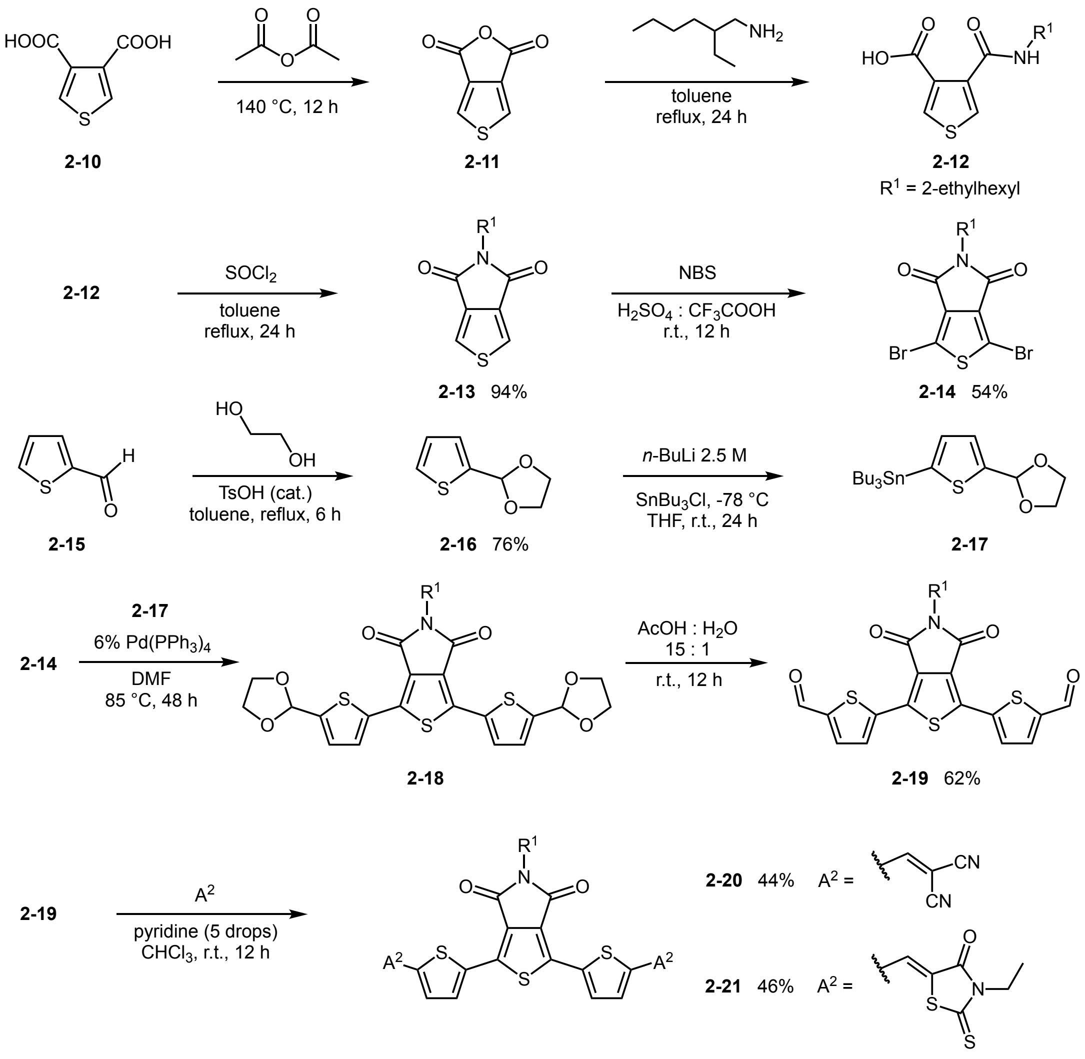

Figure 2.2 *Complete synthetic route to obtain the fused A^2-D-A^1-D-A^2 compounds (2-19 and 2-20).*

The donor thionyl building block was prepared with appropriate functional groups that will enable bridging of the TPD core as well as attachment of the peripheral secondary acceptors. To do so, organotin and aldehyde functional groups need to be present at the 2 and 5 position of the thiophene building block. Starting with 2-thiophenecarboxaldehyde (**2-15**), an intramolecular acetal protection was primarily achieved by refluxing ethylene glycol in toluene. After continuous removal of water through a Dean Stark apparatus, 2(thiophene-2-yl)-1,3-dioxolane (**2-16**) was obtained as a colourless liquid in 76% yield. This protection step was necessary to preserve the aldehyde functional group during stannylation of the thiophene donor moiety. To that end, treatment of **2-16** with n-butyllithium (n-BuLi) in dry THF at -78 °C, followed by the addition of tributyltin chloride ($SnBu_3Cl$) led to the formation of **2-17** as an opaque orange liquid from which the crude was used in the next step of the synthetic process without purification. Identity confirmation of **2-17** was limited to ^{1}H NMR only. The synthetic pathway continues with a Stille coupling between one unit of the brominated TPD core (A^1) and two units of the stannylated thiophene donor (D) to obtain the intermediate D-A^1-D structure. This coupling was accomplished by heating a solution of **2-14** and **2-17** in dry dimethylformamide (DMF) with a $Pd(PPh_3)_4$ catalyst to afford the intermediate **2-18**. Subsequent deprotection of the intramolecular acetals on the thiophene donors in acidic conditions was carried out prior to purification. The D-A^1-D product (**2-19**) was purified through flash column chromatography and subsequent recrystallization from ethanol, and isolated at 62% yield.

The final step in the synthetic pathway to isolate the targeted A^2-D-A^1-D-A^2 framework involves the addition of terminal acceptor units (A^2) to the D-A^1-D intermediate. This addition was achieved by using the terminal aldehydes present on either side of **2-19** and performing a Knoevenagel condensation with the terminal acceptor building block of choice. Two final derivatives were synthesized, one incorporating dicyanovinyl groups at the periphery of the D-A^1-D core and the second incorporating *N*-ethylrhodanine as the terminal acceptor moieties, rendering compounds **2-20** and **2-21**, respectively. Recrystallization from acetonitrile provided **2-20** as a bright red solid in 44% yield and **2-21** as a dark purple solid in 46% yield. All intermediates and final compounds were characterized by ^{1}H and ^{13}C NMRs, and high-resolution mass spectrometry (HRMS), unless stated otherwise, available in Section 2.5 Appendix. Both derivatives are soluble in chlorinated solvents such as DCM and 1,2-dichlorobenzene (*o*-DCB), although **2-21** has lower solubility in comparison to **2-20**, rendering it more challenging to dissolve. For this reason, a ^{13}C NMR spectrum could not be collected for **2-21**. Furthermore, **2-20** showed a prominent peak in its Fourier Transform Infrared (FTIR) spectrum at 2250 cm^{-1} corresponding to the nitrile units, as seen in **Figure A.2.14** of Section 2.5 Appendix. Additionally, both final compounds exhibit modest thermal stability, up to 376 °C and 365 °C for **2-20** and **2-21** respectively, at which 5% mass loss was recorded as seen in **Figure 2.3**.

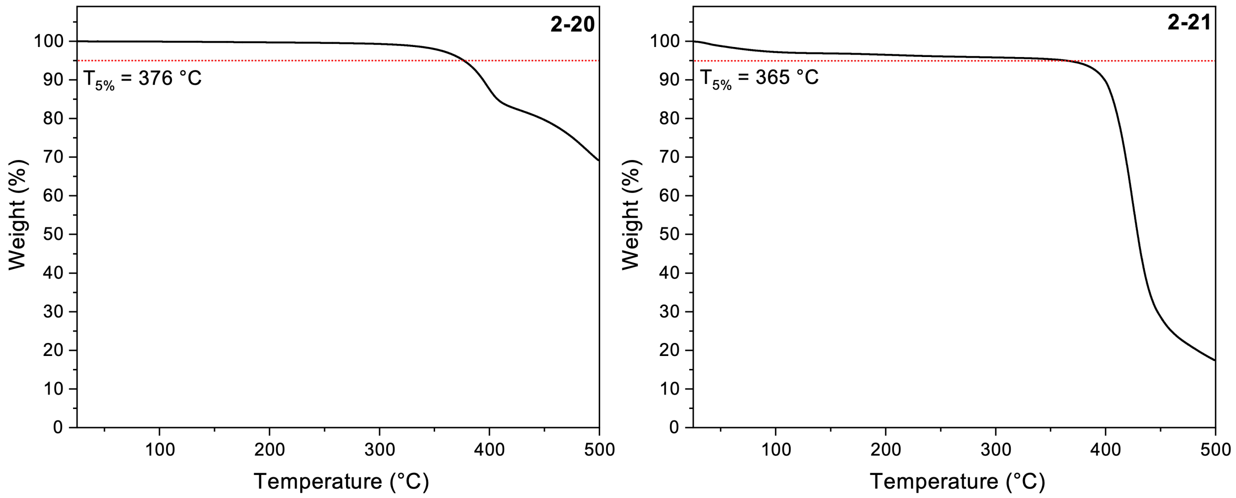

Figure 2.3 *Thermogravimetric analysis (TGA) of 2-20 (left) and 2-21 (right) collected under nitrogen with a temperature indicator of their respective 5% total mass loss (red).*

2.2.2 Optical, Theoretical and Electrochemical Studies

To probe the optical properties of **2-20** and **2-21**, their absorption and photoluminescence (PL) spectra were recorded in DCM and the results are presented in **Figure 2.4** and **Table 2.1**. Both compounds showed a strong absorbance in the visible range, with a maximum absorption peak at 477 nm and 513 nm for **2-20** and **2-21**, respectively. A bathochromic shift is observed for **2-21**, a result of the electron withdrawing effect provided by both the carbonyl and thiocarbonyl groups present on the rhodanine acceptor. Unsurprisingly, the absorption profiles between the two D-A materials are relatively similar, with a red-shifted shoulder off their maximum absorption peak; however, a second absorption peak is apparent at a higher intensity for **2-21** around 442 nm, where the equivalent peak for **2-20** appears as a shoulder at 403 nm. As for their photoluminescence, aside from a bathochromic shift, the overall fluorescent spectroscopic signatures of the two analogues are quite similar with both materials possessing a Stokes shift of 64 nm.

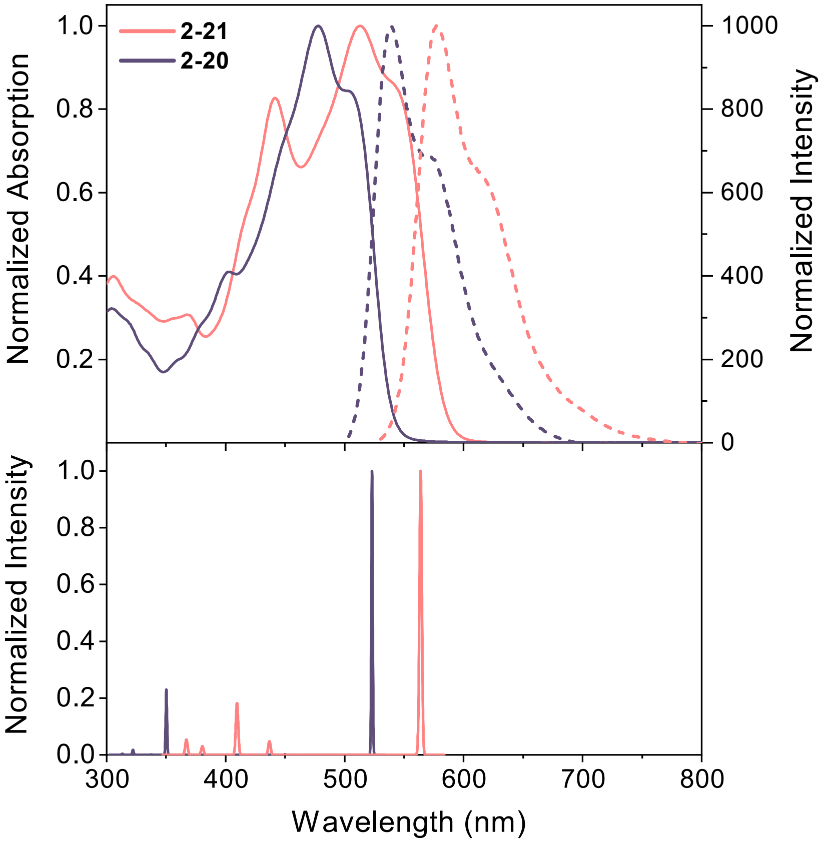

Figure 2.4 *Experimental absorption (solid) and PL (dashed) spectra of 2-20 (λ_{ex} = 477 nm, purple) and 2-21 (λ_{ex} = 513 nm, pink) in DCM solutions (top). TD-DFT calculated absorption spectra of 2-20 (purple) and 2-21 (pink) (bottom).*

Additional to the optical studies, density-functional theory (DFT) calculations using the B3LYP level of theory and 6-31G(d) basis set were performed on **2-20** and **2-21** to better analyze the optimized geometries, orbital energetics (**Table A.2.1** of Section 2.5 Appendix) and optical transitions (**Figure 2.4**) of the materials. The results of the geometry optimization suggest that both extended frameworks are completely planar. Time-Dependent (TD) DFT calculations were performed on the optimized geometries of the materials. In both cases, the simulated absorption peak with the strongest oscillator strength corresponds solely to the HOMO → LUMO transition while the other absorption peaks with weaker oscillator strengths correspond to a combination of transitions ranging from the HOMO-10 to the LUMO+3 levels (where the transitions occur in various orders, see **Table A.2.3** of Section 2.5 Appendix for more details). Interestingly, the maximum absorption for both materials does not correspond directly with the maximum absorption from the experimental UV-Vis-NIR, but rather with the red-shifted shoulders apparent at 505 and

543 nm for **2-20** and **2-21**, respectively. These shoulders could be a result of the overall dipole moment of the molecules causing a slight bathochromic shift.

The redox potentials for **2-20** and **2-21** were measured through cyclic voltammetry (CV) in solution with DCM with a 0.1 M concentration of tetrabutylammonium hexafluorophosphate ($[NBu_4][PF_6]$), and referenced to a ferrocene/ferrocenium (Fc/Fc^+) redox couple as an internal standard (+0.48 V vs SCE);[28] the results can be found in **Figure 2.5** and **Table 2.1**. Neither material portrayed an oxidation peak thus indicating that formation of the radical cation is less favorable given the high electron withdrawing properties provided by the acceptors present in both materials. Two quasi-reversable redox processes were observed for both materials, corresponding to the sequential reduction to the radical anion ($E^{0/-1}$) and dianion ($E^{-1/-2}$). The LUMO energy level (E_{LUMO}) of the materials were calculated from the onset cathodic potential of the first reduction (φ_{red}) and by assuming the energy level of Fc/Fc^+ to be -4.8 eV below the vacuum level.[29] The HOMO energy level (E_{HOMO}) of the materials was determined by reducing the E_{LUMO} with the optical bandgap value (E_g^{opt}) obtained from the onset of the first absorption band of the UV-Vis-NIR spectra for each derivative. The HOMO and LUMO energy levels of **2-21** are positively shifted compared to **2-20**, where its HOMO level sits at +0.19 eV and +0.37 eV for the LUMO level. The theoretical HOMO (E_{HOMO}^{th}) and LUMO (E_{LUMO}^{th}) energy values (**Table 2.1**) follow the same trend as the experimental values obtained, where both the HOMO and LUMO levels of **2-21** lie at a higher energy in comparison to **2-20**. The lower energy values obtained for **2-20** could be reasoned with the fact that the dicyanovinyl groups have a slightly higher polarization in comparison to the rhodanine groups, thus lowering its energy values. Furthermore, the theoretical HOMO→LUMO energy bandgap (E_g^{th}) for **2-21** is slightly smaller than that of **2-20**, which is also in line with what was observed in the experimental absorption spectra of the two materials.

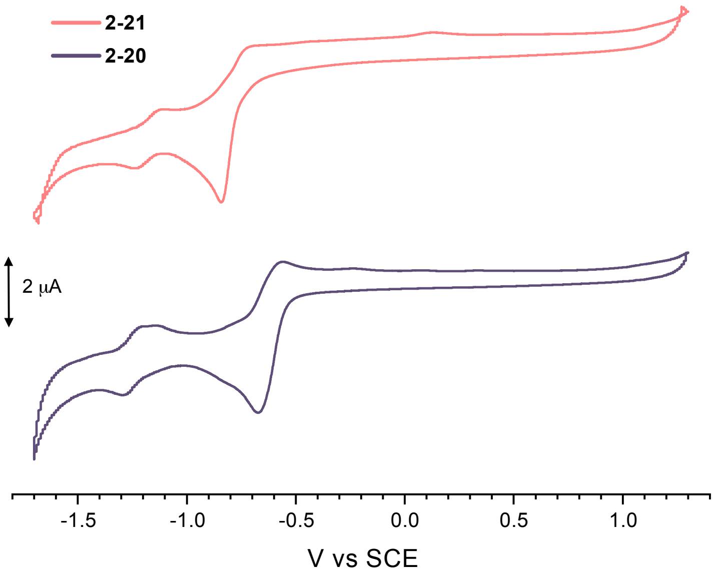

Figure 2.5 *Cyclic voltammogram of 2-20 (purple) and 2-21 (pink) in dry THF at 100 mV* s^{-1} *with 0.1 M* $TBAPF_6$ *as supporting electrolyte.*

Table 2.1 *Photophysical*[a]*, electrochemical*[a] *and theoretical*[b] *properties of 2-20 and 2-21.*

	Experimental						**Theoretical**		
Material	λ_{onset} **[nm]**	λ_{max}^{Abs} **[nm]**	λ_{max}^{PL} **[nm]**	E_g^{opt}[c] **[eV]**	E_{HOMO} **[eV]**	E_{LUMO}[d] **[eV]**	E_g^{th}[e] **[eV]**	E_{HOMO}^{th} **[eV]**	E_{LUMO}^{th} **[eV]**
2-20	539	477	540	2.30	-6.08	-3.78	2.59	-6.34	-3.75
2-21	585	513	577	2.12	-5.71	-3.59	2.42	-5.70	-3.28

[a] Measurements were performed in solution with DCM.

[b] Calculations were done using a B3LYP level of theory and a 6-31G(d) basis set.

[c] Values calculated from corresponding λ_{onset}.

[d] Values calculated using the first onset reduction potential.

[e] Values calculated from TD-DFT calculations performed on the optimized geometries.

2.2.3 OTFT Fabrication and Characterization

Bottom-gate bottom-contact (BGBC) organic thin-film transistors (OTFTs) were fabricated using *n*-doped silicon substrates with a thermally grown silicon dioxide dielectric layer. The dielectric layer underwent a surface treatment with octyltrichlorosilane (OTS), followed by the sample deposition *via* spin coating under N_2 atmosphere. Each substrate contained a total of 16 devices with four sets of different channel lengths at 2.5, 5.0, 10.0 and 20.0 μm. All devices were fabricated using either **2-20** or **2-21** as the semiconducting layer and tested under vacuum (< 0.1 Pa) under *n*-type conditions using a gate voltage range of 0 to 60 V given that the LUMO values obtained from the electrochemical studies fall in line with what is typically recognized for *n*-type semiconductors.[30] The devices were also tested under *p*-type conditions using a gate voltage range of 0 to -60 V to see if they portrayed any ambipolar character; however, no field effect was observed.

During the device studies, two key conditions were manipulated for thin-film optimization, the first being the solvent used during the spin coating process and the second being the post-deposition annealing temperature applied; all conditions are summarized in **Table 2.2**. Two different chlorinated solvents were investigated for the spin coating process of **2-20** and **2-21** onto the substrates, chloroform ($CHCl_3$) and 1,2-dichlorobenzene (*o*-DCB). The choice of having chlorinated solvents stemmed from the lower solubility held by both materials in non-chlorinated solvents. Furthermore, both solvents were chosen to investigate whether volatility had any impact on the thin-film formation during the spin coating process. The solution concentrations for spin coating were set at 10 mg mL^{-1} for **2-20** and 5 mg mL^{-1} for **2-21**. Due to the lower solubility of **2-21** compared to **2-20**, a concentration of 10 mg mL^{-1} could not be achieved. Alongside with this, the effects on OTFT device performance with regards to post-deposition annealing was also of interest. Post-deposition annealing can be favourable for certain materials as the heat helps to remove any residual solvent that may be trapped in the thin-film and can induce molecular rearrangement in certain cases to provide a more optimal molecular packing order, which in return will have a beneficial impact on the device performance. To investigate this, OTFT devices of each material were either left at room temperature (22 °C), annealed under vacuum at 70 °C for 1 h after deposition, or at 200 °C for 1 h after deposition.

Electrical characteristics of the materials for each condition are summarized in **Table 2.2** (for a channel length of 2.5 μm) and examples of the output and transfer curves are shown in **Figure 2.6**. When comparing the overall performance between the two materials, **2-21** possessed a higher performance for each condition over **2-20**, with its highest electron mobility average ($\mu_{e,avg}$) standing at 6.41×10^{-3} $cm^2\ V^{-1}\ s^{-1}$ for the devices annealed at 200 °C. Alongside portraying higher $\mu_{e,avg}$, **2-21** also holds higher on/off current ratios ($I_{on/off}$). Interestingly, **2-21** has slightly higher threshold voltages (V_T) in comparison to **2-20**, which is less favorable and could be a result of multiple factors such as a higher amount of charge trapping or higher contact resistance between the thin-film and the gold electrodes. Another factor that could have impacted the threshold voltage would be the work function (WF) of the gold with respect to the LUMO level of the materials. As previously mentioned, **2-21** has a LUMO level that sits at -3.59 eV, whereas **2-20**'s LUMO level sits at -3.78 eV; on the other hand, gold's WF sits around -5.1 eV. The larger gap between the LUMO of **2-21** and the gold's WF could explain the need for a higher threshold voltage to induce a field effect.[31,32]

Table 2.2 *List of conditions applied during the thin-film deposition process of 2-20 and 2-21 alonside the OTFT performance properties obtained for devices of channel length of 2.5 μm.*

Material	**Solvent**	**Annealing Temp [°C]**	$\mu_{e,avg}$[a] [cm^2 V^{-1} s^{-1}] ×10^{-3}	$\mu_{e,max}$ [cm^2 V^{-1} s^{-1}] ×10^{-3}	V_T [V]	$I_{on/off}$
2-20	CHCl$_3$	22	0.11 ± 0.02	0.15	7.7	10^2
		70	0.29 ± 0.02	0.49	12.0	10^3
		200	3.47 ± 0.18	3.68	14.4	10^4
	o-DCB	22	0.05 ± 0.004	0.07	5.3	$10^2 – 10^3$
		70	0.23 ± 0.02	0.32	4.6	10^3
		200	6.45 ± 0.36	8.16	19.0	$10^4 – 10^5$
2-21	CHCl$_3$	22	1.03 ± 0.41	1.34	30.0	10^4
		70	1.29 ± 0.32	1.46	22.6	10^3
		200	6.41 ± 0.54	11.00	20.1	$10^4 – 10^5$
	o-DCB	22	0.11 ± 0.01	0.18	28.8	10^3
		70	2.72 ± 0.31	4.69	24.3	10^4
		200	[b]	0.86	19.8	10^2

[a] Average values were calculated from a total of eight 2.5 μm devices, obtained from duplicate substrates.

[b] Only one device was functional, therefore an average mobility could not be calculated.

For **2-20**, the CHCl$_3$ solution appeared to form uniform films covering the entirety of the chips, whereas spin coating of the *o*-DCB solution did not produce any film at all. Instead, what was observed on the chips were very small red specs of the material that adhered onto the gold electrodes and between the channels (picture references available in **Table A.2.4** of Section 2.5 Appendix). The poor spin coating quality of the *o*-DCB solution resulted in a large number of non-functional devices. A similar trend was observed in the thin-film quality of the **2-21** material, where better film coverage was attained with the $CHCl_3$ solutions compared to the *o*-DCB solutions, leading to less functional devices from the *o*-DCB spin-coated substrates.

When analyzing the effects of post-deposition annealing temperatures on device performance, **2-20** demonstrated a significant increase in performance (approximately one order of magnitude in its $\mu_{e,avg}$) when the substrates were annealed to 200 °C, as can be seen in **Figure 2.6**. For **2-21**, the effects of increased annealing temperatures had minimal impacts on device performance. Further investigation was done through differential scanning calorimetry (DSC) and X-ray diffraction (XRD) of the thin-films (**Figures 2.7a** and **2.7b**). For **2-20**, the results of the DSC study showed an endothermic peak at 195 °C and an exothermic peak at 183 °C indicating melting and crystallizing points, respectively. In addition, XRD results demonstrated a peak appearing at $2\theta = 7°$ for the **2-20** thin-film annealed at 200 °C, further confirming a crystal packing rearrangement when annealing at 200 °C. As for **2-21**, DSC and XRD analyses of its thin-films revealed no evidence of crystallinity, indicating that the films remain amorphous across all annealing temperatures. Amorphous films can also play a role in the increase of charge traps, which could explain the reason behind the larger initial threshold voltages observed for this material at low annealing temperatures.[33]

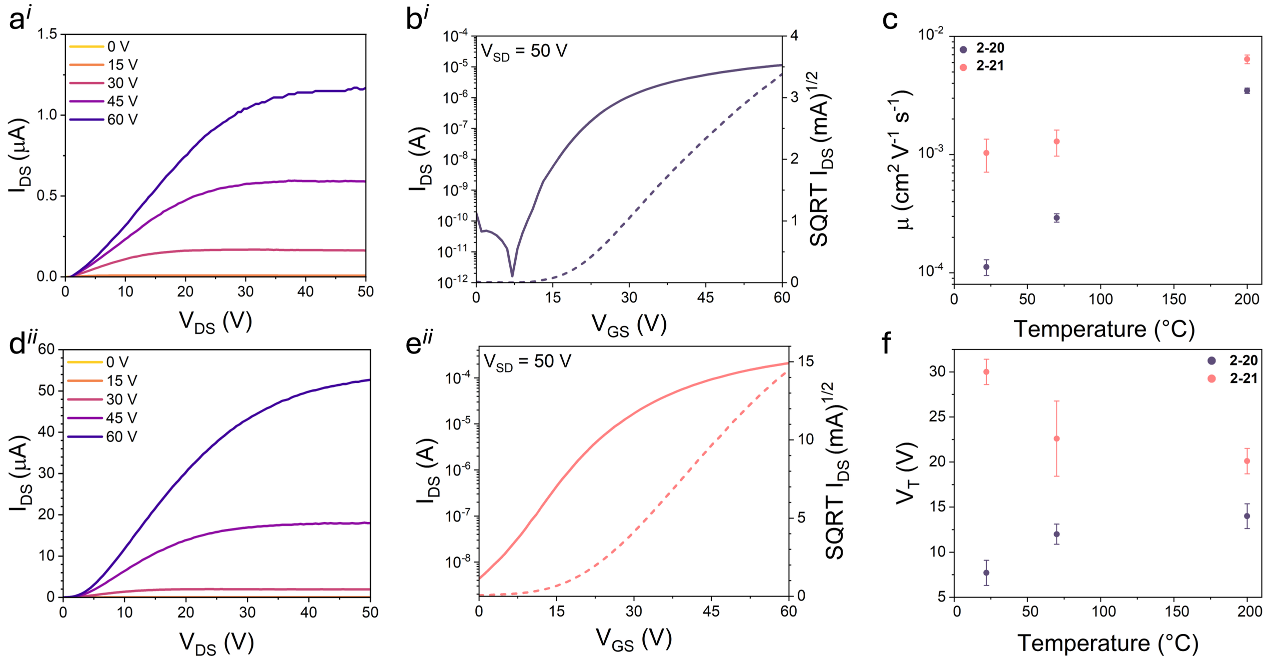

***Figure 2.6** Examples of (a,d) output and (b,e) transfer curves. Summary of (c) the average mobilities and (f) the average threshold voltages collected for 2-20 (purple) and 2-21 (pink). [i]For 2-20. [ii]For 2-21.*

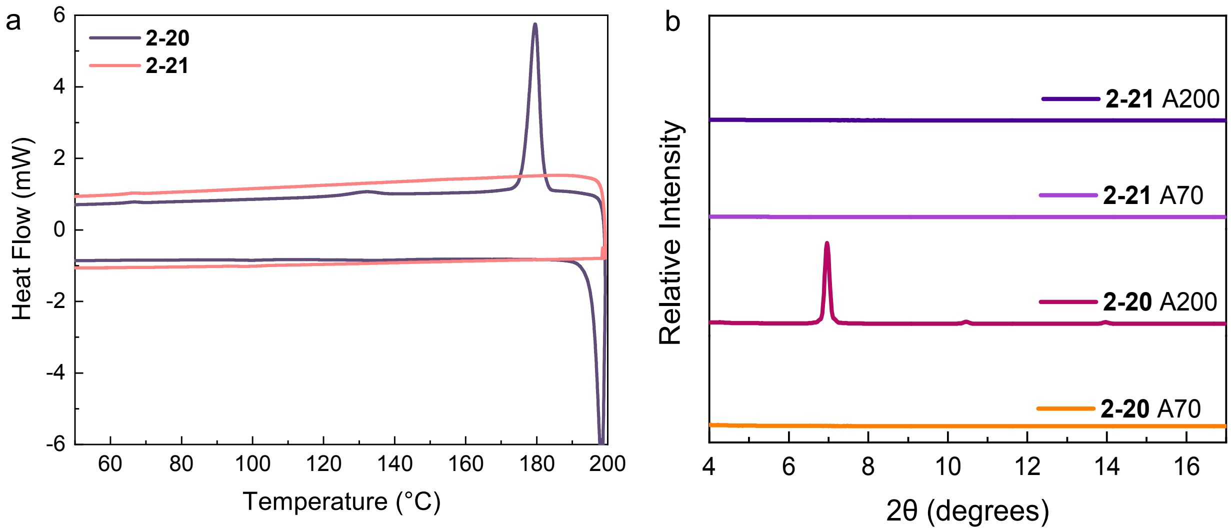

Figure 2.7 *(a) Differential scanning calorimetry (DSC) curves of heating and cooling of 2-20 (purple) and 2-21 (pink). (b) XRD pattern of 2-20 annealed at 70 °C (orange) and 200 °C (dark pink), and 2-21 annealed at 70 °C (purple) and 200 °C (blue).*

2.3 Conclusion

In summary, two new A^2-D-A^1-D-A^2 small molecules containing a thieno[3,4-c]pyrrole-4,6-dione building block as the core acceptor, thiophene donors, and either *N*-ethylrhodanine or dicyanovinyl groups as the terminal acceptors were synthesized and isolated. Both materials were characterized to study their electrochemical, optical, and computational properties. The results obtained indicated that both materials would be suitable as *n*-type organic semiconductors. The materials were then incorporated into bottom-gate bottom-contact OTFTs, where studies looked at how the choice in spin coating solvent and post-deposition annealing temperatures impacted the thin-film morphology and overall device performance. Results showed **2-21** possessed higher overall performance, although there was a higher level of improvement on device performance for **2-20**, which was due to the crystallization of the thin-film when annealed at high temperatures. Additionally, low boiling chlorinated solvents proved to create more uniform thin-films for both materials, thus leading to a higher number of functional devices. These results demonstrate how device engineering plays a critical role in optimizing the semiconducting performance.

2.4 Experimental

2.4.1 Materials

Thiophene-4,4-dicarboxilic acid was purchased from Oakwood Chemicals Inc. 2-ethylhexyl amine, thionyl chloride, trifluoroacetic acid (TFA), *n*-butyllithium (^{n}BuLi*)* and dicyanovinyl (malononitrile) were purchased from Sigma-Aldrich. 2-Thiophenecarboxaldehyde, *p*-toluenesulfonic acid monohydrate and *N*-ethylrhodanine were purchased from TCI Chemicals Inc. Ethylene glycol was purchase from ACP Chemicals Inc. Sulfuric acid was purchased from VWR Chemicals. *N*-bromosuccinimide was purchased from Alfa Aesar. Tributyltin chloride was purchased from ACROS Chemicals Inc. Tetrakis(triphenylphosphine)palladium(0) ($Pd(PPh_3)$) was purchased from TREM Chemicals Inc. All solvents used were ACS grade; dry solvents were obtained by passing them through activated alumina on a J. C. Meyer solvent purification system. NMR spectra were collected in $CDCl_3$ solutions at room temperature on a Bruker Avance 400 MHz spectrometer and the spectra were referenced to the deuterated solvent peak at 7.26 ppm and 77.6 ppm for proton and carbon NMR, respectively. IR spectra were recorded on an Agilent Technologies Cary 630 Fourier Transform Infrared (FT-IR) spectrometer. Mass spectrometry analyses were recorded using a Kratos Concept 1S, Electron impact, Magnetic Sector, high-resolution mass spectrometer instrument.

2.4.2 Synthesis of 5-(2-ethylhexyl)thieno[3,4-c]pyrrole-4,6-dione (2-13)

Thiophene-3,4-dicarboxylic acid (1.50 g, 8.71 mmol) was dissolved with acetic anhydride (32.0 mL). The solution was stirred overnight at 140 °C. The solution was then cooled to room temperature and the solvent was evaporated via cryogenic distillation to obtain a brown solid. The solid was further dissolved in toluene (60.0 mL), 2-ethylhexylamine (1.69 g, 13.07 mmol) was added and the solution was refluxed for 24 h. the mixture was cooled down to room temperature and solvent was removed under reduced pressure to obtain a dark brown solid. Thionyl chloride (90.0 mL) was added to the solid and refluxed for 3 h. Final mixture was cooled, and the solvent was removed under reduced pressure to afford the crude product as a dark red solid. The crude product was purified *via* flash column chromatography using 1:1 DCM:Hexanes to afford the title product as a white powder (2.18 g, 94% yield). ^{1}H NMR (400 MHz, $CDCl_3$) δ (ppm): 7.80 (s, 2H), 3.51 (d, J = 8 Hz, 2H), 1.6 (m, 1H), 1.35-1.25 (m, 8H), 0.94-0.86 (m, 6H). ^{13}C NMR (400 MHz, $CDCl_3$) δ (ppm): 163.0 (1), 136.63 (2), 125.5 (3), 42.4 (4), 38.2 (5), 30.5 (6), 28.5 (7), 23.8 (8), 23.0 (9), 14.1 (10), 10.4 (11). EI-HRMS m/z: [M]+ calcd. for $C_{14}H_{19}NO_2S$ [M]+: calcd. 265.11; Found, 265.11499.

2.4.3 Synthesis of 1,3-dibromo-5-(2-ethylhexyl)thieno[3,4-c]pyrrole-4,6-dione (2-14)

5-(2-ethylhexyl)thieno[3,4-c]pyrrole-4,6-dione (1.11 g, 4.19 mmol) was placed in a 100 mL Erlenmeyer flask covered in tin foil. In a separate beaker, H_2SO_4 (6.5 mL) and CF_3CO_2H (20.0 mL) were added together and stirred for ~15min. The acid mixture was added to the Erlenmeyer containing the TPD core and the solution was stirred for an additional 15 min with a glass top covered in aluminum foil. *N*-bromosuccinimide (2.31 g, 12.99 mmol) was added in 4 parts at 2-hour intervals and the solution was stirred at room temperature overnight. After 16 h, the reaction mixture was quenched with water and extracted with DCM. The organic phases were combined, dried over $NaSO_4$, and then concentrated under reduced pressure to afford the crude product as a red/brown solid. The crude product was purified *via* flash column chromatography using 3:2 DCM:Hexanes to afford the title product as a white powder (0.989 g, 56% yield). ^{1}H NMR (400 MHz, $CDCl_3$) δ (ppm): 3.51 (d, J = 8 Hz, 2H), 1.80-1.75 (m, 1H), 1.32-1.28 (m, 8H), 0.95-0.85 (m, 6H). ^{13}C NMR (400 MHz, $CDCl_3$) δ (ppm): 160.7 (1), 134.7 (2), 113.0 (3), 42.6 (4), 38.2 (5), 30.5 (6), 28.5 (7), 23.8 (8), 23.0 (9), 14.1 (10), 10.4 (11). EI-HRMS m/z: [M]+ calcd. for $C_{14}H_{17}Br_2NO_2S$ [M]+: calcd. 424.93356; Found, 424.93.

2.4.4 Synthesis of 2(thiophene-2-yl)-1,3-dioxolane (2-16)

2-thiophenecarboxaldehyde (12.0 g, 107 mmol) and ethylene glycol (29.8 mL, 535 mmol) were dissolved in toluene (100 mL) and *p*-toluenesulfonic acid monohydrate (0.407 g, 2.14 mmol) was added to the solution. Alongside continuous removal of water, the mixture was refluxed for 6 h using a Dean-Stark apparatus. The solution was then quenched with 2.5 M NaOH (12.5 mL) and extracted with water. Organic phases were combined, dried over Na_2SO_4, and concentrated under reduced pressure to afford the crude product as a dark purple/black oil. The crude product was purified *via* distillation in vacuo (b.p. 110 °C, 15 mmHg) to afford the title product as a colorless oil (12.69 g, 76%). ^{1}H NMR (400 MHz, $CDCl_3$) δ (ppm): 7.35 (dd, J = 4, 6 Hz, 1H), 7.20-7.16 (m, 1H), 7.00 (dd, J = 4, 4 Hz, 1H), 6.12 (s, 1H), 4.16-4.06 (m, 2H), 4.04-3.95 (m, 2H).

2.4.5 Synthesis of 5-(1,3-Dioxolan-2-yl)thiophen-2-yl)tributylstannane (2-17)

2-(thiophen-2-yl)-1,3-dioxolane (3.00 g, 19.23 mmol) was dissolved in dry THF (55 mL) and the solution was degassed with N_2 for 15 min. The solution was cooled to -78 °C using a dry ice/acetone cooling bath, then 2.5 M *n*-BuLi in hexane (11.54 mL, 28.84 mmol) was added dropwise over 15 min maintaining a temperature of -78 °C. The resulting solution was stirred at -78 °C for 1 h and warmed to -40 °C. After stirring for 4 h, the solution was cooled back to -78 °C, $SnBu_3Cl$ (5.48 mL, 20.19 mmol) was added dropwise. After stirring at room temperature for 24 h, the reaction mixture was quenched with saturated NH_4Cl and extracted with DCM. The organic phases were combined, dried over anhydrous Na_2SO_4, and concentrated under reduced pressure to afford the crude product as a yellow oil, which was used in subsequent steps without further purification (10.57 g, 123%). ^{1}H NMR (400 MHz, $CDCl_3$) δ (ppm):7.28 (d, *J* = 4 Hz, 1H), 7.05 (d, *J* = 4 Hz, 1H), 6.15 (s, 1H), 4.18-4.11 (m, 2H), 4.06-3.99 (m, 2H), 1.88-1.83 (m, 1H), 1.69-1.50 (m, 8H), 1.40-1.26 (m, 11H), 1.12-1.05 (m, 5H), 0.96-0.85 (m, 14H) (Excess $SnBu_3$ present in crude, which accounts for the surplus of protons present in the ^{1}H NMR).

2.4.6 Synthesis of 1,3-di((5-carbaldehyde)thien-2'-yl)-5-(2-ethylhexyl)thieno[3,4-c]pyrrole-4,6-dione (2-19)

2-14 (1.00 g, 2.38 mmol), **2-17** (3.18 g, 7.13 mmol) and tetrakis(triphenylphosphine) palladium (0.165 g, 0.14 mmol) were dissolved in dry DMF (15.0 mL). The solution was heated at 90 °C and stirred for 72 h. The reaction mixture was then cooled to room temperature and extracted with ether/water. The organic phases were combined, dried over Na_2SO_4, filtered through celite, and concentrated under reduced pressure. The crude intermediate was then dissolved in acetic acid (15.0 mL) and water (1 mL). After stirring at 50 °C with a glass top overnight, the solvent was then removed under reduced pressure to afford the crude final product as a dark orange solid. The crude was purified *via* flash column chromatography using 3:2 DCM:Hexanes and recrystallized in EtOH to afford the title product as a mustard yellow solid (0.72 g, 62%). ^{1}H NMR (400 MHz, $CDCl_3$) δ (ppm): 9.96 (s, 2H), 8.21 (d, *J* = 4 Hz, 2H), 7.78 (d, *J* = 4 Hz, 2H), 3.60 (d, *J* = 4 Hz, 2H), 1.84 (m, 1H), 1.33-1.25 (m, 8H), 0.95-0.88 (m, 6H). ^{13}C NMR (400 MHz, $CDCl_3$) δ (ppm): 182.6 (1), 162.3 (2), 145.2 (3), 140.1 (4), 136.6 (5), 136.1 (6), 131.7 (7), 130.9 (8), 42.8 (9), 38.3 (10), 30.6 (11), 28.6 (12), 23.9 (13), 23.0 (14), 14.1 (15), 10.4 (16). EI-HRMS m/z: [M]+ calcd. for $C_{24}H_{23}NO_4S_3$ [M]+: calcd. 485.07895; Found, 485.08.

2.4.7 Synthesis of 1,3-di((5'-(3'',3''-dicyano)ethenyl)thien-2'-yl)-5-(2-ethylhexyl) thieno[3,4-c]pyrrole-4,6-dione (2-20)

2-19 (0.080 g, 0.165 mmol) and malononitrile (22.9 g, 0.346 mmol) were dissolved in chloroform (10 mL), followed by five drops of pyridine. After stirring at room temperature overnight, the reaction mixture was quenched with water and extracted with chloroform. The organic phases were combined, dried over Na_2SO_4 and concentrated under reduced pressure to afford the crude product as a red/orange solid (129 mg). The crude solid was recrystallized in acetonitrile to afford the title product as a red solid (89 mg, 44%). ^{1}H NMR (400 MHz, $CDCl_3$) δ (ppm): 8.28 (d, J = 4 Hz, 2H), 7.83 (s, 2H), 7.82 (d, J = 4 Hz, 2H), 3.61 (d, J = 4 Hz, 2H), 1.84 (m, 1H), 1.32 (m, 14H), 0.91 (m, 6H). ^{13}C NMR (δ, $CDCl_3$, RT, 400 MHz): 162.1 (1), 149.6 (2), 141.4 (3), 138.8 (4), 137.2 (5), 135.4 (6), 132.7 (7), 131.4 (8), 113.4 (9), 112.8 (10), 80.1 (11), 77.2 (12), 38.3 (13), 30.5 (14), 28.5 (15), 23.9 (16), 23.0 (17), 14.1 (18), 10.4 (19). DART-HRMS m/z: [M]+ calcd. for $C_{30}H_{23}N_5O_2S_3$ [M]+: calcd. 581.10211; Found, 581.10.

2.4.8 Synthesis of 1,3-di(5'-(2''-(N-ethylrhodanine)ethenyl)thien-2'-yl)-5-(2-ethylhexyl)thieno[3,4-c]pyrrole-4,6-dione (2-21)

2-19 (0.1018 g, 0.210 mmol) and 3-ethylrhodanine (0.1663 g, 1.031 mmol) were dissolved in chloroform (6 mL), followed by five drops of piperidine. After stirring at room temperature overnight, the reaction mixture was quenched with water and an excess of chloroform sequentially. The crude product precipitated directly from the organic phase and was isolated *via* vacuum filtration as a dark purple powder. The crude solid was recrystallized in acetonitrile to afford the title product as a dark purple solid (75 mg, 46%). ^{1}H NMR (400 MHz, $CDCl_3$) δ (ppm): 8.20 (d, J = 4 Hz, 2H), 7.76 (s, 2H), 7.78 (d, J = 4 Hz, 2H), 4.18 (dd, J = 8, 20 Hz, 4H), 3.60 (d, J = 4 Hz, 2H), 1.84 (m, 1H), 1.32 (m, 14H), 0.91 (m, 6H). ESI-HRMS m/z: [M]+ calcd. for $C_{34}H_{33}N_3O_4S_7$ [M]+: calcd. 772.08; Found, 772.05888. Given the low solubility of this compound, ^{13}C NMR analysis was not possible.

2.4.9 Thermogravimetric Analysis

TGA analyses were performed in a 100 μL DTGA/Q5000 IR Platinum Pan using a Discovery 5500 equipment from TA Instruments under nitrogen atmosphere, at a 10 °C min^{-1} heating rate. Samples were heated up to 600 °C and the decomposition temperature (T_d) was determined at 5 % weight loss.

2.4.10 Optoelectronic Characterization

UV-Vis-NIR and photoluminescence (PL) spectroscopy were measured using an Agilent Technologies Cary 5000 UV-Vis-NIR spectrophotometer and an Agilent Technologies Cary Eclipse Fluorescence Spectrophotometer, respectively. Absorbance measurements were collected at ambient temperature in solution with DCM within the range of 250-800 nm. Photoluminescence measurements were collected at ambient temperature in solution with DCM within the range of 500-800 nm using λ_{max} of the respective compound from their absorbance spectrum as the excitation wavelength.

2.4.11 Electrochemical Characterization

Cyclic voltammetry was performed using a Bioanalytical Systems Inc. (BASi) Epsilon potentiostat with C3 cell stand, a glass cell and recorded using BASi Epsilon EC software (V 2.13.77 (c) 2013BASi). Platinum wires were used for the working and counter electrodes and a silver rod was used as the pseudo-reference electrode. The measurements were performed in a dry THF solution under nitrogen, using a 0.1 M tetrabutylammonium hexafluorophosphate (Aldrich) as the supporting electrolyte with a scan rate of 200 mV s^{-1}. All measurements were referenced to the Fc/Fc^+ redox couple (+0.48 V *vs.* SCE) as an internal standard.

2.4.12 Computational Chemistry

All calculations were executed using the Gaussian09 software. The geometries of the studied compounds were investigated using the hybrid density functional B3LYP with the 6-31G(d) basis set. The optimized structures were then used to examine the orbital energies and HOMO-LUMO bandgaps.

2.4.13 Organic Thin-Film Transistor (OTFT) Device Fabrication

All solvents and reagents used for device fabrication were purchased from commercial sources and used without further purification. Bottom-gate bottom-contact (BGBC) OTFTs were constructed using prefabricated chips purchased from Fraunhofer Institute for Photonic Microsystems (IPMS). The gate consisted of *n*-doped Si followed by a 230 nm thick dielectric layer of SiO_2 and Au serving as the source and drain electrodes (30 nm thick), with a 10 nm ITO adhesion layer. One chip contains 16 devices, split into four different channel lengths: 2.5, 5.0, 10.0, 20.0 μm (four devices per channel length); the width of all devices was 2000 μm. The substrates were first rinsed with acetone to remove the protective photoresist and dried under a N_2 stream followed by an oxygen plasma treatment for 15 min. Plasma treatment was performed using a Harrick Plasma Cleaner (PDC-32G). The plasma-treated substrates were then rinsed sequentially with water and iso-propanol, dried under N_2 stream, submerged in a 1% v/v octyltrichlorosilane (OTS) solution in toluene and left to react for 1 h at 70 °C. OTS-treated substrates were then sequentially rinsed with toluene and iso-propanol, dried under a N_2 stream and annealed under vacuum for 1 h at 70 °C then transferred into a glovebox. OTFTs were fabricated by spin coating a solution of the active semiconducting material onto the substrate at 2000 rpm for 60 s (solvent and solution concentration varied during the study; see discussion for further details). Spin coating of the thin-films was performed using a Laurell spin coater, Model

WS-650MZ-23NPPB. After spin coating, some of the OTFT devices were annealed at varying temperatures under vacuum (see discussion for further details).

2.4.14 OTFT Testing

Electrical testing was done using a custom electrical probe station equipped with an environmental chamber, oesProbe A10000-P290 (Element Instrumentation Inc. & Kreus Design Inc.). A Keithley 2614B was used to set the gate-source voltage (V_{GS}) and drain-course voltage (V_{DS}) and measure the drain-source current (I_{DS}). The BGBC OTFTs were tested for *n*-type characteristics at room temperature under vacuum by fixing V_{GS} at discrete values between 0 V and +60 V. The voltages were increased in a stepwise manner, rather than pulsed, with a delay of 80 ms between measurements. Each device's transfer curve was tested four times, measured in the saturation regime, and were modelled using **Equation 2.1**:

$$\mathrm{I_{DS}} = \frac{\mathrm{\mu C_i W}}{\mathrm{2L}}(\mathrm{V_{GS}} - \mathrm{V_T})^2 \qquad \textbf{[2.1]}$$

Where *L* and *W* are the channel length and width, respectively. C_i is the capacitance density of the gate dielectric, calculated using **Equation 2.2**:

$$C_i = \frac{\mathcal{E}_0 \mathcal{E}_r}{t} \qquad \textbf{[2]}$$

Where *t* is the dielectric thickness (230 nm) and ε_r is the relative dielectric constant of SiO_2 (3.9). μ is the field-effect mobility and is calculated from the slope of the best fit through the most linear region of $\sqrt{I_{DS}}$ plotted against V_{GS}. The threshold voltage (V_T) is calculated as the x-intercept of the same line fitting.

2.4.15 Differential Scanning Calorimetry

DSC analyses of were performed using a TA instruments DSC Q1000 from 20°C to 200°C at a scan rate of 10 °C cm^{-1}.

2.4.16 X-ray Diffraction

XRD measurements of the thin-films were performed using a Rigaku Ultima IV powder diffractor with a Cu-Kα (λ = 1.5418 Å) source. Measurements were taken directly from thin films deposited on silicon substrates with a scan range of 3° < 2θ < 15° and a scan rate of 0.5° min^{-1} with no spin.

2.5 Appendix

Table A.2.1 *Frontier molecular orbitals and their corresponding energies (eV) for 2-20 and 2-21.*

Frontier Molecular Orbital	**2-20**	**2-21**
LUMO+2	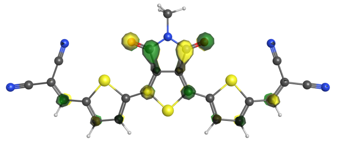 -2.177 eV	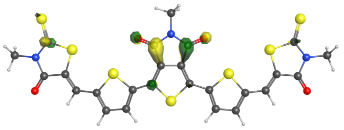 -2.019 eV
LUMO+1	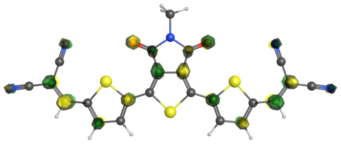 -3.286 eV	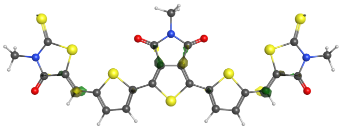 -2.922 eV
LUMO	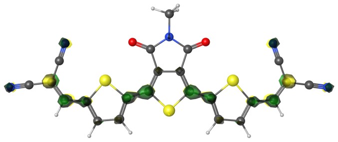 -3.771 eV	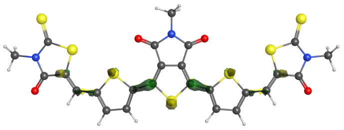 -3.313 eV
HOMO	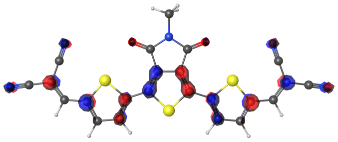 -6.364 eV	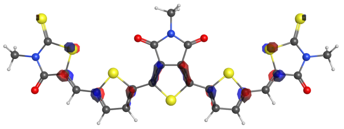 -5.740 eV
HOMO-1	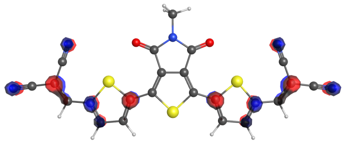 -7.112 eV	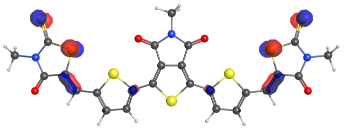 -6.270 eV
HOMO-2	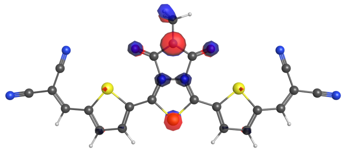 -7.826 eV	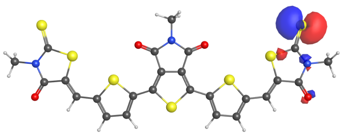 -6.372 eV

Table A.2.2 *TD-DFT optical transitions[a] for 2-20 and 2-21.*

k	**2-20**		**2-21**	
	E [eV]	*f*	*E* [eV]	*f*
1	2.4125	1.4262	2.1985	1.6119
2	2.7730	0.0026	2.5076	0.0000
3	3.2351	0.0002	2.5086	0.0000
4	3.4822	0.3284	2.5290	0.0005
5	3.4878	0.0000	2.8386	0.0776
6	3.5981	0.0021	3.0270	0.2942
7	3.6829	0.0002	3.0714	0.0000
8	3.7518	0.0163	3.0786	0.0000
9	3.7533	0.0086	3.2587	0.0482
10	3.8473	0.0055	3.3775	0.0869

[a] TD-DFT/B3LYP/6-31G(d) level of theory on geometry optimized structures (where R^1 = Me for **2-20** and R^1 = R^2 = Me for **2-21**) where k = order of excitation energy and f = oscillator strength.

Table A.2.3 *Selected TD-DFT transitions for 2-20 and 2-21 (where R_1 = Me for 2-20 and R_1 = R_2 = Me for 2-21).*

Compound	**Calculated *λ* (nm)**	**Transition**	**Oscillator Strength (*ƒ*)**
2-20	513.93	HOMO --> LUMO	1.4262
	356.05	HOMO-1 --> LUMO HOMO --> LUMO+1	0.3284
	330.47	HOMO-1 --> LUMO HOMO --> LUMO+1	0.0163
2-21	563.94	HOMO --> LUMO	1.6119
	436.79	HOMO-1 --> LUMO HOMO --> LUMO+1	0.0776
	409.60	HOMO-1 --> LUMO+1 HOMO --> LUMO+3	0.2942
	380.47	HOMO-6 --> LUMO HOMO-4 --> LUMO	0.0482
	367.09	HOMO-10 --> LUMO HOMO-4 --> LUMO+1	0.0869

Table A.2.4 *Microscope picture references of the spin-coated thin-films of 2-20 and 2-21.*

	2-20	**2-21**
$CHCl_3$ Annealed 70 °C	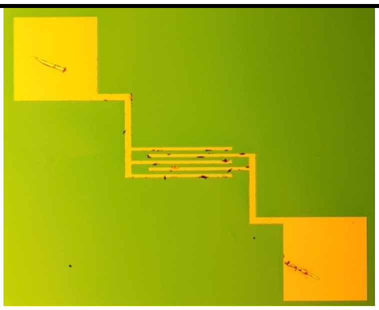	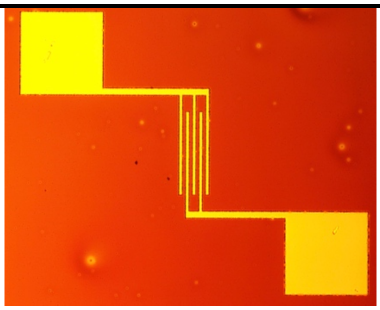
$CHCl_3$ Annealed 200 °C	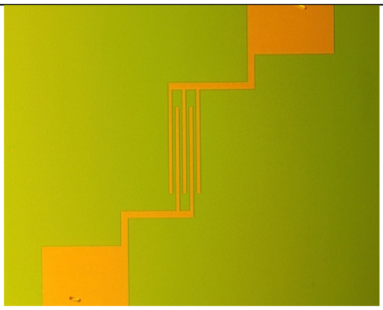	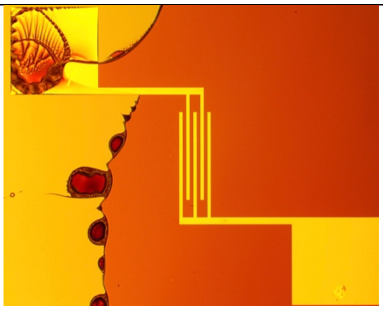
o-DCB Annealed 70 °C	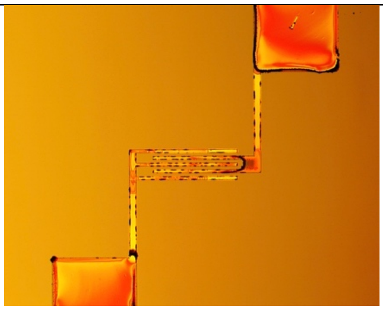	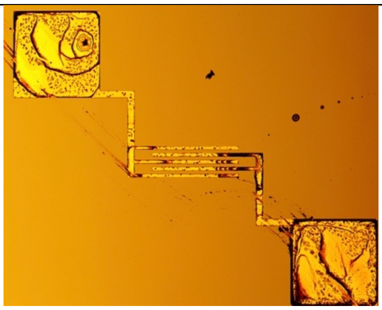

Table A.2.5 *Example of output (a) and transfer (b) curves for 2-20 and 2-21 for each condition tested during the device study.*

	2-20		**2-21**	
	a	b	a	b
CHCl₃ 22 °C	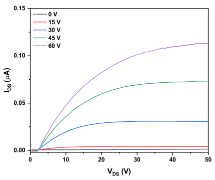	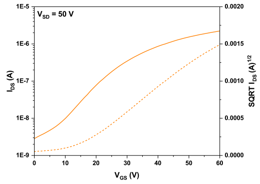	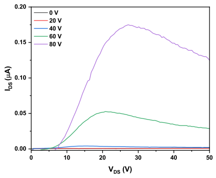	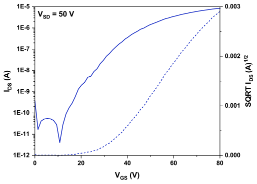
CHCl₃ 70 °C	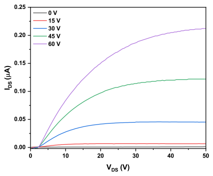	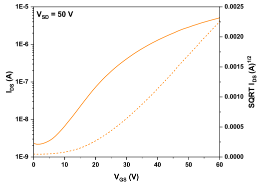	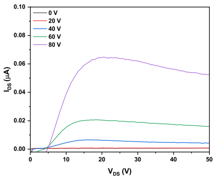	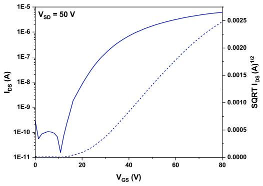
CHCl₃ 200 °C	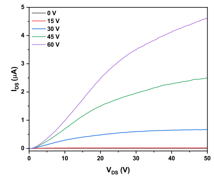	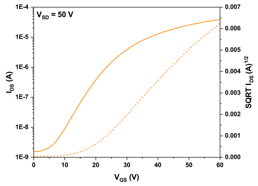	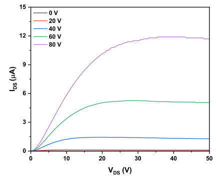	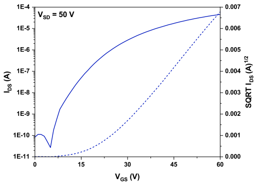
o-PhCl₂ 22 °C	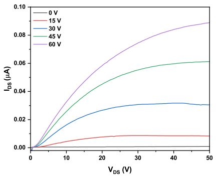	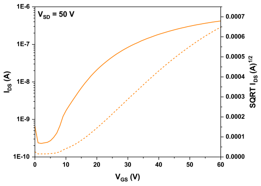	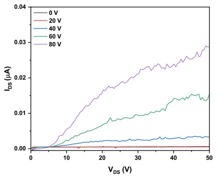	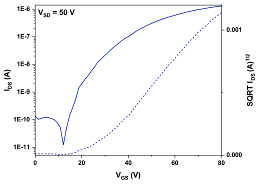
o-PhCl₂ 70 °C	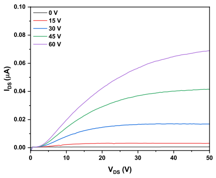	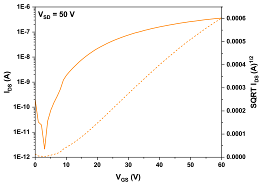	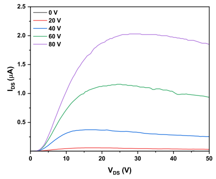	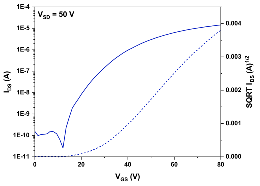
o-PhCl₂ 200 °C	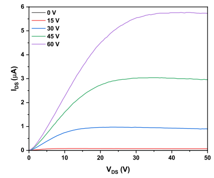	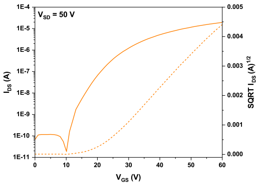	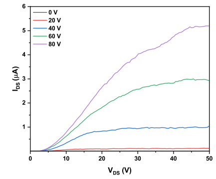	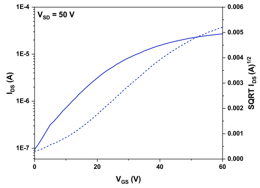

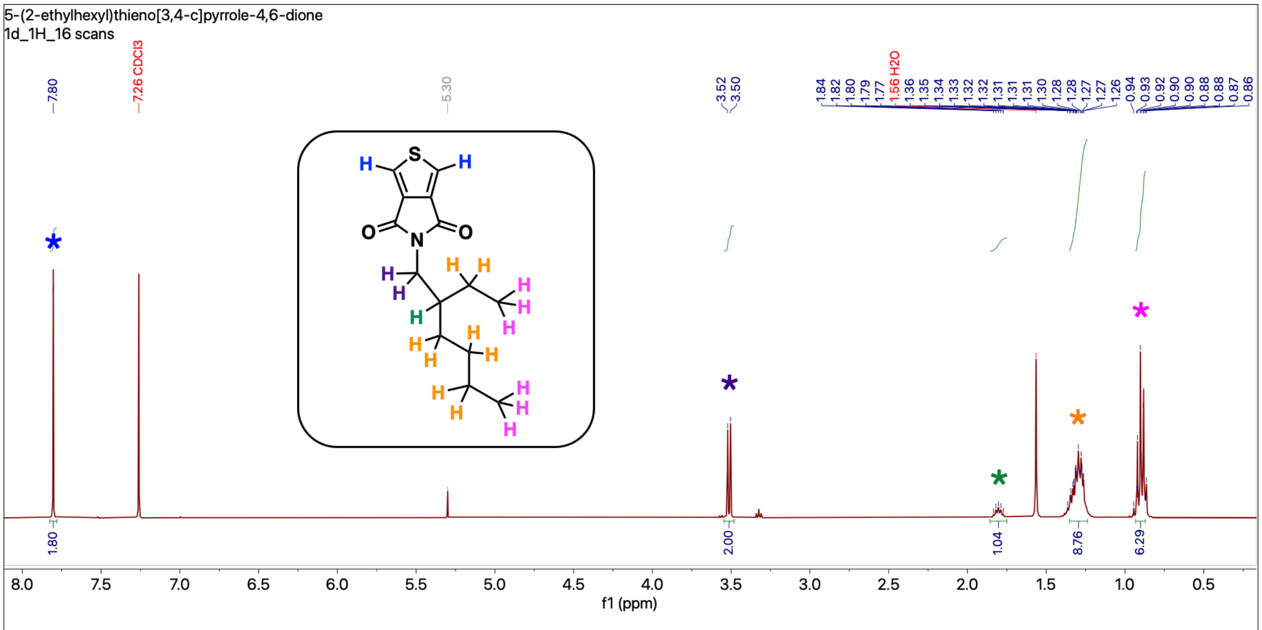

^{1}H NMR (δ, $CDCl_3$, RT, 400 MHz): 7.80 (s, 2H), 3.51 (d, *J* = 8 Hz, 2H), 1.80 (m, 1H), 1.30 (m, 8H), 0.90 (m, 6H).

Figure A.2.1 *^{1}H NMR spectrum of compound 2-13.*

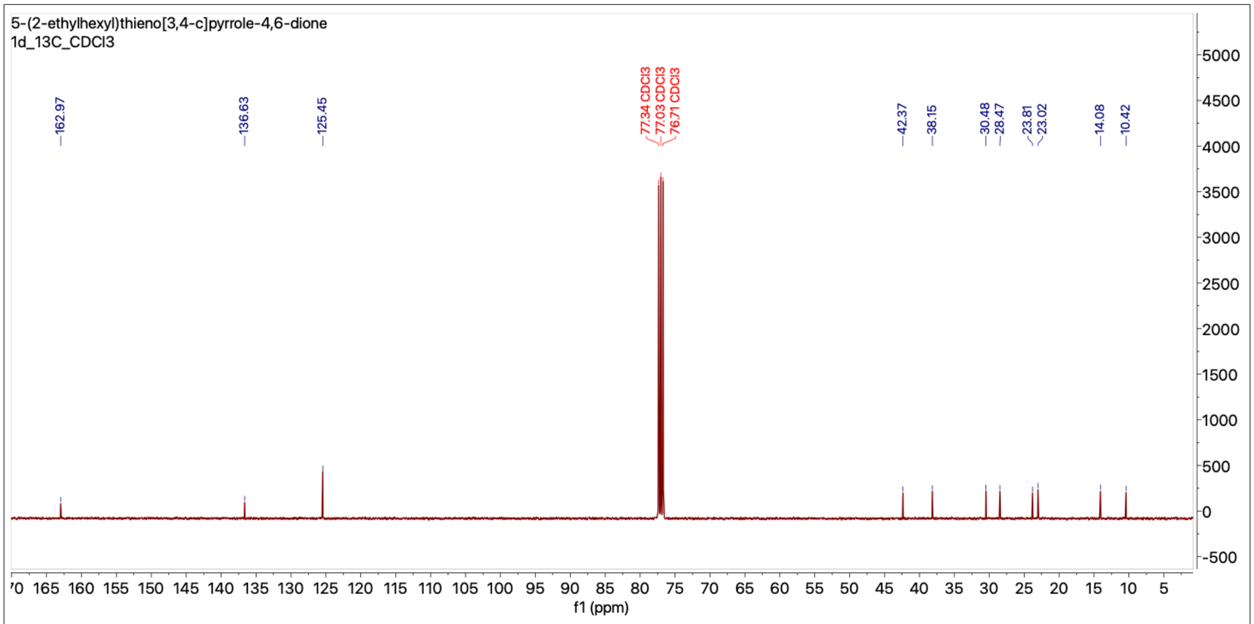

^{13}C NMR (δ, $CDCl_3$, RT, 400 MHz): 162.97 (1), 136.63 (2), 125.45 (3), 42.37 (4), 38.15 (5), 30.48 (6), 28.47 (7), 23.81 (8), 23.02 (9), 14.08 (10), 10.42 (11).

Figure A.2.2 *^{13}C NMR spectrum of compound 2-13.*

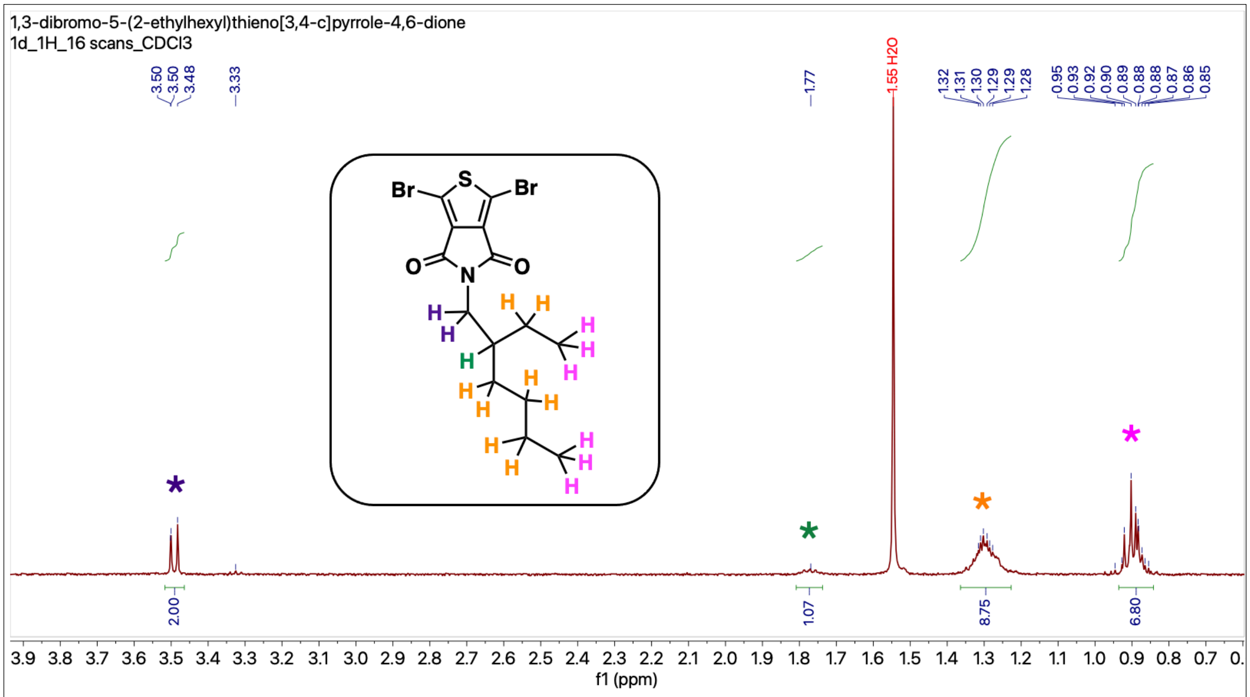

^{1}H NMR (δ, $CDCl_3$, RT, 400 MHz): 3.51 (d, *J* = 8 Hz, 2H), 1.80 (m, 1H), 1.30 (m, 8H), 0.90 (m, 6H).

Figure A.2.3 *^{1}H NMR spectrum of compound 2-14.*

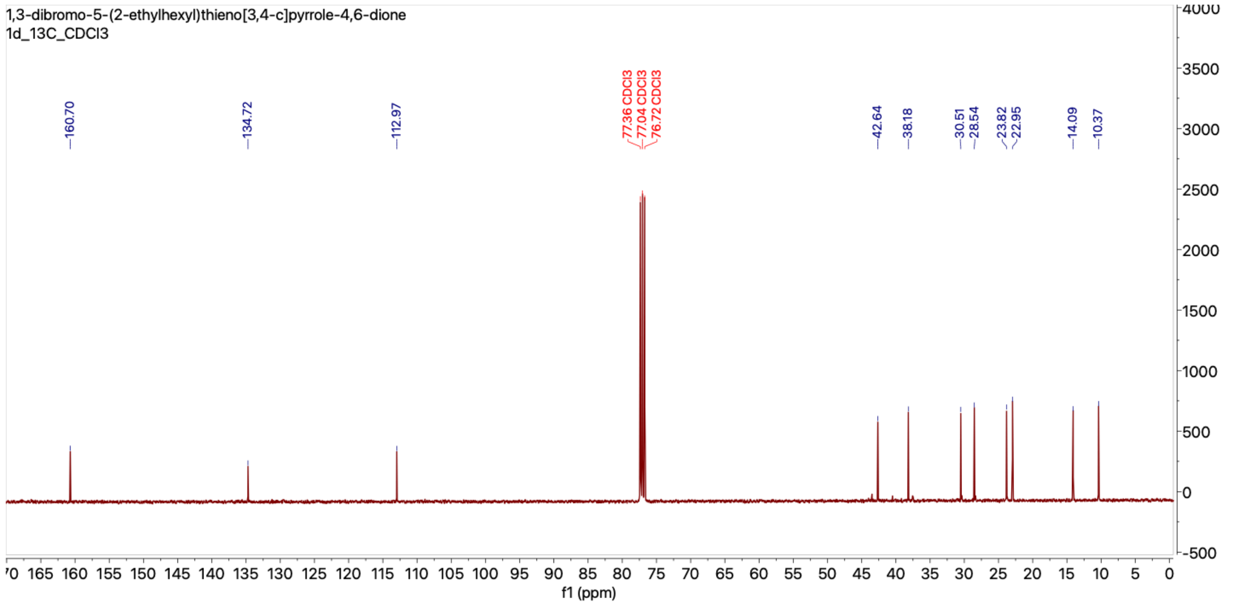

^{13}C NMR (δ, $CDCl_3$, RT, 400 MHz): 160.70 (1), 134.72 (2), 112.97 (3), 42.64 (4), 38.18 (5), 30.51 (6), 28.54 (7), 23.82 (8), 22.95 (9), 14.09 (10), 10.37 (11).

Figure A.2.4 *^{13}C NMR spectrum of compound 2-14.*

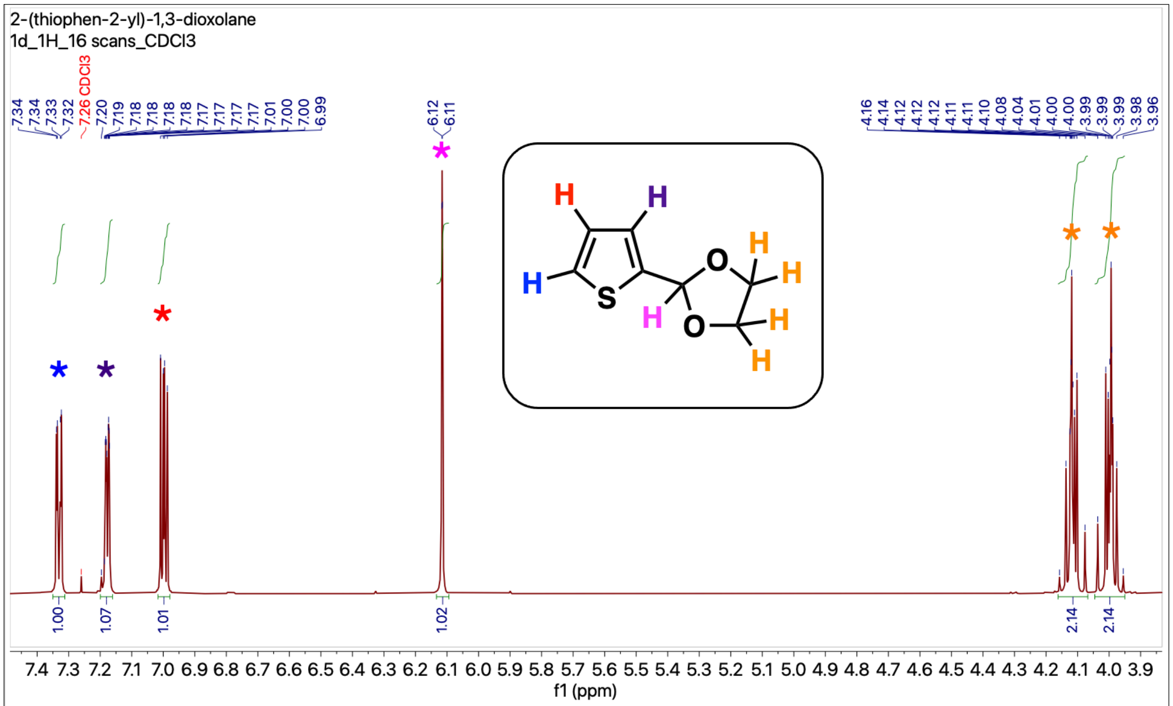

^{1}H NMR (δ, $CDCl_3$, RT, 400 MHz): 7.35 (dd, *J* = 4, 6 Hz, 1H), 7.20-7.16 (m, 1H), 7.00 (dd, *J* = 4, 4 Hz, 1H), 6.12 (s, 1H), 4.16-4.06 (m, 2H), 4.04-3.95.

Figure A.2.5 *^{1}H NMR spectrum of compound 2-16.*

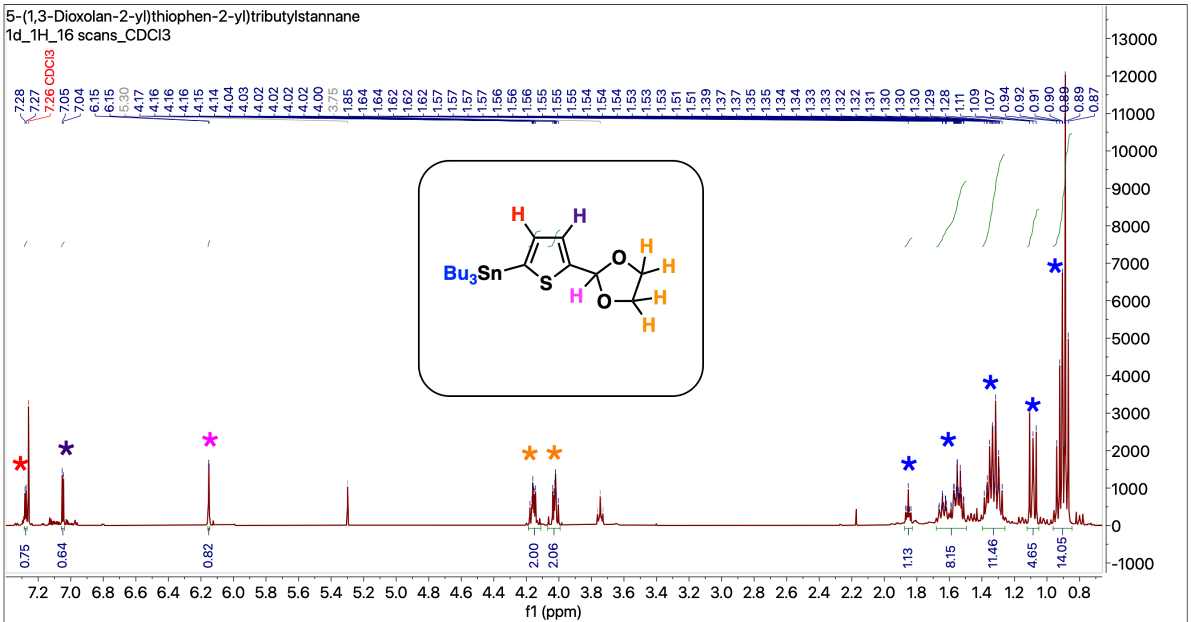

^{1}H NMR (δ, $CDCl_3$, RT, 400 MHz): 7.275 (d, *J* = 4Hz, 1H), 7.045 (d, *J* = 4Hz 1H), 6.15 (s, 1H), 4.18-4.11 (m, 2H), 4.06-3.99 (m, 2H), 1.88-1.83 (m, 1H), 1.69-1.50 (m, 8H), 1.40-1.26 (m, 11H), 1.12-1.05 (m, 5H) 0.96-0.85 (m, 14H) (Excess $SnBu_3$ present in crude)

Figure A.2.6 *^{1}H NMR spectrum of compound 2-17.*

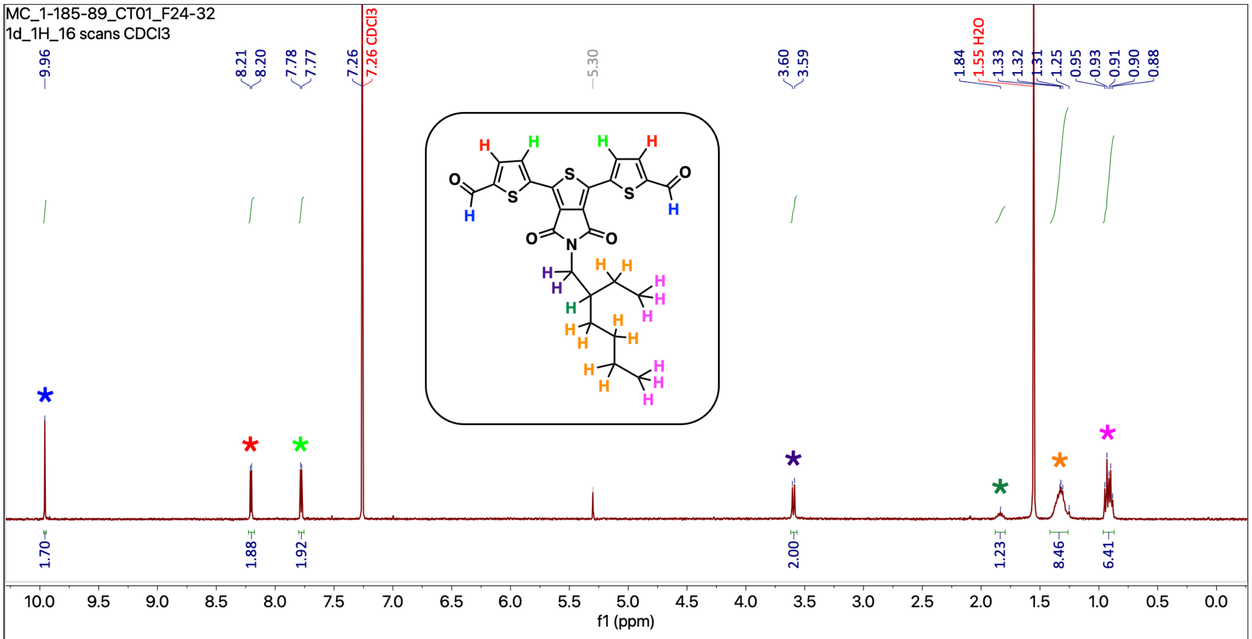

^{1}H NMR (δ, $CDCl_3$, RT, 300 MHz): 9.96 (s, 2H), 8.21 (d, *J* = 4 Hz, 2H), 7.78 (d, *J* = 4 Hz, 2H), 3.60 (d, *J* = 4 Hz, 2H), 1.84 (m, 1H), 1.32 (m, 8H), 0.91 (m, 6H).

Figure A.2.7 *^{13}H NMR spectrum of compound 2-19*

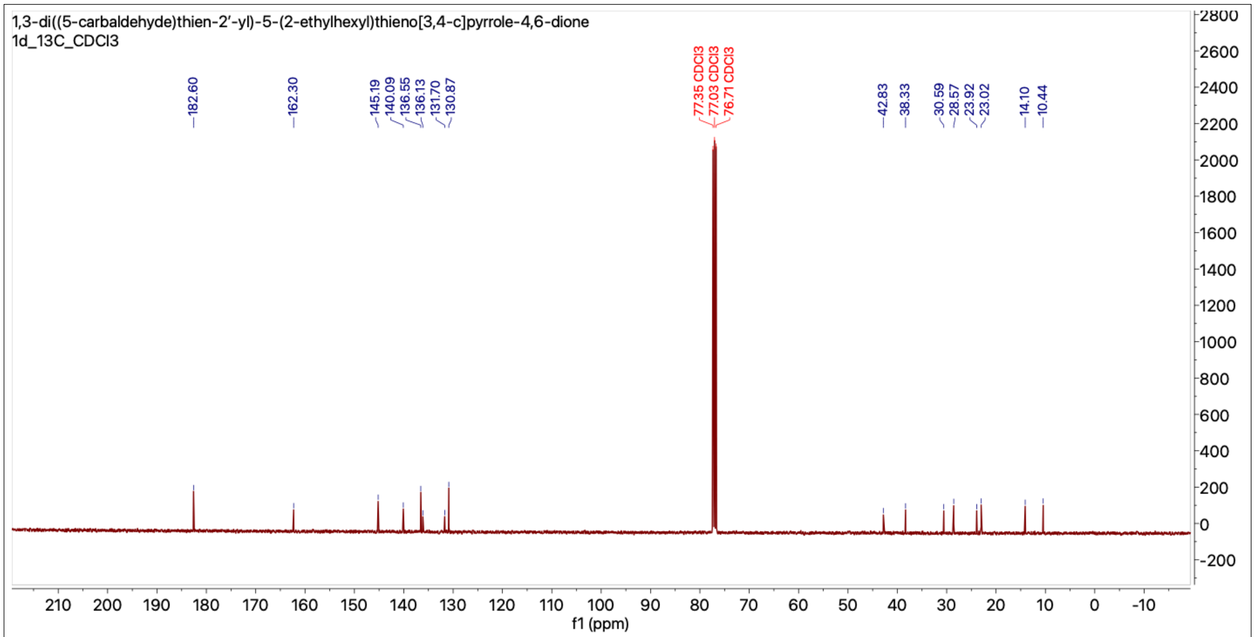

^{13}C NMR (δ, $CDCl_3$, RT, 400 MHz): 182.60 (1), 162.30 (2), 145.19 (3), 140.09 (4), 136.55 (5), 136.13 (6), 131.70 (7), 130.87 (8), 42.83 (9), 38.33 (10), 30.59 (11), 28.57 (12), 23.92 (13), 23.02 (14), 14.10 (15), 10.44 (16).

Figure A.2.8 *^{13}C NMR spectrum of compound 2-19.*

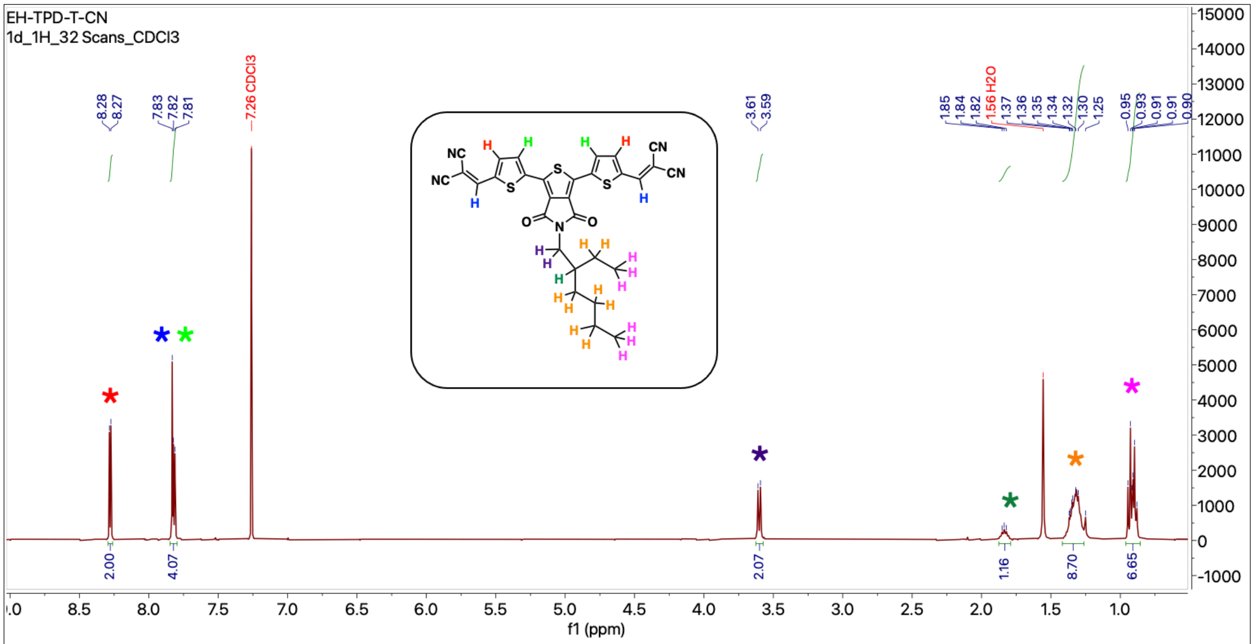

^{1}H NMR (δ, $CDCl_3$, RT, 300 MHz): 8.28 (d, *J* = 4 Hz, 2H), 7.83 (s, 2H), 7.82 (d, *J* = 4 Hz, 2H), 3.61 (d, *J* = 4 Hz, 2H), 1.84 (m, 1H), 1.32 (m, 14H), 0.91 (m, 6H).

Figure A.2.9 *^{1}H NMR spectrum of compound 2-20.*

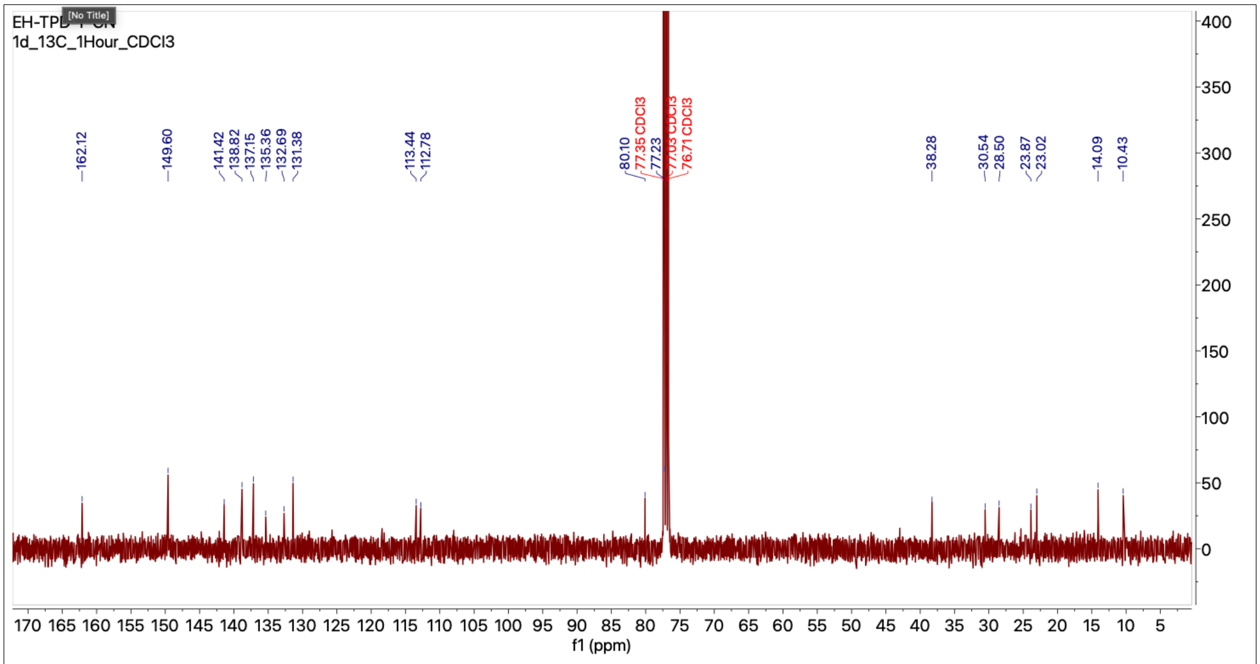

^{13}C NMR (δ, $CDCl_3$, RT, 400 MHz): 162.12 (1), 149.60 (2), 141.42 (3), 138.82 (4), 137.15 (5), 135.36 (6), 132.69 (7), 131.38 (8), 113.44 (9), 112.78 (10), 80.10 (11), 77.23 (12), 38.28 (13), 30.54 (14), 28.50 (15), 23.87 (16), 23.02 (17), 14.09 (18), 10.43 (19).

Figure A.2.10 *^{13}C NMR spectrum of compound 2-20.*

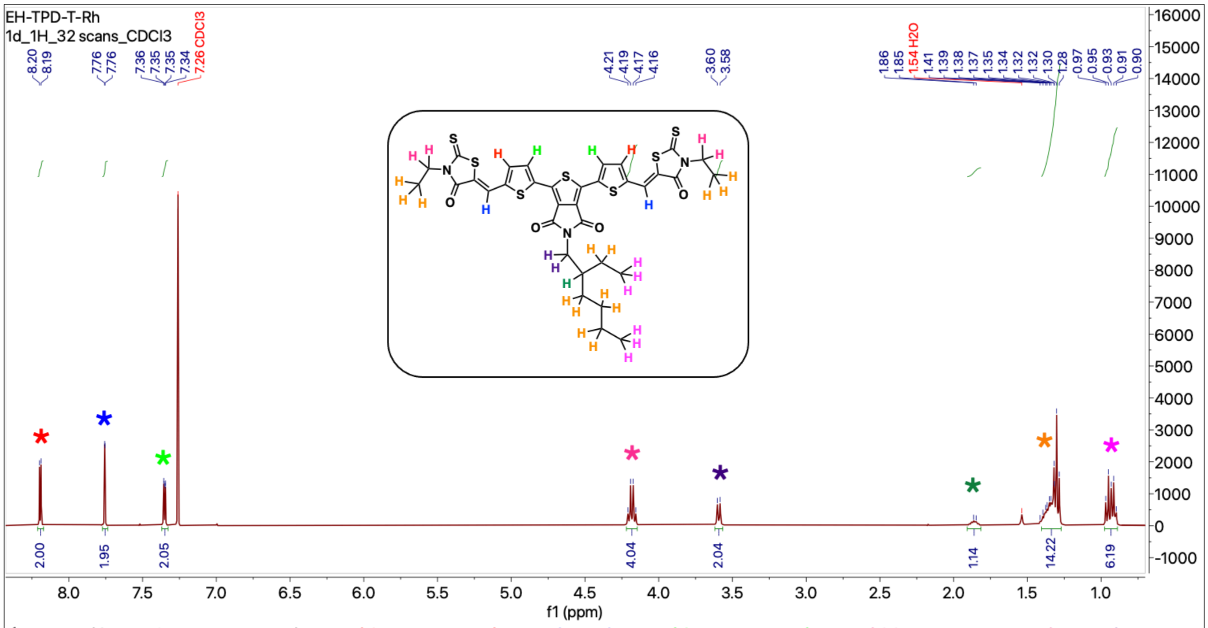

^{1}H NMR (δ, $CDCl_3$, RT, 300 MHz): 8.20 (d, *J* = 4 Hz, 2H), 7.76 (s, 2H), 7.78 (d, *J* = 4 Hz, 2H), 4.18 (dd, *J* = 8, 20 Hz, 4H), 3.60 (d, *J* = 4 Hz, 2H), 1.84 (m, 1H), 1.32 (m, 14H), 0.91 (m, 6H).

Figure A.2.11 *^{1}H NMR spectrum of compound 2-21.*

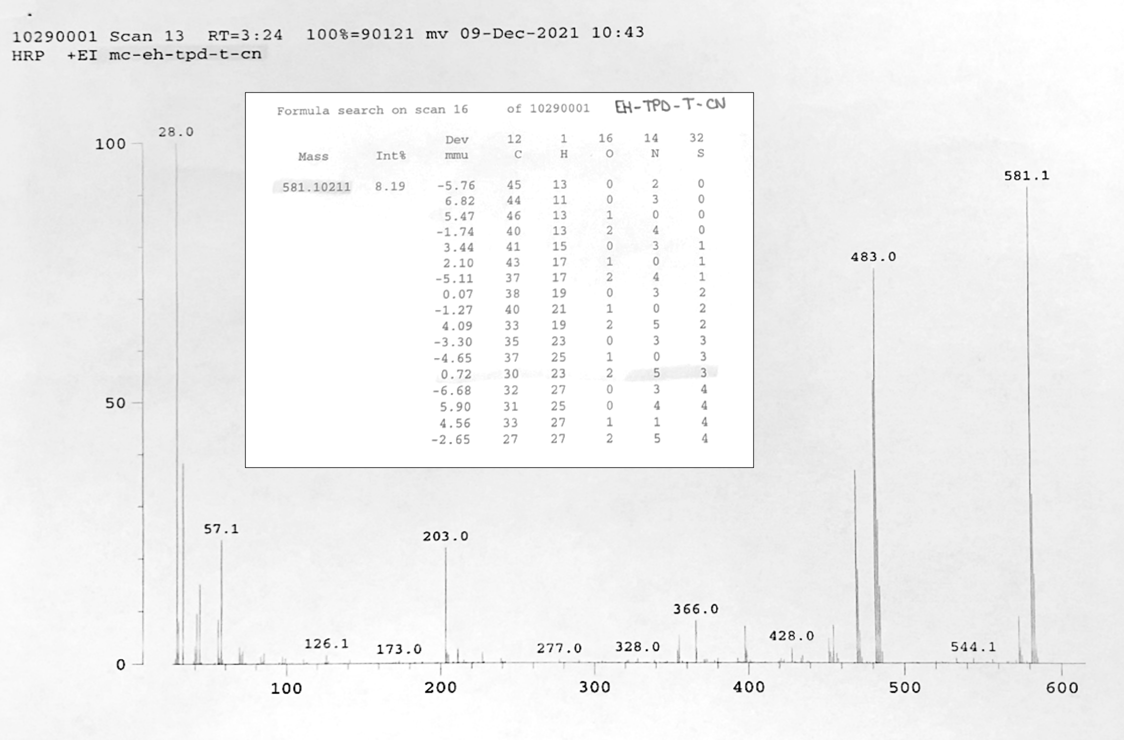

```
10290001 Scan 13  RT=3:24  100%=90121 mv 09-Dec-2021 10:43
HRP  +EI mc-eh-tpd-t-cn
```

Formula search on scan 16 of 10290001 EH-TPD-T-CN

Mass	Int%	Dev mmu	12 C	1 H	16 O	14 N	32 S
581.10211	8.19	-5.76	45	13	0	2	0
		6.82	44	11	0	3	0
		5.47	46	13	1	0	0
		-1.74	40	13	2	4	0
		3.44	41	15	0	3	1
		2.10	43	17	1	0	1
		-5.11	37	17	2	4	1
		0.07	38	19	0	3	2
		-1.27	40	21	1	0	2
		4.09	33	19	2	5	2
		-3.30	35	23	0	3	3
		-4.65	37	25	1	0	3
		0.72	30	23	2	5	3
		-6.68	32	27	0	3	4
		5.90	31	25	0	4	4
		4.56	33	27	1	1	4
		-2.65	27	27	2	5	4

Figure A.2.12 *Electron Impact (EI) high-resolution mass spectrum of 2-20.*

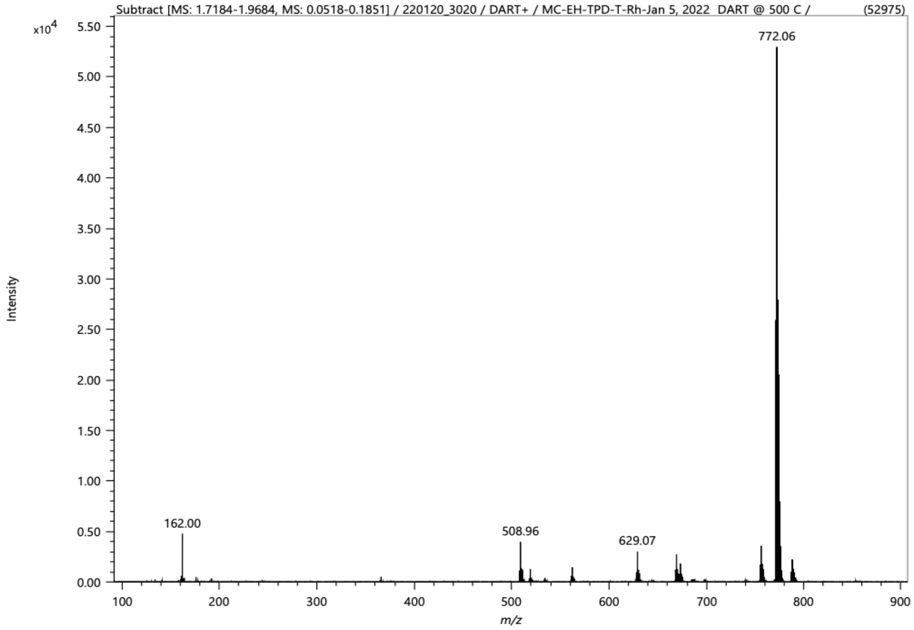

Figure A.2.13 *Direct Analysis in Real Time (DART) high-resolution mass spectrum of compound 2-20.*

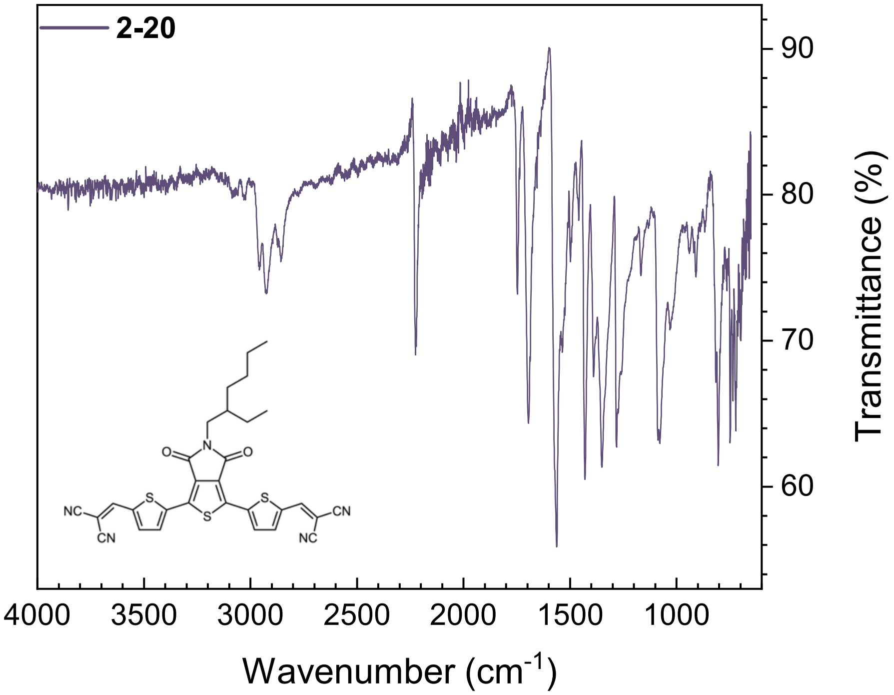

Figure A.2.14 *Infrared (IR) spectrum of compound 2-20.*

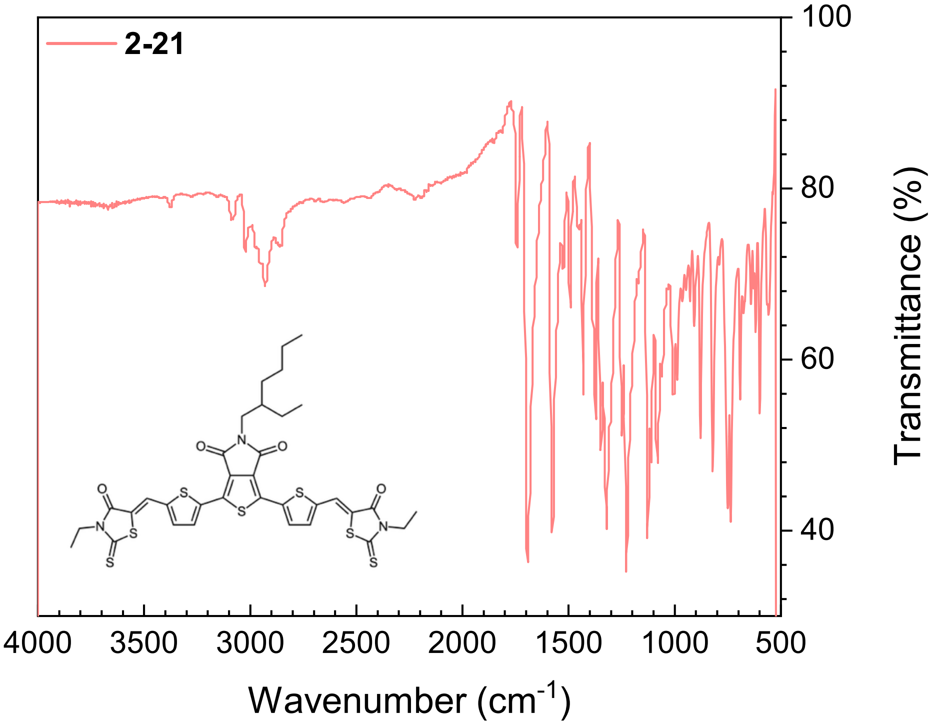

Figure A.2.15 *Infrared (IR) spectrum of compound 2-21.*

References

(1) Zhao, Z.; Liu, K.; Liu, Y.; Guo, Y.; Liu, Y. *Natl. Sci. Rev.* **2022**, *9* (6), nwac090.

(2) Grau, G.; Kitsomboonloha, R.; Swisher, S. L.; Kang, H.; Subramanian, V. *Adv. Funct. Mater.* **2014**, *24* (32), 5067.

(3) Xie, Y.; Ding, C.; Jin, Q.; Zheng, L.; Xu, Y.; Xiao, H.; Cheng, M.; Zhang, Y.; Yang, G.; Li, M.; Li, L.; Liu, M. *SmartMat* **2024**, *5* (4), e1261.

(4) Li, S.; Duan, Y.; Zhu, W.; Cheng, S.; Hu, W. *Adv. Mater.* **2024**, *36* (49), 2412379.

(5) Borchert, J. W.; Zschieschang, U.; Letzkus, F.; Giorgio, M.; Weitz, R. T.; Caironi, M.; Burghartz, J. N.; Ludwigs, S.; Klauk, H. *Sci. Adv.* **2020**, *6* (21), eaaz5156.

(6) Melville, O. A.; Lessard, B. H.; Bender, T. P. *ACS Appl. Mater. Interfaces* **2015**, *7* (24), 13105.

(7) Shaik, B.; Khan, M.; Shaik, M. R.; Sharaf, M. A. F.; Sekou, D.; Lee, S.-G. *Micromachines* **2021**, *12* (7), 817.

(8) Zhou, Q.; Jiang, Y.; Du, T.; Wang, Z.; Liang, Z.; Han, Y.; Deng, Y.; Tian, H.; Geng, Y. *J. Mater. Chem. C* **2019**, *7* (44), 13939.

(9) Ganguly, A.; King, B.; Lessard, B. H.; Brusso, J. L. *Synthetic Metals* **2022**, *287*, 117090.

(10) Zhang, J.; Xu, W.; Sheng, P.; Zhao, G.; Zhu, D. *Acc. Chem. Res.* **2017**, *50* (7), 1654.

(11) Bureš, F. *RSC Adv.* **2014**, *4* (102), 58826.

(12) Takaya, T.; Mamo, M. D.; Karakawa, M.; Noh, Y.-Y. *Dyes Pigm.* **2018**, *158*, 306.

(13) Meng, Q.; Hu, W. *Phys. Chem. Chem. Phys.* **2012**, *14* (41), 14152.

(14) In *Advances in Heterocyclic Chemistry*; Elsevier, 2017; Vol. 121, pp 133–171.

(15) Ha, J.; Kim, Y. J.; Park, J.; An, T. K.; Kwon, S.; Park, C. E.; Kim, Y. *Chem. Asian J.* **2014**, *9* (4), 1045.

(16) Luo, D.; Jiang, Z.; Shan, C.; Li, L.; Duan, C.; Liu, Q.; Wang, Z.; Wang, K.; Xu, B.; Kyaw, A. K. K. *ACS Appl. Mater. Interfaces* **2022**, *14* (21), 24374.

(17) Opoku, H.; Choy, J.-Y.; Ashok Kumar, K.; Shrestha, N. K.; Rabani, I.; Patil, S. A.; Sree, V. G.; Kim, H.-S.; Bathula, C. *Dyes Pigm.* **2021**, *186*, 108973.

(18) Zhang, C.; Yuan, D.; Wu, H.; Gann, E.; Thomsen, L.; McNeill, C. R.; Di, C.; Zhu, X.; Zhu, D. *J. Mater. Chem. C* **2017**, *5* (8), 1935.

(19) Zhang, C.; Zang, Y.; Gann, E.; McNeill, C. R.; Zhu, X.; Di, C.; Zhu, D. *J. Am. Chem. Soc.* **2014**, *136* (46), 16176.

(20) Zhao, Y.; Zhou, X.; Wu, K.; Wang, H.; Qu, S.; He, F.; Yang, C. *Dyes Pigm.* **2016**, *130*, 282.

(21) Luponosov, Y. N.; Min, J.; Khanin, D. A.; Baran, D.; Pisarev, S. A.; Peregudova, S. M.; Dmitryakov, P. V.; Chvalun, S. N.; Cherkaev, G. V.; Svidchenko, E. A.; Ameri, T.; Brabec, C. J.; Ponomarenko, S. A. *J. Photon. Energy* **2015**, *5* (1), 057213.

(22) Steinberger, S.; Mishra, A.; Reinold, E.; Müller, C. M.; Uhrich, C.; Pfeiffer, M.; Bäuerle, P. *Org. Lett.* **2011**, *13* (1), 90.

(23) Alonso-Navarro, M. J.; Harbuzaru, A.; De Echegaray, P.; Arrechea-Marcos, I.; Harillo-Baños, A.; De La Peña, A.; Ramos, M. M.; López Navarrete, J. T.; Campoy-Quiles, M.; Ponce Ortiz, R.; Segura, J. L. *J. Mater. Chem. C* **2020**, *8* (43), 15277.

(24) Kim, M. J.; Lee, Y. W.; Lee, Y.; Woo, H. Y.; Ho Cho, J. *J. Mater. Chem. C* **2018**, *6* (21), 5698.

(25) Zhang, C.; Zhu, X. *Acc. Chem. Res.* **2017**, *50* (6), 1342.

(26) Sun, Y.; Guo, Y.; Liu, Y. *Mater. Sci. Eng. R Rep.* **2019**, *136*, 13.

(27) Najari, A.; Beaupré, S.; Berrouard, P.; Zou, Y.; Pouliot, J.; Lepage-Pérusse, C.; Leclerc, M. *Adv. Funct. Mater.* **2011**, *21* (4), 718.

(28) Connelly, N. G.; Geiger, W. E. *Chem. Rev.* **1996**, *96* (2), 877.

(29) Liu, Y.; Liu, M. S.; Jen, A. K.-Y. *Acta Polym.* **1999**, *50* (2–3), 105.

(30) Sun, H.; Gerasimov, J.; Berggren, M.; Fabiano, S. *J. Mater. Chem. C* **2018**, *6* (44), 11778.

(31) Yuan, J.; Zhang, J.; Wang, J.; Yan, X.; Yan, D.; Xu, W. *App. Phys. Lett.* **2003**, *82* (22), 3967.

(32) Yuan, J.; Zhang, J.; Wang, J.; Yan, D.; Xu, W. *Thin Solid Films* **2004**, *450* (2), 316.

(33) Darbandy, G.; Roemer, C.; Leise, J.; Pruefer, J.; Borchert, J. W.; Klauk, H.; Kloes, A. In *2019 MIXDES - 26th International Conference "Mixed Design of Integrated Circuits and Systems";* IEEE: Rzeszów, Poland, 2019; pp 76–80.

Chapter 3. Oxy Phosphorus Triazatetrabenzocorrole as a p-Type Organic Semiconductor in OTFTs

This chapter is adapted from: ***Cyr, M.****, Lamontagne, H. R., Lessard, B. H., Brusso, J. L. Oxy Phosphorus Triazatetrabenzocorrole as a p-Type Organic Semiconductor in Organic Thin Film Transistors. ACS Appl. Electron. Mater.* ***2024****, 6, 6275-6283.*

Context

Although metal porphyrinoids (MPors) are considered a well-studied class of materials, the incorporation of main-group elements at the centre of these porphyrinoid macrocycles remains of large interest to the scientific community. This largely stems from the higher electronegativity and coordination diversity provided by main-group elements that renders them of unique interest to modify the electronic potentials of porphyrinoids by widening the range of their absorption profiles and modifying their HOMO and LUMO energies. To that end, I synthesized oxy phosphorus^{V} triazatetrabenzocorrole (PO-Tbc), a corrole sub-class obtained when incorporating phosphorus at the centre of a metal-free phthalocyanine macrocycle. Since PO-Tbc has been previously synthesized in literature, my focus for this work was centred around the thin-film processing of the material in OTFTs. With this work presenting a first occurrence of PO-Tbc into field effect transistors, I looked at implementing the material in both BGBC and BGTC OTFT devices to see whether this would have any effect on the device performance. Additionally, for both device architectures, I also wanted to look at a series of different dielectric surface treatments to investigate the effect on the OSC thin-film morphology when varying the deposition surface energy. I was particularly interested in this due to PO-Tbc possessing a single oxo ligand thus creating a dipole moment out-of-plane from the Tbc core and wanted to observe whether the resulting thin-film would have a more favourable morphology when deposited on a more polar surface.

Contribution

This work was completed through contributions of all authors. I synthesized, purified, and characterized the PO-Tbc material, performed the dielectric surface treatments, fabricated and tested the OTFT devices, performed the Raman mapping and wrote the manuscript. H.R.L. assisted me in the device fabrication process, trained and assisted me in performing the Raman mapping and helped interpret the performance data. B.H.L. and J.L.B. provided supervision for the project. All authors assisted with editing the manuscript.

Abstract

Triazatetrabenzocorroles (Tbc) consist of a sub-class of molecules derived from the phthalocyanine and porphyrin families that is less commonly synthesized and utilized in applications for organic electronics. In this work, we have synthesized oxy phosphorus^{V} Tbc (PO-Tbc) and integrated it as an organic semiconductor in organic thin-film transistors (OTFTs). Both bottom-gate bottom-contact (BGBC) and bottom-gate top-contact (BGTC) OTFTs fabricated with PO-Tbc as the organic semiconducting layer resulted in a clear *p*-type performance, both in air and under inert conditions. A series of solution-based silanes and thermally evaporated *para*-sexiphenylene were employed as dielectric surface treatments to modify the surface energy of the dielectric-semiconductor interface prior to depositing the PO-Tbc thin-films. Other fabrication conditions were also explored such as the deposition rate of PO-Tbc, substrate surface temperature during deposition and post-deposition annealing conditions. Optimized OTFT performing devices were obtained from *n*-octadecyltrichlorosilane (ODTS) coated substrates where PO-Tbc was deposited at 100 °C, which afforded an average field effect mobility of 8.18 × 10^{-3} cm^{2} V^{-1} s^{-1} and a threshold voltage of -23.2 V. Subsequent X-ray diffraction and polarized Raman microscopy indicated a significant increase in PO-Tbc film crystallinity and a film morphology adopting deeper “face-on’ molecular configuration when deposited on ODTS treated surfaces. These results represent the first report of OTFTs fabricated using POTbc, including structure-property relationships related to thin-film optimization and device performance.

3.1 Introduction

Metal and main group porphyrinoids (MPors) form a broad family of materials that are continuously evolving in the field of organic electronics.[1–4] In addition to their highly conjugated system, the incorporation of certain metal and metalloid elements at the center of their framework allows to finetune their unique electronic behaviour, thus improving the overall semiconducting abilities of these materials.[3,5–7] The added advantage of having higher oxidation state (+3 or higher) elements occupying the central position of MPors is the incorporation of axial components to the macrocycle that can be exploited to tailor the chemical and physical properties of the material.[8–11] Additional derivatization can also be probed at the periphery of the conjugated macrocycles, which can either lead to modulation of the bulk properties or further finetuning of the electrochemical characteristics to enhance performance in desired applications.[12,13] As such, porphyrinoids have been exploited as active materials in a plethora of applications including, but not limited to, organic photovoltaics (OPVs),[14–16] organic thin-film transistors (OTFTs),[4,17,18] and sensors.[19–21]

Triazatetrabenzocorroles (Tbcs) represent a class of macrocyclic molecules derived from the phthalocyanine (Pc) and corrole (Corr) families, where the conjugated Pc core undergoes a truncation by losing one of the bridging imine nitrogen atoms; however, the number of π-electrons remains the same due to rearrangement of the conjugated system.[22,23] Tbc made its first appearance in 1986 by Fujiki *et al.* who reacted a germanium phthalocyanine ($PcGeCl_2$) with sodium borohydride to obtain its Tbc analogue.[22] In the following years, Tbcs were synthesized using a variety of high valent metal and metalloid elements at the centre including phosphorus, silicon, aluminium, gallium and more, *via* either top-down or bottom-up synthetic approaches. Although a variety of elements have been successfully included into the Tbc framework, phosphorus remains the most commonly synthesized analogue to date.[24,25] Phosphorus-derived Tbc can be readily achieved by reacting metal-free Pc with PBr_3 in pyridine (**Figure 3.1a**). By incorporating phosphorus into the Tbc core, it adopts a pentavalent state, resulting in the presence of axial substituents, which are typically fulfilled by plain oxygen or hydroxyl functional groups.[26] In past reports, questions arose regarding the true form of phosphorus Tbc and whether it predominantly adopts two hydroxyl components (i.e. $P(OH)_2$-Tbc) or one doubly bonded oxygen (i.e. PO-Tbc).[24] In 2017, Raboui *et al.* confirmed that although both analogues can occur, the sole analogue present after purification *via* train sublimation is PO-Tbc.[27]

In evaluating the difference between the absorption profiles of PO-Tbc with its H_2Pc precursor, both the B and Q bands are present with high intensities, which is most likely due to the conservation of the π-electrons in the macrocycle.[27] From an organic semiconducting perspective, this therefore leaves PO-Tbc in good standing to promote charge transport, yet only a few reports have implemented PO-Tbc as the active material in organic electronic devices[28,29] and none have studied its semiconducting capabilities in field effect transistors. Intrigued by its potential, we herein report the synthesis and characterization of PO-Tbc, which was subsequently implemented as a *p*-type organic semiconducting material in both bottom-gate bottom-contact (BGBC) and bottom-gate top-contact (BGTC) OTFTs (**Figure 3.1c**). For both device configurations, a variety of surface treatments were investigated on the dielectric layer (**Figure 3.1b**), leading to a change in water contact angle (θ_w) and therefore influencing the surface energy of the dielectric-semiconductor interface. The increasing hydrophobicity of the interface was employed as a means to potentially improve the orientation and stacking of PO-Tbc upon deposition, which can then lead to higher device performance. The average hole field-effect mobility (μ_h), threshold voltage (V_T), and on/off current ratio ($I_{on/off}$) of the OTFTs were measured and compared between the different surface treatments. The morphology and crystallinity of the films were evaluated by thin-film X-ray diffraction (XRD) and polarized Raman microscopy to further explore the impact of the film formation onto the treated surfaces.

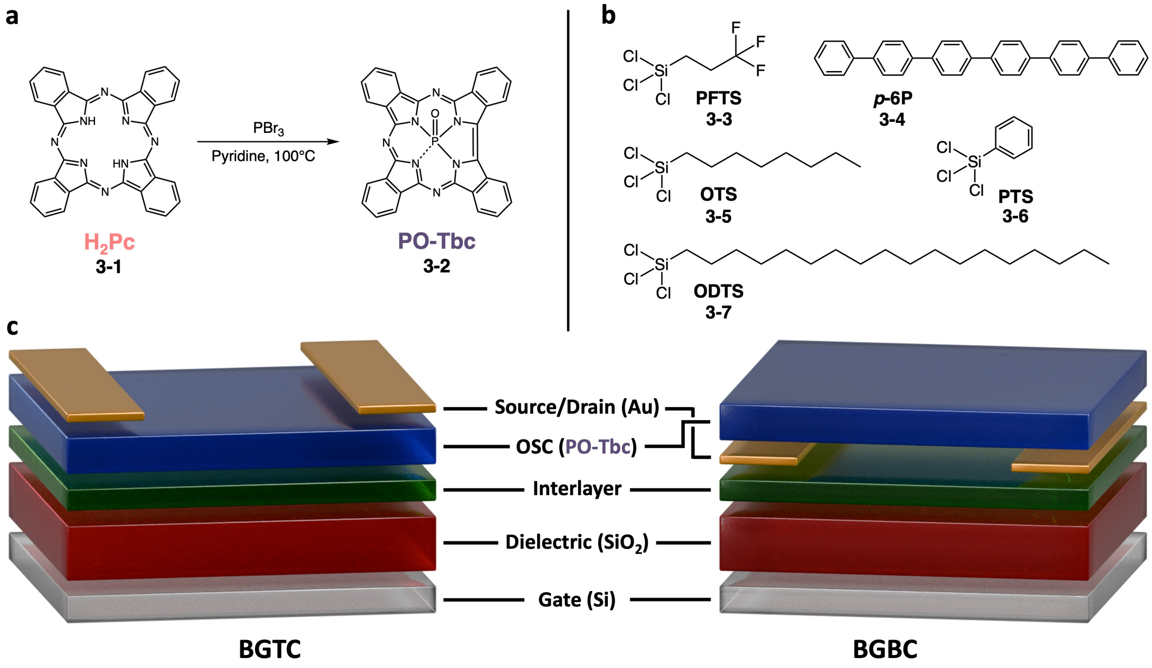

***Figure 3.1** (a) Synthetic route towards PO-Tbc. (b) Structure of the various silane-based and para-sexiphenylene used for interlayer surface treatment during the device fabrication. (c) Diagram of a bottom-gate top-contact (BGTC; left) and bottom-gate bottom-contact (BGBC; right) OTFT architecture.*

3.2 Results and Discussion

3.2.1 Synthesis and Initial Characterization

The synthetic route opted to form PO-Tbc (outlined in **Figure 3.1a**) was adopted from previous work reported by Li *et al.*,[30] where metal-free phthalocyanine was mixed with 30 molar equivalents of PBr_3 in pyridine at reflux for 24 h. During the phosphorus insertion, the phthalocyanine loses one of the bridging imine nitrogen atoms from its core, thus converting the Pc into Tbc. The crude product was purified twice *via* train sublimation with CO_2 as a carrier gas to afford the pure PO-Tbc as a dark blue microcrystalline powder in 35% yield that was confirmed *via* Matrix-Assisted Laser Desorption/Ionization (MALDI) high resolution mass spectrometry

(**Figure A.3.1** of Section 3.5 Appendix). UV-Vis-NIR spectroscopy and Time-Dependent Density Functional Theory (TD-DFT) calculations were done for both the synthesized PO-Tbc as well as the H_2Pc starting material (**Figure 3.2**). Both the experimental and calculated spectra portrayed the same trends when comparing PO-Tbc to its Pc starting material. A slight bathochromic shift occurs in the Q band region, which is likely due to the truncation of the macrocyclic core. Additionally, PO-Tbc also displays a large hypsochromic shift and increase in peak intensity in the B band region (400-450 nm range). This change in absorption profile is likely caused by insertion of phosphorus at the centre of Tbc and the resulting interaction between the π-electrons of the Tbc macrocycle and the vacant *d*-orbitals of the phosphorus atom, given that π-*d* transitions are often characteristic of the B band in porphyrinoid materials.[31] Thermogravimetric analysis (TGA) was also measured for PO-Tbc (**Figure A.3.3** of Section 3.5 Appendix), depicting stability of the material up to 543 °C, where the 5% total weight loss of the sample is observed.

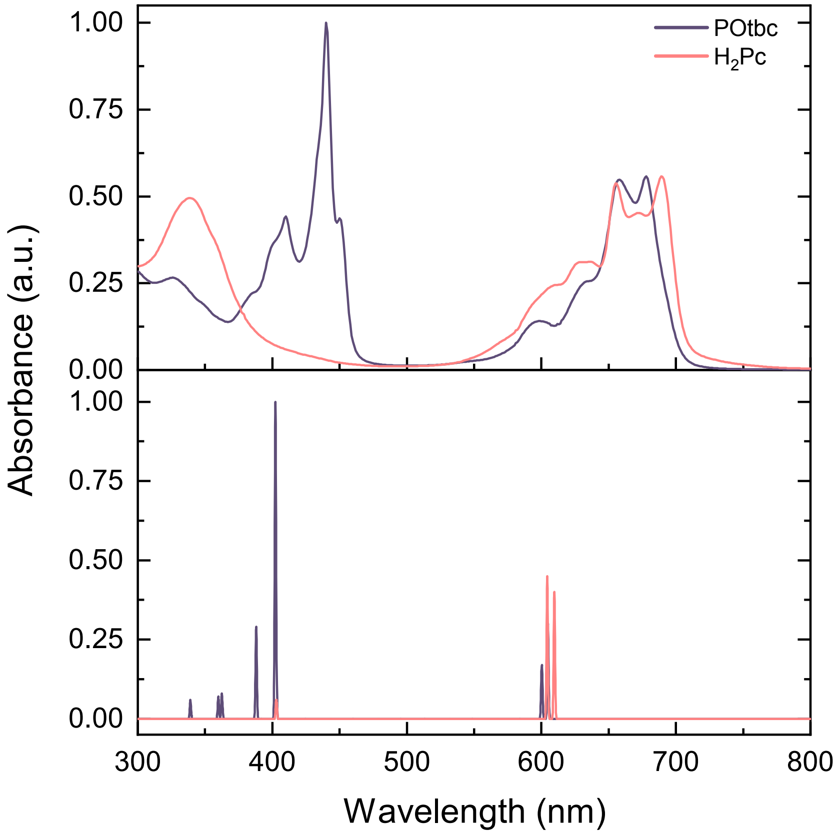

Figure 3.2 *Experimental absorption spectra of PO-Tbc (purple) and H_2Pc (pink) in DCM solutions (top). TD-DFT calculated absorption spectra of PO-Tbc (purple) and H_2Pc (pink) using the hybrid density functional B3LYP with the Accurate: 6-311+G(2d,p) basis set (bottom).*

3.2.2 OTFT Fabrication and Characterization

PO-Tbc was previously employed as an electron donor material in organic photovoltaic (OPV) devices, where Raboui *et al.* reported HOMO and LUMO levels of –5.1 and -3.15 eV, respectively.[27] These results suggest PO-Tbc will act as a *p*-type organic semiconductor when integrated into OTFTs, where the HOMO level matches well with the use of gold electrodes (gold work function: -5.1 eV).[32] Two series of devices were fabricated using bottom-gate bottom-contact (BGBC) and bottom-gate top-contact (BGTC) device architectures. In both cases the substrate consisted of *n*-doped Si acting as the gate, followed by a thermally grown SiO_2 dielectric layer. For the BGBC OTFTs, each substrate incorporated 16 individual gold source and drain electrodes deposited *via* photolithography, organized into four groups with channel lengths of 2.5, 5.0, 10.0, and 20.0 µm. In the case of the BGTC OTFTs, each substrate held 20 individual devices where the gold electrodes were deposited *via* physical vapour deposition (PVD) on top of the semiconducting layer using shadow masks containing 20 µm channel lengths. In both cases the PO-Tbc was deposited by PVD on the treated SiO_2 dielectric surface. The resulting PO-Tbc thin-film growth and corresponding morphology depends significantly on the surface chemistry of the dielectric.[33,34] Favourable packing of the semiconductor can be achieved when the surface energy of the dielectric surface matches that of the semiconductor.[35,36] As such, a set of four different silanes (shown in **Figure 3.1b**) were selected to perform solution surface treatments on the dielectric surface for the BGBC devices prior to the deposition of the semiconducting layer, alongside one substrate undergoing no surface treatment (i.e. bare SiO_2). The silanes were selected based on polarity, which was quantified by water contact angle (θ_w), making the bare SiO_2 surface the most hydrophilic, thus having the highest surface energy and the ODTS (*n*-octadecyltrichlorosilane) treated surface the most hydrophobic, therefore having lowest surface energy. After performing the dielectric surface treatments, PO-Tbc was deposited onto each substrate via PVD at room temperature under vacuum at a deposition rate of 0.1 Å s^{-1}, followed by post-deposition annealing at either 150 °C or 200 °C for 1 h. The maximum and average hole mobilities ($\mu_{h,max}$ and $\mu_{h,avg}$), as well as the threshold voltage (V_T) and the on/off current ratio ($I_{on/off}$) for the devices annealed at 150 °C are reported in **Table 3.1**. Characteristic transfer and output curves of OTFTs performances from each surface treatment are provided in **Figure A.3.6** of Section 3.5 Appendix. For the devices that underwent post-deposition annealing at 200 °C, the average electrical characteristics were found to be lower than those annealed at 150 °C, suggesting that optimal film growth occurs at temperatures lower than 200 °C. It is important to note that the average electrical characteristics reported in **Table 3.1** for the BGBC devices encompasses only those with a 5.0 µm channel length. This is because the devices' electrical performance varies between different channel lengths, where devices with larger channel lengths will usually have lower performance due to increased bulk resistance.[37] For this reason, the electrical characteristics should not be averaged between all channel lengths in BGBC substrates (16 total devices), rather one subset of the devices containing the same channel length value should be used for the calculations of the electrical characteristics (4 total devices). The best BGBC OTFTs were obtained when using more hydrophobic surface treatments, with OTS (*n*-octyltrichlorosilane) exhibiting the highest $\mu_{h,avg}$ of 6.5 × 10^{-3} $cm^2\ V^{-1}\ s^{-1}$ and a V_T of -22.5 V, and ODTS exhibiting a similar $\mu_{h,avg}$ of 6.2 × 10^{-3} $cm^2\ V^{-1}\ s^{-1}$ and a V_T of -24.5 V. Alternatively, devices fabricated using PFTS (3,3,3-trifluoropropyl trichlorosilane) provided the lowest performance and, although it is not the most hydrophilic surface, the presence of fluorine atoms could have negatively influenced the film formation. We have previously shown that fluorinated dielectric interfaces can either improve or be a detriment to small molecule semiconductors by modifying their growth mode, ultimately impacting the resulting thin-film structure and their device performance.[9,38–41]

Table 3.1 *Electrical characteristics of bottom-gate bottom-contact (BGBC) OTFTs calculated from n unique transistors.*

Surface treatment	**θ_w[a]**	**Post-depo annealing [°C]**	**$\mu_{h,max}$ × 10^{-3} [$cm^2\ V^{-1}\ s^{-1}$]**	**$\mu_{h,avg}$ × 10^{-3} [$cm^2\ V^{-1}\ s^{-1}$]**	**V_T [V]**	**$I_{on/off}$**	**n[a]**
SiO_2	43°	150	0.27	0.15 ± 0.06	-19.7 ± 2.8	10^2	3
PTS	80°	150	1.35	0.73 ± 0.02	-19.7 ± 0.2	10^2	4
PFTS	88°	150	0.23	0.05 ± 0.01	-16.0 ± 0.3	10^2	4
OTS	96°	150	8.54	6.50 ± 1.73	-22.5 ± 0.6	10^3	4
ODTS	109°	150	7.84	6.15 ± 1.55	-24.5 ± 1.8	10^3	4
SiO_2	43°	200	0.96	0.47 ± 0.02	-14.8 ± 0.9	10^2	4
PTS	80°	200	1.29	1.21 ± 0.06	-18.9 ± 0.2	10^2	4
PFTS	88°	200	0.23	0.12 ± 0.05	-20.7 ± 0.6	10^2	4
OTS	96°	200	0.02	0.02 ± 0.01	-21.7 ± 4.7	10^1	4
ODTS	109°	200	0.05	0.05 ± 0.01	-8.22 ± 1.7	10^1	4

In an attempt to reduce contact resistance (R_C) and improve device performance, we fabricated a second series of devices using a BGTC architecture. OTFTs were fabricated with PTS, *p*-6P (*p*-sexiphenylene), OTS and ODTS. *p*-6P was chosen as a new candidate for surface treatment since it has demonstrated to promote weak epitaxial growth of other planar phthalocyanine materials such as ZnPc, and CuPc[42,43], as well as umbrella phthalocyanines such as TiO-Pc and VO-Pc,[44,45] due to strong interactions between the treatment layer and the semiconducting molecules which can lead to better device performance.[42,43] PO-Tbc was deposited *via* PVD on the substrates at a temperature of 100 °C during deposition. Film thicknesses of 25 nm and 50 nm were explored for the BGTC architecture; however, the 25 nm-thick devices were rendered non-functional, thus continuing all device studies using the standard 50 nm film thickness. The corresponding $\mu_{h,max}$, $\mu_{h,avg}$, V_T and the $I_{on/off}$ are reported in **Table 3.2**. Transfer curves as well as the $\mu_{h,avg}$ for each surface treatment is displayed in **Figures 3.3a** and **3.3b**, respectively. All transfer curves show negligible hysteresis (current lag between the forward and reverse V_{GS} sweeps), which suggests there is little to no current leakage during device performance.[46] Remarkably, an upwards trend is observed in $\mu_{h,avg}$ with increased hydrophobicity of the surface treatment. PTS and *p*-6P, having almost identical water contact angles, seem to behave similarly in terms of device parameters, which may be attributed to their comparable surface energies. On the other hand, OTS and ODTS are once again the top performing devices, this time ODTS holding the highest $\mu_{h,avg}$ of 8.2×10^{-3} cm^2 V^{-1} s^{-1} and a V_T of -23.2 V, and OTS exhibiting the second highest $\mu_{h,avg}$ of 1.5×10^{-3} cm^2 V^{-1} s^{-1} and a V_T of -25.0 V. The champion OTS and ODTS treated substrates were also tested under air, which resulted in similar electronic performances as to what was observed during the nitrogen glovebox testing (comparative electronic characteristics are reported in **Table A.3.1** of Section 3.5 Appendix). A slight decrease in V_T was observed for the more hydrophilic surface treatments, with PFTS holding the lowest V_T, even though the more hydrophobic surface treatments showcased better quality films (showcased by XRD analysis, **Figure 3.3c**) which led to higher overall mobility. This slight decrease in V_T is possibly a result of the inductive effect of the phenyl substituents in the surface treatments (PTS and *p*-6P), making it easier to promote the dipole at the dielectric-semiconductor interface thus facilitating charge injection into the semiconducting material. The larger electron withdrawing effect provided by the fluorine atoms in the PFTS surface treatment (BGBC architecture) would also produce a similar effect.[9,47–50]

Table 3.2 *Comparative average electrical characteristics of BGBC and BGTC OTFTs calculated from n unique transistors.*

Device	**surface treatment**	**θ_w**[a]	**$\mu_{h,max}$ × 10^{-3} [cm^2 V^{-1} s^{-1}]**	**$\mu_{h,avg}$ × 10^{-3} [cm^2 V^{-1} s^{-1}]**	**V_T [V]**	**$I_{on/off}$**	**n**[b]
BGBC	SiO_2	43°	0.27	0.15 ± 0.06	-19.7 ± 2.8	10^2	3
	PTS	80°	1.35	0.73 ± 0.02	-19.7 ± 0.2	10^2	4
	PFTS	88°	0.23	0.05 ± 0.01	-16.0 ± 0.3	10^2	4
	OTS	96°	8.54	6.50 ± 1.73	-22.5 ± 0.6	10^3	4
	ODTS	109°	7.84	6.15 ± 1.55	-24.5 ± 1.8	10^3	4
BGTC	PTS	79°	0.79	0.35 ± 0.07	-19.2 ± 0.9	10^2	31
	p-6P	80°	0.89	0.23 ± 0.15	-21.6 ± 0.6	10^2	33
	OTS	96°	3.82	1.45 ± 0.42	-25.0 ± 0.6	10^2	37
	ODTS	109°	15.36	8.18 ± 2.57	-23.2 ± 0.9	10^2	38

[a] Water contact of the surface treatment material measure on SiO_2, data acquired from literature.[40]

[b] Number of unique transistors used for calculation of the averages; a total of 4 transistors were tested for the BGBC devices, and 40 transistors were tested for the BGTC devices.

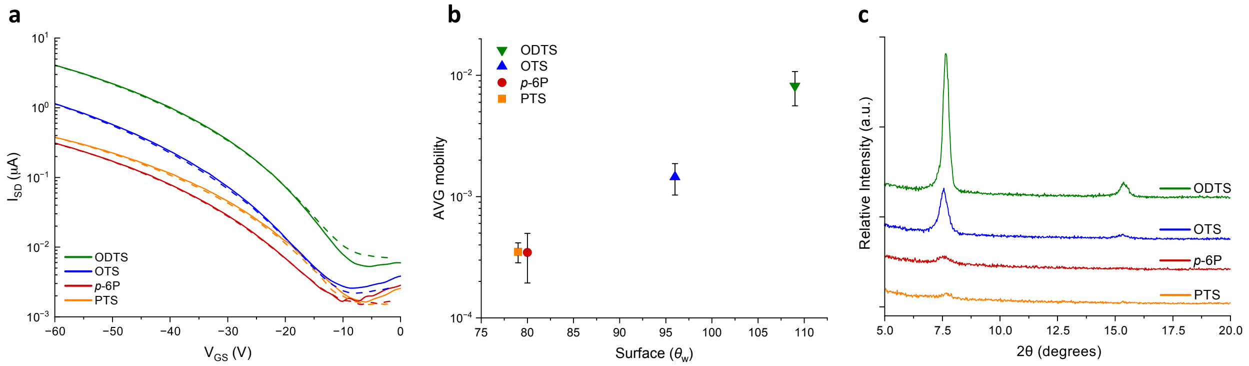

Figure 3.3 *(a) Forward (solid) and backward (dashed) characteristic transfer curves for each surface treatment used. (b) Average μ_h with respect to surface treatment. (c) Thin-film XRD pattern of PO-Tbc BGTC OTFTs with surface treated substrates.*

Overall, the results obtained from both series of devices (BGBC and BGTC) show improved performance when migrating towards a more hydrophobic, low energy surface treatment. For both the BGBC and BGTC devices, OTS and ODTS both showed an increase of one order of magnitude in their average charge mobilities compared to bare SiO_2, PTS, PFTS, and *p*-6P-treated surfaces. The BGTC devices demonstrated a clear linear increase in charge mobility with respect to the water contact angle of the surface treatments, with ODTS holding the best performance overall with a maximum μ_h of 1.54×10^{-2} cm^2 V^{-1} s^{-1}. The results extracted from these device studies demonstrate the importance of surface chemistry and the direct impact it holds on the semiconductor thin-film growth and overall device performance.

Although the PO-Tbc BGTC devices hold moderate performance, they do not match the current leading MPor organic semiconducting materials.[2] Reasoning behind the lower performance characteristics could lie within the thin-film morphology. Often times, device performance is not a result of a poor semiconducting material but rather the OSC adopting poor molecular packing in its thin-film state. This can lead to defect densities and charge traps, ultimately hindering the electrical performance of the OSC. To probe this further, the defect density (*N*) was calculated for the BGTC devices and the results are provided in **Table 3.3**. *N* was calculated using **Equation 3.1**, Where *S* refers to the subthreshold slope, estimated graphically from the transfer curves, *q* is the electronic charge, *k* is the Boltzmann's constant, *T* is the temperature, and C_{ox} is the dielectric constant.

$$N = \left(\frac{Sq}{kT\ln(10)} - 1\right)\frac{C_{ox}}{q} \qquad \textbf{[3.1]}$$

The calculated results demonstrate a decrease in defect density when moving towards lower energy surface treatments, which adheres to the linear increase in mobility that was also observed during testing. As the water contact angle of the surface increases, the number of defects in the thin-film that can act as charge traps decreases, indicating an improved morphology that can lead to an improved electrical performance. To investigate this further, a more in-depth analysis was conducted on the thin-film morphology of PO-Tbc BGTC devices.

Table 3.3 *Defect density values calculated for PO-Tbc thin films deposited on BGTC OTFTs using various gate dielectric surface treatments.*

	PTS	*p*-6P	OTS	ODTS
Defect density (*N*)[a]	26.92	39.46	20.37	16.78

3.2.3 Thin-Film Characterization

To better understand the influence of surface treatment on the formation of the thin-films and their inherent performance, X-ray diffraction (XRD; **Figure 3.3c**) and polarized Raman microscopy (**Figure 3.4**) were collected on the surfaces of the BGTC devices for each surface treatment. The XRD patterns depict a low intensity peak at $2\theta = 7.68°$ corresponding to a *d*-spacing of 11.5 Å, which becomes far more prominent as the surface treatments decrease in polarity, thus confirming that more hydrophobic, low energy surface treatments lead to better crystallinity in the resulting PO-Tbc thin-films. This XRD pattern also has a strong resemblance to those of TiO-Pc and VO-Pc thin-films, materials that also adopt an umbrella conformation similar to PO-Tbc, when deposited on OTS-treated surfaces, suggesting that the PO-Tbc film adopts a similar crystal structure, and is likely also arranged face-to-face (though this cannot be confirmed without single crystal data).[51,52] Although the XRD pattern resembles the aforementioned leading MPc OSC materials, the device performance recorded for PO-Tbc is not as comparable.

To further examine the thin-films, we employed polarized Raman microscopy. We[53], and others[54–61], have demonstrated that quantifying the intensity changes in Raman signals associated to the in-plane bonds of small molecule semiconductors with different laser polarities makes it possible to extract the molecular orientation relative to the surface (**Figure 3.4c**). When applying this analysis across each pixel, we can provide average molecular orientation maps that demonstrate the degree of edge-on versus face-on orientation across the film. **Figure 3.4a, b, d and e** are the corresponding molecular angle maps of the polarized Raman microscope images for each PO-Tbc thin-film deposited on different surface treatments (10 x 10 μm scale). The results show that PO-Tbc thin-films deposited on *p*-6P and OTS devices lead to larger, more uniform domains where the molecular angle remains similar, whereas the films deposited on PTS and ODTS had smaller domains with a larger distribution of molecular angles. The probability density functions of the corresponding molecular angles are shown in **Figure 3.4f** for each film deposited on the various surface treatments, which shows that the average molecular angle is significantly smaller for the ODTS treated film (approximately 44°) compared to the other three surface treatments (averaging around 50°). This suggests that the PO-Tbc molecules possess a more face-on orientation when deposited on ODTS treated surfaces versus other surfaces. Nevertheless, these calculated angles are relatively similar and their distributions overlap with one another.

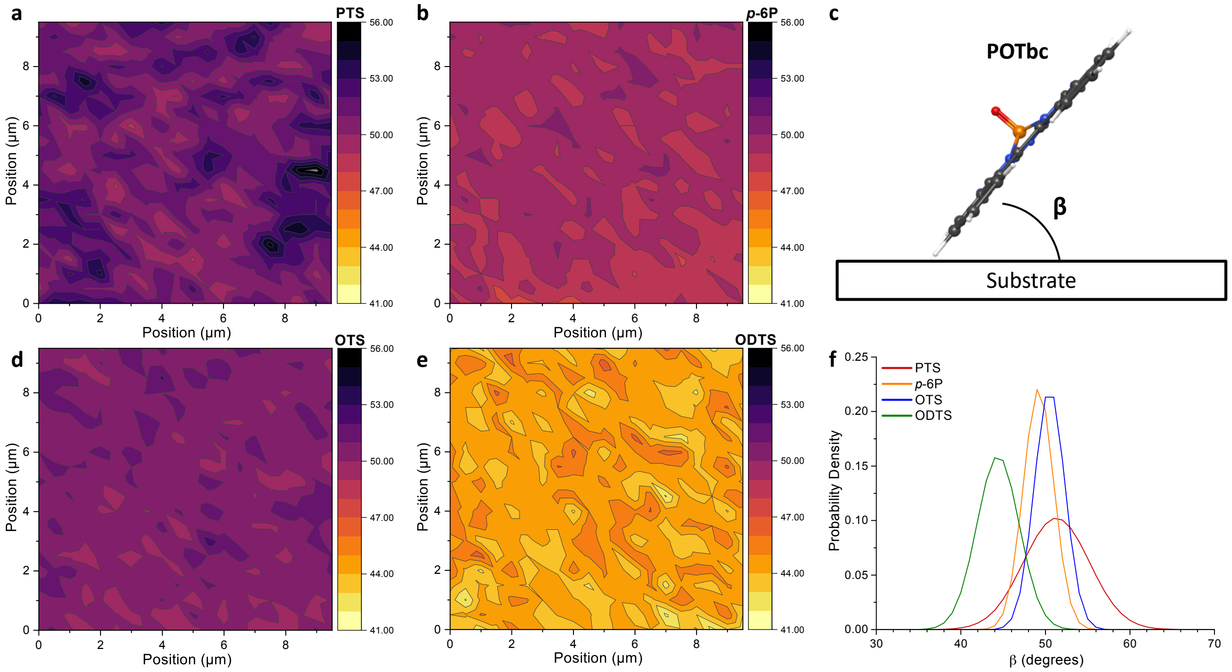

Figure 3.4 *(a,b,d,e) Raman map depicting the molecular angle of PO-Tbc thin films with respect to the substrate. (c) Schematic diagram representing the molecular angle, β, of the calculated optimized geometry of PO-Tbc with respect of the substrate surface. f) Probability density function of β for each treated surface.*

With the XRD clearly depicting a larger degree of crystallinity on the ODTS treated surfaces, this leads us to believe that the improved charge transport is likely governed by the higher packing order of the molecules in the thin-film rather than their relative orientation with respect to the surface of the substrate. In general, the observed angles are lower, and the molecules are oriented more face-on than what is typically observed for high performing MPcs, such as TiO-Pc and VO-Pc, and could be a contributing factor to the lower observed performance for these PO-Tbc devices.[52,62] Having a more predominant face-on orientation can in turn have an impact on the intermolecular electronic couplings, which can affect the ease with which charge transport is carried out.[63] Overall, XRD and Polarized Raman microscopy clearly identify differences in the PO-Tbc film morphology which are consistent and suggest a relationship between a more highly ordered film and the corresponding OTFT device performance.

3.3 Conclusion

PO-Tbc was synthesized and integrated into OTFTs as a *p*-type organic semiconductor. Both BGBC and BGTC devices were fabricated with PO-Tbc as the active semiconducting layer and gold was used as the source and drain electrodes. A variety of surface treatments with varying polarities at the dielectric-semiconductor interface were employed, along with the variation of deposition rates and post-deposition annealing temperatures. BGBC results demonstrated that the more hydrophobic surface treatments, such as OTS and ODTS, resulted in improved device performance. Subsequently, BGTC OTFTs led to similar observations with surface chemistry, but with improved device performance reaching μ_h of 1.54×10^{-2} cm^2 V^{-1} s^{-1} when using ODTS treated substrates along with holding a temperature of 100 °C during deposition of the PO-Tbc. XRD results also confirm a higher degree of crystallinity for the PO-Tbc thin-films deposited on ODTS treated substrates compared to other surface treatments. Polarized Raman microscopy demonstrated that although ODTS treated surfaces hold a higher degree of crystallinity, they also possess a more face-on orientation between the PO-Tbc molecule and substrate surface, which could ultimately have an impact on the charge transport abilities of the OSC. Overall, these results show great promise for phosphorus functionalized Tbc materials as organic semiconductors in OTFTs with clear structure-property relationships that can be employed to optimize future device performance.

3.4 Experimental

3.4.1 Materials

All solvents used for synthesis and device fabrication were ACS grade and used without any further purification. Metal-free phthalocyanine was purchased from TCI America and used as received. PBr_3 was purchase from Sigma-Aldrich Chemical Company and use as received. All silanes were purchased from Sigma Aldrich and used as received. *para*-sexiphenylene was purchased from Finetech and sublimed at 260 °C for 3 days prior to use.

3.4.2 Synthesis of Oxy Phosphorus Triazatetrabenzocorrole (PO-Tbc; 3-1)

The synthesis of PO-Tbc was derived from Li *et al.*[30] with minor changes in the protocol and characterized as previously published. In a 2-neck round bottom flask under argon atmosphere, metal-free phthalocyanine (1.0 g, 1.94 mmol) was mixed with PBr_3 (5.5 mL, 58.3 mmol) in 25 mL of pyridine. The mixture was brought to 115 °C and stirred for 24 h. Afterwards, the mixture was cooled to 55 °C and slowly quenched with 3 M HCl in MeOH until all unreacted PBr_3 was consumed. The mixture was kept stirring at 55 °C for 4 h, then brought to room temperature and poured into 200 mL of H_2O. The resulting mixture was stirred overnight, then filtered under vacuum and rinsed with 75 mL of MeOH. The resulting crude solid (green powder, 1.59 g) was purified *via* two consecutive train sublimations using CO_2 as a carrier gas, giving the title product as a blue microcrystalline powder. Due to low solubility of the product, no NMR spectra could be successfully collected (35% yield). HRMS (EI) m/z: [M]+ calcd. for $C_{32}H_{16}N_7OP$ [M]+: calcd. 545.1154; Found, 545.11454. UV-Vis (CH_2Cl_2) λ_{max} = 441 nm.

3.4.3 Optoelectronic Characterization

The UV-vis-NIR spectra were measured using an Agilent Technologies Cary 5000 UV-Vis-NIR spectrophotometer. Absorbance measurements were collected at ambient temperature in solution with DCM within the range of 250-800 nm.

3.4.4 Computational Chemistry

All calculations were executed using Gaussian09 software. The geometries of the studied compounds were investigated using the hybrid density functional theory B3LYP with the Accurate: 6-311+G(2n,p) basis set. The optimized structures were then used to examine the orbital energies and HOMO-LUMO gaps. The calculated UV-Vis-NIR spectra was determined using Time Dependent Density Functional Theory (TD-DFT), which employed the optimized B3LYP ground states.

3.4.5 Thermogravimetric analysis

TGA analyses were performed in a 100 μL DTGA/Q5000 IR Platinum Pan using a Discovery 5500 equipment from TA Instruments under nitrogen atmosphere, starting with an isothermal equilibration at 70 °C for 1 min, followed by a heating rate of 20 °C min^{-1} 70-600 °C. The decomposition temperature (T_d) was determined at 5 % weight loss.

3.4.6 Bottom-Gate Bottom-Contact (BGBC) OTFT Fabrication

BGBC OTFTs were constructed using 15 x 15 mm^2 prefabricated chips purchased from Fraunhofer Institute for Photonic Microsystems (IPMS). The gate consisted of *n*-doped Si followed by a thermally grown 230 nm thick dielectric layer of SiO_2 and gold serving as the source and drain electrodes (30 nm thick), with a 10 nm ITO adhesion layer. One chip contains 16 devices, split into four different channel lengths: 2.5, 5.0, 10.0, 20.0 μm (four devices per channel length); the width of all devices was 2000 μm. The substrates were first rinsed with acetone to remove the protective photoresist and dried under a N_2 stream followed by an air plasma treatment for 15 min under vacuum. Plasma treatment was performed using a Harrick Plasma Cleaner (PDC-32G). The plasma-treated substrates were then rinsed sequentially with water and iso-propanol, dried under a N_2 stream, submerged in a 1% v/v solution of the silane surface treatment (PTS, PFTS, OTS, or ODTS) in toluene and left to react for 1 h at 70 °C. The treated substrates were then sequentially rinsed with toluene and iso-propanol, dried under a N_2 stream, annealed under vacuum for 1 h at 70 °C then subsequently transferred into a glovebox. OTFTs were fabricated by depositing PO-Tbc onto the substrate *via* PVD using an Angstrom Engineering evaporator at a rate of 0.1 Å s^{-1} under vacuum ($P < 2\times10^{-6}$ Torr). After deposition, the OTFT devices were annealed at 150 °C under vacuum ($P < 1\times10^{-2}$ Torr).

3.4.7 Bottom-Gate Top-Contact (BGTC) OTFT Device Fabrication

BGTC OTFTs were constructed using *n*-doped Ossila Si substrates with a thermally grown 230 nm thick dielectric layer of SiO_2. The substrates were first cleaned by sonication (VWR ultrasonic cleaner (model no.97043-964)) sequentially in soapy water, DI water, acetone, and methanol for 5 min each. Afterwards, the substrates were dried under a N_2 stream and plasma treated for 15 min under vacuum. Plasma treatment was performed using a Harrick Plasma Cleaner (PDC-32G). The plasma-treated substrates were then rinsed sequentially with water and iso-propanol, dried under a N_2 stream, submerged in a 1% v/v solution of the silane surface treatment (PTS, OTS, or ODTS) in toluene and left to react for 24 h at 70 °C. The treated substrates were then sequentially rinsed with toluene and iso-propanol, dried under a N_2 stream, annealed under vacuum for 1 h at 70 °C, then subsequently transferred into a glovebox. For the *p*-6P surface treatment, the substrates were directly transferred into a glovebox after plasma treatment for the *p*-6P deposition. The substrates were placed in a substrate holder and *p*-6P was deposited *via* PVD using an Angstrom Engineering evaporator at a rate of 0.05 Å s^{-1} under vacuum ($P < 2\times10^{-6}$ Torr). The substrates were heated to 180 °C and left to soak for 1 h prior to the *p*-6P deposition. Following all the surface treatments, PO-Tbc was deposited onto the substrates *via* PVD at a rate of 0.05 Å s^{-1} under vacuum ($P < 2\times10^{-6}$ Torr). The substrates were heated to 100 °C and left to soak for 1 h prior to the PO-Tbc deposition. Afterwards, the substrates were placed in a source-drain shadow mask (L = 30 μm, W = 1000 μm) purchased from Ossila. A 50 nm-thick layer of gold was deposited onto the substrates at a rate of 1 Å s^{-1} under vacuum ($P < 2\times10^{-6}$ Torr). Each substrate was patterned to have 20 unique transistors.

3.4.8 OTFT Testing

BGBC OTFT electrical testing was done under vacuum using a custom electrical probe station equipped with an environmental chamber, oesProbe A10000-P290 (Element Instrumentation Inc. & Kreus Design Inc.), whereas the BGTC OTFT electrical testing was done in a N_2 glovebox at atmospheric pressure using a custom-built auto tester (OTS and ODTS-treated BGTC OTFT devices were also tested in air at atmospheric pressure using a custom-built auto tester). A Keithley 2614B was used to set the gate-source voltage (V_{GS}) and drain-course voltage

(V_{DS}) and measure the drain-source current (I_{DS}) for both BGBC and BGTC devices. All OTFTs were tested for *p*-type characteristics at room temperature under vacuum by fixing V_{GS} at discrete values between 0 V and -60 V. The voltages were increased in a stepwise manner, rather than pulsed, with a delay of 80 ms between measurements. Each device's transfer curve was tested four times, measured in the saturation regime, and were modelled using **Equation 3.2**.

$$\mathrm{I_{DS}} = \frac{\mu \mathrm{C_i W}}{2\mathrm{L}}(\mathrm{V_{GS}} - \mathrm{V_T})^2 \qquad \textbf{[3.2]}$$

Where *L* and *W* are the channel length and width, respectively. C_i is the capacitance density of the gate dielectric, calculated using **Equation 3.3**.

$$C_i = \frac{\varepsilon_0 \varepsilon_r}{t} \qquad \textbf{[3.3]}$$

Where *t* is the dielectric thickness (230 nm) and ε_r is the relative dielectric constant of SiO_2 (3.9), μ_h is the field-effect mobility and is calculated from the slope of the best fit through the most linear region of $\sqrt{I_{DS}}$ plotted against V_{GS}. The $\mu_{h,avg}$ represents the calculated mean of *n* working transistors for each condition, and the $\mu_{h,max}$ represents the maximum calculated μ_h for each set of conditions. The threshold voltage (V_T) is calculated as the x-intercept of the same line fitting.

3.4.9 Raman Mapping

Thin films of PO-Tbc were characterized by both Z(X,X)Z' and Z(X,Y)Z' polarized Raman spectroscopy on a Renishaw inVia InSpec confocal Raman microscope, using a Leica Microsystems bright field microscope with a DM2700 light source. A 500 mW 532 nm laser with a 2400 l/mm grating was used to obtain measurements in the spectral range of 550 cm^{-1} to 1700 cm^{-1}, focused on the sample with the X50L objective. With the objective and laser combination described, the Raman microscope has a spectral resolution of 0.3 cm^{-1}, a theoretical spatial resolution of 640 nm, and a theoretical depth of focus of approximately 3.0 μm. Calibration was performed prior to all measurements against the 520 cm^{-1} silicon reference peak within 0.5 cm^{-1}. Each Raman map was taken at the same location on the film, and each individual spectra was taken with 5% laser power (25 mW) and a 2-second exposure time every 0.5 μm over a 10 x 10 μm area. Under these conditions, every Raman image contains 441 individual Raman spectra. The ratio of the intensity of the Raman peak at 1640 cm^{-1}, the location of the pyrrole stretch, for both polarizations (I_{XY}/I_{XX}) was used to calculate the angle, β, of the PO-Tbc core to the substrate using **Equation 3.4**[54] for non-symmetrical, inverted Pc thin-films. The resulting angles were then mapped on a contour plot for the entire 10x10 μm area.

$$\frac{I_{XY}}{I_{XX}} = \sin^4 b \qquad \textbf{[3.4]}$$

A baseline spectrum was also collected for every PO-Tbc thin-film on each surface treatment and compared to a spectrum collected from purified PO-Tbc powder (5% laser power, 2-second exposure time, 20 accumulations). The Raman spectrum of a clean SiO_2 substrate can also be found in **Figure A.3.5** of Section 3.5 Appendix for reference.

3.4.10 X-Ray Diffraction

XRD measurements of the surface treated thin-films were performed using a Rigaku Ultima IV vertical theta-theta diffractometer in reflection mode equipped with a sealed-tube Cu-Kα (λ = 1.5418 Å) source. Measurements were taken directly from thin films deposited on surface treated substrates with a scan range of 3° < 2θ < 20° and a scan rate of 0.5° min^{-1} with no spin.

3.5 Appendix

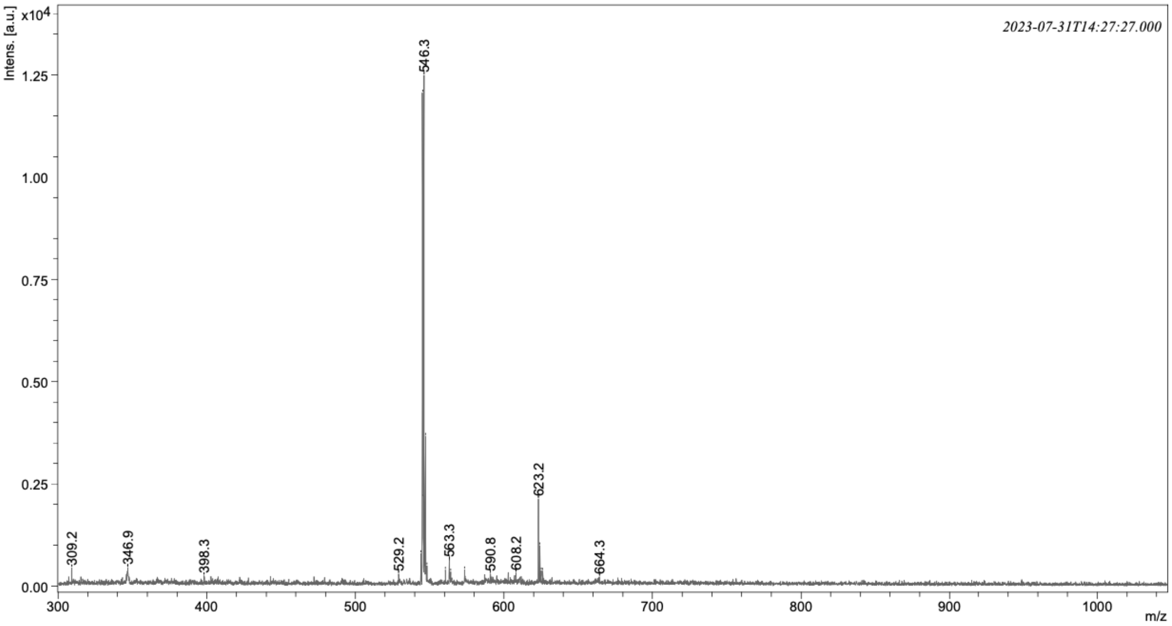

Figure A.3.1 *Matrix-Assisted Laser Desorption Ionization Time-of-Flight (MALDI-TOF) high resolution mass spectrum of PO-Tbc.*

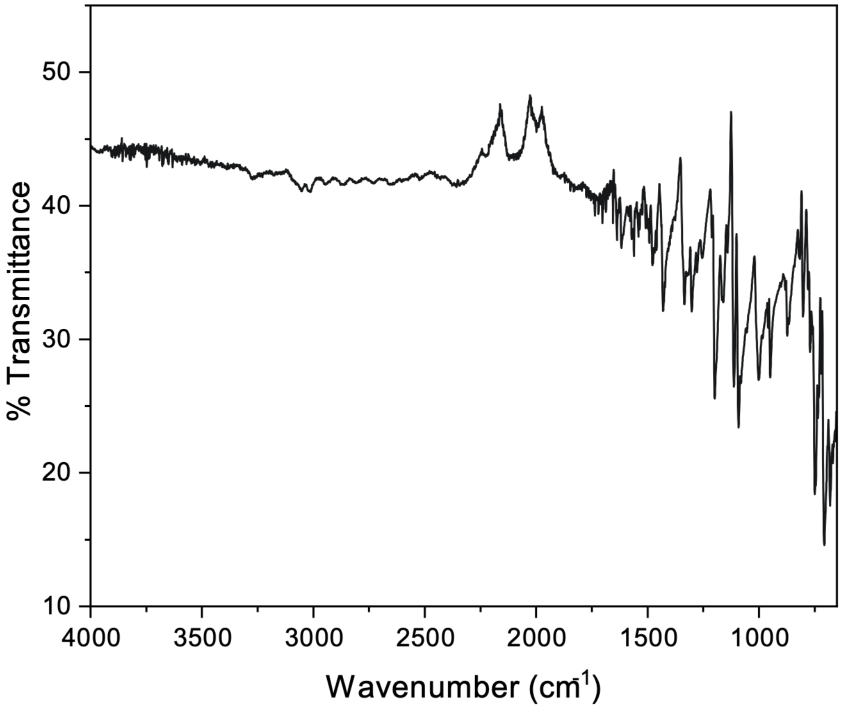

Figure A.3.2 *Infrared (IR) spectrum of PO-Tbc.*

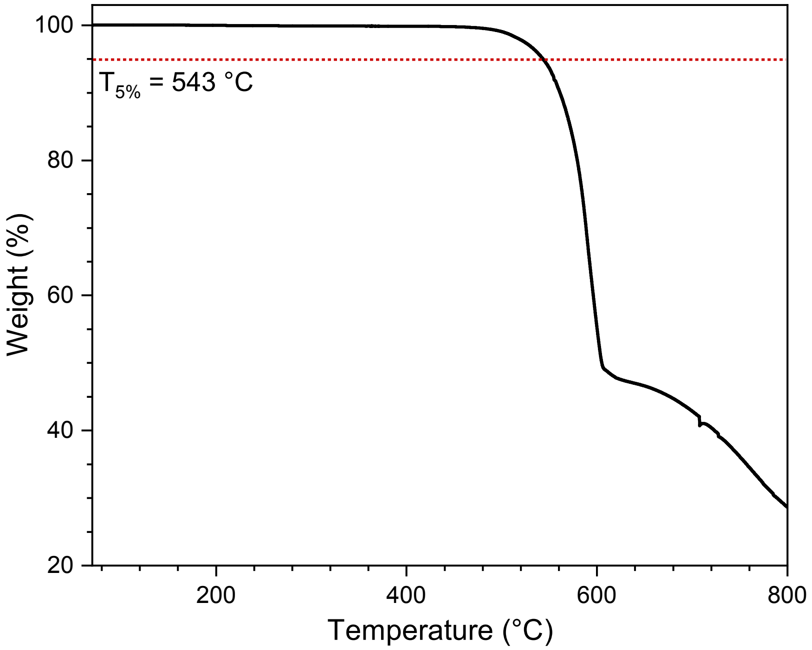

Figure A.3.3 *Thermogravimetric analysis (TGA) of PO-Tbc collected under nitrogen atmosphere with a temperature indicator of the 5% total mass loss of the sample (red).*

Table A.3.1 *Electrical characteristics of PO-Tbc BGTC OTFTs for OTS and ODTS treated substrates calculated from n unique transistors tested in a nitrogen glovebox and under air.*

	OTS		**ODTS**	
	N_2	**Air**	**N_2**	**Air**
$\mu_{h,max}$ × 10^{-3} [cm^2 V^{-1} s^{-1}]	3.82	7.54	15.4	8.86
$\mu_{h,avg}$ × 10^{-3} [cm^2 V^{-1} s^{-1}]	1.45 ± 0.42	1.52 ± 0.93	8.18 ± 2.57	4.48 ± 1.38
V_T [V]	-25.0 ± 0.6	-29.6 ± 1.3	-23.2 ± 0.9	-22.9 ± 2.5
$I_{on/off}$	10^2	10^2	10^2	10^2
n	37	37	38	38

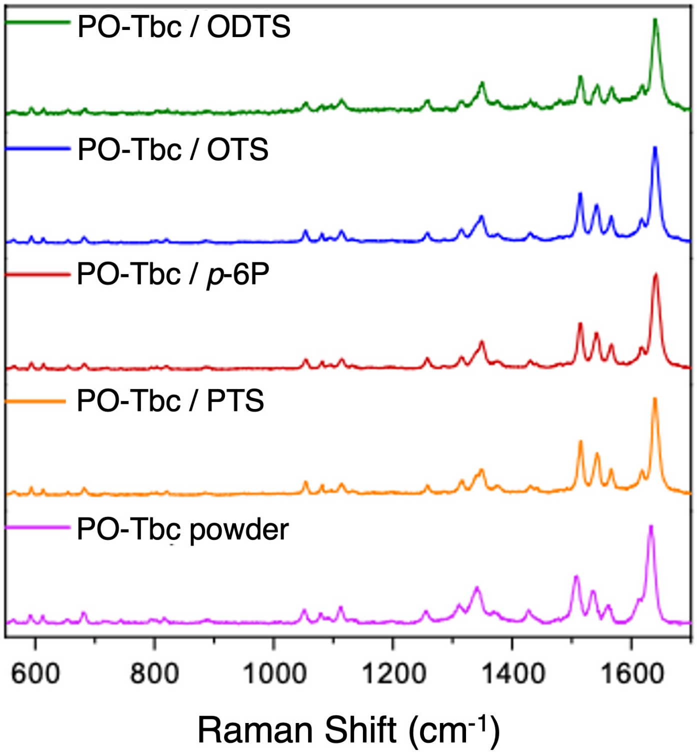

Figure A.3.4 *Polarized Raman spectra of PO-Tbc BGTC OTFT thin-film surfaces along with PO-Tbc powder for comparative purposes.*

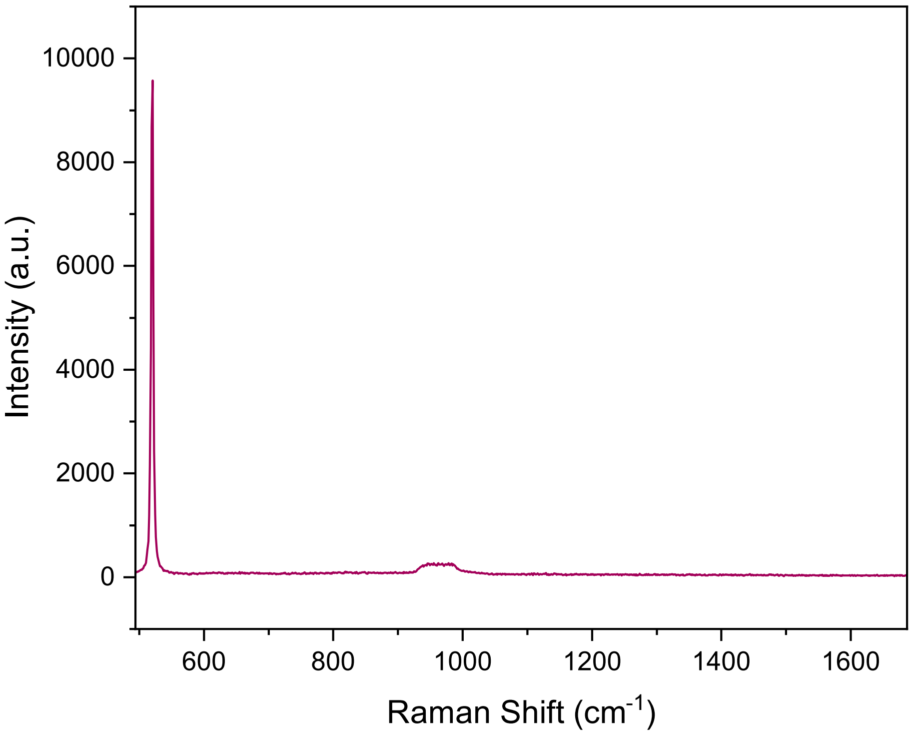

Figure A.3.5 *Polarized Raman spectra of a n-doped Ossila Si substrate with a thermally grown 230 nm thick dielectric layer of* SiO_2.

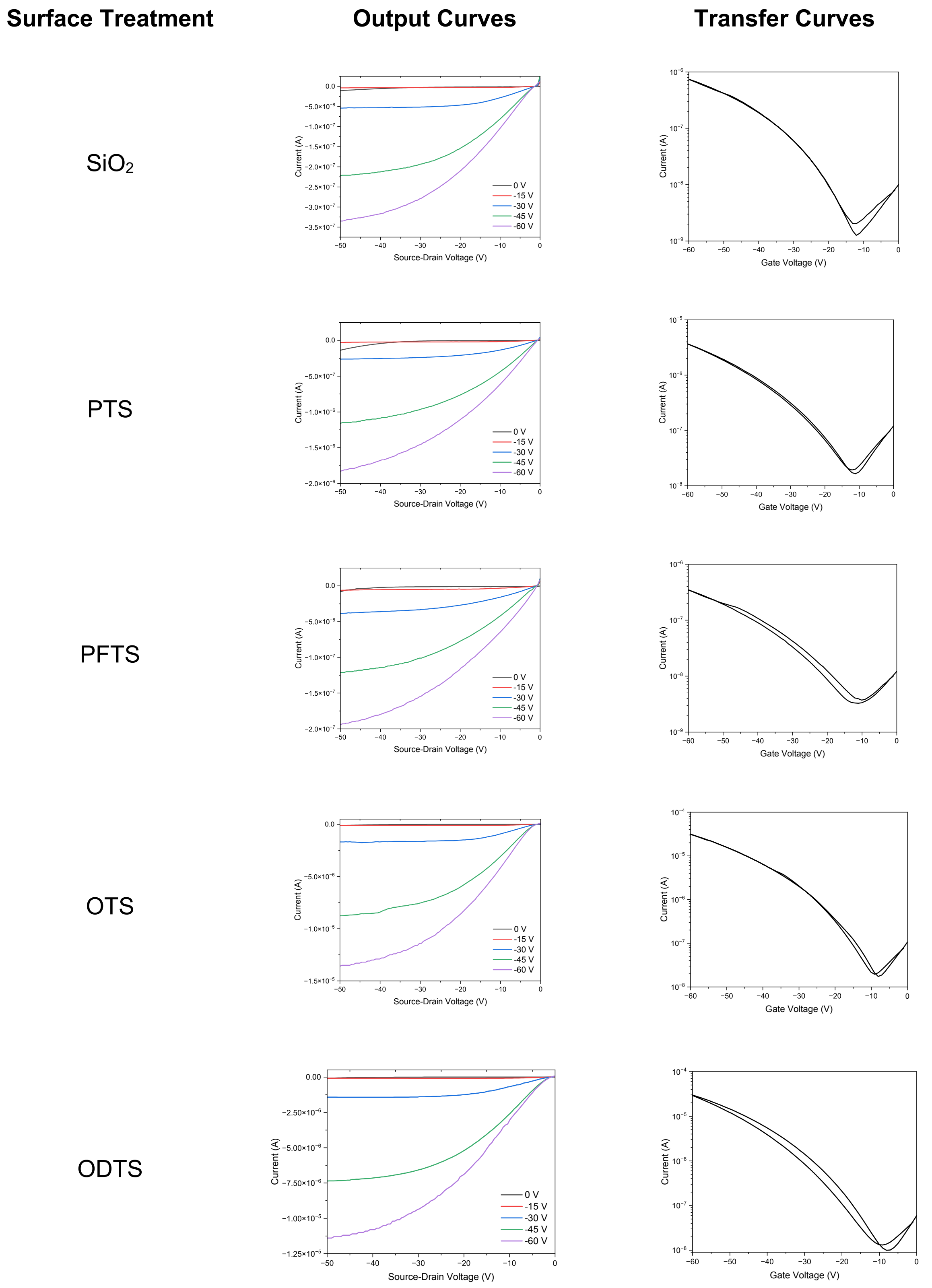

Figure A.3.6 *Output curves for PO-Tbc derivatives in BGBC OTFTs with a channel length of 5 μm measured under vacuum alongside the corresponding transfer curves (V_{DS} = -50 V) for each surface treatment used.*

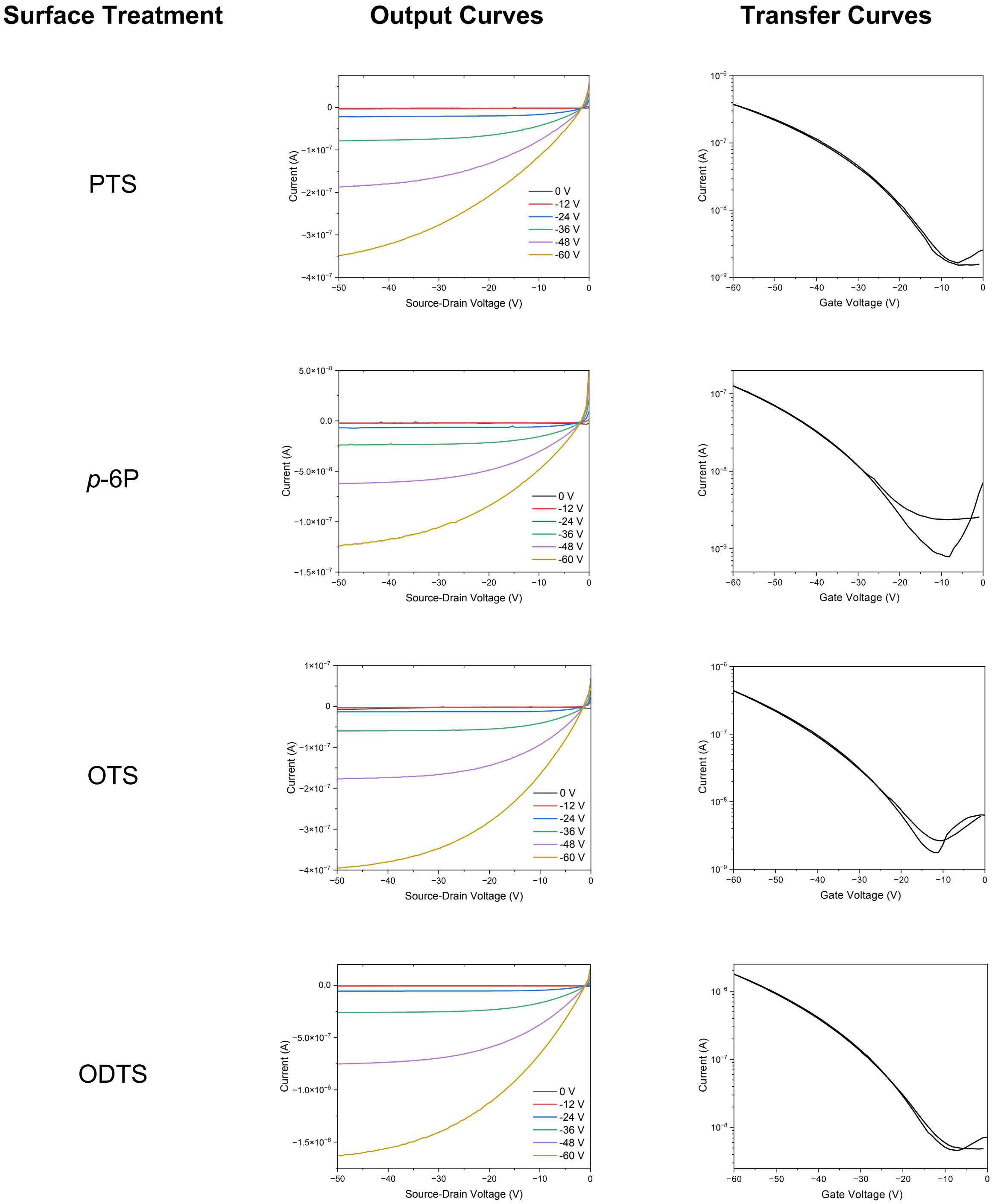

__Figure A.3.7__ Output curves for PO-Tbc derivatives in BGTC OTFTs with a channel length of 20 μm measured in a nitrogen glovebox alongside the corresponding transfer curves (V_{DS} = -50 V) for each surface treatment used.

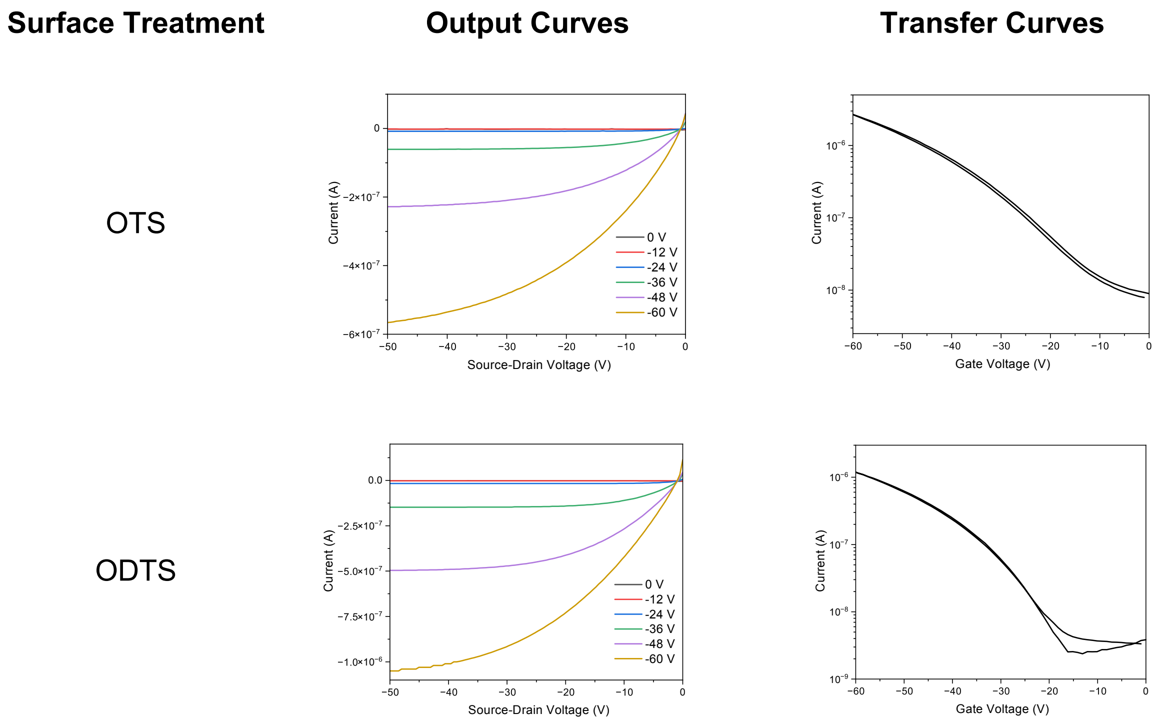

Figure A.3.8 *Output curves for PO-Tbc derivatives in BGTC OTFTs with a channel length of 20 μm measured air alongside the corresponding transfer curves (V_{DS} = -50 V) for the OTS and ODTS treated surfaces.*

References

(1) Abdulrahman Hamad, O.; Kareem, R.; Khdir Omer, P. *J. Chem. Rev.* **2023**, *6* (1), 39.

(2) Zhou, W.; Yutronkie, N. J.; Lessard, B. H.; Brusso, J. L. *Mater. Adv.* **2021**, *2* (1), 165.

(3) Boileau, N. T.; Cranston, R.; Mirka, B.; Melville, O. A.; Lessard, B. H. *RSC Adv.* **2019**, *9* (37), 21478.

(4) Melville, O. A.; Lessard, B. H.; Bender, T. P. *ACS Appl. Mater. Interfaces* **2015**, *7* (24), 13105.

(5) Karmakar, S.; Mukhopadhyay, M. K.; Sanyal, M. K. *Phys. Rev. Mater.* **2024**, *8* (2), 024601.

(6) Williams, G.; Sutty, S.; Klenkler, R.; Aziz, H. *Sol. Energy Mater. Sol. Cells* **2014**, *124*, 217.

(7) Yuen, A. P.; Jovanovic, S. M.; Hor, A.-M.; Klenkler, R. A.; Devenyi, G. A.; Loutfy, R. O.; Preston, J. S. *Sol. Energy* **2012**, *86* (6), 1683.

(8) McKeown, N. B. *Phthalocyanine materials: synthesis, structure, and function*; Chemistry of solid state materials; Cambridge University Press: Cambridge, U.K., 1998.

(9) King, B.; Radford, C. L.; Vebber, M. C.; Ronnasi, B.; Lessard, B. H. *ACS Appl. Mater. Interfaces* **2023**, acsami.2c22789.

(10) Vebber, M. C.; Grant, T. M.; Brusso, J. L.; Lessard, B. H. *Langmuir* **2020**, *36* (10), 2612.

(11) Lamontagne, H. R.; Cranston, R. R.; Comeau, Z. J.; Harris, C. S.; Shuhendler, A. J.; Lessard, B. H. *Adv. Sci.* **2024**, 2305515.

(12) Yutronkie, N. J.; King, B.; Melville, O. A.; Lessard, B. H.; Brusso, J. L. *J. Mater. Chem. C* **2021**, *9* (31), 10119.

(13) King, B.; Vebber, M. C.; Ewenike, R.; Dupuy, M.; French, C.; Brusso, J. L.; Lessard, B. H. *Chem. Mater.* **2023**, *35* (20), 8517.

(14) Lu, C.; Yu, Z.; Cao, J. *Chin. J. Struct. Chem.* **2024**, *43* (3), 100240.

(15) Sundaresan, C.; Vebber, M. C.; Brusso, J. L.; Tao, Y.; Alem, S.; Lessard, B. H. *ACS Omega* **2023**, *8* (1), 1588.

(16) De La Torre, G.; Bottari, G.; Torres, T. *Adv. Energy Mater.* **2017**, *7* (10), 1601700.

(17) King, B.; Lessard, B. H. *J. Mater. Chem. C* **2024**, *12* (16), 5654.

(18) Lessard, B. H. *ACS Appl. Mater. Interfaces* **2021**, *13* (27), 31321.

(19) Ganesh Moorthy, S.; Arvidson, J.; Meunier-Prest, R.; Wang, H.; Bouvet, M. *ACS Sens.* **2024**, *9* (2), 883.

(20) King, B.; Moorthy, S. G.; Lesniewska, E.; Meunier-Prest, R.; Bouvet, M.; Lessard, B. H. *Sens. Actuators B Chem.* **2024**, *408*, 135507.

(21) Di Zazzo, L.; Ganesh Moorthy, S.; Meunier-Prest, R.; Lesniewska, E.; Di Natale, C.; Paolesse, R.; Bouvet, M. *Sensors* **2023**, *23* (15), 6773.

(22) Fujiki, Michiya.; Tabei, Hisao.; Isa, Kimio. *J. Am. Chem. Soc.* **1986**, *108* (7), 1532.

(23) Pomarico, G.; Nardis, S.; Stefanelli, M.; Cicero, D. O.; Vicente, M. G. H.; Fang, Y.; Chen, P.; Kadish, K. M.; Paolesse, R. *Inorg. Chem.* **2013**, *52* (15), 8834.

(24) Zhang, X.-F. *Coord. Chem. Rev.* **2015**, *285*, 52.

(25) Lu, X.; Zhang, X.-F. *Dyes and Pigm.* **2020**, *179*, 108421.

(26) Breusova, M. O.; Pushkarev, V. E.; Tomilova, L. G. *Russ. Chem. Bull.* **2007**, *56* (7), 1456.

(27) Raboui, H.; Thibau, E. S.; Josey, D. S.; Lu, Z.-H.; Bender, T. P. *J. Mater. Chem. A* **2017**, *5* (22), 10978.

(28) Zhang, X.-F.; Xu, B. *Dyes and Pigm.* **2024**, *224*, 112030.

(29) Raboui, H.; Josey, D. S.; Jin, Y.; Bender, T. P. *ACS Omega* **2020**, *5* (39), 25264.

(30) Li, J.; Subramanian, L. R.; Hanack, M. *Eur. J. Org. Chem.* **1998**, *1998* (12), 2759.

(31) Farag, A. A. M. *Opt. Laser Technol.* **2007**, *39* (4), 728.

(32) Michaelson, H. B. *J. App. Phys.* **1977**, *48* (11), 4729.

(33) Xu, Q.; Wei, H.; Lin, Y.; Yan, Z.; Wang, W. *App. Phys. Lett.* **2024**, *124* (14), 143301.

(34) Yang, S. Y.; Shin, K.; Park, C. E. *Adv. Funct. Mater.* **2005**, *15* (11), 1806.

(35) Zhou, S.; Tang, Q.; Tian, H.; Zhao, X.; Tong, Y.; Barlow, S.; Marder, S. R.; Liu, Y. *ACS Appl. Mater. Interfaces* **2018**, *10* (18), 15943.

(36) Di, C.; Liu, Y.; Yu, G.; Zhu, D. *Acc. Chem. Res.* **2009**, *42* (10), 1573.

(37) Liu, C.; Xu, Y.; Noh, Y.-Y. *Mater. Today* **2015**, *18* (2), 79.

(38) Ewenike, R. B.; King, B.; Battaglia, A. M.; Quezada Borja, J. D.; Lin, Z. S.; Manion, J. G.; Brusso, J. L.; Kelly, T. L.; Seferos, D. S.; Lessard, B. H. *ACS Appl. Electron. Mater.* **2023**.

(39) Peltekoff, A. J.; Tousignant, M. N.; Hiller, V. E.; Melville, O. A.; Lessard, B. H. *Polymers* **2020**, *12* (6), 1231.

(40) Cranston, R. R.; Vebber, M. C.; Faleiro Berbigier, J.; Brusso, J.; Kelly, T. L.; Lessard, B. H. *Adv. Electron. Mater.* **2022**, *8* (12), 2200696.

(41) Melville, O. A.; Grant, T. M.; Lessard, B. H. *J. Mater. Chem. C* **2018**, *6* (20), 5482.

(42) Yang, J.; Yan, D.; Jones, T. S. *Chem. Rev.* **2015**, *115* (11), 5570.

(43) Wang, H.; Zhu, F.; Yang, J.; Geng, Y.; Yan, D. *Adv. Mater.* **2007**, *19* (16), 2168.

(44) Zhang, Y.; Wei, X.; Zhang, H.; Chen, X.; Wang, J. *App. Surf. Sci.* **2018**, *427*, 452.

(45) Pan, F.; Tian, H.; Qian, X.; Huang, L.; Geng, Y.; Yan, D. *Org. Electron.* **2011**, *12* (8), 1358.

(46) Kumar, B.; Kaushik, B. K.; Negi, Y. S. *Polym. Rev.* **2014**, *54* (1), 33.

(47) Kobayashi, S.; Nishikawa, T.; Takenobu, T.; Mori, S.; Shimoda, T.; Mitani, T.; Shimotani, H.; Yoshimoto, N.; Ogawa, S.; Iwasa, Y. *Nat. Mater.* **2004**, *3* (5), 317.

(48) Pernstich, K. P.; Haas, S.; Oberhoff, D.; Goldmann, C.; Gundlach, D. J.; Batlogg, B.; Rashid, A. N.; Schitter, G. *J. App. Phys.* **2004**, *96* (11), 6431.

(49) King, B.; Daszczynski, A. J.; Rice, N. A.; Peltekoff, A. J.; Yutronkie, N. J.; Lessard, B. H.; Brusso, J. L. *ACS Appl. Electron. Mater.* **2021**, *3* (5), 2212.

(50) King, B.; Melville, O. A.; Rice, N. A.; Kashani, S.; Tonnelé, C.; Raboui, H.; Swaraj, S.; Grant, T. M.; McAfee, T.; Bender, T. P.; Ade, H.; Castet, F.; Muccioli, L.; Lessard, B. H. *ACS Appl. Electron. Mater.* **2021**, *3* (1), 325.

(51) Ji, Z.; Liu, M.; Shang, L.; Hu, W.; Liu, G.; Liu, X.; Wang, H. *J. Mater. Chem.* **2009**, *19* (31), 5507.

(52) Li, L.; Tang, Q.; Li, H.; Hu, W. *J. Phys. Chem. B* **2008**, *112* (34), 10405.

(53) Cranston, R. R.; Lanosky, T. D.; Ewenike, R.; Mckillop, S.; King, B.; Lessard, B. H. *Small Sci.* **2024**, 2300350.

(54) Latteyer, F.; Peisert, H.; Aygül, U.; Biswas, I.; Petraki, F.; Basova, T.; Vollmer, A.; Chassé, T. *J. Phys. Chem. C* **2011**, *115* (23), 11657.

(55) Bhardwaj, B. S.; Sugiyama, T.; Namba, N.; Umakoshi, T.; Uemura, T.; Sekitani, T.; Verma, P. *Sci. Rep.* **2019**, *9* (1), 15149.

(56) Szybowicz, M.; Makowiecki, J. *J Mater Sci.* **2012**, *47* (3), 1522.

(57) Szybowicz, M.; Bała, W.; Fabisiak, K.; Paprocki, K.; Drozdowski, M. *J. Mater. Sci.* **2011**, *46* (20), 6589.

(58) Szybowicz, M.; Bała, W.; Fabisiak, K.; Paprocki, K.; Drozdowski, M. *Cryst. Res. Technol.* **2010**, *45* (12), 1265.

(59) Szybowicz, M.; Bała, W.; Dümecke, S.; Fabisiak, K.; Paprocki, K.; Drozdowski, M. *Thin Solid Films* **2011**, *520* (1), 623.

(60) Szybowicz, M.; Runka, T.; Drozdowski, M.; Bała, W.; Grodzicki, A.; Piszczek, P.; Bratkowski, A. *J. Mol. Struct.* **2004**, *704* (1–3), 107.

(61) Lamontagne, H. R.; Cyr, M.; Vebber, M. C.; Swaraj, S.; Harris, C. S.; Brusso, J. L.; Shuhendler, A. J.; Lessard, B. H. *RSC Appl. Interfaces* **2024**.

(62) Li, L.; Tang, Q.; Li, H.; Yang, X.; Hu, W.; Song, Y.; Shuai, Z.; Xu, W.; Liu, Y.; Zhu, D. *Adv. Mater.* **2007**, *19* (18), 2613.

(63) Coropceanu, V.; Cornil, J.; Da Silva Filho, D. A.; Olivier, Y.; Silbey, R.; Brédas, J.-L. *Chem. Rev.* **2007**, *107* (4), 926.

Chapter 4. Synthesis and Axial Electropolymerization of Novel Amino-Derived Silicon Phthalocyanines

This chapter is adapted from: ***Cyr, M.****, Magna, G., Pizzoli, F., Mita, A., Di Zazzo, L., Paolesse, R., Lessard, B. H., Brusso, J. L. Synthesis and Axial Electropolymerization of Novel Amino-Derived Silicon Phthalocyanine-Based Organic Semiconductors. J. Mater. Sci.* ***2025****, manuscript submitted.*

Context

During my PhD studies, I synthesized various known fluorinated silicon phthalocyanines to assist my colleagues with their projects related to OTFTs, which sparked my interest in the development of novel axially derived SiPc materials. This ultimately led to a collaborative project with Dr. Roberto Paolesse at the University of Rome Tor Vergata, where I designed various axially-derived amino-aryl silicon phthalocyanines to undergo amino-catalyzed electropolymerization. This work was done to investigate the possibility of axial polymerization of SiPc materials to create semiconducting thin-films directly onto a substrate surface in a cost-effective manner, forgoing traditional thermal evaporation methods that are typically required for non-alkylated SiPcs. I synthesized five amino-functionalized SiPcs, three bearing amino phenoxyl and two bearing amino benzoate functional groups, to investigate whether having electron donating or withdrawing moieties would cause any substantial differences in the electrochemical properties of the materials. Within these derivatives, the positioning of the amine on the aryl component was different (i.e. *para* vs. *meta* vs. *ortho*) to see if this would have any effect on the polymerization process or the resulting thin-film. To further characterize the electropolymerization process, I also conducted spectroelectrochemical measurements to better understand the polymerization process and how it affects the overall absorption profile of each material.

Contribution

This work was completed through contributions of all authors. I synthesized, purified, and characterized the axially-derived amino SiPc monomers, performed the electrochemical characterization, electropolymerization and spectroelectrochemistry on all materials and wrote the manuscript. G.M. and F.P. trained me on the electropolymerization techniques. A.M. obtained the single crystals of the SiPc monomers and A.L. (University of Toronto) completed the X-ray experiments. L.D. trained me on how to perform the spectroelectrochemistry and assisted in interpreting the data. R.P., B.H.L. and J.L.B. provided supervision for the project. All authors assisted with editing the manuscript.

Abstract

Silicon phthalocyanines (SiPcs) are a class of molecules that have garnered large amounts of interest in the past decades, notably in the field of organic electronics. Their high level of conjugation allows them to promote charge transfer in an easy and efficient manner, in addition to holding high thermal and chemical stability. Herein, the synthesis of five novel amino-derived silicon phthalocyanines is reported, where the monomers are probed for *in situ* electropolymerization onto ITO conductive glass. Conductive films are obtained for the *para* and *ortho*-bis(aminophenoxy) SiPc derivatives. The other three monomeric derivatives, however, did not yield any electropolymerized films. The polymerization is catalyzed by oxidation of the amino groups, introducing a phenazine bridge between the axial positions of the SiPcs. The electropolymerization is performed using cyclic voltammetry and further investigated through optical and spectroelectronic spectroscopy.

4.1 Introduction

Metal and main group phthalocyanines (MPcs) are an established class of materials that are actively and increasingly pursued due to their low-cost, versatile syntheses, and wide range of potential applications, which span from dyes and pigments to organic electronics.[1,2] Among these, silicon phthalocyanines (SiPcs) have proven particularly promising, notably in the field of organic electronics.[3,4] Due to the oxidation state of silicon, two axial substituents are present perpendicular to the Pc macrocycle which serve as key components to modify the material and finetune its bulk properties without compromising the rich electrochemical and optical properties contributed by the phthalocyanine framework itself.[5,6] Previously, incorporating alkylated chains at the axial positions has improved the solubility of SiPcs enabling their implementation as the active layer in organic electronic devices, such as organic thin-film transistors (OTFTs)[7,8] and organic photovoltaics (OPVs)[9,10], using low cost solution processing methods including blade coating and spin coating. Additionally, employing perfluorinated aryl substituents at the axial positions allows for finetuning of the energy levels allowing SiPcs to serve as *n*-type organic semiconductors (OSCs) in OTFTs and organic sensors, whereas the majority of reported SiPcs and MPcs (e.g. CuPc, ZnPc, TiOPc, Cl-AlPc) tend to favour hole transport and typically operate as *p*-type OSCs.[11–13] Furthermore, phthalocyanines can also interact with redox active species through electron transfer, making them great candidates for various sensing applications.[13–17]

Aside from its monomeric form, phthalocyanine polymers (poly-MPcs) also represent attractive candidates for catalysis[18] and sensing[19] applications. In the past, poly-MPcs have been synthesized using various different metals at the core including copper, nickel, cobalt, and usually require some type of linker to allow polymerization to occur. These linkers typically consist of a boronic acid building block that would react with an amino functional group that is attached at the periphery of the MPc *via* coupling reaction.[20] Polymerization at the periphery of the phthalocyanine core allows for expansion of the π-conjugated surface area, which can ultimately have an impact on the ease with which poly-MPcs are able to transport charges.[21–23] Furthermore, peripherally polymerized poly-MPcs fall under the category of porous organic polymers (POPs), as pockets are formed at the centre of four connected units. These pores can also serve as a vessel for analyte interaction should the poly-MPc be used for sensing applications.[20,24,25] Although peripheral poly-MPcs have been reported, axially polymerized phthalocyanines remain a field with untapped potential. SiPcs are perfect candidates to further explore axial polymerization as they allow installation of two axial components on opposite sides of the Pc core, thus allowing for a continuous axial network to form during the polymerization process.

Electropolymerization of porphyrins and other porphyrinoid materials bearing electroactive functional groups is a facile and cost-effective method for obtaining polymeric thin-films. In most cases, these materials contain amino functional groups, which undergo electrochemical oxidation that ultimately leads to the formation of a new intermolecular C–N bond.[26,27] This polymerization (**Figure 4.1**) from start to finish is a 6 e^- process that results in the formation of a phenazine bridge between two monomeric units.[26,28]

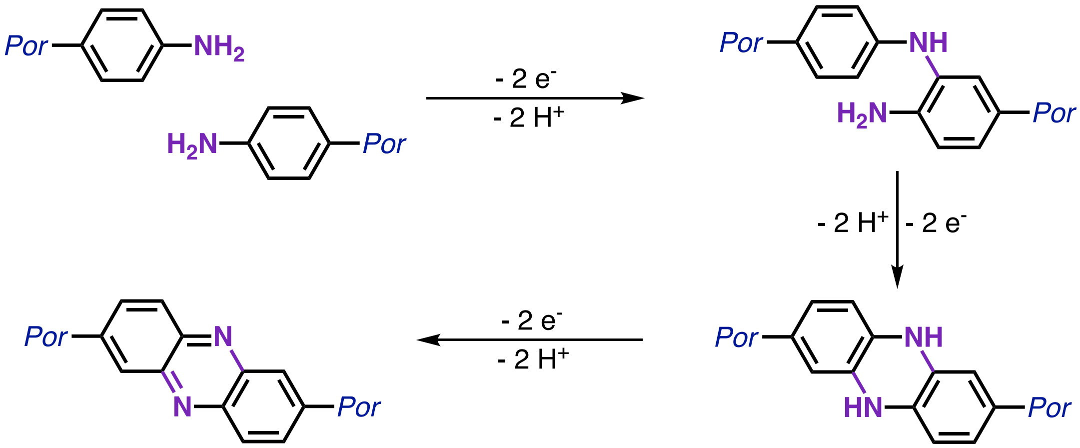

***Figure 4.1** Electropolymerization process of porphyrinoid (Por) materials bearing aminophenyl substituents.*

Inspired by this, we herein present the synthesis of novel *para*, *meta* and *ortho* oriented bis(aminophenoxy) silicon phthalocyanines (SiPcs) as well as *para* and *meta* bis(aminobenzoate) SiPcs as monomeric units for polymerization. The optical and electrochemical properties of the five monomers were investigated *via* UV-Vis-NIR spectroscopy, cyclic voltammetry and spectroelectrochemistry. Subsequent *in-situ* electropolymerization was conducted for all five SiPcs, where the formation of the phenazine linkers occurs at the axial position rather than the periphery of the phthalocyanine. This creates an axial polymer where the SiPc cores will be parallel to one another. If the Pc macrocycles are successful in obtaining such a confirmation, this can potentially create a solid-state morphology where the electron clouds provided by the π-orbitals of the Pc core could feasibly overlap with one another. This type of favourable molecular packing has been shown to be ideal for charge transfer within other types of MPc materials.[29] The CV spectra indicated that the *para* and *ortho*-bis(aminophenoxy) SiPcs were successful in forming a polymer thin-film directly onto conductive ITO-coated glass. Characterization of these polymeric films was conducted *via* optical spectroscopy and compared to their monomeric counterparts. This practical polymerization technique serves as a cost-effective and promising route to exploit these new polymers in a variety of potential applications through direct thin-film formation onto a conductive substrate. These novel polymerized materials thus hold significant potential for low-cost processing applications in fields such as chemical sensing and semiconducting organic devices.

4.2 Results and Discussion

4.2.1 Monomer Synthesis and Characterization

The synthesis of five amino-functionalized SiPcs was achieved using a synthetic pathway adapted from Lessard *et. al.* (**Figure 4.2**).[30] Dichloro silicon phthalocyanine (Cl_2-SiPc) was prepared according to methods previously reported.[31] From there, axial substitution of the chlorine atoms was done by reacting Cl_2-SiPc with either an excess of aminophenol or aminobenzoic acid in chlorobenzene at reflux. This allows for either the hydroxyl or the benzoic acid groups to attach to the silicon, thus releasing hydrochloric acid in the process. During the workup, the resulting crude solution is quenched with saturated $NaHCO_3$ in order to neutralize any protonated amines. Three aminophenoxyl derivatives were designed by shifting the amino group in the *para*, *meta*, and *ortho* positions and two aminobenzoate derivatives were designed bearing the amino group at the *para* and *meta* positions. The *ortho*-phenoxy derivative necessitated the addition of a catalytic amount of 1,8-diazabicyclo[5.4.0]undec-7-ene (DBU) to catalyze the deprotonation of the hydroxyl group to promote the attack on the silicon. Although the *ortho*-oriented aminobenzoate would complete this set, the synthesis was attempted with and without the use of DBU and no product was yielded in both cases, therefore only five derivatives were used in this study. All five monomers were successfully characterized by ^{1}H Nuclear Magnetic Resonance (NMR), Fourier Transform Infrared (FT-IR), High Performance Liquid Chromatography (HPLC) and mass spectrometry. Recrystallization was attempted on all five materials using dimethylformamide (DMF) and methanol, from which **4-3**, **4-6**, and **4-7** yielded single crystals (**Figure 4.2b-d**).

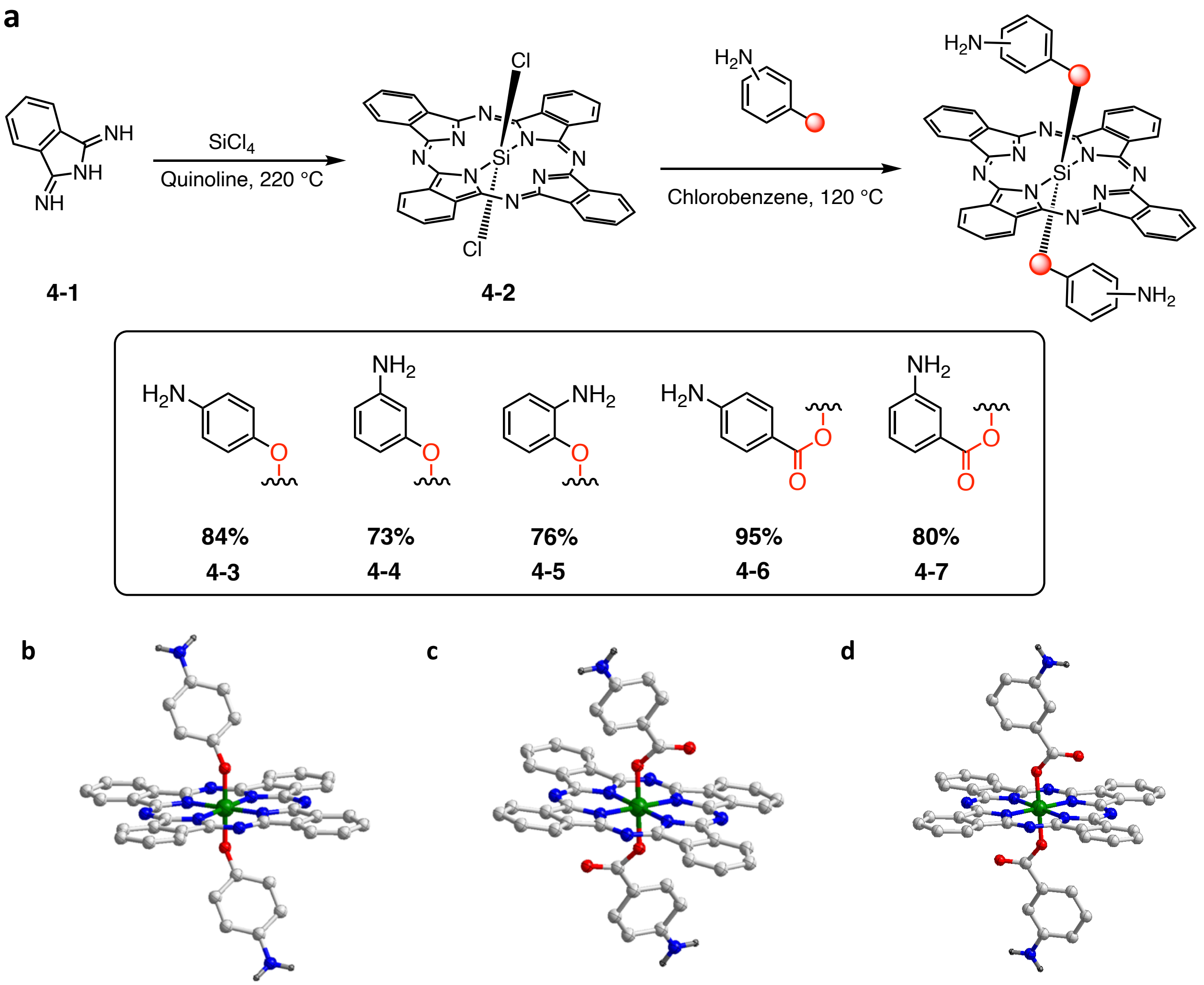

Figure 4.2 *(a) Synthetic route towards preparing bis(amino)-functionalized silicon phthalocyanines from diiminoisoindoline (DIII) with final yields referring to the final step. Single crystal structures of (b) compound 4-3, (c) compound 4-6 and (d) compound 4-7, obtained from recrystallization in DMSO/MeOH. Hydrogen atoms have been omitted from the carbon atoms in the crystal structures for clarity (C = white; N = blue; O = red; Si = green; H = grey).*

4.2.2 Optical Properties

The optical properties of all synthesized SiPc monomers were evaluated using UV-Vis-NIR spectroscopy in solution with DMF (**Figure 4.3**). In comparison with the Cl_2-SiPc precursor (**4-2**), all products undergo a slight blue shift in the Q-band region, which can be explained by the addition of arylamine electron-donating groups onto the molecule.[32] Furthermore, compounds **4-3** and **4-4** possess a slightly stronger blue shift compared to **4-6** and **4-7** due to the phenoxyl group providing additional electron-donating character, whereas the benzoate acts as an electron-withdrawing group. However, **4-5** undergoes the same shift as observed in **4-6** and **4-7** despite having a phenoxyl group, which may be attributed to intramolecular hydrogen bonding between the *ortho*-oriented amine and phenoxyl substituents.[33] Similar shifts can be observed in the B band (Soret) region, although **4-5** now sits in-line with its two other phenoxyl counterparts. Moreover, **4-5** also exhibits a set of three additional absorption peaks in its spectrum at 441, 472, and 503 nm. Although these new peaks are not typically associated with the B and Q bands of phthalocyanines, they may originate from ligand-to-macrocycle charge transfer arising from the *ortho* positioning of the amino groups, where electronic transitions occur from the 2-aminophenoxy π or *n* orbitals to the Pc π^* system.[34,35] Alternatively, these absorption features may result from aggregation or exciton coupling facilitated by hydrogen bonding between the *ortho*-amino groups.[36,37]

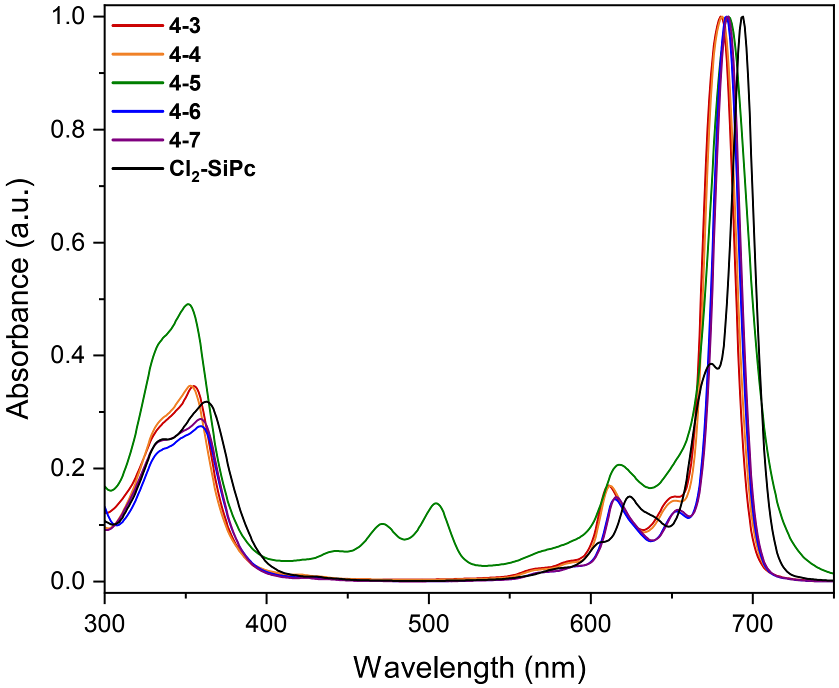

Figure 4.3 *Normalized UV-Vis-NIR spectra of all monomeric compounds and the Cl_2-SiPc starting material collected in a dilute DMF solution in the range of 300-750 nm, demonstrating the absorbance shift in the B and Q bands related to the structural changes of each material.*

4.2.3 Electrochemical Properties

The electrochemical properties of all amino-derived SiPcs were evaluated using cyclic voltammetry (CV) in solution with 1,2-dichlorobenzene (*o*-DCB) using 0.1 M tetrabutyl ammonium perchlorate (TBAP) as the electrolyte, the results of which are presented in **Figure 4.4** and **Table 4.1**. All five materials possess two quasi-reversible reduction processes, often characteristic of phthalocyanines. For all materials, the first reduction occurs around -0.65 V (± 0.04 V) and the second around -1.07 V (± 0.1 V). The oxidation processes exhibited by each material are governed by the amino group located on the axial position rather than the phthalocyanine core and vary in both voltage range and reversibility for each compound. **4-3** shows three oxidation processes at 0.54 V, 0.88 V, and 1.10 V. **4-4** shows one larger oxidation peak at 1.15 V on the forward sweep and a reduction peak at 0.13 V on the reverse sweep. **4-5** has two oxidation peaks at 0.96 V and 1.15 V on the forward sweep and a reduction peak at 0.09 V on the reverse sweep. As for **4-6** and **4-7**, both materials show a more quasi-reversible redox process that occurs in a closer voltage range. The oxidation peaks also occur at a slightly higher voltage: 1.20 V and 1.28 V for **4-6** and **4-7**, respectively. The higher voltage could result from the benzoic groups pulling electron density away from the amino group, thus requiring higher energy to successfully oxidize the amino group. Furthermore, the more pronounced reversibility could stem from the enhanced conjugation effect and charge delocalization from the generated amine radical of the benzoate group, an effect that can potentially compromise the material's ability to polymerize.[38]

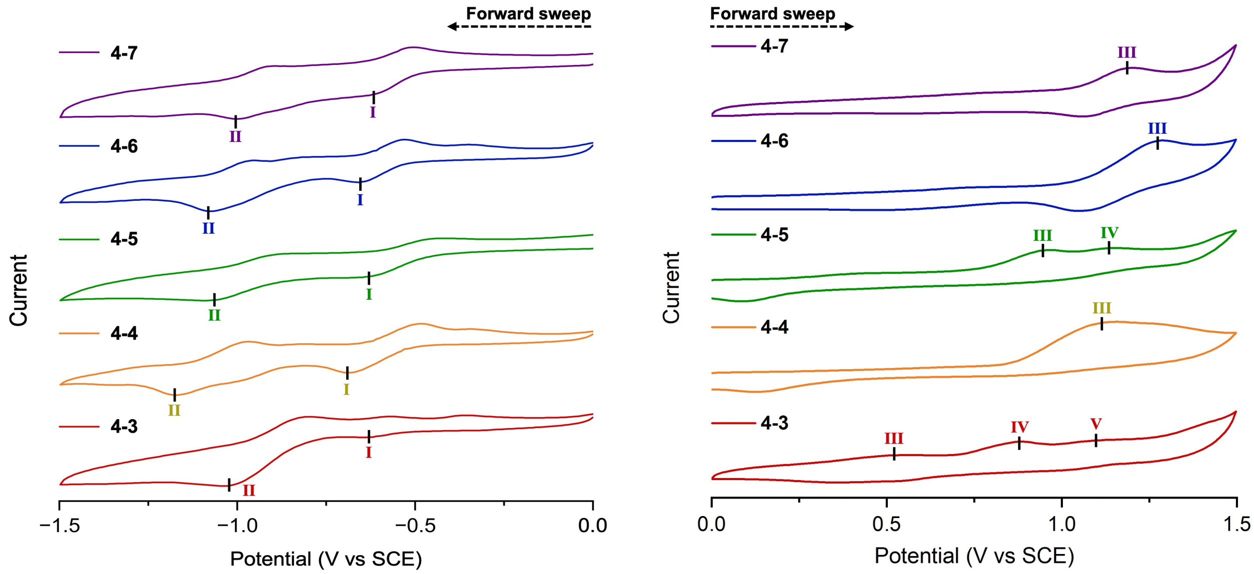

Figure 4.4 *Reduction (left) and oxidation (right) cyclic voltammograms of all amino-derived SiPc compounds recorded in a* 10^{-3} *M solution in o-DCB at 50 mV* s^{-1} *with 0.1 M TBAP as the supporting electrolyte.*

Table 4.1 *Reduction and oxidation half potentials of all monomeric compounds recorded in a 10^{-3} M solution in o-DCB at 50 mV s^{-1} with 0.1 M TBAP as the supporting electrolyte. The reduction and oxidation half potentials are ordered using roman numerals for each individual material as depicted in Figure 4.3.*

Complex	Reduction Potential[a] (V)		Oxidation Potential[b] (V)		
	I	**II**	**III**	**IV**	**V**
4-3	-0.63	-1.03	+0.54	+0.88	+1.10
4-4	-0.69	-1.17	+1.15	-	-
4-5	-0.63	-1.05	+0.96	+1.15	-
4-6	-0.65	-1.08	+1.28	-	-
4-7	-0.62	-1.00	+1.20	-	-

[a] Reduction potentials are obtained from the forward sweep of the reduction voltage range [0 to -1.5] V

[b] Oxidation potentials are obtained from the forward sweep of the oxidation voltage range [0 to +1.5] V

4.2.4 Electropolymerization

To probe the potential for creating thin-films, oxidative polymerization was carried out *via* cyclic voltammetry (CV). CV was performed with the same conditions used during the characterization process with the glassy carbon working electrode. The CV spectra (**Figure 4.5**) reveal a slight positive shift of the anodic peak (situated near 1.0 V) corresponding to the oxidation of the amino group for compounds **4-3** and **4-5**, suggesting the formation of a polymeric film.[28] Once the CV process is completed, both materials formed a vibrant blue film on the ITO coated glass. Furthermore, an increase in the current amplitude for compounds **4-3** and **4-5** is apparent in the CV spectra, suggesting a rise in conductivity and electroactive surface area as the polymeric film is deposited onto the ITO glass. Upon inspection of the CV spectra for **4-6** and **4-7**, a similar increase in the current amplitude in both the oxidation and reduction sweeps is observed as the CV cycling progresses, however these derivatives did not form any polymeric films as evidenced by the solid-state absorption of the UV-Vis-NIR spectra (**Figure 4.5**). The observed increase in current amplitude may arise from several factors, including an enhanced double-layer capacitance at the electrode surface, irreversible oxidation of monomers in solution or adsorption of monomeric species onto the electrode, which can modify interfacial charge-transfer processes. [39] The quasi-reversible process is also apparent when the CV is run with the ITO coated glass (similar to what was observed with the glassy carbon electrode), which could also compromise the polymerization. The stabilization of the radical cation through resonance with the benzoate group is hypothesized to be responsible for the absence of polymer formation. Moreover, the larger size of the benzoate groups in comparison to the phenoxyl derivatives could also contribute to steric hindrance between the monomers, serving as another factor that could have come in play and have an effect on the lack of polymerization for these materials. The concentration of radical cations formed in solution with the increased number of scans causes the current elevation, however the inherent stability of the radical cation is insufficient to catalyse the polymerization.[38] This can be further argued with the fact that the anodic peak does not undergo any positive voltage shift with the increased number of scans. To further analyze the polymerization process, solid-state UV-Vis-NIR (**Figure 4.6**) and solution spectroelectrochemistry (**Figure A.4.11** of Section 4.5 Appendix) were performed. The UV-Vis-NIR spectra of the resulting ITO glass after CV show remnants of the monomer for **4-4**, **4-6**, and **4-7** through the small peak that appears near the Q band maximal absorption near 690 nm. For **4-3** and **4-5**, although this same peak is also apparent, a much broader and intense peak takes shape in the 850-900 nm range, a result of polymer formation.

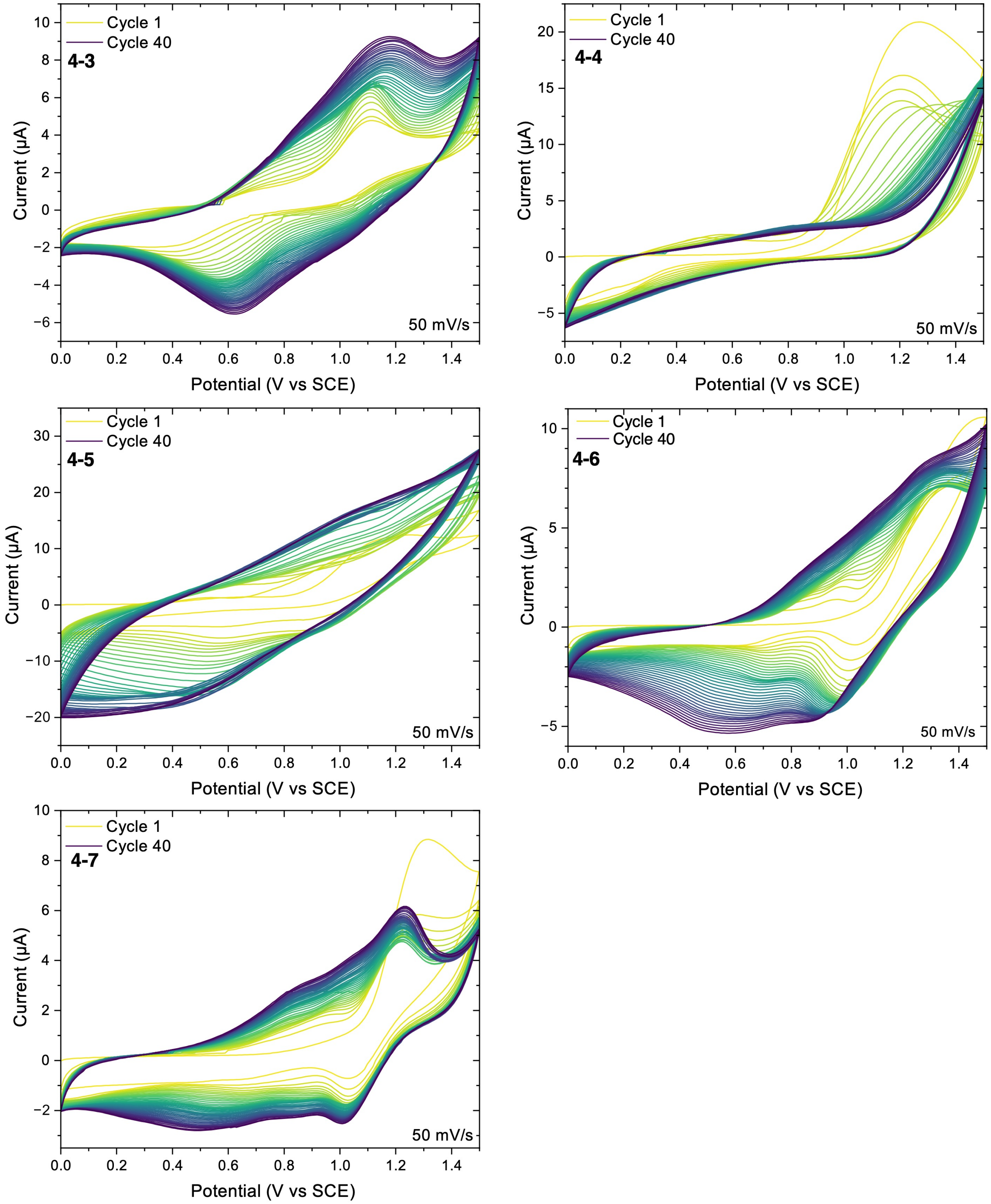

Figure 4.5 *Cyclic voltammograms of* ***a)*** *compound 4-3,* ***b)*** *compound 4-4,* ***c)*** *compound 4-5,* ***d)*** *compound 4-6 and* ***e)*** *compound 4-7. All CV graphs were collected from a* 10^{-3} *M solution in o-DCB with 0.1 M TBAP in from [0 to 1.5] V at a scan rate of 50 mV* s^{-1} *repeated for 40 cycles.*

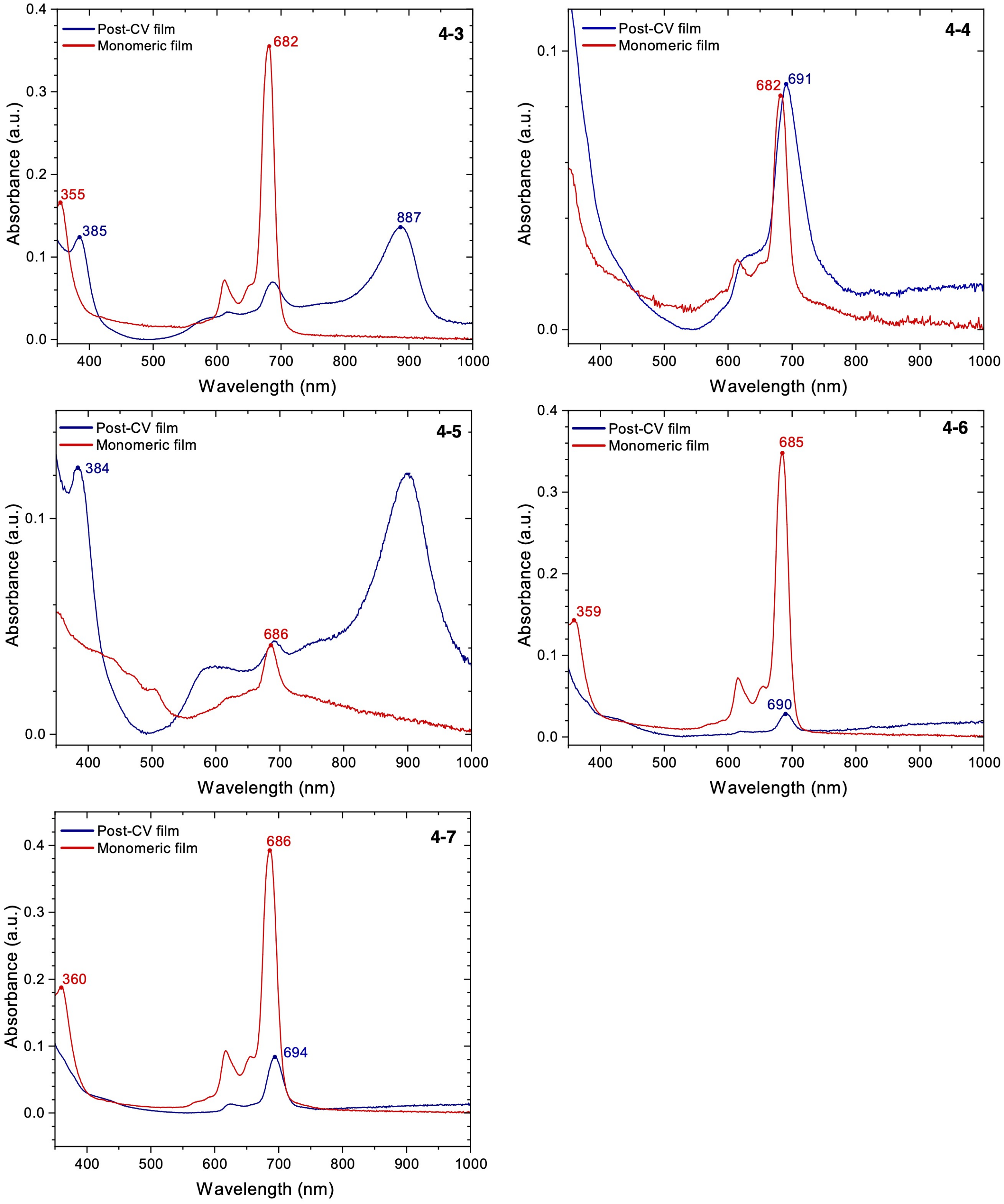

Figure 4.6 *Solid-state UV-Vis-NIR spectra of compounds 4-3, 4-4, 4-5, 4-6 and 4-7 in their monomeric form (red) by drop casting a 10^{-3} M solution onto a glass slide and from the film present on ITO glass post-CV (blue) after running 40 scans from [0 to +1.5] V.*

4.2.5 Spectroelectrochemistry

To probe the effects of the applied voltage on the optical properties of these materials, spectroelectrochemical analysis was conducted in solution with dichloromethane (DCM) and TBAP at a concentration of 0.1 M as the supporting electrolyte (**Figure A.4.11** of Section 4.5 Appendix) using chronoamperometry (CA) as the electrochemical technique. For all five materials, two reduction potentials and one oxidation potential were applied (reflecting the reduction and oxidation voltages that were recorded by cyclic voltammetry using the glassy carbon as the working electrode, i.e. **Table 4.1**). This allows to see how the applied voltage alters the optical absorption behaviour of each material. Furthermore, the reversibility of the absorption profiles can be used as an indicator to evaluate if any material has undergone a structural change during the chronoamperometric process, allowing to better evaluate whether the electropolymerization occurred or not. All compounds, apart from **4-3**, showed signs of dimerization after the first applied reduction potential, an effect that became even more prominent for all materials at the second reduction potential. Dimerization is a common effect observed for phthalocyanine molecules and can be readily distinguished by the reduction of the maximal Q band peak, followed by the appearance of a new absorption peak around 580 nm, and is reversible once the voltage potential is stopped.[40] The reversibility observed in the optical spectra after the duration of the applied voltage also serves as an additional indicator that the electrochemical effects were not permanent, thus excluding the possibility for electropolymerization through the formation of the phenazine bridge. For each derivatives, a small rise in absorbance between 800-850 nm was observed upon applying the second reduction potential, as well as a decrease in absorbance in the B band region. The oxidation spectroelectrochemical spectra for all five amino-derived compounds can be seen in **Figure 4.7**. Upon exposure to the oxidation potential, **4-4**, **4-6** and **4-7** did not seem to undergo a significant spectral change. They were subject to a small decrease in the Q and B band regions, all of which were fully reversible once the applied voltage was terminated, suggesting that none of these compounds underwent a permanent structural change. As for **4-3** and **4-5**, a decrease and shift of the Q band were observed upon exposure to the oxidation potential. **4-3** underwent a bathochromic broadening of the Q band shoulder, whereas **4-5** underwent a hypsochromic shift of the Q band peak. **4-5** also showed a decrease in absorbance in the 460-515 nm range, followed by an increase in absorbance in the 515-610 nm range. Additionally, both materials underwent a small decrease in absorbance in the B band region. These changes were sustained for both **4-3** and **4-5** after termination of the applied voltage, further indicating that they are a consequent effect of the electropolymerization process.

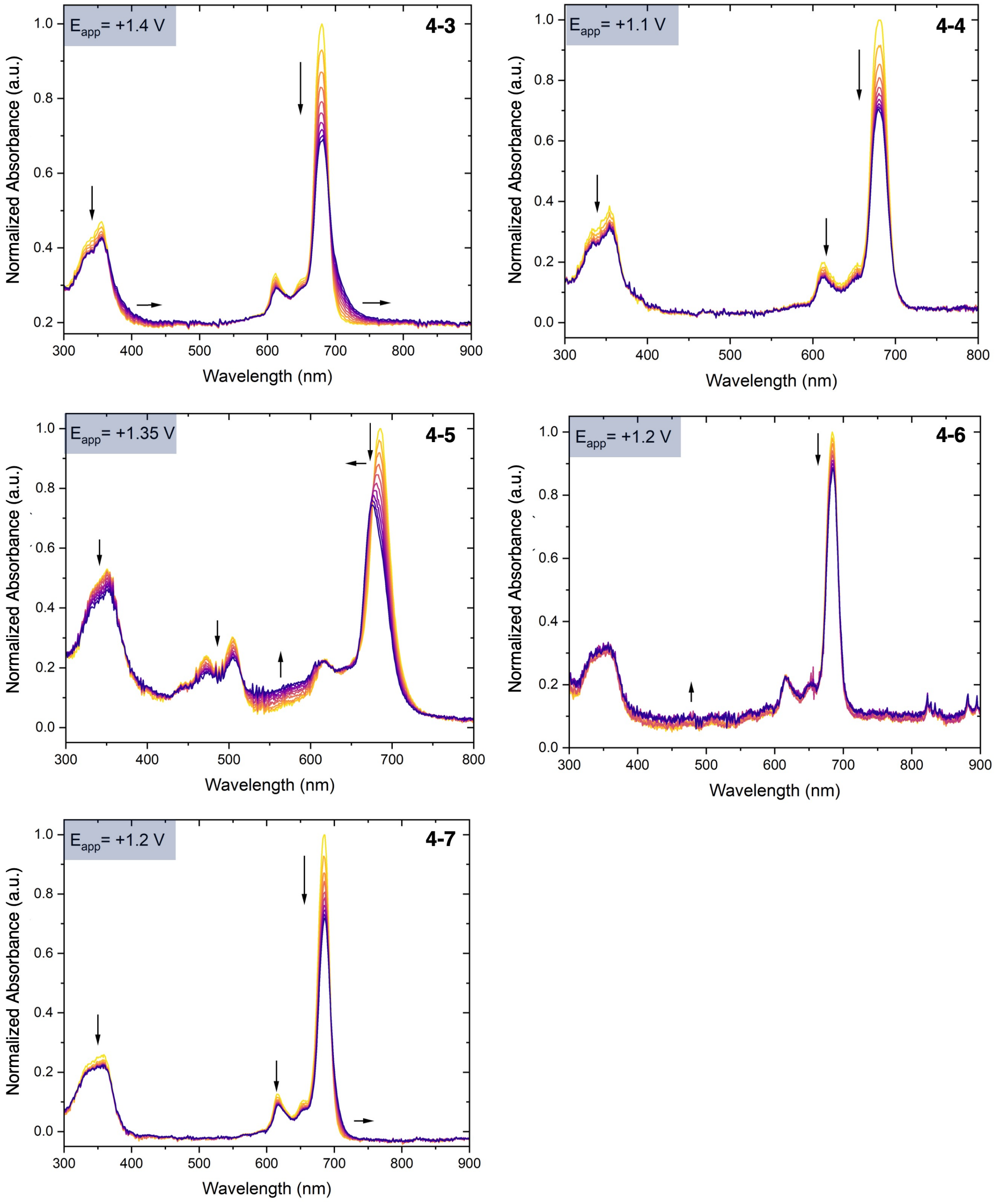

Figure 4.7 *Oxidation spectroelectrochemical spectra of all amino-derived SiPc compounds in a* 10^{-3} *M solution in DCM using 0.1 M TBAP as the supporting electrolyte. Spectroelectrochemical analysis was carried out using a Pt mesh, Pt wire, and Ag/AgCl as the working, counter, and reference electrodes, respectively, at the designated applied voltage (*E_{app}*) .*

4.3 Conclusion

In conclusion, five novel amino-derived SiPcs were successfully synthesized and characterized in a simple two-step manner. UV-Vis-NIR characterization clearly depicts the standard optical nature of the phthalocyanine by its strong Q and B bands, and also shows small subtle effects from having either electron donating phenoxyl or electron withdrawing benzoate groups as axial linkers to the Pc core. Cyclic voltammetry was conducted for all five materials to evaluate their potential for electropolymerization catalyzed through the axial aminophenyl groups. Post-CV optical analysis confirms successful polymerization was achieved for the *para* and *ortho*-substituted bis(aminophenoxy) SiPcs (**4-3** and **4-5**). Supplementary spectroelectrochemical analysis was done on all five materials, where irreversible changes in the absorbance spectra were observed for **4-3** and **4-5** after applying the oxidation potential corresponding to the amine oxidation, further confirming that polymerization occurred. On the other hand, the *meta*-substituted bis(aminophenoxy) SiPcs as well as the *para* and *meta*-substituted bis(aminobenzoate)SiPcs did not produce any polymeric films, likely due to quenching of the amino radical cation or stabilization of the radical cation through resonance with the benzoate group. Overall, this study confirms that axially substituted amino SiPcs are viable materials for electropolymerization opening the door for their use in a variety of thin-film applications.

4.4 Experimental

4.4.1 Materials

All solvents used for synthesis were ACS grade and used without any further purification. Diiminoisoindoline (98%) was purchased from Ambeed Inc. and used as received. $SiCl_4$ (99%) was purchased from Sigma-Aldrich Chemical Company and used as received. *Para*, *meta*, and *ortho*-aminophenols (98%) were purchased from Oakwood Chemicals and used as received. *Para*-aminobenzoic acid (99%) was purchased from Alfa Aesar and *meta*-aminobenzoic acid (98%) was purchased from Sigma-Aldrich Chemical Company. Dichlorosilicon phthalocyanine (Cl_2-SiPc) was synthesized as described in the literature.[31] ITO coated glass was purchased from Solems, France (9 mm diameter of active surface, 8-12 Ω of square resistance). NMR spectra were recorded in DMSO-D_6 mixtures at room temperature on a Bruker Advance 600 MHz spectrometer, and spectra were referenced to the deuterated solvent peak at 2.50 ppm for proton NMR. HPLC spectra were recorded using a Waters e2695 separation module equipped with a Symmetry C18 reverse phase column and a Waters 2998 PDA detector; all samples were run in

100% DMF for a total run time of 3 minutes. IR spectra were recorded on an Agilent Technologies Cary 630 Fourier Transform Infrared (FT-IR) spectrometer.

4.4.2 Synthesis of bis(4-aminophenoxy)silicon phthalocyanine ((4-NH_2PhO)$_2$SiPc; 4-3)

In a 2-neck round bottom flask under argon atmosphere, Cl_2-SiPc (0.50 g, 0.82 mmol) was mixed with 4-aminophenol (0.54 g, 4.91 mmol) in 30 mL of anhydrous chlorobenzene. After stirring the reaction mixture at 132 °C for 24 h, it was cooled to room temperature, transferred to a separatory funnel with 150 mL sat. $NaHCO_3$ and shaken vigorously until no more gas formation occurred, then filtered through a Büchner funnel. The crude solid was subsequently sonicated and filtered sequentially with H_2O (200 mL), MeOH (200 mL), and acetone (200 mL). The resulting matte indigo solid was dried in an oven at 100 °C for 2 hours to recover a purple microcrystalline powder (0.52 g, 84% yield) and recrystallized using a DMF/MeOH mixture to recover a single crystal. ^{1}H NMR (400 MHz, DMSO-d6) δ (ppm): 9.73-9.69 (m, 8H), 8.58-8.53 (m, 8H), 4.82 (d, J = 8 Hz, 4H), 3.70 (s, NH_2), 2.03 (d, J = 8 Hz, 4H). MS (ESI-TOF) m/z: [M]+ calcd. for $C_{44}H_{28}N_{10}O_2Si$: 756.86; Found: 757.15. IR v (cm^{-1}) = 3446 (s, N-H stretch), 3354 (s, N-H stretch), 1505 (d, N-H bend), 1246 (s, C-N stretch), 760 (s, N-H wag). UV-Vis-NIR (CH_2Cl_2) λ_{max} = 680 nm.

4.4.3 Synthesis of bis(3-aminophenoxy)silicon phthalocyanine ((3-NH_2PhO)$_2$SiPc; 4-4)

(3-NH_2PhO)$_2$SiPc was synthesized in a similar procedure to **4-3** using 3-aminophenol (0.54 g, 4.91 mmol) as the phenol reagent. Title product was obtained as a purple microcrystalline powder (0.45 g, 73% yield). ^{1}H NMR (400 MHz, DMSO-d6) δ (ppm): 9.67-9.61 (m, 8H), 8.50-8.44 (m, 8H), 5.12 (t, J = 4 and 16 Hz, 2H), 4.83 (d, J = 8 Hz, 2H), 3.61 (s, NH_2), 1.67 (s, 2H), 1.33 (d, J = 8 Hz, 2H). MS (ESI-TOF) m/z: [M]+ calcd. for $C_{44}H_{28}N_{10}O_2Si$: 756.86; Found: 755.17. IR v (cm^{-1}) = 3449 (s, N-H stretch), 3377 (s, N-H stretch), 1582 (d, N-H bend), 1334 (s, C-N stretch), 759 (s, N-H wag). UV-Vis-NIR (CH_2Cl_2) λ_{max} = 681 nm.

4.4.4 Synthesis of bis(2-aminophenoxy)silicon phthalocyanine ((2-NH_2PhO)$_2$SiPc; 4-5)

(2-NH_2PhO)$_2$SiPc was synthesized in a similar procedure to **4-3** using 2-aminophenol (0.54 g, 4.91 mmol) as the phenol reagent and 1,8-Diazabicyclo[5.4.0]undec-7-ene (10 drops) was used as the catalytic base. Title product was obtained as a purple microcrystalline powder (0.47 g, 76% yield). ^{1}H NMR (400 MHz, DMSO-d6) δ (ppm): 9.62-9.59 (m, 8H), 8.46-8.43 (m, 8H), 5.33 (t, J =

8 and 16 Hz, 2H), 4.98 (d, J = 8 Hz, 2H), 4.73 (t, J = 8 and 16 Hz, 2H), 4.42 (s, NH_2), 1.61 (d, J = 8 Hz, 2H). MS (ESI-TOF) m/z: [M]+ calcd. for $C_{44}H_{28}N_{10}O_2Si$: 756.86; Found: 757.17. IR v (cm^{-1}) = 3469 (s, N-H stretch), 3424 (s, N-H stretch), 1607 (d, N-H bend), 1290 (s, C-N stretch), 761 (s, N-H wag). UV-Vis-NIR (CH_2Cl_2) λ_{max} = 685 nm.

4.4.5 Synthesis of bis(4-aminobenzoate)silicon phthalocyanine ((4-NH₂PhCOO)₂SiPc; 4-6)

(4-$NH_2PhCOO)_2$SiPc was synthesized in a similar procedure to **4-3** using 4-aminobenzoic acid (1.0 g, 1.64 mmol) as the benzoic acid reagent. Title product was obtained as a matte blue powder (1.0 g, 75 % yield). Product was recrystallized using a DMF/MeOH mixture to recover single crystal. ^{1}H NMR (400 MHz, DMSO-d6) δ (ppm): 9.76-9.69 (m, 8H), 8.61-8.52 (m, 8H), 5.38 (d, 4H), 5.20 (s, 4H), 4.63 (s, NH_2). MS (ESI-TOF) m/z: [M]+ calcd. for $C_{46}H_{28}N_{10}O_4Si$: 812.89; Found: 813.11. IR v (cm^{-1}) = 3481 (s, N-H stretch), 3366 (s, N-H stretch), 1617 (d, N-H bend), 1280 (s, C-N stretch), 760 (s, N-H wag).UV-Vis-NIR (CH_2Cl_2) λ_{max} = 684 nm.

4.4.6 Synthesis of bis(3-aminobenzoate)silicon phthalocyanine ((3-NH₂PhCOO)₂SiPc; 4-7)

(3-$NH_2PhCOO)_2$SiPc was synthesized in a similar procedure to **2a** using 3-aminobenzoic acid (0.67 g, 4.91 mmol) as the benzoic acid reagent. Title product was obtained as a matte blue powder (0.54 g, 81% yield). Product was recrystallized using a DMF/MeOH mixture to recover single crystal. ^{1}H NMR (400 MHz, DMSO-d6) δ (ppm): 9.78-9.66 (m, 8H), 8.61-8.52 (m, 8H), 5.82 (s, 2H), 5.30 (s, 2H), 4.56 (s, 2H), 4.35 (s, 2H), 3.71 (s, NH_2). MS (ESI-TOF) m/z: [M]+ calcd. for $C_{46}H_{28}N_{10}O_4Si$: 812.88; Found: 813.17. IR v (cm^{-1}) = 3459 (s, N-H stretch), 3371 (s, N-H stretch), 1609 (d, N-H bend), 1289 (s, C-N stretch), 763 (s, N-H wag). UV-Vis-NIR (CH_2Cl_2) λ_{max} = 685 nm.

4.4.7 Single Crystal Data Collection

Single crystal data were collected on a Bruker Kappa APEX-DUO diffractometer using CuKα radiation from an Incoatec IμS source with multi-layer optics and a PHOTON II CMOS detector and were measured using a combination of ϕ scans and ω scans. The data were processed using APEX4 (Bruker, 2022). Absorption corrections were carried out using SADABS (Krause et al., 2015).[41] The structures were solved with SHELXT (Sheldrick, 2015a)[42] and refined using SHELXL-2019 (Sheldrick, 2015b)[43] for full-matrix least-squares refinement that was based on F^2. H atoms bonded to C and N atoms were included in calculated positions and allowed to refine in riding-motion approximation with U~iso~ tied to the carrier atom.

4.4.8 Optoelectronic Characterization

The UV-Vis-NIR spectra were measured using an Agilent Technologies Cary 6000*i* UV-Vis-NIR spectrophotometer. Absorbance measurements were collected at ambient temperature in solution with DCM within the range of 250-800 nm. The UV-Vis-NIR spectra of the electropolymerized thin-films deposited on ITO glass substrates were measured using an Agilent Technologies Cary 60 UV-Vis-NIR spectrophotometer within the range of 350-1000 nm.

4.4.9 Electrochemical Characterization

All electrochemical measurements (polymer characterization and deposition) were performed using a PalmSens3 potentiostat/galvanostat equipped with PSTrace software. The measurements were recorded in a glass cell using glassy carbon, platinum wire, and SCE as the working, counter, and reference electrodes, respectively. Each material was collected in a *o*-DCB solution at approximately 10^{-1} M concentration with 0.1 M of TBAP as the supporting electrolyte. Solutions were heated and sonicated, then brought to room temperature and passed through a 0.45 μm PTFE syringe filter to remove any undissolved particulates. The solutions were then degassed with nitrogen for 10 minutes prior to the collection of the spectra. All spectra were collected at a step potential of 0.005 V and a scan rate of 50 mV s^{-1} in the range of [0 to -1.5] V for the reduction sweep and [0 to +1.5] V for the oxidation sweep. Electropolymerization was performed in the conditions described above, however changing the working electrode for ITO, which was sonicated sequentially in acetone and DCM then wiped with a Kimwipe to remove any dirt or dust particles from the glass. Before recording the electrochemical measurements of the target system, blank scans were conducted in solvent and supporting electrolyte only, in order to assess electrode cleanliness and exclude the presence of residual electroactive species. The electropolymerization was completed by doing a cyclic potential sweep from [0 to +1.5] V for a total of 40 cycles. After polymerization, the films were rinsed in DCM to remove any excess solvent, unreacted monomer, and electrolyte, then dried for 2-3 hours under fume hood airflow in laboratory ambient conditions (T = 22 ± 1 °C, avg. 30-40 % humidity).

4.4.10 Spectroelectrochemical Characterization

Spectroelectrochemical measurements were performed using a PalmSens potentiostat/galvanostat equipped with PSTrace software and a Cary 60 UV-Vis-NIR spectrophotometer within the range of 300-900 nm. A three-electrode system was used within a quartz thin layer cell of 0.1 cm internal optical path length. A platinum minigrid was used as the working electrode, in the presence of a small Ag/AgCl reference electrode and a platinum auxiliary electrode. All measurements were performed using a 10^{-3} M solution of the respective amino-derived SiPc material in DCM with 0.1 M TPAB as the supporting electrolyte. All solutions were sonicated for 10 min, passed through a 0.45 μm syringe filter, and degassed with N_2 for 5 min prior to collecting the spectroelectrochemical measurements. The applied voltage potentials (indicated in blue in **Figure 4.6**) for compounds **4-4**, **4-6** and **4-7** are selected uniquely for each individual material to reflect the oxidation voltage of the amino group. The applied voltage potentials for compounds **4-3** and **4-5** are selected at a slightly higher voltage to better observe the spectral changes undergone during the electropolymerization process of the materials.

4.5 Appendix

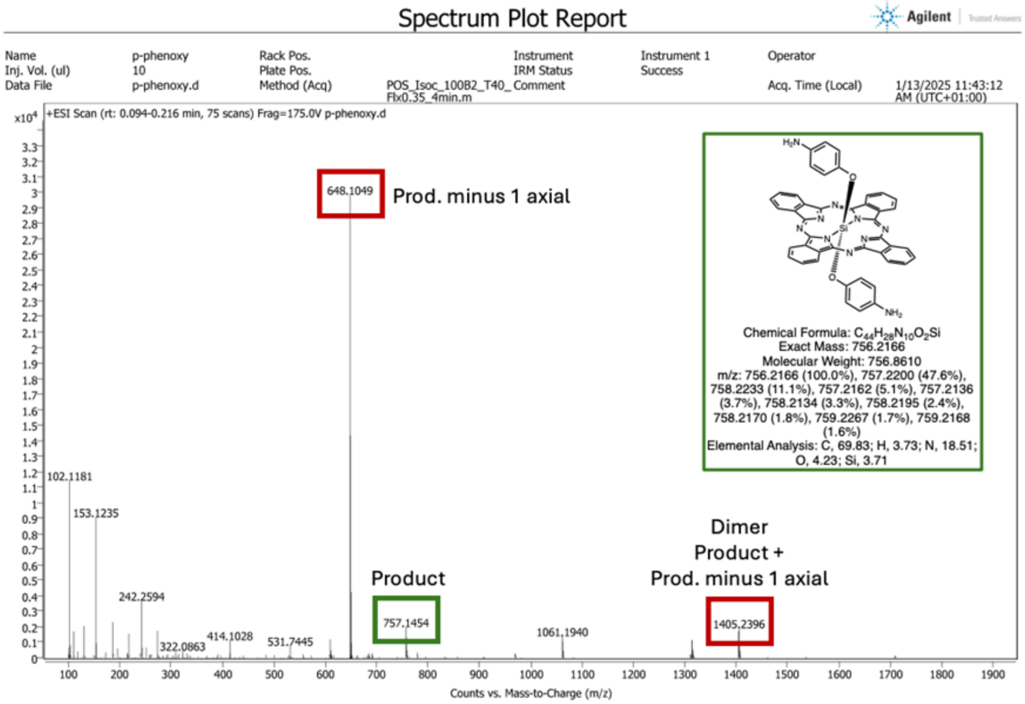

Spectrum Plot Report

Name p-phenoxy
Inj. Vol. (ul) 10
Data File p-phenoxy.d
Rack Pos.
Plate Pos.
Method (Acq) POS_Isoc_100B2_T40_Flx0.35_4min.m
Instrument Instrument 1
IRM Status Success
Comment
Operator
Acq. Time (Local) 1/13/2025 11:43:12 AM (UTC+01:00)

+ESI Scan (rt: 0.094-0.216 min, 75 scans) Frag=175.0V p-phenoxy.d

Chemical Formula: $C_{44}H_{28}N_{10}O_2Si$
Exact Mass: 756.2166
Molecular Weight: 756.8610
m/z: 756.2166 (100.0%), 757.2200 (47.6%), 758.2233 (11.1%), 757.2162 (5.1%), 757.2136 (3.7%), 758.2134 (3.3%), 758.2195 (2.4%), 758.2170 (1.8%), 759.2267 (1.7%), 759.2168 (1.6%)
Elemental Analysis: C, 69.83; H, 3.73; N, 18.51; O, 4.23; Si, 3.71

Figure A.4.1 *Electrospray Ionization (ESI) high-resolution mass spectrum of compound 4-3.*

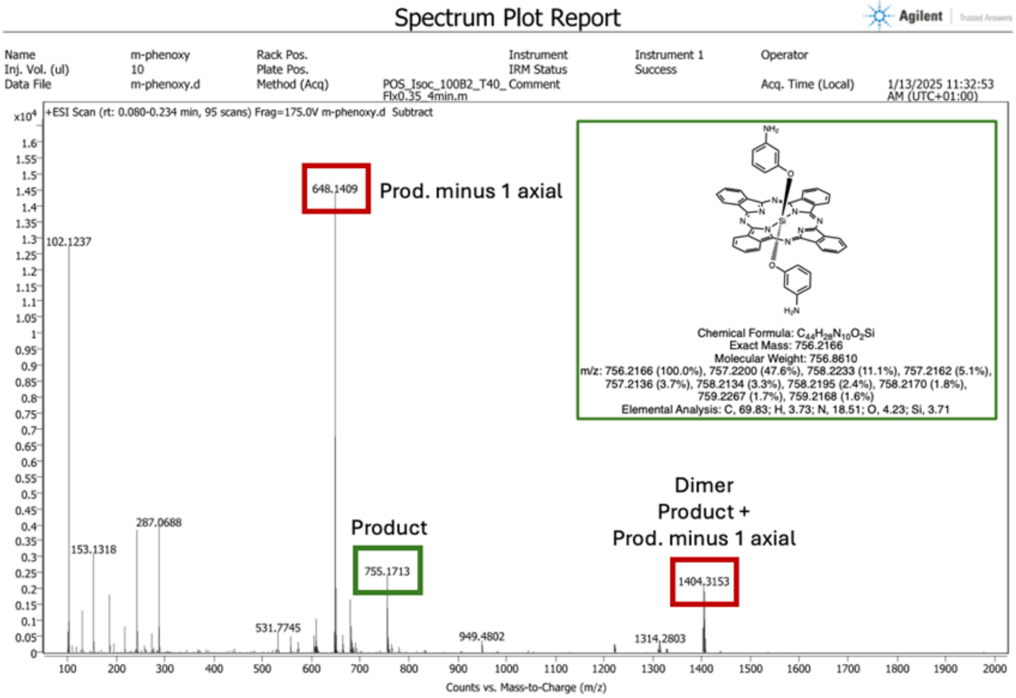

Spectrum Plot Report

Name m-phenoxy
Inj. Vol. (ul) 10
Data File m-phenoxy.d
Rack Pos.
Plate Pos.
Method (Acq) POS_Isoc_100B2_T40_Flx0.35_4min.m
Instrument Instrument 1
IRM Status Success
Comment
Operator
Acq. Time (Local) 1/13/2025 11:32:53 AM (UTC+01:00)

+ESI Scan (rt: 0.080-0.234 min, 95 scans) Frag=175.0V m-phenoxy.d Subtract

Chemical Formula: $C_{44}H_{28}N_{10}O_2Si$
Exact Mass: 756.2166
Molecular Weight: 756.8610
m/z: 756.2166 (100.0%), 757.2200 (47.6%), 758.2233 (11.1%), 757.2162 (5.1%), 757.2136 (3.7%), 758.2134 (3.3%), 758.2195 (2.4%), 758.2170 (1.8%), 759.2267 (1.7%), 759.2168 (1.6%)
Elemental Analysis: C, 69.83; H, 3.73; N, 18.51; O, 4.23; Si, 3.71

Figure A.4.2 *Electrospray Ionization (ESI) high-resolution mass spectrum of compound 4-4.*

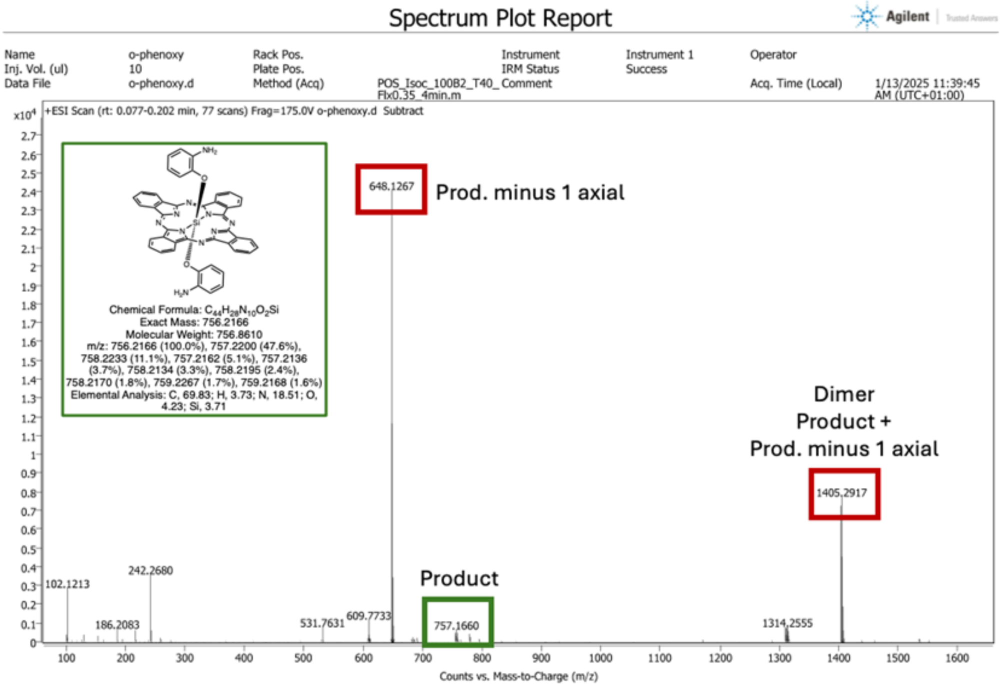

Spectrum Plot Report

Name o-phenoxy
Inj. Vol. (ul) 10
Data File o-phenoxy.d
Rack Pos.
Plate Pos.
Method (Acq) POS_Isoc_100B2_T40_Flx0.35_4min.m
Instrument Instrument 1
IRM Status Success
Comment
Operator
Acq. Time (Local) 1/13/2025 11:39:45 AM (UTC+01:00)

+ESI Scan (rt: 0.077-0.202 min, 77 scans) Frag=175.0V o-phenoxy.d Subtract

Chemical Formula: $C_{44}H_{28}N_{10}O_2Si$
Exact Mass: 756.2166
Molecular Weight: 756.8610
m/z: 756.2166 (100.0%), 757.2200 (47.6%), 758.2233 (11.1%), 757.2162 (5.1%), 757.2136 (3.7%), 758.2134 (3.3%), 758.2195 (2.4%), 758.2170 (1.8%), 759.2267 (1.7%), 759.2168 (1.6%)
Elemental Analysis: C, 69.83; H, 3.73; N, 18.51; O, 4.23; Si, 3.71

Figure A.4.3 *Electrospray Ionization (ESI) high-resolution mass spectrum of compound 4-5.*

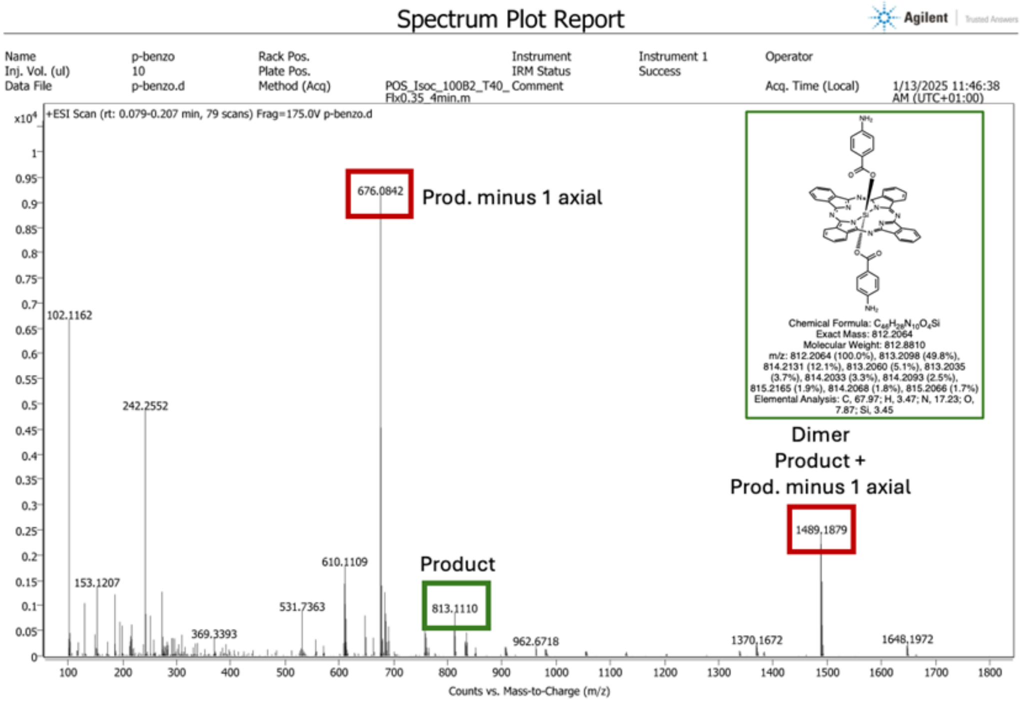

Spectrum Plot Report

Name p-benzo
Inj. Vol. (ul) 10
Data File p-benzo.d
Rack Pos.
Plate Pos.
Method (Acq) POS_Isoc_100B2_T40_Flx0.35_4min.m
Instrument Instrument 1
IRM Status Success
Comment
Operator
Acq. Time (Local) 1/13/2025 11:46:38 AM (UTC+01:00)

+ESI Scan (rt: 0.079-0.207 min, 79 scans) Frag=175.0V p-benzo.d

Chemical Formula: $C_{46}H_{28}N_{10}O_4Si$
Exact Mass: 812.2064
Molecular Weight: 812.8810
m/z: 812.2064 (100.0%), 813.2098 (49.8%), 814.2131 (12.1%), 813.2060 (5.1%), 813.2035 (3.7%), 814.2033 (3.3%), 814.2093 (2.5%), 815.2165 (1.9%), 814.2068 (1.8%), 815.2066 (1.7%)
Elemental Analysis: C, 67.97; H, 3.47; N, 17.23; O, 7.87; Si, 3.45

Figure A.4.4 *Electrospray Ionization (ESI) high-resolution mass spectrum of compound 4-6.*

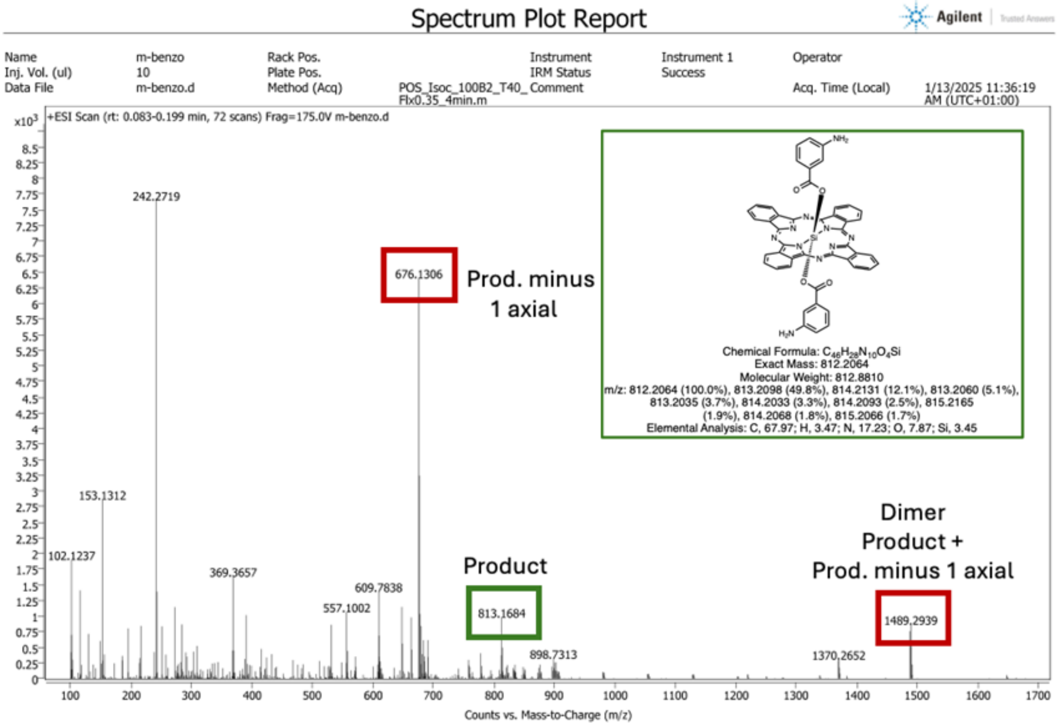

Spectrum Plot Report

Name m-benzo
Inj. Vol. (ul) 10
Data File m-benzo.d
Rack Pos.
Plate Pos.
Method (Acq) POS_Isoc_100B2_T40_Flx0.35_4min.m
Instrument Instrument 1
IRM Status Success
Comment
Operator
Acq. Time (Local) 1/13/2025 11:36:19 AM (UTC+01:00)

+ESI Scan (rt: 0.083-0.199 min, 72 scans) Frag=175.0V m-benzo.d

Chemical Formula: $C_{46}H_{28}N_{10}O_4Si$
Exact Mass: 812.2064
Molecular Weight: 812.8810
m/z: 812.2064 (100.0%), 813.2098 (49.8%), 814.2131 (12.1%), 813.2060 (5.1%), 813.2035 (3.7%), 814.2033 (3.3%), 814.2093 (2.5%), 815.2165 (1.9%), 814.2068 (1.8%), 815.2066 (1.7%)
Elemental Analysis: C, 67.97; H, 3.47; N, 17.23; O, 7.87; Si, 3.45

Figure A.4.5 *Electrospray Ionization (ESI) high-resolution mass spectrum of compound 4-7.*

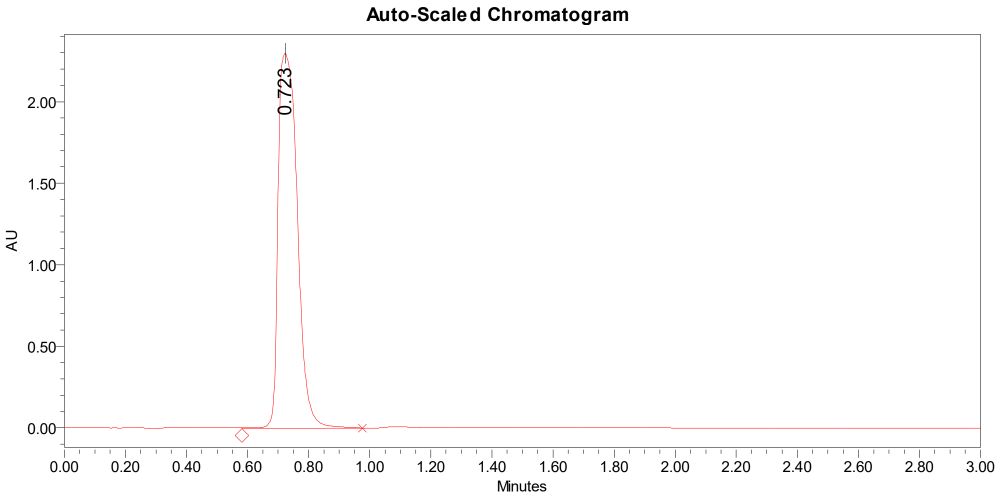

Processed Channel: 2998 Ch1 677nm@4.8nm

	Processed Channel	Retention Time (min)	Area	% Area	Height
1	2998 Ch1 677nm@4.8nm	0.723	10050139	100.00	2300364

Figure A.4.6 *High-Performance Liquid Chromatography (HPLC) spectrum with UV-Vis-NIR detector of 4-3.*

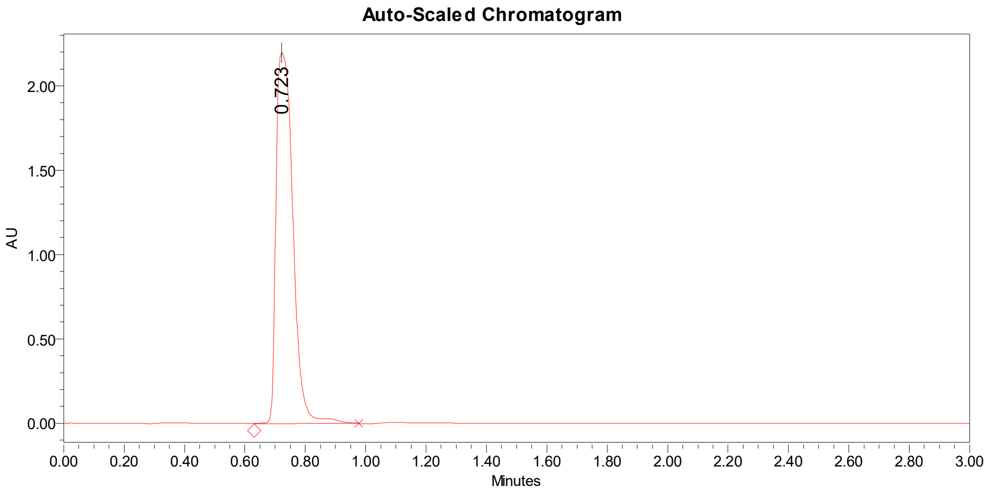

Processed Channel: 2998 Ch1 677nm@4.8nm

	Processed Channel	Retention Time (min)	Area	% Area	Height
1	2998 Ch1 677nm@4.8nm	0.723	8566891	100.00	2200139

Figure A.4.7 *High-Performance Liquid Chromatography (HPLC) spectrum with UV-Vis-NIR detector of 4-4.*

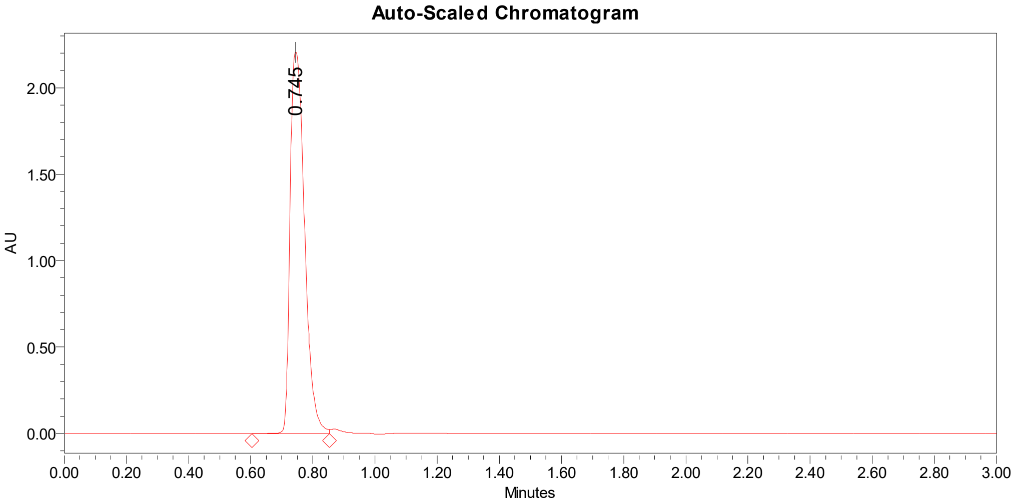

Processed Channel: 2998 Ch1 677nm@4.8nm

	Processed Channel	Retention Time (min)	Area	% Area	Height
1	2998 Ch1 677nm@4.8nm	0.745	7147166	100.00	2205579

Figure A.4.8 *High-Performance Liquid Chromatography (HPLC) spectrum with UV-Vis-NIR detector of 4-5.*

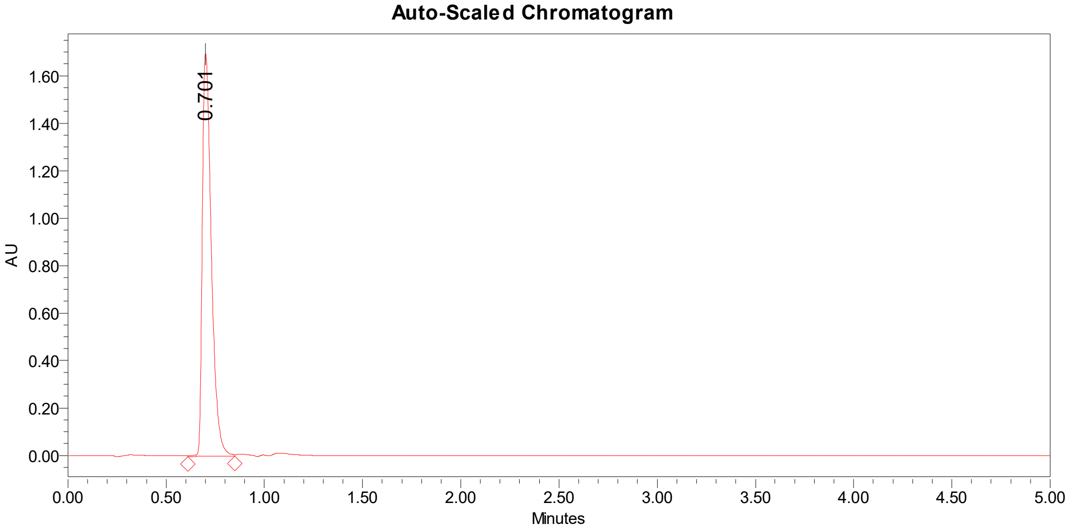

Processed Channel: 2998 Ch1 677nm@4.8nm

	Processed Channel	Retention Time (min)	Area	% Area	Height
1	2998 Ch1 677nm@4.8nm	0.701	5462363	100.00	1696444

Figure A.4.9 *High-Performance Liquid Chromatography (HPLC) spectrum with UV-Vis-NIR detector of 4-6.*

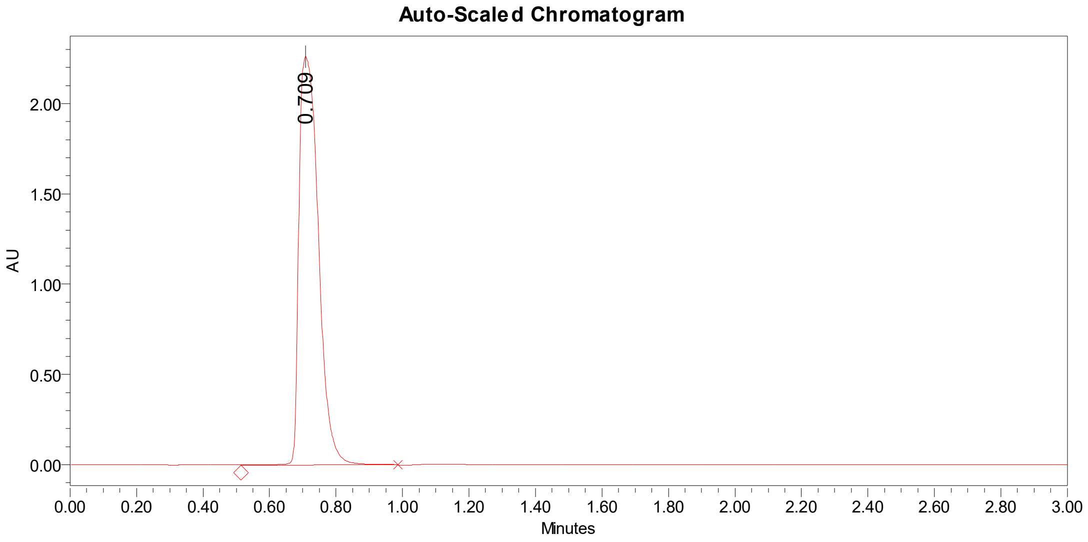

Processed Channel: 2998 Ch1 677nm@4.8nm

	Processed Channel	Retention Time (min)	Area	% Area	Height
1	2998 Ch1 677nm@4.8nm	0.709	9181398	100.00	2261491

Figure A.4.10 *High-Performance Liquid Chromatography (HPLC) spectrum with UV-Vis-NIR detector of 4-7.*

Table A.4.1 *Crystallographic table of compounds 4-3, 4-6 and 4-7.*

Compound	bis(4-aminophenoxy)silicon phthalocyanine (**4-3**) CCDC#2477678	bis(4-aminobenzoate)silicon phthalocyanine (**4-6**) CCDC#2477788	bis(3-aminobenzoate)silicon phthalocyanine (**4-7**) CCDC#2478577
Formula	C44 H28 N10 O2 Si, 2(C3 H7 N O)	C46 H28 N10 O4 Si, 2(C3 H7 N O)	C46 H28 N10 O4 Si, 2(C3 H7 N O)
MW	903.04	959.06	959.06
a (Å)	*11.5245(4)*	*11.0896(9)*	*11.3198(6)*
b (Å)	*16.7208(6)*	*13.4934(11)*	*17.4777(9)*
c (Å)	*11.2747(4)*	*16.1026(13)*	*11.5647(6)*
α (°)	90	90	90
β (°)	94.135(2)	104.062(4)	101.885(3)
γ (°)	90	90	90
V (Å^3)	*2166.97(13)*	*2337.3(3)*	*2239.0(2)*
Z	*2*	*2*	*2*
***Dc* (g.cm^{-3})**	*1.384*	*1.363*	*1.423*
Crystal system	monoclinic	monoclinic	monoclinic
Space group	P 21/c	P 21/n	P 21/n
T (K)	150	150	150
Wavelength Mo-Kα (Å)	1.54178	1.54178	1.54178
μ (mm^{-1})	0.995	0.990	1.034
***F* (000)**	*944.0*	*1000.0*	*1000.0*
θ max (°)	66.161	66.403	66.271
h, k, l max	13, 19,13	13,15,19	13,20,13
Reflections collected	3726	4008	3885
Independent reflections	3169	3569	3211
Data completeness	0.983	0.977	0.990
Goodness-of-fit on *F*^{2}	1.081	1.135	1.036
R indices (all data)	R = 0.0367	R = 0.0407	R = 0.0390
	wR2 = 0.1078	wR2 = 0.1282	wR2 = 0.1050

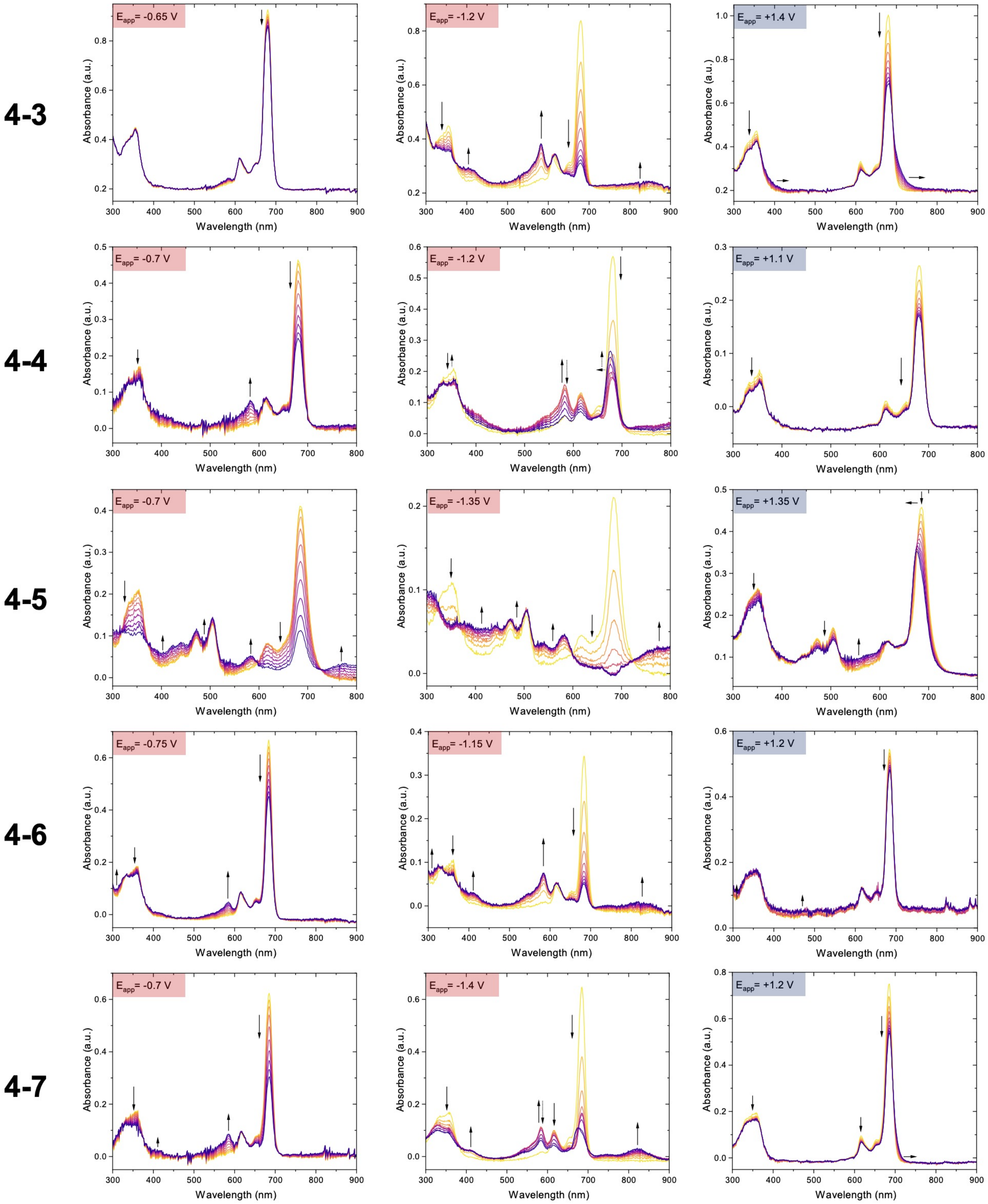

***Figure A.4.11** Spectroelectrochemical spectra of all amino-derived SiPc compounds in a 10^{-3} M DCM solution using 0.1 M TBAP as the supporting electrolyte. Spectroelectrochemical analysis was carried out using a Pt mesh, Pt wire, and Ag/AgCl as the working, counter, and reference electrodes, respectively.*

References

(1) Zhou, W.; Yutronkie, N. J.; Lessard, B. H.; Brusso, J. L. *Mater. Adv.* **2021**, *2* (1), 165.

(2) Melville, O. A.; Lessard, B. H.; Bender, T. P. *ACS Appl. Mater. Interfaces* **2015**, *7* (24), 13105.

(3) Lessard, B. H. *ACS Appl. Mater. Interfaces* **2021**, *13* (27), 31321.

(4) Mitra, K.; Hartman, M. C. T. *Org. Biomol. Chem.* **2021**, *19* (6), 1168.

(5) Hofman, J.-W.; Van Zeeland, F.; Turker, S.; Talsma, H.; Lambrechts, S. A. G.; Sakharov, D. V.; Hennink, W. E.; Van Nostrum, C. F. *J. Med. Chem.* **2007**, *50* (7), 1485.

(6) Gümrükçü Köse, G.; Karaoğlan, G. K.; Erdağ Maden, Y.; Koca, A. *Dyes Pigm.* **2022**, *207*, 110686.

(7) Cranston, R. R.; Vebber, M. C.; Faleiro Berbigier, J.; Brusso, J.; Kelly, T. L.; Lessard, B. H. *Adv. Electron. Mater.* **2022**, *8* (12), 2200696.

(8) Cranston, R. R.; Vebber, M. C.; Berbigier, J. F.; Rice, N. A.; Tonnelé, C.; Comeau, Z. J.; Boileau, N. T.; Brusso, J. L.; Shuhendler, A. J.; Castet, F.; Muccioli, L.; Kelly, T. L.; Lessard, B. H. *ACS Appl. Mater. Interfaces* **2021**, *13* (1), 1008.

(9) Vebber, M. C.; Grant, T. M.; Brusso, J. L.; Lessard, B. H. *Langmuir* **2020**, *36* (10), 2612.

(10) Sundaresan, C.; Vebber, M. C.; Brusso, J. L.; Tao, Y.; Alem, S.; Lessard, B. H. *ACS Omega* **2023**, *8* (1), 1588.

(11) Yutronkie, N. J.; King, B.; Melville, O. A.; Lessard, B. H.; Brusso, J. L. *J. Mater. Chem. C* **2021**, *9* (31), 10119.

(12) Vebber, M. C.; King, B.; French, C.; Tousignant, M.; Ronnasi, B.; Dindault, C.; Wantz, G.; Hirsch, L.; Brusso, J.; Lessard, B. H. *Can. J. Chem. Eng.* **2023**, *101* (6), 3019.

(13) King, B.; Moorthy, S. G.; Lesniewska, E.; Meunier-Prest, R.; Bouvet, M.; Lessard, B. H. *Sens. Actuators B Chem.* **2024**, *408*, 135507.

(14) Comeau, Z. J.; Cranston, R. R.; Lamontagne, H. R.; Harris, C. S.; Shuhendler, A. J.; Lessard, B. H. *Commun. Chem.* **2022**, *5* (1), 178.

(15) Lamontagne, H. R.; Comeau, Z. J.; Cranston, R. R.; Boileau, N. T.; Harris, C. S.; Shuhendler, A. J.; Lessard, B. H. *Sens. Diagn.* **2022**, *1* (6), 1165.

(16) Ivanova, V.; Basova, T.; Klyamer, D.; Sukhikh, A.; Büyükekşi, S. I.; Atilla, D.; Gürek, A. G. *New J. Chem.* **2025**, *49* (20), 8279.

(17) Hu, R.; Yao, B.; Geng, Y.; Zhou, S.; Li, M.; Zhong, W.; Sun, F.; Zhao, H.; Wang, J.; Ge, J.; Wei, R.; Liu, T.; Jin, J.; Xu, J.; Fu, J. *Adv. Mater.* **2024**, *36* (35), 2403111.

(18) Ye, Q.; Yu, H.; Wang, S.; Zhuo, H.; Li, W.; Jin, T.; Feng, L.; Fu, Z.; Liu, Z.; Liu, H.; Chen, W. *ACS Appl. Polym. Mater.* **2025**, *7* (10), 5979.

(19) Liu, Q.; Sun, Q.; Li, H.; Zhang, Y.; Feng, L.; Chen, W.; Chen, Y. *Sens. Actuators B Chem.* **2025**, *428*, 137250.

(20) Ji, W.; Wang, T.-X.; Ding, X.; Lei, S.; Han, B.-H. *Coord. Chem. Rev.* **2021**, *439*, 213875.

(21) Mani, V.; Huang, S.-T.; Devasenathipathy, R.; Yang, T. C. K. *RSC Adv.* **2016**, *6* (44), 38463.

(22) Lokesh, K. S.; Adriaens, A. *Dyes Pigm.* **2015**, *112*, 192.

(23) Li, Z.; Zhou, S. *IEEE J. Electron. Devices Soc.* **2025**, *13*, 954.

(24) Liu, C.; Xu, Y.; Noh, Y.-Y. *Mater. Today* **2015**, *18* (2), 79.

(25) Xiang, G.; Xu, W.; Zhuge, W.; Huang, Q.; Zhang, C.; Peng, J. *Analyst* **2023**, *148* (24), 6274.

(26) Day, N. U.; Walter, M. G.; Wamser, C. C. *J. Phys. Chem. C* **2015**, *119* (30), 17378.

(27) Walter, M. G.; Wamser, C. C. *J. Phys. Chem. C* **2010**, *114* (17), 7563.

(28) Di Zazzo, L. *Chem. Eng. J.* **2023**, *458*, 141465.

(29) King, B.; Radford, C. L.; Vebber, M. C.; Ronnasi, B.; Lessard, B. H. *ACS Appl. Mater. Interfaces* **2023**, acsami.2c22789.

(30) Lessard, B. H.; White, R. T.; AL-Amar, M.; Plint, T.; Castrucci, J. S.; Josey, D. S.; Lu, Z.-H.; Bender, T. P. *ACS Appl. Mater. Interfaces* **2015**, *7* (9), 5076.

(31) Lowery, M. K.; Starshak, A. J.; Esposito, J. N.; Krueger, P. C.; Kenney, M. E. *Inorg. Chem.* **1965**, *4* (1), 128.

(32) Tahir, M. H.; Mubashir, T.; Shah, T.; Mahmood, A. *J. Phys. Org. Chem.* **2019**, *32* (3), e3909.

(33) Cao, C.; Li, L.; Cao, C.; Liu, J. *J. Phys. Org. Chem.* **2021**, *34* (4), e4164.

(34) Li, S.; Xue, J.; Fu, C.; Liu, L.; Liu, W.; Kong, L.; Sun, Y.; Xin, H.; Li, H.; Zhang, J. *Dyes Pigm.* **2025**, *243*, 113038.

(35) Zhang, X.-F.; Li, X.; Niu, L.; Sun, L.; Liu, L. *J. Fluoresc.* **2009**, *19* (6), 947.

(36) Bunin, D. A.; Martynov, A. G.; Gvozdev, D. A.; Gorbunova, Y. G. *Biophys. Rev.* **2023**, *15* (5), 983.

(37) Demuth, J.; Bednarik, S.; Machan, R.; Mocak, I.; Malinsky, T.; Abo El Dahabova, M.; Holcak, J.; Miletin, M.; Labuta, J.; Novakova, V.; Zimcik, P. *Inorg. Chem. Front.* **2025**, *12* (4), 1590.

(38) Zhao, Y.; Xue, D.; Qi, H.; Zhang, C. *RSC Adv.* **2017**, *7* (37), 22882.

(39) Gerasimov, J. Y.; Donahue, M. J.; Gao, D.; Tu, D.; Fabiano, S. *Chem. Rev.* **2025**, acs.chemrev.5c00183.

(40) Leznoff, C. C.; Lever, A. B. P. *Phthalocyanines: Properties and Applications*; Wiley, 1997; Vol. 4.

(41) Krause, L.; Herbst-Irmer, R.; Sheldrick, G. M.; Stalke, D. *J. Appl. Crystallogr.* **2015**, *48* (1), 3.

(42) Sheldrick, G. M. *Acta Crystallogr A Found Adv* **2015**, *71* (1), 3.

(43) Sheldrick, G. M. *Acta Crystallogr. C Struct. Chem.* **2015**, *71* (1), 3.

Chapter 5. Electropolymerization of Porphyrinoid Materials for Mass-Based Chemical Sensing

This chapter is adapted from: ***Cyr, M.****, Magna, G., Pizzoli, Di Natale, C., Brusso, J. L., Lessard, B. H. Paolesse, R. Electropolymerization of Phthalocyanine and Corrole Materials for Mass-Based Chemical Sensing and e-Nose Applications.* ***2025****, manuscript submitted.*

Context

During my time at the University of Rome Tor Vergata, I was interested in exploring the use of silicon phthalocyanine (SiPcs) based polymers as sensing materials for mass-based chemical sensing using quartz microbalances (QMBs). This work became an application for the polymers presented in **Chapter 4**, where I studied the electropolymerization of various axially-functionalized aminophenyl SiPcs. The work completed in this chapter focuses on three porphyrinoid polymers, two axially polymerized SiPcs (*poly-SiPcs*) and one peripherally-polymerized copper corrole (*poly-CuCorr*). These materials were selected to study the effects on their sensing behaviour when exposed to various analytes. Given that the *poly-SiPcs* are polymerized axially and the *poly-CuCorr* is polymerized peripherally, this allowed for a better understanding on the effects of analyte interaction with the porphyrinoid macrocycle (*poly-SiPcs*) in comparison to interaction with the central transition metal ion (*poly-CuCorr*). This work also explores the effects of polymerization technique on the thin-film formation and sensing behaviour through the use of cyclic voltammetry and chronoamperometry. The newly fabricated poly-porphyrinoid QMBs were not only studied individually for their potential selectivity, but also collectively to investigate their combined sensing behaviours for their use as an electronic nose. Here we demonstrate that the combined sensing behaviour of all polymeric materials was in fact successful in differentiating various classes of compounds such as water, Lewis acids/bases and alcohols through the use of a Principal Component Analysis performed on all sensors.

Contribution

This work was completed through contributions of all authors. I performed the electropolymerization and characterization of the amino-derived SiPcs and CuCorr materials, fabricated and tested the QMB sensors, performed the PCA analysis and wrote the manuscript. G.M. and F.P. trained me on the how to test the QMB sensors against gases and VOCs and help interpret the data. G.M. trained me on how to perform the PCA analysis and helped me interpret the data. C.D. designed the QMB gas testing chamber and provided expertise on the sensing results. R.P., B.H.L. and J.L.B. provided supervision for the project. All authors assisted with editing the manuscript.

Abstract

The need for development of efficient sensing materials and processing methods without compromising device performance for organic sensors is one that is continuously growing. We herein report the fabrication of porphyrinoid polymer-coated piezoelectric quartz microbalance (QMB) sensors. Three materials, *para*- and *ortho*-bis(aminophenoxy)SiPc as well as 5,10,15-tris-(4-aminophenyl)copper corrole, were processed through two electropolymerization techniques, cyclic voltammetry and chronoamperometry, to create sensing films for potential mass-based and electronic nose (e-nose) applications. The resulting QMB sensors were exposed to a broad panel of gases (CO, NO, CO_2 and trimethylamine), water, and volatile organic compounds (VOCs), revealing that while individual sensors exhibit limited intrinsic selectivity, their responses are strongly dependent on both molecular design and deposition protocol. When operated as a sensor array, the orthogonal response patterns arising from different porphyrinoid polymers and polymerization routes enable effective discrimination of humidity, alcohols, and Lewis acids/bases. These results highlight electropolymerized porphyrinoids, particularly functionalized silicon phthalocyanine polymers, as a versatile and underexplored class of sensing materials, and demonstrate how subtle variations in molecular functionalization and film growth can be exploited to tailor sensitivity profiles in electronic nose platforms.

5.1 Introduction

The field of organic chemical sensing has evolved tremendously in recent decades, driven by the growing demand for small and low-cost devices for analyte detection in various fields, including healthcare diagnostics, food safety, environmental monitoring, and more.[1,2] Chemical sensors can operate differently based on diverse physical principles such as electrical, optical, or mass-sensitive transduction.[3,4] Many of these sensors are now commonly used in commercial applications, notably electrochemical sensors, thermoconductive sensors, optical and spectroscopic sensors, and gas detectors, from which each device is tailored for specific analytes and environmental settings.[5–7] The use of organic materials has also led to many advancements in developing devices that are highly flexible and compact in size, allowing for innovative architectures such as lab-on-a-chip platforms, wearable sensors, and electronic noses.[8–10]

Among the popular commercially used sensing devices are quartz microbalances (QMBs), which are piezoelectric sensors commonly used to detect various chemical species through mass-based sensitivity measurements.[11] QMBs operate through the use of a piezoelectric quartz crystal that is cut in an explicit direction and embedded between two gold electrodes. When an alternating electric field is applied to the outer electrodes, this configuration causes the QMB to oscillate at a specific frequency.[12] When oscillating, any change in mass on the quartz surface will induce a frequency shift that will allow for quantitative detection, as described by the Sauerbrey equation.[11] This has led QMBs to become sought out analytical tools for the detection of chemical species.[13–15]

To achieve selectivity towards target compounds, QMBs are functionalized with organic sensing materials that incorporate specific functionalities, allowing them to interact with compounds of interest. These organic sensing materials can range from polymers to supramolecular structures (such as carbon nanotubes or molecular organic frameworks) or small molecule organic semiconductors (OSCs).[16,17] The nature of the chosen material will play a crucial role in forging the sensor's sensitivity, selectivity, and stability. For example, polymeric materials like polypyrrole and polyaniline are frequently employed for the detection of volatile organic compounds (VOCs) as well as acidic or basic gases, largely owing to their ease of chemical tunability. Alternatively, small molecule OSCs can be engineered as thin-films to interact with target analytes through hydrogen bonding, π–π interactions, or hydrophobic interactions, thus enhancing recognition and response performance.[18,19]

The inherent non-selectivity of the mass-transduction mechanism led to the employment of QMBs in real-time applications where selectivity is not provided by a single sensor but rather arises from the combinatorial principle in sensor matrices. Platforms based on this concept are called electronic noses (e-noses), where, for example, QMBs coated with different sensing thin-films will work together to recognize complex chemical mixtures in a way that resembles an olfactory system.[20] The collective response relies on the ability of each sensing material to distinctively interact with various analytes through different interaction mechanisms. Thus, combinatorial selectivity arises when the sensitivity patterns of sensors in the array are low-correlated with each other. Through statistical analysis of the response patterns, the e-nose is able to discriminate between numerous VOCs and even complex gas environments.[21–23]

Among popular small molecule OSCs is the family of porphyrinoids, a group of conjugated macrocycles with structural similarities to porphyrins having high absorption, tunable redox potentials, and good electronic properties.[3] Among them, corroles and phthalocyanines are two very interesting classes to be exploited in the context of organic electronics. Corroles, containing a smaller macrocyclic ring, exhibit rich redox chemistry and optoelectronic properties, making them suitable for application in organic photovoltaics and photodetectors.[24] On the other hand, phthalocyanines possess a larger π-conjugated ring that confers them an outstanding semiconducting behaviour, which can be exploited in organic field effect transistors and other conductive applications.[25] Additionally, both materials possess high chemical and thermal stability with access to tunable synthetic handles as well as a customizable metal centre, allowing optimization and fine-tuning of their redox and conductive properties. Overall, these porphyrinoids represent versatile, tunable materials that bridge molecular design and device performance in emerging organic electronic technologies. Furthermore, these materials can also be exploited as functionalities in larger interfaces, such as graphene or carbon nanotube, to serve as selective sensing layers.[26–28]

The work reported herein focuses on the electropolymerization of two types of porphyrinoid materials, copper corrole (CuCorr) and silicon phthalocyanine (SiPc), to fabricate sensing thin-films onto QMB devices (**Figure 5.1**). The CuCorr was decorated with three amino groups along the periphery of its macrocycle, yielding a planar polymer thin-film. In addition, two axially derived bis(aminophenoxy)-SiPcs were used, one bearing the amino groups at the *para* position and the other bearing the amino groups at the *ortho* position; both materials yielded axial polymers, but with varying gaps between the parallel Pc macrocycles. Silicon phthalocyanines[29] have recently emerged as versatile semiconductors with tunable axial groups enabling their use in organic photovoltaics,[30,31] organic thin-film transistors[32–34] and sensors.[18,35] Notably, the polymerization strategy employs the same electroactive groups differently: in one case, the amino groups are located at the periphery of the corrole macrocycle, while in the second, they are located in the axial position to the central silicon of the phthalocyanine. These two approaches are supposed to complement each other in exploiting the chemical sensing properties of the conjugated macrocycles. In the case of corroles, the polymerization occurring at the periphery will emphasize the interaction of target analytes with the central coordination metal, while in the case of phthalocyanines, the polymerization is propagated along the central axes of the macrocycle, thus hindering the interaction with the central silicon, ultimately confining the sensing mechanism to the interactions with the Pc ring. Hence, by combining these two approaches, it is hypothetically possible to preferentially preserve the interactions with either central metals or peripheral groups, allowing the rational design of macrocycles accordingly.

In addition, the materials were polymerized using both cyclic voltammetry and chronoamperometry techniques to evaluate whether each process was successful in creating a viable sensing thin-film (although the *poly-CuCorr* attempted to be polymerized *via* chronoamperometry did not yield a functional QMB sensor). The resulting five sensors were exposed to a series of gases and volatile organic compounds (VOCs), after which multivariate data analysis was conducted to evaluate whether the different porphyrinoid materials and polymerization techniques created sensing films suitable for distinguishing between the different classes of compounds tested. The results from this study confirm that the different natures of porphyrinoid polymeric films and the various electropolymerization techniques can be used to modulate the sensitivity of polymers, which in turn can be utilized in an e-nose approach to cluster different classes of compounds, notably water, alcohols and Lewis acids/bases. This work confirms the potential of exploiting porphyrinoid materials as viable chemical sensors and further highlights the potential held by small modifications in device processing to achieve changes in sensor sensitivity and selectivity.

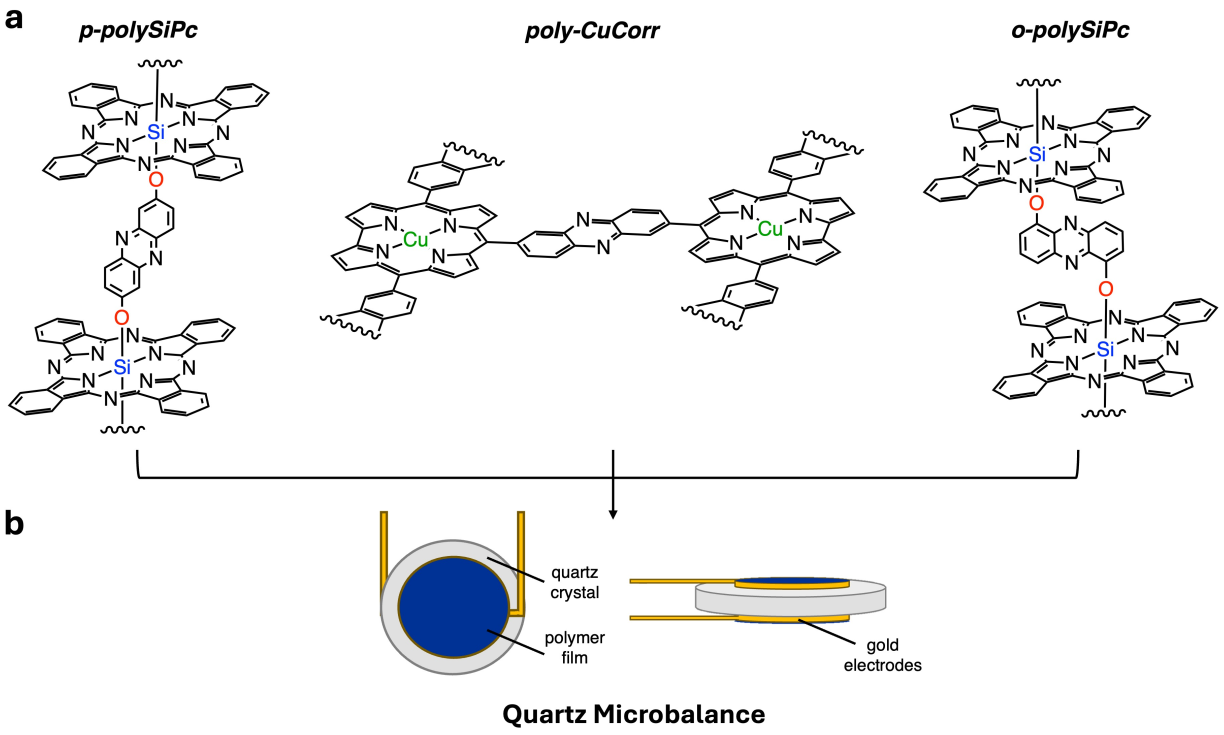

Figure 5.1 *(a) Porphyrinoid polymers that were incorporated onto quartz microbalance (QMB) sensors. (b) Device architecture of QMB sensor.*

5.2 Results and Discussion

5.2.1 Electropolymerization of Thin-Films

In previously reported work, oxidative polymerization of *para, meta* and *ortho*-bis(aminophenoxy) SiPcs (**Figure 5.2a**) was probed *via* cyclic voltammetry onto ITO conductive glass, from which the *para* and *ortho* derivatives yielded polymeric thin-films.[36] The polymerization is centred around the formation of the amino radical cation, which catalyzes the formation of a phenazine bridge between two neighboring monomers. In this work, the cyclic voltammetry was performed in the range of [0 to +1.5] V for 40 cycles at a scan rate of 50 mV s^{-1}, whereas the chronoamperometry was performed by applying the direct voltage corresponding to the amine oxidation (+0.95 V and +1.05 V for the *para* and *ortho*-bis(aminophenoxy)SiPc, respectively) for a total of 1000 seconds. After the electropolymerization process, UV-Vis-NIR spectroscopy was performed on the ITO glass to confirm the presence of the newly formed polymer film through the appearance of a new absorption peak in the 800-950 nm range (as seen in **Figure A.5.1** of Section 5.5 Appendix). Similar methods were used in the fabrication process of the chemical sensors. 20 MHz Quartz Microbalances (KVG Gmbh, Nezkarbishofsheim, Germany), equipped with a 9 mm crystal diameter and 4 mm diameter gold electrodes deposited on the top and bottom surfaces, were used as the device foundation. During the electropolymerization process, the gold surface was used as the working electrode, alongside a Pt wire and a saturated calomel electrode (SCE) serving as the counter and reference electrodes, respectively. Both cyclic voltammetry (CV) and chronoamperometry (CA) techniques were explored for depositing polymer films onto the QMB sensors. The use of QMBs as transducers also allows the quantitative determination of the deposited masses of sensing materials by measuring the frequency before and after the electropolymerization process.[37] This enables the possibility of finely controlling the sensing material coating, optimizing the deposition process, and more easily comparing the performances among sensors. For the CV process, the electropolymerization was done by cycling the potential from [0 to +1.5] V for a total of 15 cycles on each of the top and bottom electrodes of the QMB sensor. For the CA process, the controlled potential corresponding to the amine oxidation (+0.95 V for *p*-bis(aminophenoxy) SiPc and +1.05 V for *o*-bis(aminophenoxy) SiPc) is applied for a total of 1000 seconds for each gold electrode of the QMB sensor. In addition to the *poly-SiPc* QMBs, 5,10,15-tris-(4-aminophenyl)copper corrole (*CuCorr*, molecular structure in **Figure 5.2b**), was also explored as a tertiary sensing polymer in a QMB sensor. *CuCorr* polymerizes at the periphery of the macrocycle rather than axially, allowing for analyte interaction with the central metal, which would not be feasible in the case of the *poly-SiPcs* given that the silicon holds valency with the phenazine bridges for the axial polymerization. It is then evident that the two strategies may be used alternatively to emphasize the contribution of the core or the periphery of macrocycles in the sensing mechanism. The *CuCorr* monomer was prepared according to previously reported methods by Di Zazzo *et. al.*[38] and further electropolymerized *via* CV and CA in using the same experimental conditions as the *poly-SiPcs*. Following the CuCorr polymerization *via* CA, the fundamental oscillation frequency of the functionalized QMB could not be recorded by the electronics, preventing its testing with the analytes. This outcome may be attributed to nonuniformity in layer deposition (e.g. the presence of clusters) and/or to excessive viscoelastic behaviour leading to dissipation of the QMB oscillatory motion.

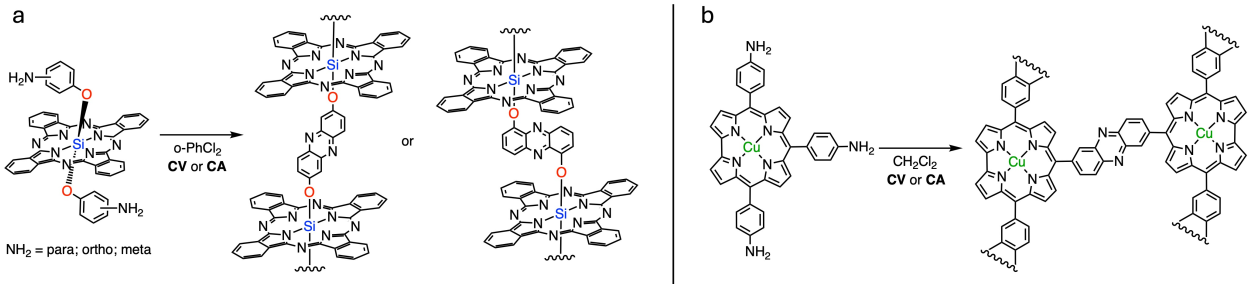

NH_2-SiPc

p-polySiPc
5-1

o-polySiPc
5-2

CuCorr

poly-CuCorr
5-3

Figure 5.2 *Electropolymerization process for using (a) NH_2-SiPc and (b) CuCorr, obtained from either cyclic voltammetry (CV) or chronoamperometry (CA).*

5.2.2 Quartz Microbalance (QMB) Sensing

All five sensors, *p-poly-SiPc* [CV], *p-poly-SiPc* [CA], *o-poly-SiPc* [CV], *o-poly-SiPc* [CA], *poly-CuCorr* [CV], were tested considering different concentrations of a total of 11 analytes (water, 4 different gases and 6 different volatile organic compounds). The volatile organic compound (VOC) analytes were carefully selected as a means to scope the different interactions they could initiate with the polymer films (modelled by the Linear Solvation-Energy Relationship (LSER)). These parameters include polarizability (R), dipolarity (π), hydrogen bond acidity (α^{H}) and basicity (β^{H}), and the solubility term ($\text{Log}L^{16}$). These help dictate an analyte's ability to participate in different types of interactions such as dipole-dipole, dipole-induced dipole, polar, hydrogen bonding and hydrogen accepting interactions. All values corresponding to each tested VOC can be seen in **Table A.5.1** of Section 5.5 Appendix.[39]

The sensors were first exposed to four gases: carbon monoxide (CO), trimethylamine (TMA), nitric oxide (NO), and carbon dioxide (CO_2). The sensors were also exposed to water and six selected VOCs: toluene, hexane, ethanol, pentanol, triethylamine and acetic acid (all water, gas and VOC concentrations tested are presented in **Table A.5.2** of Section 5.5 Appendix). Concentration differences among analytes were minimized as much as possible; however, in some cases, the resolution limits of the mass flow controller setup and the large differences in saturated vapor pressure values of certain compounds resulted in occasionally significant concentration discrepancies. This effect is even more pronounced for gaseous analytes, whose concentrations are provided by certified gas cylinders at fixed values relevant to the target compounds. As a consequence, as will be further discussed below, these constraints may limit a quantitative analysis and instead favor a qualitative, electronic nose-type approach.

Each exposure phase lasted 5 minutes to ensure that the sensor array responses reached a steady-state plateau, followed by a 15-minute recovery period under pure nitrogen flow, allowing for the complete desorption of analytes from the sensing film (as shown in **Figure 5.3a**). This protocol is routinely adopted for e-noses based on QMBs. Although sensor response and recovery times may vary depending on the gas species and concentration, they are consistently shorter than the durations employed in this protocol. This ensures that the recorded responses correspond to equilibrium conditions and therefore depend solely on the analyte concentration, rather than on the kinetics of the chemical stimulus. The sensor response is determined by taking the difference in frequency recorded from the QMB devices immediately before analyte exposure and immediately after the 5-minute exposure (Δf_{exp}). **Figures A.5.2** and **A.5.3** of Section 5.5 Appendix show the frequency response with respect to increasing concentration of analytes for each sensor.

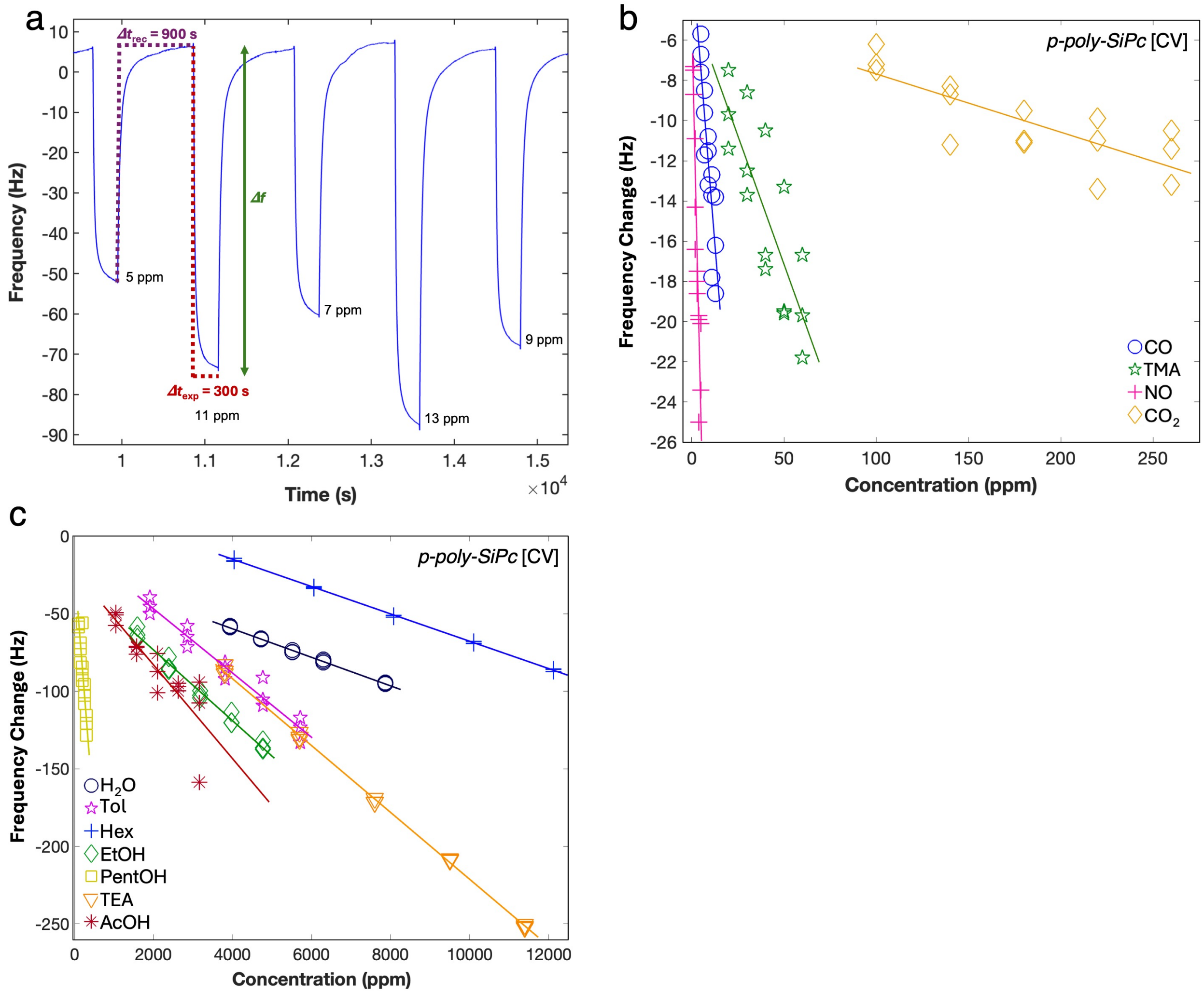

***Figure 5.3** (a) Time evolution of the frequency shift of the p-poly-SiPc [CV] functionalized sensor, where the sensor is kept under pure nitrogen flow during a 15 min recovery time (Δt_{rec}; purple) and is then followed by a 5 min exposure to CO_2 gas (Δt_{exp}; red) for a series of 5, 11, 7, 13 and 9 ppm (derived from the gas partial pressure), respectively. The double-arrow line (green) indicates the response segment (Δf) used for further analysis. (b) Gas analyte response for p-poly-SiPc [CV] QMB. (c) VOCs analyte response for p-poly-SiPc [CV] QMB.*

All five sensors demonstrated a response to each analyte tested, with the exception of *poly-CuCorr*, which showed a negligible response to hexane, alcohols, TEA and AcOH. Considering the response of each sensor as a function of the compound concentration, $R = f(c)$, the sensitivity at a given concentration, c_0, can be defined by **Equation 5.1**:

$$Sensitivity = \left.\frac{\partial R}{\partial c}\right|_{c=c_0} \qquad \textbf{[5.1]}$$

Here, the fitting equation is a first-order polynomial; therefore, the sensitivity is constant in the whole range considered. It is important to note that the validity of this parameter is strictly limited to the experimentally investigated concentration range, defined by the minimum and maximum tested concentrations, and should not be extrapolated beyond these boundaries. Consequently, the use of this sensitivity for quantitative metrics that rely on near-zero concentration behavior, such as the calculation of the limit of detection (LOD), would be inappropriate when the investigated concentrations are far from zero.

Overall, the sensors exhibited relatively higher sensitivities towards gases compared to VOCs. For the gas analysis, all five sensors displayed a similar response trend, with their highest sensitivities allocated to NO and CO, followed by TMA, and their lowest sensitivity to CO_2 (as shown in **Figure 5.4a**). For the VOC analysis, all *poly-SiPc* sensors demonstrate higher sensitivity towards pentanol and lowest sensitivity towards hexane (**Figure 5.4b**). On the other hand, the *poly-CuCorr* sensor demonstrate selectivity towards water and hexane, and negligible sensitivity towards the remaining VOCs. It is worth noting that, in the case of VOCs, the concentrations considered are higher than those of gases, due to differences in measurement protocols. In this case, the calculation of sensitivity from a linear fit may underestimate the actual sensitivity at lower concentrations. A straightforward way to notice the occurrence of linearization in fitting at higher concentrations is the presence of a non-null constant term in the first-order fitting equations, as responses are expected to be zero in the absence of analyte stimuli. In general, *poly-CuCorr* demonstrated a lower sensitivity towards VOCs compared to *poly-SiPcs*, with the exception of water and hexane. Furthermore, as a general trend, the QMB devices formed *via* cyclic voltammetry tend to have slightly higher sensitivities compared to their chronoamperometric counterparts. This suggests that both techniques yield different thin-film morphologies during the polymerization process, which may ultimately affect how the polymeric thin-films interact with individual analytes. Surface morphology studies were attempted *via* Atomic Force Microscopy (AFM) and Scanning Electron Microscopy (SEM); however, the images obtained were inconclusive and did not provide any proper novel insight on the thin-film morphologies (not included). This could be due to the films having a higher surface roughness from the electropolymerization process, which would impact the uniformity of the film and ultimately hinder the imaging process.

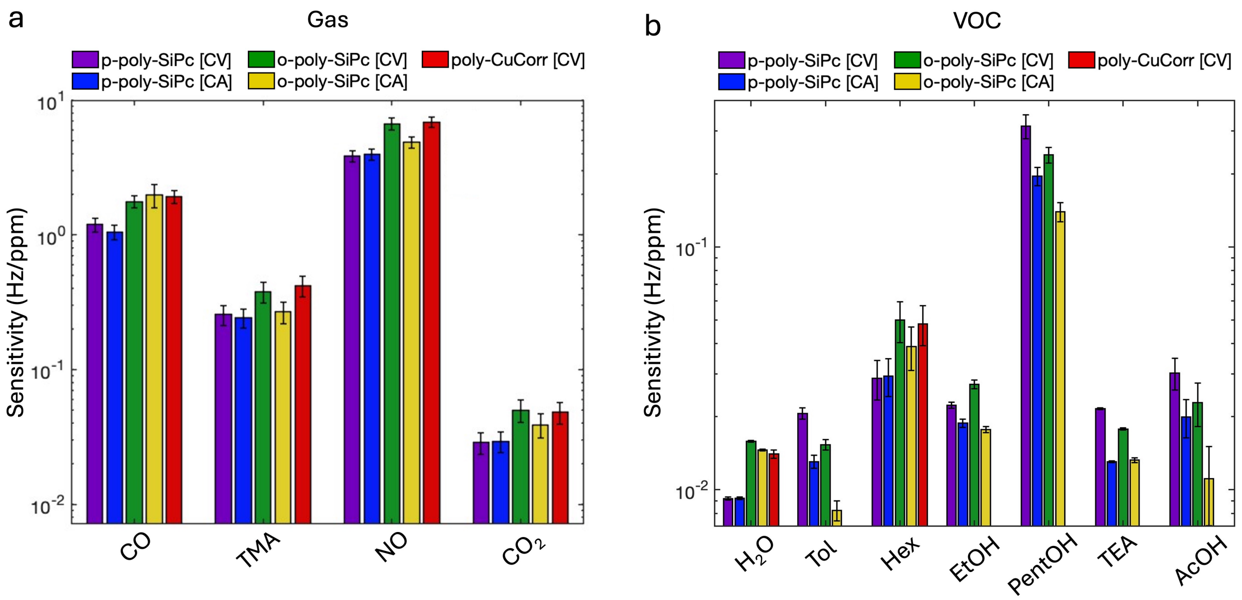

Figure 5.4 *Sensors' sensitivity with respect to each (a) gas and (b) VOC tested.*

Overall, this initial study reveals that all the sensors exhibit higher responses to reducing agents (NO and CO) or electron-donating gases (TMA) compared to oxidizing or Lewis acid agents (such as CO_2). At the same time, **Figure 5.4b** shows that films generally have lower sensitivities toward VOCs, although it is worth noting that, as previously mentioned, the different concentration ranges of analytes make this comparison inequitable. In the case of volatile compounds, the pattern of responses appears less correlated with each other, considering both the polymer material (SiPc vs. CuCorr) and the polymerization techniques used to build the QMBs (CV vs. CA). This opens a potential application for these materials in the e-nose platforms, where all sensors could gain selectivity by working together. E-noses rely on every sensor working together simultaneously to detect specific analytes (or a specific class of analytes), an approach that mimics the process of human olfaction, where a limited number of different receptor types can work together to detect a large number of volatile scents.

5.2.3 Principal Component Analysis (PCA)

Principal Component Analysis (PCA) is a multivariate statistical method used to project variables (i.e. analyte samples) into a new orthogonal coordinate system defined by linear combinations of the original sensor responses.[40] This transformation maximizes the variance of the data while ensuring that the new axes are mutually uncorrelated. The first principal component (PC1) accounts for the largest fraction of the total variance and typically reflects the dominant response pattern of the sensor array. The second (PC2) and third (PC3) principal components capture progressively smaller, yet still significant, sources of variance, often highlighting more subtle differences among analytes. In electronic nose applications, the distribution of samples along PC1, PC2 and PC3 enables the visualization of the sensor array's clustering and discrimination capabilities, providing insight into its ability to differentiate between chemically distinct compounds or concentration levels. These components are not referred to a single sensor, but to all the sensors in the array, each having different contributions. The biplot can help to disclose the contribution of the original basis (QMB sensors) to PC components. As a common practice, data are normalized by using autoscaling (data on each dimension/sensor has zero mean and unitary variance). **Figure 5.5** illustrates the distribution of the different class samples across the first three Principal Components (PCs), which collectively account for over 99% of the total variance. The principal components are ranked according to the amount of variance explained in the dataset. Accordingly, PC1 accounts for the largest fraction of the total variance. PC2 captures the largest remaining variance and is computed orthogonally to PC1, while PC3 represents the third source of variance and is orthogonal to both PC1 and PC2. Higher-order components, such as PC3, highlight finer differences once the dominant and secondary trends have been removed. Inspection of the PC score boxplots shows that PC1 primarily discriminates gaseous analytes from VOCs, PC2 is mainly associated with water recognition, and PC3 enables the differentiation of alcohols as well as acidic and basic compounds. Overall, PCA shows that the five QMB sensors operate collectively, enabling the discriminative detection of water, alcohols, and Lewis acids/bases.

In line with the normalization utilized, the variance percentages reported for the principal components tend to favor the first components due to the large diversity among compounds and the wide concentration ranges, which induce intrinsic correlations in the sensor responses. It is important to note that the small variance percentage for PC3 should not necessarily be interpreted as insignificant; rather, its relevance must be evaluated in relation to the within-class dispersion of the data. There is no universally accepted protocol in the literature for assigning a specific threshold of explained variance or an equivalent signal-to-noise criterion for the significance of individual PCs. Nonetheless, by performing a cross-validation procedure on the dataset, we obtained repeatable and comparable results across different PCA models (data not shown).

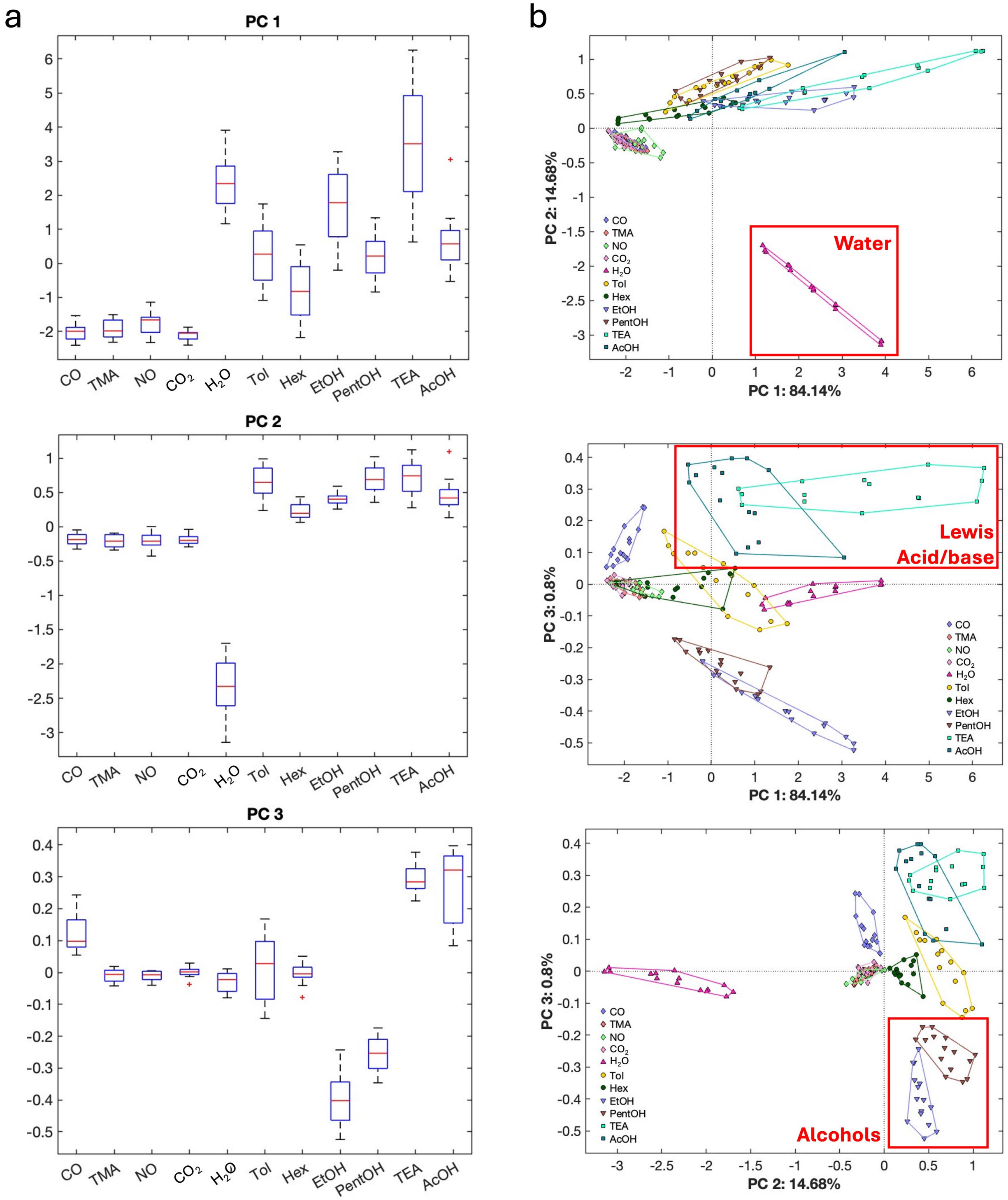

Figure 5.5 *Results of the PCA for the QMB sensor data. (a) Boxplots of the first three principal components. PC1 represents the axis along which the data varies the most. PC2 represents the axis that captures the largest remaining variance. PC3 represents the axis that is orthogonal to both PC1 and PC2. (b) Scores plot of combinations of the first three principal components.*

It is interesting to note that the similarities in response patterns toward gases cluster these groups of compounds together and make them difficult to be singularly recognized by this technique. The graphs on the right-hand side of **Figure 5.5** show different 2-D plots considering all the combinations between the first three PCs. The PC1-PC2 plot aligns with the aforementioned observations, as three distinct regions can be identified: water (IV quadrant), gases (III quadrant), and VOCs (I-II quadrant). In the case of water, the samples are well clustered because of the peculiar sensitivity pattern. Water molecules preferentially interact with the central metal (coordination) of sensing molecules; however, in the case of *poly-SiPcs*, the silicon is already axially involved in the formation of the polymer, resulting in low water sensitivity. In the PC2-PC3 projection, the samples appear to be almost clustered, with a separation between alcohols and acid/base volatile compounds. Finally, a depiction between all three classes of compounds can be observed in the PC1-PC3 projection (with a clear distinction between water and alcohols). Although the successful discrimination between water and certain VOCs is achieved, no distinction is made between different gases, suggesting that the sensors are too closely correlated in their interaction with different gases, thus rendering them incapable to isolate different gas mixtures.

Figure 5.6 presents the biplots to illustrate the contributions made by each sensor in distinguishing specific analytes or classes of analytes. The biplots represent the original variables (i.e. each sensor's frequency shifts) in the new space defined by the PCA algorithm. The direction and magnitude of each arrow indicate the strength and nature with which that variable contributes to the principal component. Additionally, the relative positions of the points indicate the degree of similarity (or difference) among samples across all measured variables. Generally, samples that are located in close proximity to one another will behave similarly during analyte-sensor interactions. Vectors that point in the same direction are positively correlated, while those pointing in opposite directions are negatively correlated; if the directions are perpendicular, the sensors are not correlated and provide complementary information. The concept of designing or optimizing an e-nose will typically rely on having a sensor array that possesses vectors that show orthogonality to one another for multiple analytes. This reflects the fact that each sensor is able to detect a specific analyte in a stronger manner in comparison to another, and combining the different sensing mechanisms of the sensor array will allow you to then gain selectivity for the combination of analytes. This concept is particularly sought out for applications in which the sensor array will be used to isolate the detection of a targeted analyte, without interference of external compounds that may also be present in the environment.

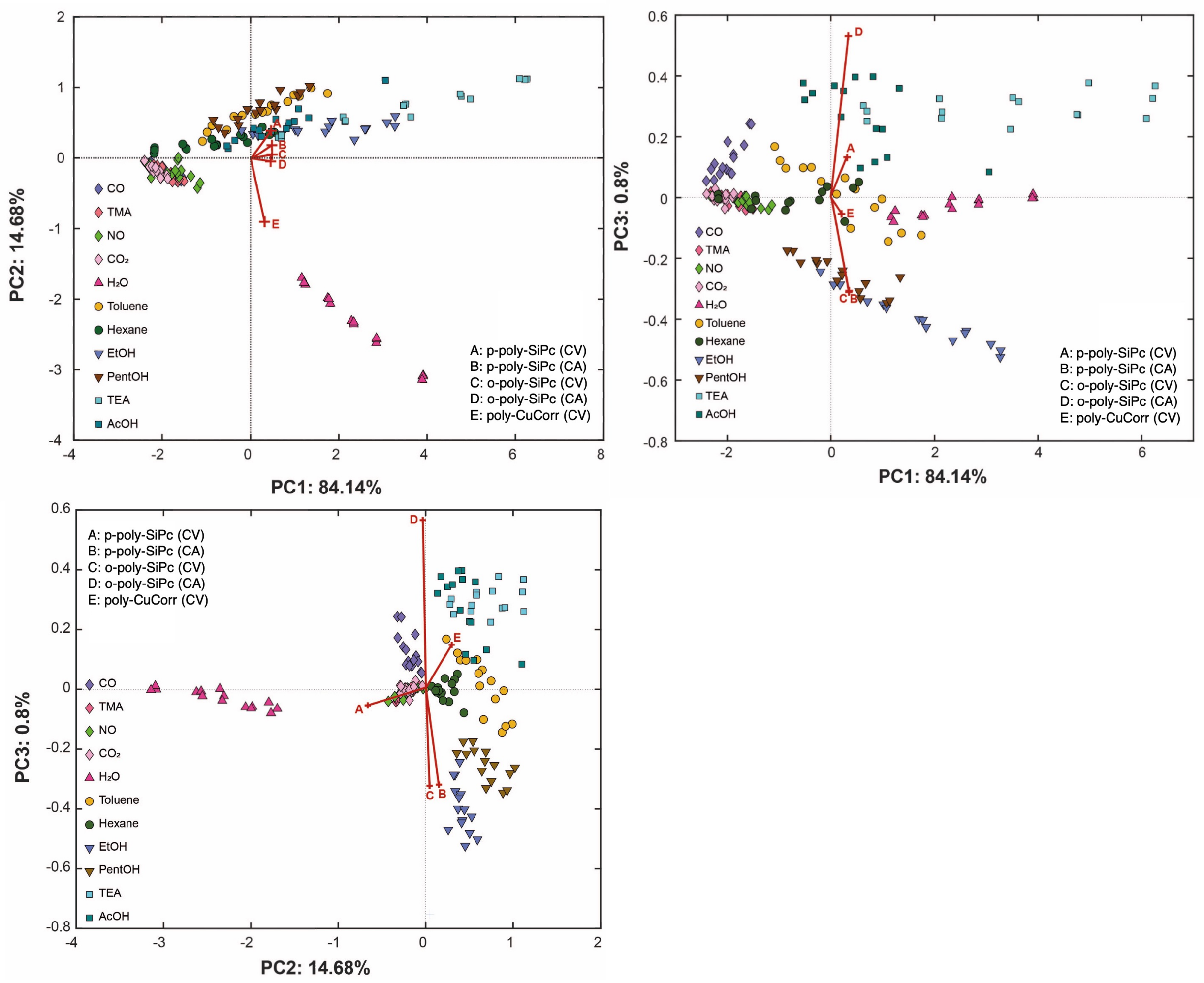

Figure 5.6 *Biplots of the combinations of the first three Principal Components of the normalized sensor data.*

The results of the PC1/PC2 biplot show a general orthogonality between *poly-SiPc*-based sensors and the *poly-CuCorr* sensor. PC1/PC3 and PC2/PC3 biplots indicate that the corrole-based film exhibits a greater affinity for water, whereas the poly-SiPc sensors are more effective in recognizing alcohols and amines. They also show opposing vectors for the *poly-SiPc* sensors and the different electropolymerization techniques utilized to fabricate the thin-films. Overall, the biplots show that *poly-CuCorr* is largely responsible for distinguishing water from gases and other VOCs. Alternatively, the *poly-SiPc* sensors predominantly control the separation of the alcohols, toluene/hexane, and the acids/bases from one another. Although the PCA analysis can also discern gases from VOCs, it is unable to differentiate the types of gases from one another, even though the QMB sensors possessed varying sensitivities when tested against each gas analyte, which could be a result of the sensors being too closely correlated to each other, preventing gas selectivity.

To better evaluate the degree of correlation between the five sensors, a correlation map can be plotted, depicting the magnitude with which each sensor tends to detect in a similar fashion. **Figure 5.7a** shows a close correlation between the *poly-SiPc* QMBs in comparison to *poly-CuCorr*, which is unsurprising given the different polymerization mechanisms (axial vs. peripheral) involved in the thin-film formations. It is also likely a result of having different central elements at the polymer centre. The copper from the *poly-CuCorr* could have stronger binding affinities for certain analytes, whereas the tetravalent silicon is not as accessible for analyte interaction, therefore the *poly-SiPc* analyte affinity is most likely centered around the Pc core or the axial pockets created between the Pc macrocycles during the polymerization process. However, omitting the *poly-CuCorr* and simply looking at the *poly-SiPc* sensors (**Figure 5.7b**), small variations can also be seen between the positioning of the amino groups creating the phenazine bridge (i.e. *para* vs. *ortho*) as well as the electropolymerization technique used to create the polymeric thin-film (CV vs. CA). This illustrates how simple molecular changes and device processing can ultimately have a noticeable impact on device behaviours.

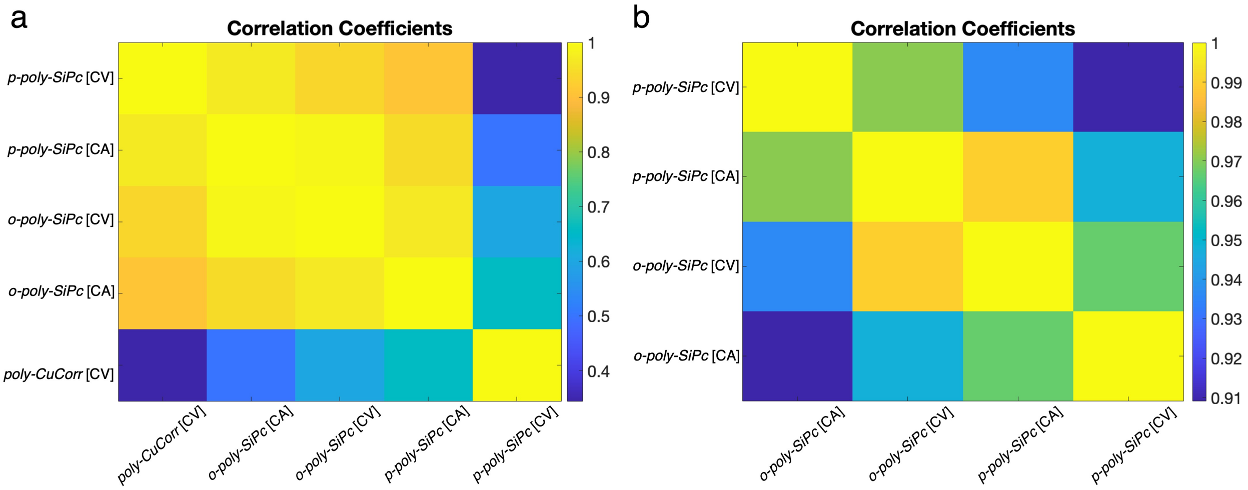

Figure 5.7 *Map of linear correlations of sensor data, where the magnitude of correlation is given in a color scale. (a) All five sensors. (b) Only the poly-SiPc sensors.*

5.3 Conclusion

In conclusion, five novel piezoelectric QMB sensors were fabricated using cost-effective electropolymerization techniques to create polymeric thin-films of the sensing materials directly onto the QMB devices. Two classes of porphyrinoid compounds, phthalocyanine and corrole, were studied for their sensing behaviour against a variety of target gases and VOCs. Two electrochemical techniques, cyclic voltammetry and chronoamperometry, were employed in the fabrication of the thin-films thereby yielding two prototype sensors for each *poly-SiPc* material. However, the *poly-CuCorr* only yielded polymeric films from the cyclic voltammetry technique. The use of quartz microbalances as the device platform allows for quantitative monitoring of the mass that was deposited onto each electrode to ensure that the thin-films were relatively similar in terms of film thickness and material concentration. Although six different sensors were initially designed, the *poly-CuCorr* fabricated using the chronoamperometry technique did not yield an adequate thin-film that produced any sensing response; therefore, only five sensors were utilized in the sensing analysis.

The sensors were exposed to eleven different analytes (water, four gases and six VOCs) at varying concentrations for five minutes, followed by recovery under nitrogen. The results demonstrated that each individual sensor interacted with almost every analyte at varying degrees of sensitivity. This confirms that both the *poly-SiPcs* and *poly-CuCorr* are viable sensing materials; however, the wide range of analyte sensitivity also eliminates the possibility of selectivity. Principal Component Analysis of the signals when the sensors are evaluated as an array shows that there is still some degree of uncorrelation between each sensor, leading to the ability to distinguish different classes of analytes, such as gases, water, alcohols, and Lewis acids/bases. Remarkably, the position of electroactive groups responsible for the polymerization can be utilized as tuning parameters to selectively drive the interaction with analytes toward the periphery or to the central coordination metals. The findings obtained from this study showcase the potential for exploiting porphyrinoid materials in simple thin-film processing of chemical sensors and further highlight the potential held by small modifications in device processing to achieve changes in sensor sensitivity and selectivity.

5.4 Experimental

5.4.1 Optoelectronic Characterization

The solid-state absorption spectra were measured using an Agilent Technologies Cary 60 UV-Vis-NIR spectrophotometer within the range of 350-1000 nm. Phthalocyanine monomeric films were prepared by drop casting a 10^{-3} M solution in DCM onto a glass slide and letting the solvent evaporate prior to collecting the spectra. Phthalocyanine polymeric films were collected from ITO conductive glass post-electropolymerization (the ITO slide was rinsed with 1,2-dichlorobenzene (*o*-DCB) and DCM sequentially to remove any excess monomer or supporting electrolyte prior to taking the measurements).

5.4.2 Electrochemical Deposition

All electrochemical measurements (polymer characterization and deposition) were performed using a PalmSens3 potentiostat/galvanostat equipped with PSTrace software. The measurements were recorded in a glass cell using ITO or the QMB gold as the working electrode, followed by a Pt wire and SCE as the counter and reference electrodes, respectively. QMB sensors were fabricated in duplicates. Each material was collected in a *o*-DCB solution at approximately 10^{-3} M concentration, and 0.1 M of tetrabutylammonium perchlorate (TBAP) was used as the supporting electrolyte. Solutions were heated and sonicated, then brought to room temperature and passed through a 0.45 μm syringe filter to remove any undissolved particulates. The solutions were then degassed with nitrogen for 10 minutes prior to the collection of the spectra. All spectra were collected at a scan rate of 50 mV s^{-1}. For QMBs, the polymerization was carried out either by cyclic voltammetry (0 to +1.5 V range, 50 mV s^{-1} scan rate) for 15 cycles or by chronoamperometry (+0.95 V appl. voltage for *p-polySiPc*, +1.05 V appl. voltage for *o-polySiPc*) for 1000s, until a film resulting in a frequency shift of about 15 KHz was attained for each top and bottom QMB electrode deposition. CuCorr deposition was carried out as outlined by Di Zazzo *et. al*.[41]

5.4.3 Chemical Sensing

The QMB sensors were housed in a stainless-steel measurement chamber that had a volume of 10 mL. Sensors were connected to oscillator circuits. Frequencies were measured by means of an integrated frequency counter. The difference of the recorded frequencies for the sensors when exposed to pure N_2 versus when exposed to a blend of gas/N_2 or VOC vapours/N_2 was considered as the sensor response. Sensors were calibrated measuring their response to a series of compounds representative of different chemical families, such as CO, TMA, NO, CO_2, H_2O, Toluene, Hexane, EtOH, PentOH, TEA, AcOH. Vapours were generated by bubbling an N_2 stream into a liquid sample of the compounds and diluted with nitrogen gas. The dilution rate was controlled by a computer-driven 4-channel mass-flow system controller (MKS). The concentration of VOCs was calculated by Antoine's law using the parameters listed in the NIST database.[4]

Statistical Analysis

For each QMB sensor, 220 samples were measured in total (5 concentrations repeated 4 times) for the following analytes: CO, TMA, NO, CO_2, H_2O, Toluene, Hexane, EtOH, PentOH, TEA, AcOH. The concentrations tested for each analyte are reported in **Table A.5.2** of Section 5.5 Appendix. In the case of gases (CO, TMA, NO, and CO_2), cylinders with certified concentrations of analytes in nitrogen mixtures (ppm (mol/mol)) have been utilized. In the case of water and VOCs, the saturated vapor pressure has been considered at 20 °C in the Antoine equation and converted into parts per million (ppm) concentrations. The first five measurements were removed from the PCA analysis calculations. In the case of error bars, the plots report the mean ± standard deviation (SD). The data were autoscaled before the PCA analysis (meaning that each column had a mean equal to zero and SD equal to one). Sensitivity is defined as the slope of the curve fitting the relative response as a function of the concentration of each analyte. The error for the sensitivity is calculated using a t-test with a 90% confidence bound. Data analysis was performed in MatLab 2023b using the "Statistics and Machine Learning Toolbox."

5.5 Appendix

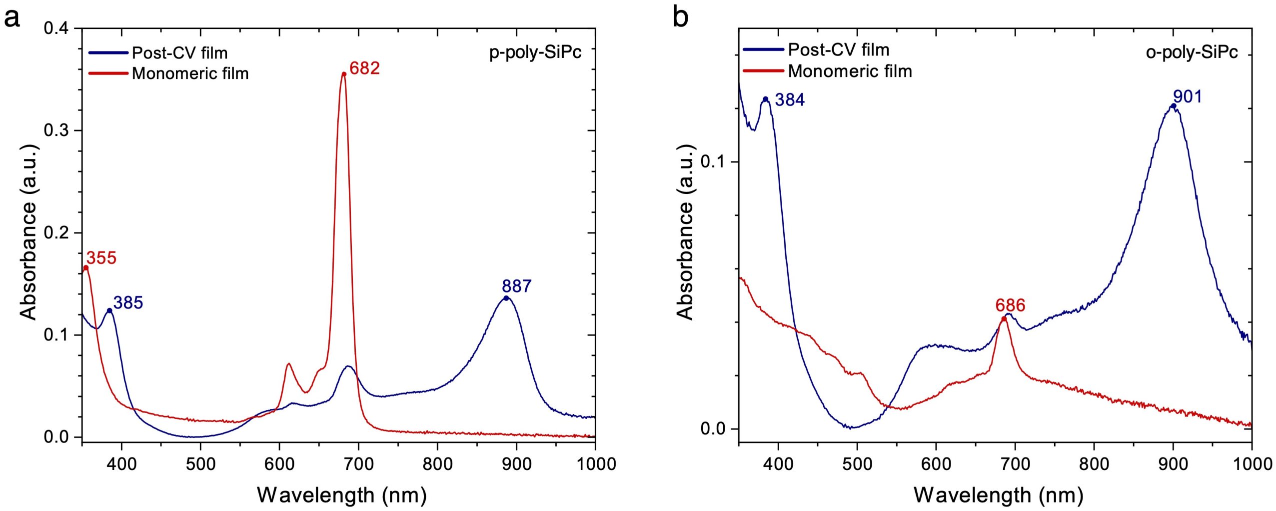

Figure A.5.1 *Solid-state UV-Vis-NIR spectra of (a) p-poly-SiPc and (b) o-poly-SiPc in their monomeric form (red) by drop casting a* 10^{-3} *M solution in DCM onto a glass slide and as a polymeric thin-film (blue) deposited on ITO coated glass post-CV after running 40 scans from [0 to +1.5] V.*

Table A.5.1 *List of the Linear Solvation-Energy Relationship (LSER) parameters of water and the volatile organic compounds selected for the QMB study.*

Analyte	***R***	***π***	α^H	β^H	**LogL**[16]
H_2O	0.000	0.45	0.82	0.35	0.260
Toluene	0.601	0.52	0.00	0.14	3.325
Hexane	0.000	0.00	0.00	0.00	2.668
EtOH	0.246	0.42	0.37	0.48	1.485
PentOH	0.219	0.42	0.37	0.48	3.106
Triethylamine	0.101	0.15	0.00	0.79	3.040
AcOH	0.265	0.65	0.61	0.44	1.750

Table A.5.2 *Concentration gradients tested for each gas, water and VOC during QMB study. Gas concentrations were derived from the gas partial pressures.*

Analyte	**Concentration Gradient (ppm)**				
CO	5	7	9	11	13
Trimethylamine	20	30	40	50	60
NO	1	2	3	4	5
CO_2	100	140	180	220	260
H_2O	3935	4722	5509	6296	7870
Toluene	1906	2858	3811	4764	5717
Hexane	4040	6060	8080	10100	12120
EtOH	1588	2383	3177	3971	4765
PentOH	100	150	200	250	300
Triethylamine	3800	5700	7600	9500	11400
AcOH	1052	1578	2104	2630	3157

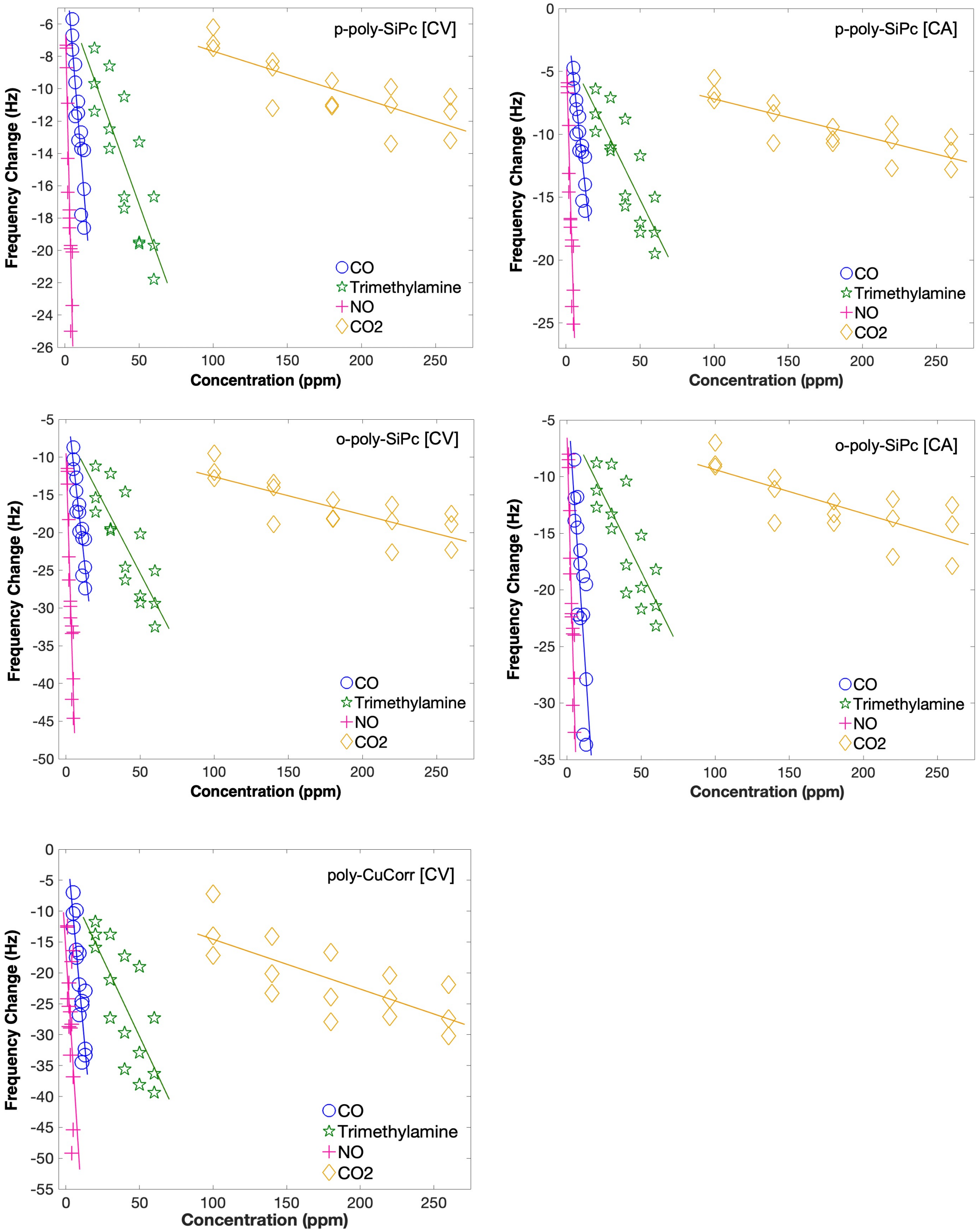

Figure A.5.2 *Frequency response with respect to increasing concentrations of gases for each QMB sensor.*

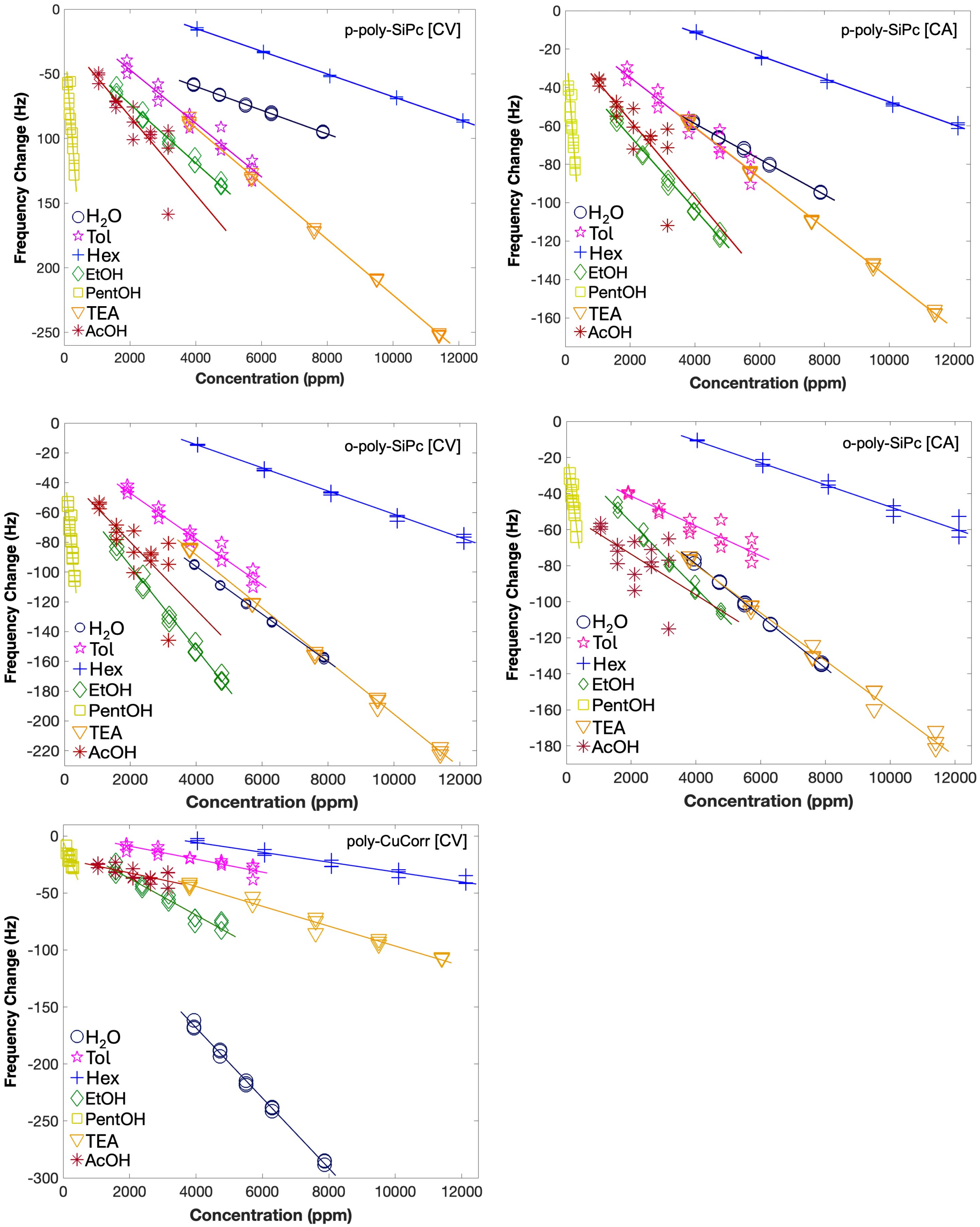

***Figure A.5.3** Frequency response with respect to increasing concentrations of water and VOCs for each QMB sensor.*

References

(1) Arakawa, T.; Dao, D. V.; Mitsubayashi, K. *IEEJ Trans.* **2022**, *17* (5), 626.

(2) Anisimov, D. S.; Abramov, A. A.; Gaidarzhi, V. P.; Kaplun, D. S.; Agina, E. V.; Ponomarenko, S. A. *ACS Omega* **2023**, *8* (5), 4649.

(3) Paolesse, R.; Nardis, S.; Monti, D.; Stefanelli, M.; Di Natale, C. *Chem. Rev.* **2017**, *117* (4), 2517.

(4) Khatib, M.; Haick, H. *ACS Nano.* **2022**, *16* (5), 7080.

(5) Gardner, E. L. W.; Gardner, J. W.; Udrea, F. *Sensors* **2023**, *23* (2), 681.

(6) Siu, V. S.; Lu, M.; Hsieh, K. Y.; Raines, K.; Asaad, Y. A.; Patel, K.; Afzali-Ardakani, A.; Wen, B.; Budd, R. *ACS Omega* **2022**, *7* (13), 11126.

(7) Nie, W.; Chen, Y.; Zhang, H.; Liu, J.; Peng, Z.; Li, Y. *Anal. Bioanal. Chem.* **2022**, *414* (20), 6017.

(8) Comeau, Z. J.; Rice, N. A.; Harris, C. S.; Shuhendler, A. J.; Lessard, B. H. *Adv Funct Materials* **2022**, *32* (7), 2107138.

(9) Lee, M. Y.; Lee, H. R.; Park, C. H.; Han, S. G.; Oh, J. H. *Acc. Chem. Res.* **2018**, *51* (11), 2829.

(10) Koklu, A.; Wustoni, S.; Musteata, V.-E.; Ohayon, D.; Moser, M.; McCulloch, I.; Nunes, S. P.; Inal, S. *ACS Nano.* **2021**, *15* (5), 8130.

(11) Vellekoop, M. J. *Sens. Actuators A Phys.* **1997**, *63* (1), 79.

(12) King, W. H. *Anal. Chem.* **1964**, *36* (9), 1735.

(13) Torad, N. L.; Zhang, S.; Amer, W. A.; Ayad, M. M.; Kim, M.; Kim, J.; Ding, B.; Zhang, X.; Kimura, T.; Yamauchi, Y. *Adv. Mater. Interfaces* **2019**, *6* (20), 1900849.

(14) Liu, J.; Zhao, W.; Liu, J.; Cai, X.; Liang, D.; Tang, S.; Xu, B. *RSC Adv.* **2022**, *12* (21), 13235.

(15) Haghighi, E.; Zeinali, S. *RSC Adv.* **2019**, *9* (42), 24460.

(16) Si, P.; Mortensen, J.; Komolov, A.; Denborg, J.; Møller, P. J. *Anal. Chim. Acta* **2007**, *597* (2), 223.

(17) Chappanda, Karumbaiah. N.; Shekhah, O.; Yassine, O.; Patole, S. P.; Eddaoudi, M.; Salama, K. N. *Sens. Actuators B Chem.* **2018**, *257*, 609.

(18) King, B.; Moorthy, S. G.; Lesniewska, E.; Meunier-Prest, R.; Bouvet, M.; Lessard, B. H. *Sens. Actuators B Chem.* **2024**, *408*, 135507.

(19) Zhou, X.; Wang, Z.; Song, R.; Zhang, Y.; Zhu, L.; Xue, D.; Huang, L.; Chi, L. *J. Mater. Chem. C* **2021**, *9* (5), 1584.

(20) Gardner, J. W.; Bartlett, P. N. *Sens. Actuators B Chem.* **1994**, *18* (1–3), 210.

(21) Sun, P.; Han, H.; Xia, X.-C.; Dai, J.-Y.; Xu, K.-Q.; Zhang, W.-H.; Yang, X.-L.; Xie, M.-H. *Talanta* **2024**, *269*, 125484.

(22) Julian, T.; Hidayat, S. N.; Rianjanu, A.; Dharmawan, A. B.; Wasisto, H. S.; Triyana, K. *ACS Omega* **2020**, *5* (45), 29492.

(23) Catini, A.; Kumar, R.; Capuano, R.; Martinelli, E.; Paolesse, R.; Di Natale, C. *Sensors* **2016**, *16* (10), 1640.

(24) Di Natale, C.; Gros, C. P.; Paolesse, R. *Chem. Soc. Rev.* **2022**, *51* (4), 1277.

(25) Leznoff, C. C.; Lever, A. B. P. *Phthalocyanines: Properties and Applications*; Wiley, 1997; Vol. 4.

(26) Perilli, D.; Rizzi, A. M.; Di Valentin, C. *Nanomaterials* **2025**, *15* (9), 691.

(27) Gai, S.; Wang, B.; Wang, X.; Zhang, R.; Miao, S.; Wu, Y. *Sens. Actuators B Chem.* **2022**, *357*, 131352.

(28) Perilli, D.; Freddi, S.; Zanotti, M.; Drera, G.; Casotto, A.; Pagliara, S.; Schio, L.; Sangaletti, L.; Di Valentin, C. *Commun. Mater.* **2024**, *5* (1), 254.

(29) Lessard, B. H. *ACS Appl. Mater. Interfaces* **2021**, *13* (27), 31321.

(30) Vebber, M. C.; Rice, N. A.; Brusso, J. L.; Lessard, B. H. *ACS Appl. Energy Mater.* **2022**, *5* (3), 3426.

(31) Grant, T. M.; Dindault, C.; Rice, N. A.; Swaraj, S.; Lessard, B. H. *Mater. Adv.* **2021**, *2* (8), 2594.

(32) King, B.; Radford, C. L.; Vebber, M. C.; Ronnasi, B.; Lessard, B. H. *ACS Appl. Mater. Interfaces* **2023**, acsami.2c22789.

(33) Cranston, R. R.; Vebber, M. C.; Faleiro Berbigier, J.; Brusso, J.; Kelly, T. L.; Lessard, B. H. *Adv. Electron. Mater.* **2022**, *8* (12), 2200696.

(34) Melville, O. A.; Grant, T. M.; Mirka, B.; Boileau, N. T.; Park, J.; Lessard, B. H. *Adv. Electron. Mater.* **2019**, *5* (8), 1900087.

(35) Ganesh Moorthy, S.; King, B.; Kumar, A.; Lesniewska, E.; Lessard, B. H.; Bouvet, M. *Adv. Sens. Res.* **2023**, *2* (3), 2200030.

(36) Cyr, M.; Magna, G.; Pizzoli, F.; Mita, A.; Di Zazzo, L.; Paolesse, R.; Lessard, B. H.; Brusso, J. L. *J. Mater. Sci.* **2025**, *manuscript submitted*.

(37) Magna, G.; Belugina, R.; Mandoj, F.; Catini, A.; Legin, A. V.; Paolesse, R.; Di Natale, C. *Sens. Actuators B Chem.* **2020**, *320*, 128373.

(38) Di Zazzo, L. *Chem. Eng. J.* **2023**, *458*, 141465.

(39) Abraham, M. H. *Chem. Soc. Rev.* **1993**, *22*, 73.

(40) Jolliffe, I. Principal Component Analysis. In *Wiley StatsRef: Statistics Reference Online*; 2014.

(41) Zazzo, L. D.; di Filippo, I.; Guido, L.; Magna, G.; Lvova, L.; Caroleo, F.; Stefanelli, M.; Duranti, L.; Nardis, S.; Natale, C. D.; Paolesse, R. *Adv. Sens. Res.* **2024** 3 (10), 240005.

Chapter 6. Exploring Electropolymerized Silicon Phthalocyanines for Gas Detection in Chemiresistors

This chapter presents the preliminary results obtained for poly-SiPc materials integrated into interdigitated electrode (IDE) sensors for the very first time and tested for chemiresistive gas detection. This work is currently ongoing as further sensing conditions are being explored alongside morphological characterizations.

Context

Given the high intrinsic conductivity of phthalocyanine materials, this work explored the potential of *para*- and *ortho*-bis(aminophenoxy) silicon phthalocyanine (SiPc) polymers as sensing layers for chemiresistive devices. In **Chapter 5**, electropolymerization of both materials onto piezoelectric quartz microbalances (QMBs) demonstrated effective interactions with a range of gases and volatile organic compounds (VOCs). However, a well-known limitation of QMB-based sensors is their poor selectivity, as detection relies exclusively on mass changes resulting from analyte adsorption. To address this limitation, the preliminary studies presented in **Chapter 6** extended the application of *poly-SiPc* materials toward resistive sensing by integrating them onto interdigitated electrode (IDE) platforms. *Para*- and *ortho*-substituted amino SiPcs were electropolymerized onto the IDEs using either cyclic voltammetry (CV) or chronoamperometry (CA) and were subsequently exposed to carbon monoxide (CO), nitric oxide (NO), and trimethylamine (TMA). These gas analytes were chosen due to their reducing nature, which is compatible with the *p*-type behavior of the *poly-SiPc* films. This approach enables a more direct assessment of how different gas species influence the electronic properties of the sensing layers, thereby offering a potential route toward improved selectivity, as different analytes may induce distinct electrical responses despite interacting with the same film. Additionally, the sensors were evaluated under varying humidity conditions to assess the stability of their baseline resistance across different environments. The results presented herein represent preliminary findings for these novel chemiresistive sensors, with ongoing studies focusing on simultaneous gas and humidity sensing, as well as morphological characterization to better understand film formation *via* CV and CA electropolymerization techniques.

Contribution

This work was completed through contributions of all authors. I performed the electropolymerization and characterization of the amino-derived SiPcs, fabricated and tested the

IDE sensors, interpreted the gas sensing data and currently writing the manuscript. Gabriele Magna and Francesco Pizzoli helped collect and interpret the gas sensing data, as well as performing the ongoing work from this chapter. Roberto Paolesse, Benoît H. Lessard and Jaclyn L. Brusso provided supervision for the project.

Abstract

In recent years, metal phthalocyanine (MPc) materials have gained increasing attention for their potential use in chemical sensing applications. Their high degree of chemical tunability combined with strong semiconducting properties makes them well suited for incorporation into electronic sensors capable of detecting a wide range of chemical species. Traditionally, sensing mechanisms in phthalocyanines and other porphyrinoid materials have focused on the metal center, as transition metals readily coordinate with specific analytes. However, the extended conjugated macrocycle of phthalocyanines also offers significant potential for analyte interactions, particularly through strong π–π interactions. This work demonstrates the axial electropolymerization of *para*- and *ortho*-bis(aminophenoxy) silicon phthalocyanines (SiPc) onto interdigitated electrode (IDE) sensors to fabricate novel *p*-type poly-SiPc chemiresistors. Both SiPc monomers were electropolymerized using cyclic voltammetry and chronoamperometry and subsequently exposed to three reducing gases (CO, NO, and trimethylamine). Sensor performance was further evaluated under varying relative humidity levels to assess the effect of humidity on baseline resistance. Preliminary results indicate that SiPc polymers can effectively interact with gaseous analytes *via* their conjugated macrocycles, yielding quantifiable sensing responses. Additionally, the results demonstrate that subtle variations in molecular structure and polymer film processing can significantly influence sensor sensitivity toward reducing gases. Ongoing work is underway to further investigate the structure-property relationships of these chemiresistors.

6.1 Introduction

New and convenient organic electronic technologies are continuously being investigated to answer demands in various fields. These include the production of rapid and efficient gas sensors for environmental monitoring and detecting harmful gases in public spaces.[1] It is also imperative for these sensors to hold strong selectivity towards target analytes to ensure they do not produce false detection signals through interactions with other environmental gases.[2] In addition, these sensors should also be resistant towards varying humidity levels as they could be employed in different climates.[3] With these considerations in mind, researchers are continuously developing new materials to fulfill various gas sensing applications in different environments. In recent decades, the use of organic materials to be employed for chemical sensing applications has captured the interest of many as this provided a gateway to develop sensing devices that are flexible, lightweight and low-cost.[4,5] Organic chemical sensors are now being commercialized in multiple fields to fulfill applications such as indoor air-quality sensing, gas leak detection, breath analysis, skin-mounted sweat monitoring patches, real-time pollution mapping and more.[6–9]

One of the commonly employed sensing devices used today is the chemiresistor, a device in which the electrical resistance changes in response to chemical adsorption. In the early stages of chemiresistor development, metal-oxides were employed as the sensing material. Unfortunately, these devices required high operating temperatures and suffered from slow response times, high power consumption and a limited shelf-life.[10] However, the emergence of organic nanomaterials to replace metal-oxides opened the door for a new generation of chemiresistors that hold properties which enable faster detection, higher sensitivity and overall more reliable operation at room temperature.[11] As a result, chemiresistors have become far more practical for portable and low-power systems and are now being employed commercially for gas sensing applications.

Since chemiresistors use electrical resistance to produce their detection signal, it is imperative that the sensing material employed for these devices holds good charge-transport properties to maintain a good resistance baseline. For this reason, organic materials such as graphene, carbon nanotubes, semiconducting polymers or highly conjugated small molecules are often used in organic chemiresistors.[12–14] Metal phthalocyanines (MPcs) are an extremely versatile class of π-conjugated macrocyclic compounds. Derived from the porphyrinoid family, they are comprised of four isoindole units bridged with four imine linkers completed with a central metal ion.[15] Their unique electronic characteristics, inherent chemical stability and tunable properties have made them useful across multiple fields including catalysis, organic field effect transistors (OFETs)[16], organic photovoltaics (OPVs)[17], organic light emitting diodes (OLEDs)[18] and more. From a chemical sensing standpoint, MPcs stand out as they provide various well-defined interaction sites for target analytes either through their delocalized π-system or through their metal centre. As such, subtle changes in adsorption, charge-transfer or coordination can produce measurable variations in their electrical signal.[19] Furthermore, MPcs can also undergo chemical functionalization either at the periphery of the macrocycle or axially through the metal centre to finetune the chemical structure by adding specific functional groups that may attract specific analytes and promote better selectivity during chemical sensing.[20] In addition, MPcs can also be designed as polymers to form a more cohesive conjugated network that can ultimately lead to enhanced conductive properties by having multiple macrocycles covalently linked to one another. This combination of structural robustness, electronic responsiveness and modular chemical design underpins the growing use of MPcs as high-performance sensing materials.

Among popular MPcs, silicon phthalocyanines (SiPcs) have attracted the interest of many researchers given that silicon serves as one of the few central elements that allows for functionalization *via* two covalent axial bonds attached directly to the silicon centre given its +4 oxidation state.[21] As such, this enables chemical modification without compromising the Pc macrocycle itself. In the past, SiPcs have been functionalized with many different functional groups, ranging from solubilizing alkyl chains to halogenated aryls which increased the electronic density of the material.[22–24] From a chemical sensing perspective, this feature is quite enticing as it enables modification of the material's chemical properties all the while leaving the Pc ring undisturbed to allow it to interact with target analytes through π-π interactions.

In previous work, we have reported that SiPcs functionalized with aminoaryl functional groups at the axial positions can be exploited to enable electropolymerization of the material.[25] This concept has also been applied to other porphyrinoids such as copper corroles (CuCorr) to produce a peripheral polymeric network onto interdigitated electrode (IDE) devices for chemical sensing of gases and volatile organic compounds (VOCs).[26] However, whereas the CuCorr polymer utilizes the metal centre to target potential analyte interaction and the macrocycle is used to propagate the polymerization, the SiPc materials have the inverse effect where the polymerization is done through the axial ligands leaving the Pc ring for sensing. Having the polymerization done axially can also leave access at the periphery of the macrocycle to add specific functional groups that would preferentially interact with specific analytes in order to narrow the selectivity of the sensing Pc material. Overall, with their high conductivity and high chemical stability, SiPcs serve as promising organic sensing materials to be exploited in chemiresistor applications.

This work explores the use of *para*- and *ortho*-bis(aminophenoxy)SiPc polymers for their chemiresistive gas sensing potential (**Figure 6.1**). Both materials have been previously electropolymerized and employed in mass-based sensing devices using piezoelectric quartz microbalances (QMBs).[27] The results obtained from the QMB devices demonstrated successful analyte interaction between various gases and VOCs with slight differences in sensitivities between the different materials as well as the different polymerization techniques. Given the strong conductive nature of Pcs, this work was done to analyze how various gases impact the resistance and whether higher affinity is obtained for certain gases. Four IDE sensors were designed where the material (*para* vs. *ortho* bis(aminophenoxy)SiPc) and polymerization technique (cyclic voltammetry vs. chronoamperometry) were investigated as independent variables. All four sensors were subjected to different gases to analyze their sensing behaviours. Results demonstrated that the sensors held higher sensitivities for nitric oxide (NO) and trimethylamine (TMA) gases, with the *para*-derived polymer demonstrating a selective affinity for carbon monoxide (CO). Interestingly, differences in sensing affinities were not only observed between the different SiPc materials, but also within the different electropolymerization techniques used to fabricate the IDE sensors suggesting that variations in the structure-property relationships also translate to the sensing behaviours. Overall, with chemiresistors serving as inexpensive and scalable sensing device architectures, they are well-positioned to serve as foundational components in next generation sensing technologies enabled by SiPc polymers.

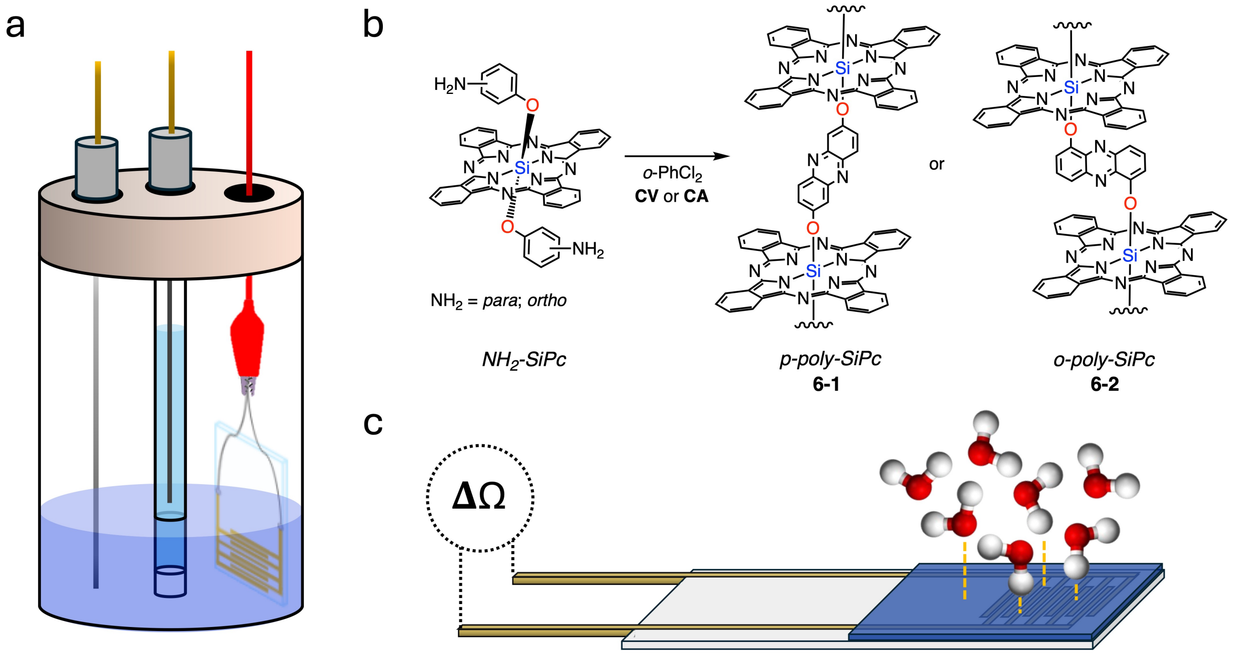

Figure 6.1 *(a) Schematic of the electrochemical setup used to fabricate the polymeric films on the IDE sensors. (b) Electropolymerization process of NH_2-SiPc monomers to obtain poly-SiPc polymers. (c) Visual representation of a target analyte interacting with an IDE sensor.*

6.2 Results and Discussion

6.2.1 Electropolymerization of poly-SiPc Films

The sensing films were prepared through direct electropolymerization of the corresponding amino-derived SiPc monomer directly onto interdigitated electrodes (IDEs) deposited onto glass. The electropolymerization process was completed according to previously published work.[25] Prior to the electropolymerization, the *para*- and *ortho*-bis(aminophenoxy)SiPcs were dissolved at a 10^{-3} M concentration in 1,2-dichlorobenzene (*o*-DCB). Tetrabutylammonium perchlorate (TBAP) was added at a 0.1 M concentration to serve as the supporting electrolyte. Silver wires were soldered onto the gold IDE electrodes to allow for a proper connection of the alligator clamp from the electrochemical setup to be used as the working electrode. Similarly to previous reports, both cyclic voltammetry (CV) and chronoamperometry (CA) techniques were explored for the polymerization of both SiPc monomers.[28] As each technique employs a distinct mode of operation, differences in how the potential is applied during the electrochemical process may lead to the formation of varied films, ultimately impacting nucleation, growth and chain dispersity during polymerization.[29] With cyclic voltammetry, the potential is swept back-and-forth between two limits, meaning that the polymerization occurs whenever the potential crosses the monomeric oxidation potential. This in turn means that polymer growth can become intermittent, where it is “on” during the oxidation sweep and “off” during the reduction sweep. Alternatively, chronoamperometry involves the application of a constant potential, typically equal to or slightly exceeding the monomer oxidation potential, for a predetermined time. While this enables continuous polymerization, current decay can occur as the growing polymeric film coats the electrode surface which could impede diffusion.[30] For the polymeric films produced by cyclic voltammetry, both *para*- and *ortho*-derived amino SiPcs were cycled through a potential bias of [0 to +1.5] V for a total of 40 cycles at a scan rate 50 mV s^{-1}. For the chronoamperometry films, the materials were subjected to the appropriate potential for amine oxidation (+0.95 V and +1.05 V for the *para* and *ortho*-bis(aminophenoxy)SiPcs, respectively) for a duration of 1000 seconds. A royal blue film was apparent on the IDE glass surface after electropolymerization for each sensor. Post-electrochemical characterization was done by UV-Vis-NIR spectroscopy to observe the newly formed characteristic polymeric peak in the range of 800-950 nm (**Figure A.6.1** of Section 6.5 Appendix).

6.2.2 Gas Sensing

The sensitivity of all four IDE sensors was investigated by exposing them to NO, CO and TMA. Given that the SiPc polymers act as *p*-type semiconductors, electron donating gases were selected as the target analytes. Consequently, when interacting with the sensing films the gases will interact with the hole charge carriers, which would increase the resistance. Concentration differences among the various gas analytes were minimized as much as possible; however, the concentrations were determined by certified gas cylinders with fixed values relevant to the target compounds and the resolution limits of the mass flow controller system resulted in slight discrepancies between gases. The exact concentration ranges are presented in **Table A.6.1** of Section 6.5 Appendix. During the testing process, the sensors were housed in a chamber maintained under an inert nitrogen environment. The chamber was also covered with aluminium foil to prevent light exposure during the testing process. This precaution was necessary to eliminate any bias arising from ambient or natural light, which could otherwise influence the baseline resistance of the sensors. Phthalocyanine-based sensing materials exhibit strong absorption in the visible region of the electromagnetic spectrum; consequently, illumination can induce photoexcitation effects that alter charge carrier density and mobility within the sensing layer. Such photoinduced changes may manifest as shifts in baseline resistance or transient resistance fluctuations that are unrelated to analyte interactions with the Pc sensing film. By excluding light, the sensor response could therefore be attributed solely to analyte adsorption and desorption processes, improving the reproducibility and reliability of the measurements and ensuring that observed resistance changes were driven exclusively by chemical, rather than optical, stimuli.[31,32] For each gas, five concentration levels were tested, with four repeated cycles per level. Each exposure lasted five minutes, followed by a 30-minute recovery period under pure nitrogen flow to allow analytes to completely desorb from the sensing film. The sensitivity responses for each sensor, along with the corresponding limit of detection (LOD) values for each gas, are summarized in **Figure 6.2b** and **Table 6.1**. The detection response for each sample was expressed as the relative change in resistance and can be calculated from **Equation 6.1**:

$$Relative\ Resistance\ Change = \frac{R_{gas} - R_{air}}{R_{air}} \qquad \textbf{[6.1]}$$

Where R_{air} represents the baseline resistance measured before gas exposure and R_{gas} is the resistance recorded at the end of the exposure period. Moreover, the limits of detection (LODs) were calculated for each gas based on the noise level measured under pure nitrogen atmosphere and the corresponding sensor sensitivity, *S*, outlined in **Equation 6.2**:

$$LOD = 3 \times \frac{noise}{S} \qquad [6.2]$$

where *S* is the sensitivity slope obtained from the relative resistance change obtained for all concentrations tested.

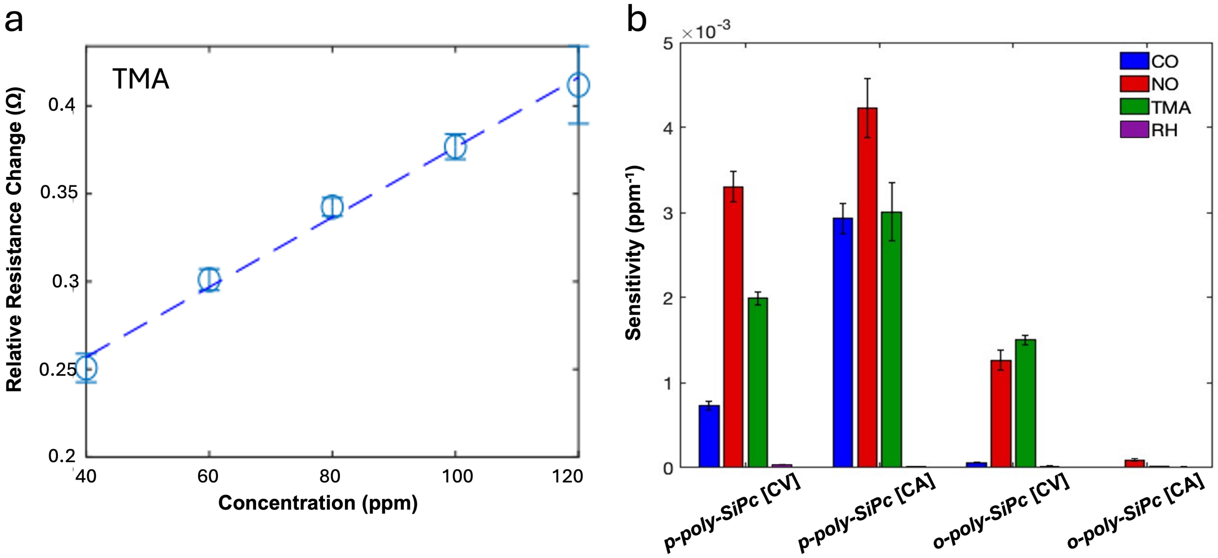

Figure 6.2 *(a) Relative resistance change as a function of concentration of para-poly-SiPc polymerized via cyclic voltammetry onto an IDE sensor and exposed to TMA in a nitrogen atmosphere. (b) Sensors' sensitivity with respect to each gas tested.*

Table 6.1 *Limit of detection (LOD) values obtained for each gas tested by each sensor.*

	Limit of Detection (LOD) [ppm]		
	CO	**NO**	**TMA**
p-poly-SiPc [CV]	5.8	0.6	7
p-poly-SiPc [CA]	4.5	0.8	11
o-poly-SiPc [CV]	5.5	1.1	5
o-poly-SiPc [CA]	> 30	3.8	26

Overall, all sensors, apart from *o-poly-SiPc* [CA], show remarkable sensitivity towards NO and TMA gases. When comparing *p-poly-SiPc* versus *o-poly-SiPc* sensors, it is evident that the films prepared using the *para*-derived material displayed greater sensitivity towards the exposed gases. This could be an effect of the polymeric structure obtained through the formation of the phenazine bridges during the polymerization process. Having the amino group located at the *para* position would ultimately create a large gap between the two Pc macrocycles and the phenazine linker (as seen on **Figure 6.1b**). The resulting larger inter-ring spacing could facilitate greater analyte access to the polymeric surface and strengthen π–π interactions with the *poly-SiPc* sensing layer. Moreover, the *p-poly-SiPc* exhibited distinct sensitivity toward CO, with this effect being particularly pronounced in films prepared via chronoamperometry. This again highlights the possible pronounced effects of the electropolymerization technique and how this might alter the film morphologies and structure-property relationships of the polymeric materials. On the other hand, *o-poly-SiPc* shows minimal response towards CO for the sensors prepared *via* both CV and CA. When compared with previous studies in which the same sensing materials were integrated into mass-based quartz microbalance (QMB) sensors, the present sensors exhibit a markedly higher sensitivity towards CO gas.[27] This observation indicates that carbon monoxide is capable of adsorbing onto the sensing films, contributing to a measurable mass change detectable by QMB devices. However, the absence of a corresponding response in IDE-based sensors suggests that CO adsorption does not significantly alter the electrical properties of the films, such as charge carrier concentration or conductivity. Consequently, while CO interactions with *o-poly-SiPc* occur at the surface level, they appear insufficient to induce an electrical transduction mechanism in IDE sensors, highlighting a fundamental difference in sensing behavior between mass-sensitive and conductometric sensing platforms. Lastly, all sensors showed relatively low, or negligible, sensitivity towards humidity. This low sensitivity response is optimal because humidity is a pervasive and highly influential environmental variable that can otherwise dominate the sensor's electrical response, obscuring the signal from the intended analyte. By minimizing moisture interference, the sensor achieves greater selectivity, signal clarity, stability and repeatability, ultimately reducing the need for intricate calibration or compensation strategies when sensors are used in complex environments.

6.3 Conclusion

In this preliminary study, both *para-* and *ortho*-bis(aminophenoxy) SiPc materials were successfully electropolymerized onto interdigitated electrode (IDE) platforms for chemiresistive gas sensing applications. The resulting polymeric SiPc films exhibited *p*-type semiconducting behavior. Accordingly, sensor responses were evaluated using three reducing gases: carbon monoxide (CO), nitric oxide (NO), and trimethylamine (TMA). Overall, both *p-poly-SiPc* and *o-poly-SiPc* demonstrated sensitivity toward NO and TMA, with *p-poly-SiPc* additionally exhibiting a measurable response to CO. Two electrochemical deposition techniques, cyclic voltammetry (CV) and chronoamperometry (CA), were employed for film fabrication, yielding sensors with distinct sensitivities. This outcome further confirms that the electropolymerization method significantly influences polymer film formation, leading to variations in structure–property relationships. Ongoing studies aim to investigate film morphology in greater detail to provide deeper insight into these effects. Furthermore, all sensors were tested under varying relative humidity conditions and exhibited minimal response variation, indicating limited sensitivity to moisture. Additional gas sensing experiments under controlled humidity environments are currently underway to further assess sensor robustness. Overall, the preliminary results of this study highlight the strong potential of polymeric SiPc materials for use in next-generation chemiresistive sensing devices.

6.4 Experimental

6.4.1 Reagents and Chemicals

p-poly-SiPc and *o-poly-SiPc* were synthesized according to previously reported literature methods (**Chapter 4**).[25] 1,2-dichlorobenzene (99%) (*o*-DCB) and tetrabutylammonium perchlorate (>98%) (TBAP) were purchased from Sigma-Aldrich and used without further purification.

6.4.2 Electrochemical Deposition

Sensors were prepared on gold interdigitated electrodes (IDE) deposited onto glass (model DRP-G-IDEAU5, Metrohm, Italy). The IDE comprises 250 pairs of electrodes spaced by 5 µm. All electrochemical measurements were performed using a PalmSens3 potentiostat/galvanostat equipped with PSTrace software. The measurements were recorded in a glass cell with a conventional three-electrodes setup, using the gold deposited onto the interdigitated electrode (IDE) as the working electrode, saturated calomel electrode (SCE) as the reference electrode, and a Pt wire as the counter electrode. Each material was collected in a *o*-DCB solution at approximately 10^{-3} M concentration, with 0.1 M of TBAP was used as the supporting electrolyte. Solutions were heated and sonicated, then brought to room temperature and passed through a 0.45 µm syringe filter to remove any undissolved particulates. The solutions were then degassed with nitrogen for 10 minutes prior to the collection of the spectra. The polymerization onto IDEs was carried out either by cyclic voltammetry (0 to +1.5 V range, 50 mV s^{-1} scan rate) or by chronoamperometry (+0.95 V appl. voltage for *p-poly-SiPc*, +1.05 V appl. voltage for *o-poly-SiPc* for a total time of 1000 seconds).

6.4.3 Physical Characterization

Polymer films were deposited on IDE-coated glass for spectroscopic characterization. The solid-state absorption spectra were measured using an Agilent Technologies Cary 60 UV-Vis-NIR spectrophotometer within the range of 350-1000 nm.

6.4.4 Electrochemical Impedance Spectroscopy

Electrochemical impedance spectroscopy (EIS) was carried out using a PARSTAT 2273 potentiostat/galvanostat. The impedance experiments were performed in a wide frequency range from 10 to 2 MHz, at an AC amplitude of 100 mV and a DC potential of 5 V. The data were analyzed with the Zsimp software.

6.4.5 Chemical Sensing

The IDE sensors were housed in a small chamber equipped with an inlet and outlet for gas flow. The chamber was covered with aluminium foil to prevent light from entering the chamber during the testing process. Nitrogen (N_2) was used as the background gas to determine the resistance baseline, dilute the test gases and desorb the absorbed molecules to recover the baseline after each exposure. The sensors were exposed to a total of three different analyte gases: nitric oxide (NO), carbon monoxide (CO) and trimethylamine (TMA). The test gases were selected to consider different chemical properties of each gas and how they could interact with the sensors. The gas concentrations were provided by certified cylinders (Rivoira, Italy) and further diluted with N_2 using a mass-flow system controller (MKS). The sensors were also exposed to varying levels of relative humidity. Water vapours were generated by bubbling an N_2 stream into water and diluted with N_2 using a mass-flow system controller (MKS). Each concentration was measured four times for every analyte with the order of concentration measurements randomized. Each acquisition consisted of an initial exposure to N_2 to establish a baseline, followed by a 5-minute exposure of the analyte gas and then a 30-minute recovery period in N_2. The total airflow in the sensor chamber was always maintained at 200 sccm. The sensor resistance values were recorded in parallel by remotely operating a Keithley 2001 multimeter equipped with TCSCAN and GPIB cards, with data automatically logged to a PC via an in-house developed MatLab script. The sensor response used for subsequent analysis was defined as the relative change in resistance between the end of the exposure period and the baseline.

6.5 Appendix

Table A.6.1 *Concentration gradients tested for each gas. Gas concentrations were derived from the gas partial pressures.*

Analyte	**Concentration Gradient (ppm)**				
CO	5	7	9	11	13
Trimethylamine	20	30	40	50	60
NO	1	2	3	4	5

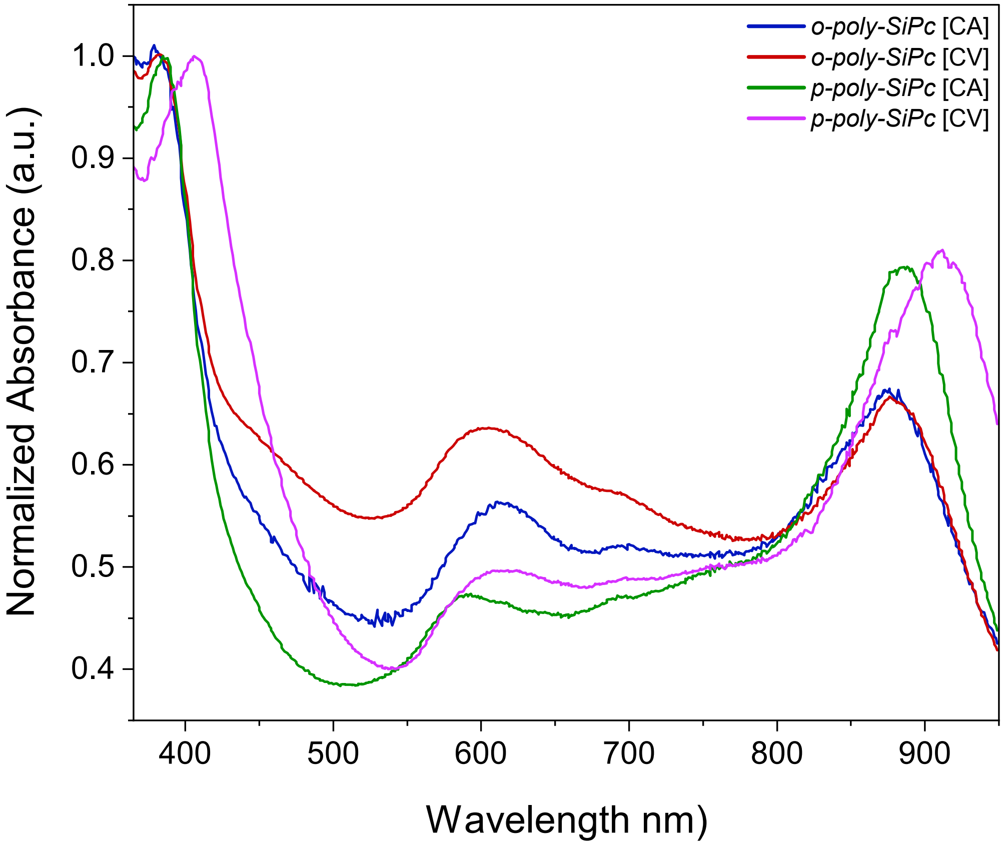

Figure A.6.1 *Solid-state UV-Vis-NIR spectra of p-polySiPc and o-polySiPc after electropolymerization on ITO glass via cyclic voltammetry and chronoamperometry.*

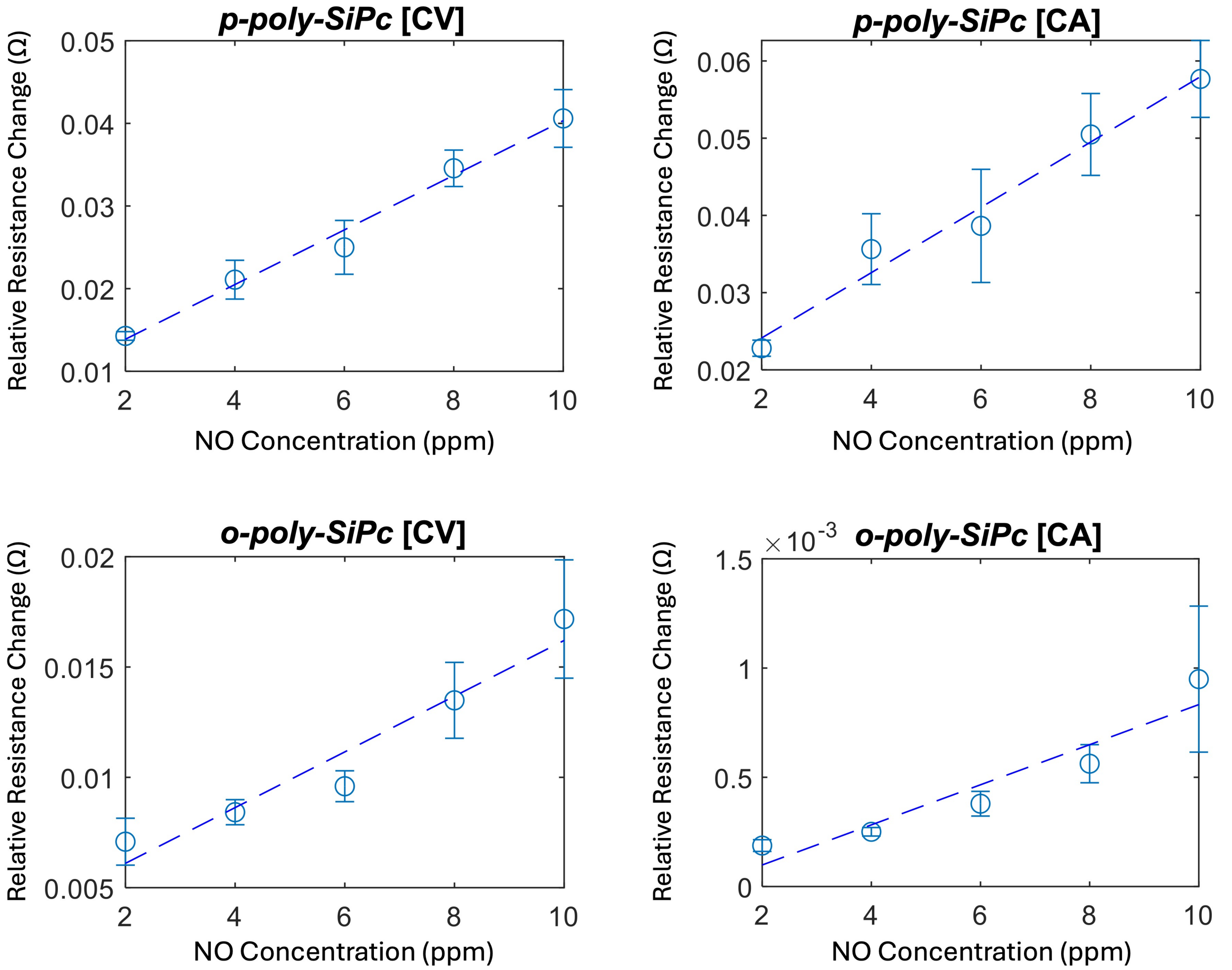

Figure A.6.2 *Relative resistance response with respect to increasing concentrations of NO gas under N_2 atmosphere captured from 20 samples.*

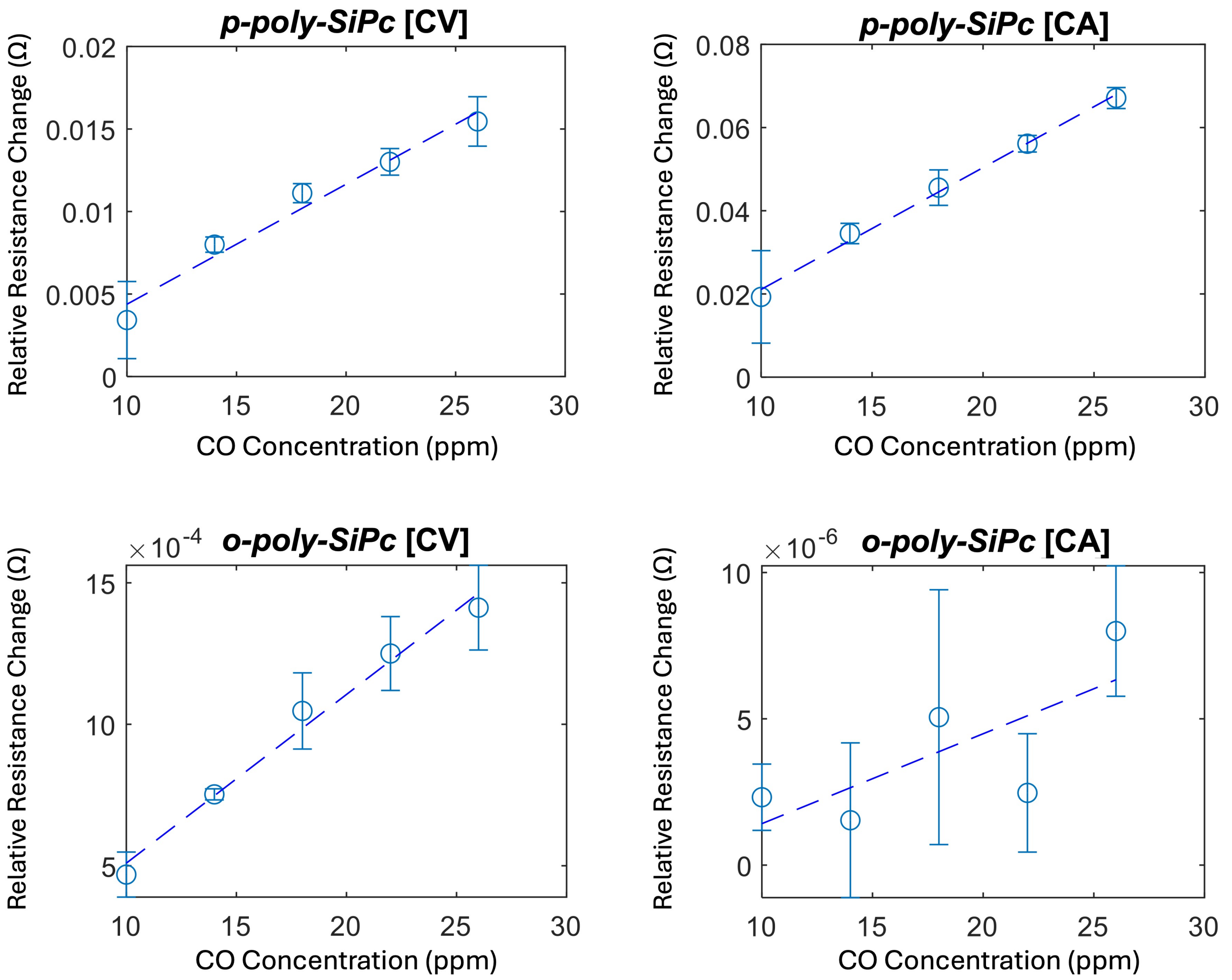

Figure A.6.3 *Relative resistance response with respect to increasing concentrations of CO gas under N_2 atmosphere captured from 20 samples.*

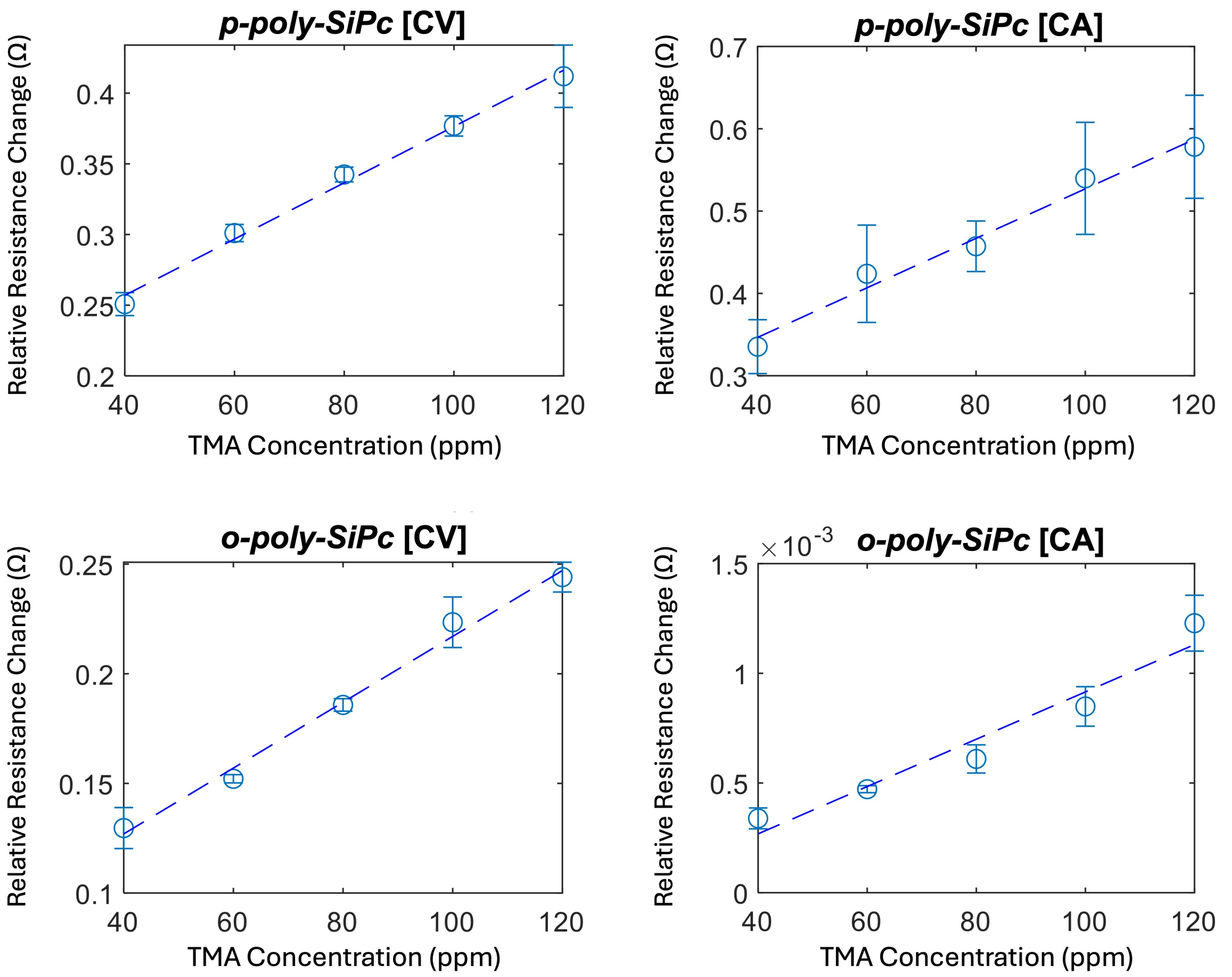

Figure A.6.4 *Relative resistance response with respect to increasing concentrations of TMA gas under N_2 atmosphere captured from 20 samples.*

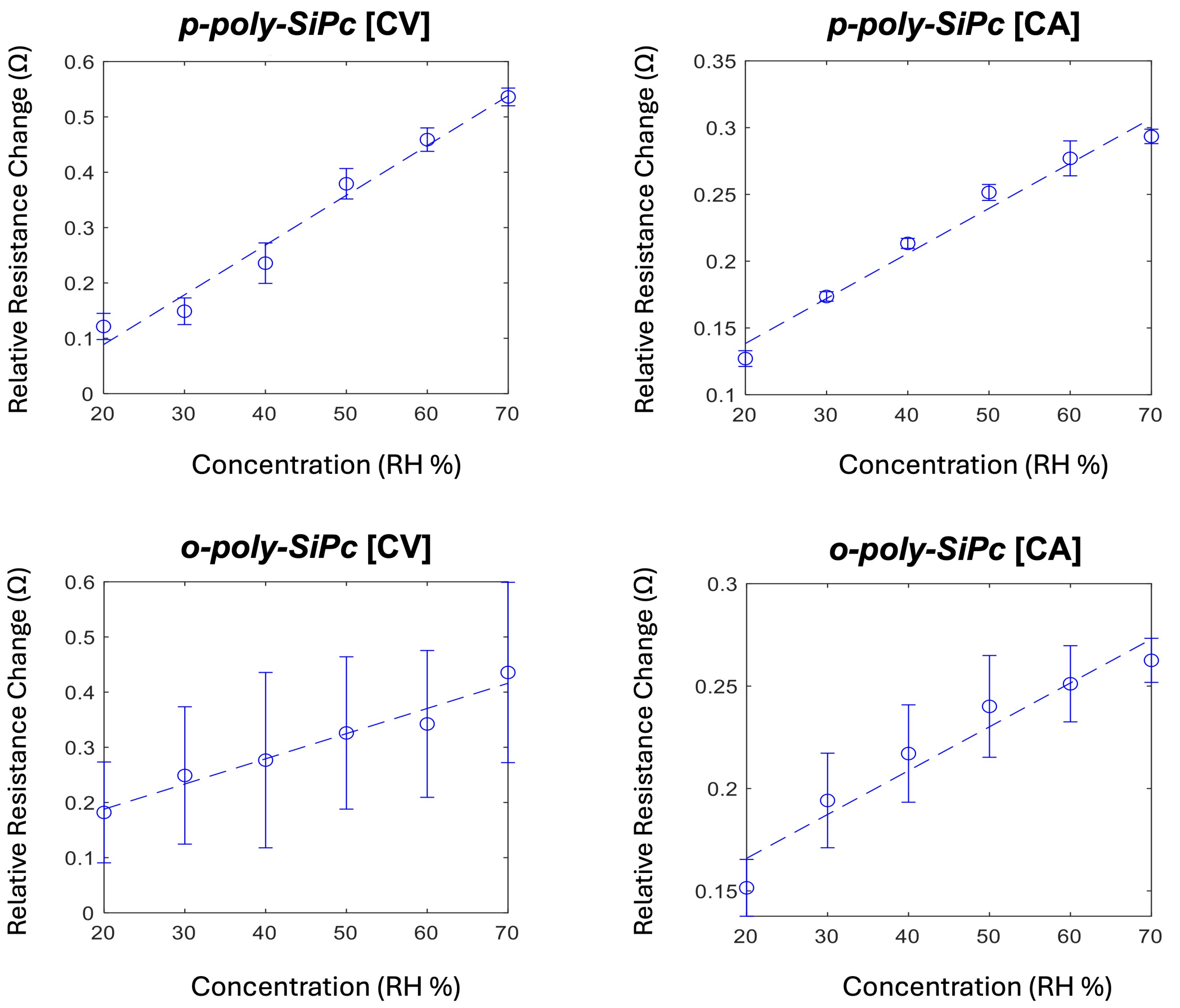

Figure A.6.5 *Relative resistance response with respect to increasing concentrations of NO gas under* N_2 *atmosphere captured from 20 samples.*

References

(1) Seesaard, T.; Kamjornkittikoon, K.; Wongchoosuk, C. *Sci. Total Environ.* **2024**, *951*, 175696.

(2) Li, J.; Zhao, H.; Wang, Y.; Zhou, Y. *Sens. Diagn.* **2024**, *3* (3), 336.

(3) Wei, P.; Ning, Z.; Ye, S.; Sun, L.; Yang, F.; Wong, K.; Westerdahl, D.; Louie, P. *Sensors* **2018**, *18* (2), 59.

(4) Sharma, A.; Eadi, S. B.; Noothalapati, H.; Otyepka, M.; Lee, H.-D.; Jayaramulu, K. *Chem. Soc. Rev.* **2024**, *53* (5), 2530.

(5) Dong, R.; Yang, M.; Zuo, Y.; Liang, L.; Xing, H.; Duan, X.; Chen, S. *Sensors* **2025**, *25* (9), 2724.

(6) Cavallari, M. R.; Pastrana, L. M.; Sosa, C. D. F.; Marquina, A. M. R.; Izquierdo, J. E. E.; Fonseca, F. J.; Amorim, C. A. D.; Paterno, L. G.; Kymissis, I. *Materials* **2020**, *14* (1), 3.

(7) Currano, L. J.; Sage, F. C.; Hagedon, M.; Hamilton, L.; Patrone, J.; Gerasopoulos, K. *Sci. Rep.* **2018**, *8* (1), 15890.

(8) Mondal, D.; Nair, A. M.; Mukherji, S. *Med. Biol. Eng. Comput.* **2023**, *61* (8), 2001.

(9) Schneider, P.; Castell, N.; Vogt, M.; Dauge, F. R.; Lahoz, W. A.; Bartonova, A. *Environment International* **2017**, *106*, 234.

(10) Seiyama, T.; Kato, A.; Fujiishi, K.; Nagatani, M. *Anal. Chem.* **1962**, *34* (11), 1502.

(11) Kong, J.; Franklin, N. R.; Zhou, C.; Chapline, M. G.; Peng, S.; Cho, K.; Dai, H. *Science* **2000**, *287* (5453), 622.

(12) Wen, J.; Wang, S.; Feng, J.; Ma, J.; Zhang, H.; Wu, P.; Li, G.; Wu, Z.; Meng, F.; Li, L.; Tian, Y. *J. Mater. Chem. A* **2024**, *12* (11), 6190.

(13) Tang, R.; Shi, Y.; Hou, Z.; Wei, L. *Sensors* **2017**, *17* (4), 882.

(14) Zamiri, G.; Haseeb, A. S. M. A. *Materials* **2020**, *13* (15), 3311.

(15) Leznoff, C. C.; Lever, A. B. P. *Phthalocyanines: Properties and Applications*; Wiley, 1997; Vol. 4.

(16) Boileau, N. T.; Cranston, R.; Mirka, B.; Melville, O. A.; Lessard, B. H. *RSC Adv.* **2019**, *9* (37), 21478.

(17) Vebber, M. C.; Rice, N. A.; Brusso, J. L.; Lessard, B. H. *ACS Appl. Energy Mater.* **2022**, *5* (3), 3426.

(18) Blochwitz, J.; Pfeiffer, M.; Fritz, T.; Leo, K. *Appl. Phys. Lett.* **1998**, *73* (6), 729.

(19) Ouedraogo, S.; Meunier-Prest, R.; Kumar, A.; Bayo-Bangoura, M.; Bouvet, M. *ACS Sens.* **2020**, *5* (6), 1849.

(20) King, B.; Moorthy, S. G.; Lesniewska, E.; Meunier-Prest, R.; Bouvet, M.; Lessard, B. H. *Sens. Actuators B Chem.* **2024**, *408*, 135507.

(21) Lessard, B. H. *ACS Appl. Mater. Interfaces* **2021**, *13* (27), 31321.

(22) Cranston, R. R.; Vebber, M. C.; Berbigier, J. F.; Rice, N. A.; Tonnelé, C.; Comeau, Z. J.; Boileau, N. T.; Brusso, J. L.; Shuhendler, A. J.; Castet, F.; Muccioli, L.; Kelly, T. L.; Lessard, B. H. *ACS Appl. Mater. Interfaces* **2021**, *13* (1), 1008.

(23) Yutronkie, N. J.; King, B.; Melville, O. A.; Lessard, B. H.; Brusso, J. L. *J. Mater. Chem. C* **2021**, *9* (31), 10119.

(24) King, B.; Melville, O. A.; Rice, N. A.; Kashani, S.; Tonnelé, C.; Raboui, H.; Swaraj, S.; Grant, T. M.; McAfee, T.; Bender, T. P.; Ade, H.; Castet, F.; Muccioli, L.; Lessard, B. H. *ACS Appl. Electron. Mater.* **2021**, *3* (1), 325.

(25) Cyr, M.; Magna, G.; Pizzoli, F.; Mita, A.; Di Zazzo, L.; Paolesse, R.; Lessard, B. H.; Brusso, J. L. *J. Mater. Sci.* **2025**, *manuscript submitted*.

(26) Di Zazzo, L.; di Filippo, I.; Guido, L.; Magna, G.; Lvova, L.; Caroleo, F.; Stefanelli, M.; Duranti, L.; Nardis, S.; Natale, C. D.; Paolesse, R. *Adv. Sens. Res.* **2024**, 3 (10), 2400005.

(27) Cyr, M.; Magna, G.; Pizzoli, F.; Brusso, J. L.; Lessard, B. H.; Paolesse, R. *ACS Sens.* **2026**, *manuscript submitted*.

(28) Cyr, M.; Magna, G.; Pizzoli, F.; Di Natale, C.; Brusso, J. L.; Lessard, B. H.; Paolesse, R. *ACS Sens.* **2026**, *manuscript submitted*.

(29) Rafiee, M.; Abrams, D. J.; Cardinale, L.; Goss, Z.; Romero-Arenas, A.; Stahl, S. S. *Chem. Soc. Rev.* **2024**, *53* (2), 566.

(30) Martinez, J. G.; Mehraeen, S.; Jager, E. W. H. *Chem. Electron. Chem.* **2023**, *10* (15), e202300188.

(31) Fielding, P. E.; Gutman, F. *The J. Chem. Phys.* **1957**, *26* (2), 411.

(32) Pankow, J. W.; Arbour, C.; Dodelet, J. P.; Collins, G. E.; Armstrong, N. R. *J. Phys. Chem.* **1993**, *97* (32), 8485.

Chapter 7. Conclusions and Future Outlook

Summary of Main Findings

Overall, the work completed in this thesis highlights the importance of chemical functionalization in finetuning the optoelectronic properties of organic semiconducting materials. This thesis also highlights the importance of optimizing device fabrication conditions to enable novel organic semiconducting (OSC) materials to achieve their highest performance potential. As research progresses, donor-acceptor (D–A) small-molecules and macrocyclic porphyrinoids continue to provide a powerful platform as OSCs for exploring structure–property relationships and for realizing high-performance, flexible and sustainable organic electronic devices. Compared with polymeric semiconductors, they offer several advantages, including well-defined structures, high batch-to-batch reproducibility and easier processing. Their modular architectures allow systematic tailoring of molecular packing, crystallinity and solid-state morphology, properties that play key roles in determining charge mobility and device performance.

In **Chapter 2**, I developed two novel donor-acceptor small molecule frameworks centered around a thieno[3,4-c] pyrrole-4,6-dione (TPD) core and thiophene donors. Both frameworks were designed in a A^2-D-A^1-D-A^2 configuration where terminal acceptors were also employed in addition to the TPD core. Dicyanovinyl (malononitrile) and *N*-ethylrhodanine were used as the terminal acceptors to slightly modify the electronic properties of both materials. Once synthesized and characterized on the molecular level, both materials were then incorporated into bottom-gate bottom-contact (BGBC) organic thin-film transistors (OTFTs) to study their abilities to perform as *n*-type organic semiconductors. Results from the spin-coating process confirmed that a low-boiling chlorinated solvent (such as chloroform) was more effective in forming a uniform thin-film across the OTFT substrates in comparison to a higher-boiling chlorinated solvent (such as 1,2-dichlorobenzene). Furthermore, it was shown that post-deposition annealing with temperatures approaching 200 °C allows for crystallization of the dicyanovinyl derivative, which helps increase its average electron mobility by almost two orders of magnitude. Although there is no crystallization observed when annealing the *N*-ethylrhodanine derivative at higher temperatures, the material is also subjected to increased mobility values when annealed, most likely due to removal of any residual solvent trapped in the thin-film. The *N*-ethylrhodanine derivative also held the highest overall mobility value between both materials. Although these two new materials didn’t quite adopt a similar level of OTFT performance as the current leading D-A small molecule, derived from a benzothienobenzothiophene (BTBT) network, this work highlights the introduction of TPD in the field of OTFTs and how it can be exploited as an acceptor moiety, as well as how structural modifications impacted the materials' semiconducting properties. This work also highlighted the impact of different OTFT fabrication conditions with the resulting semiconductive performance of each material.

In **Chapter 3**, I exploited a group-15 functionalized porphyrinoid material for its *p*-type semiconducting properties in OTFTs. To obtain the material, I first had to react metal-free phthalocyanine with PBr_3 which led to the phosphorus insertion at the centre as well as a loss of one bridging imine atom, yielding a phosphorus^V oxide triazatetrabenzocorrole compound (PO-Tbc). PO-Tbc was incorporated in both BGBC and bottom-gate top-contact (BGTC) OTFT devices through physical vapour deposition (PVD). Prior to deposition, a series of dielectric surface treatments were conducted using silanes and *para*-sexiphenylene that held a range of varying hydrophobicity to probe how the thin-film morphology would be affected. Both the BGBC and BGTC devices demonstrated cohesive trends where the hole mobility would increase when the material was deposited on a more hydrophobic surface. Further investigations were made on the thin-film morphologies of the BGTC devices, where XRD and polarized Raman microscopy were conducted to obtain more information of the molecular packing arrangement of the PO-Tbc material. The XRD spectra showed an increase in film crystallinity when using *n*-octyltrichlorosilane (OTS) and *n*-octadecyltrichlorosilane (ODTS)-treated surfaces, with ODTS holding the highest degree of crystallinity. Alternatively, the Raman mapping revealed that while ODTS-treated substrates exhibit a higher degree of crystallinity, they also promote a more face-on orientation of the PO-Tbc molecules relative to the substrate surface, which may ultimately influence the charge transport abilities of the OSC. While this material did not compare to the leading TiO-Pc in its semiconducting performance as a *p*-type OSC in OTFTs, this work nevertheless provided valuable insight on the structure-property relationships adopted by PO-Tbc when varying the surface energy of the dielectric layer during the OTFT fabrication process.

In **Chapter 4**, I focused on designing a series of axially functionalized silicon phthalocyanines (SiPcs) bearing different aminophenyl groups for the purpose of exploring axial electropolymerization. During the synthetic process, I was successful in developing five different amino-derived SiPcs, three of which possessed aminophenoxyl groups and two that possessed aminobenzoate groups. The positioning of the amino group on the aryl ring was also explored and how this would ultimately affect the polymerization process of these materials. During the electrochemical characterization process, each material was first studied by cyclic voltammetry

(CV) using glassy carbon as the working electrode to study the reduction and oxidation potentials held by each material. The materials then underwent polymerization through of cyclic voltammetry by repeating multiple voltage cycles using ITO-coated glass as the working electrode. To confirm the presence of polymeric materials, the ITO glass was studied using UV-Vis-NIR spectroscopy after the CV process to observe the appearance of a new broad absorption band in the NIR region. This confirmed that both the *para*- and *ortho*-bis(aminophenxy)SiPc materials were successful in polymerizing onto the ITO glass, whereas the other three derivatives were not. To further confirm these results, spectroelectrochemistry was also studied where irreversible changes were observed for both the *para-* and *ortho*-bis(aminophenoxy)SiPc materials after undergoing the oxidation process.

In both **Chapter 5** and **Chapter 6,** we sought to explore the potential use of the electropolymerized *para-* and *ortho*-bis(aminophenoxy)SiPc materials in organic sensing applications. **Chapter 5** describes the use of the poly-SiPc materials alongside *poly-CuCorr* in mass-based piezoelectric quartz microbalance sensors against a total of 11 analytes varying from water, gases and volatile organic compounds (VOCs). This work was done with the intention to look at how differently axially-polymerized versus peripherally-polymerized materials would interact with target analytes. In addition to this, two electropolymerization techniques were explored to obtain the sensing films, the first being cyclic voltammetry and the second being chronoamperometry (although this technique was unsuccessful for the CuCorr material). The preliminary sensing results demonstrated that all five sensors were successful in producing a sensing response to every analyte they were exposed to, which reinforces the notion that the sensing element provided by porphyrinoid materials is not solely reliant on the central metal ion but can also be established by the conjugated macrocyclic core as well. However, the broad range of analyte sensitivities inherently limits selectivity. When a Principal Component Analysis was conducted on the sensor responses to evaluate the sensors as an array, it was revealed that the individual sensors retain a degree of uncorrelated behaviour, enabling discrimination among different classes of analytes including gases, water, alcohols and Lewis acids and bases.

Chapter 6 integrates the aforementioned poly-SiPc materials into chemiresistive sensors given the high conductive nature of Pc materials. Both *para*- and *ortho*-bis(aminophenoxy)SiPc materials were polymerized onto interdigitated electrodes through either cyclic voltammetry or chronoamperometry techniques. Since the poly-SiPc materials act as *p*-type polymers, the sensors were exposed to different electron-donating gases, such as nitric oxide (NO), carbon monoxide (CO) and trimethylamine (TMA). The preliminary results obtained from this chapter further highlight that the polymerization technique (cyclic voltammetry vs. chronoamperometry) does in fact play a role in obtaining different film morphologies which in turn impacts the sensitivity and limit of detection (LOD) for each gas. Ongoing work on these sensors is being done to explore the film morphologies between the different materials and polymerization techniques as well as changes in sensitivity when the sensors are exposed to analytes in different environments, such as varying humidity levels and synthetic air.

Recommendations for Future Outlooks

The results and information gained from the work presented in this thesis hold great promise in future explorations of small molecule OSCs for the development of next-generation organic electronics. The work I conducted alongside coworkers and collaborators allows for a deeper understanding of the potential that is held by both donor-acceptor frameworks and porphyrinoid materials for OTFTs and chemical sensing purposes. I believe that several interesting avenues could be explored in the future in light of what we have reported.

Firstly, I believe it would be compelling to explore the possibility of axially functionalizing silicon phthalocyanine macrocycles with electron rich donors to investigate how electron donating properties would impact the charge transport of the material. There have been many reports of silicon phthalocyanines harbouring various fluorinated aryls at the axial position, in which the electroattractive nature of these functional groups significantly alters the electronic properties of the material, leading to a shift from *p*-type to *n*-type behaviour.[1–3] Considering the fact that silicon forms covalent bonds with its axial substituents, it would be equally intriguing to explore the possibilities of having strong electron donating groups that would be able to feed electron density into the Pc macrocycle rather than withdrawing it. This increase in electron density could in turn ease the *p*-type behaviour of the macrocycle as it would most likely raise the HOMO level of the material for easier hole injection. A strong electron donating group like carbazole would be an ideal candidate to fulfill this role. Given that amines will not readily attach themselves directly onto silicon, an alcohol-derived carbazole, such as Carbalexin A, would likely need to be used for the functionalization to be carried out successfully.[4] One thing that I believe will be important to keep in mind for this work would be to probe the air stability of the material once it is incorporated into an electronic device, as materials with more elevated HOMO levels are more susceptible to oxidation in open air. For this reason, I believe it would be important for the preliminary round of fabricated devices to be tested under vacuum or under inert atmosphere (such as a nitrogen or argon glovebox) to remove any potential bias towards oxidation.

Another interesting avenue to explore is that of peripheral amination of phthalocyanine materials for electropolymerization and chemical sensing. The work completed in this thesis demonstrated that aminoaryl-functionalized SiPcs are viable candidates to undergo electropolymerization, from which polymer films can be directly deposited onto glass or electrode surfaces for chemical sensing. It would be highly interesting to explore the possibility of harvesting the polymerization in-plane with the macrocycle, which would form a 2-D network (similar to the phenomenon occurring during the electropolymerization of the amino-derived copper corrole).[5] This in turn would also give access to the central metal ion, from which the sensor could possibly gain higher selectivity by having designated central metals to discriminatively interact with specific analytes. Given the stronger conductive nature of Pcs in comparison to corroles, these types of sensing materials would be viable candidates for OTFT-based sensors.

Lastly, in the same vein of peripheral amino functionalization of Pcs, I believe these materials would be interesting to incorporate into OTFTs as amines are also known to interact with silicon oxide either through hydrogen bonding ($-NH_2$) or electrostatic interactions ($-NR_2$).[6,7] If the amino groups are located on the periphery of the macrocycle, this would in turn suggest that once the material is processed into OTFTs they would adopt an edge-on orientation with respect of the substrate surface owing to the amine-SiO_2 interactions. As it has been shown that edge-on oriented Pcs tend to hold higher device performance due to better intermolecular charge transport throughout the thin-film,[8] this could serve as a viable option to optimize the structure-property relationships of these materials to obtain higher performing OTFT devices.

References

(1) King, B.; Melville, O. A.; Rice, N. A.; Kashani, S.; Tonnelé, C.; Raboui, H.; Swaraj, S.; Grant, T. M.; McAfee, T.; Bender, T. P.; Ade, H.; Castet, F.; Muccioli, L.; Lessard, B. H. *ACS Appl. Electron. Mater.* **2021**, *3* (1), 325.

(2) Yutronkie, N. J.; King, B.; Melville, O. A.; Lessard, B. H.; Brusso, J. L. *J. Mater. Chem. C* **2021**, *9* (31), 10119.

(3) Vebber, M. C.; King, B.; French, C.; Tousignant, M.; Ronnasi, B.; Dindault, C.; Wantz, G.; Hirsch, L.; Brusso, J.; Lessard, B. H. *Can. J. Chem. Eng.* **2023**, *101* (6), 3019.

(4) Çapan, İ.; Hawash, M.; Jaradat, N.; Sert, Y.; Servi, R.; Koca, İ. *BMC Chem.* **2023**, *17* (1), 60.

(5) Di Zazzo, L. D.; Filippo, I. D.; Guido, L.; Magna, G.; Lvova, L.; Caroleo, F.; Stefanelli, M.; Duranti, L.; Nardis, S.; Di Natale, C.; Paolesse, R. *Adv. Sens. Res.* **2024**, *3* (10), 2400005.

(6) Diosa, J.; Poveda-Jaramillo, J. C.; Ramirez-Rodríguez, F.; Mesa, M. *J. Mater. Res. Tech.* **2020**, *9* (4), 8092.

(7) Patwardhan, S. V.; Emami, F. S.; Berry, R. J.; Jones, S. E.; Naik, Rajesh. R.; Deschaume, O.; Heinz, H.; Perry, C. C. *J. Am. Chem. Soc.* **2012**, *134* (14), 6244.

(8) King, B.; Radford, C. L.; Vebber, M. C.; Ronnasi, B.; Lessard, B. H. *ACS Appl. Mater. Interfaces* **2023**, acsami.2c22789.

Copyright Permissions

Chapter 2

Reprinted with permissions from:

Synthesis of thieno[3,4-c] pyrrole-4,6-dione-based small molecules for application in organic thin-film transistors. Mélanie Cyr, Samantha Brixi, Anindya Ganguly, Benoît H. Lessard, Jaclyn L. Brusso. *Dyes and Pigments* **2023**, 210, 110964.

Copyright © 2022 Elsevier Ltd.

Chapter 3

Reprinted with permissions from:

Oxy Phosphorus Triazatetrabenzocorrole as a p-Type Organic Semiconductor in Organic Thin Film Transistors. Mélanie Cyr, Halynne Lamontagne, Benoît H. Lessard, Jaclyn, L. Brusso. *ACS Applied Electronic Materials*, **2024**, 6 (8), 6275-6283.

Copyright © 2024 American Chemical Society.

License Number: 6183231226002

Chapter 4

Reprinted with permissions from:

Synthesis and axial electropolymerization of novel amino-derived silicon phthalocyanine-based organic semiconductors. Mélanie Cyr, Gabriele Magna, Francesco Pizzoli, Alessandro Mita, Lorena Di Zazzo, Roberto Paolesse, Benoît H. Lessard, Jaclyn L. Brusso. *Journal of Materials Science*, **2026**, 61, 7621-7632.

Copyright © 2026 Springer Nature.

License Number: 6263070371038

Chapter 5

Reprinted with permissions from:

Electropolymerization of Phthalocyanine and Corrole Materials for Mass-Based Chemical Sensing and e-Nose Applications. Mélanie Cyr, Gabriele Magna, Francesco Pizzoli, Corrado Di Natale, Jaclyn L. Brusso, Benoît H. Lessard, Roberto Paolesse. *ACS Sensors*, **2026**, 11 (2), 1625-1633.

Copyright © 2026 American Chemical Society.

License Number: 6263061431831

Chapter 6

Currently unpublished work.